BAŞKENT UNIVERSITY
INSTITUTE OF SCIENCE AND ENGINEERING

MICROFLUIDIC BIOSENSORS FOR POINT OF CARE APPLICATIONS USING ELECTRICAL IMPEDANCE ANALYSIS AND PORTABLE LENSLESS WIDE-FIELD MICROSCOPY IMAGING

MEHMET YÜKSEKKAYA

DOCTOR OF PHILOSOPHY THESIS
2017

MICROFLUIDIC BIOSENSORS FOR POINT OF CARE APPLICATIONS USING ELECTRICAL IMPEDANCE ANALYSIS AND PORTABLE LENSLESS WIDE-FIELD MICROSCOPY IMAGING

YERİNDE BAKIM UYGULAMALARI İÇİN ELEKTRİKSEL EMPEDANS ANALİZİ VE TAŞINABİLİR LENS GEREKTİRMEYEN GENİŞ ALAN MİKROSKOBİK GÖRÜNTÜLEME KULLANAN MİKROAKIŞKAN BİYOSENSÖRLER

MEHMET YÜKSEKKAYA

Thesis submitted
in partial fulfillment of the requirements for
the Degree of Doctor of Philosophy
in Department of Electrical-Electronics Engineering
at Başkent University

2017

This thesis, titled: “MICROFLUIDIC BIOSENSORS FOR POINT OF CARE APPLICATIONS USING ELECTRICAL IMPEDANCE ANALYSIS AND PORTABLE LENSLESS WIDE-FIELD MICROSCOPY IMAGING”, has been approved in partial fulfilment of the requirements for the degree of DOCTOR OF PHILOSOPHY in ELECTRICAL-ELECTRONICS ENGINEERING, by our jury, on 19/6/2017.

Chairman (Advisor) : Prof. Dr. Mustafa Kocakulak

Member : Assoc. Prof. Dr. İsmail Cengiz Koçum

Member : Assoc. Prof. Dr. Memed DUMAN

Member : Assoc. Prof. Dr. Halil Murat Aydın

Member : Assist. Prof. Dr. Derya Yılmaz

APPROVAL

…../…../…..

Prof. Dr. Murat Emin AKATA
Director
Institute of Science and Engineering

BAŞKENT ÜNİVERSİTESİ FEN BİLİMLERİ ENSTİTÜSÜ
DOKTORA TEZ ÇALIŞMASI ORİJİNALLİK RAPORU

Tarih: 22 /06 / 2017

Öğrencinin Adı, Soyadı: Mehmet Yüksekkaya

Öğrencinin Numarası: 21020021

Anabilim Dalı: Elektrik-Elektronik Mühendisliği

Programı: Doktora

Danışmanın Unvanı/Adı, Soyadı: Prof. Dr. Mustafa Kocakulak

Tez Başlığı: Microfluidic Biosensors for Point of Care Applications Using Electrical Impedance Analysis and Portable Lensless Wide-Field Microscopy Imaging

Yukarıda başlığı belirtilen Doktora tez çalışmamın; Giriş, Ana Bölümler, Sonuç ve Ekler Bölümünden oluşan, toplam 187 sayfalık kısmına ilişkin, 22/06/2017 tarihinde şahsım/tez danışmanım tarafından Turnitin adlı intihal tespit programından aşağıda belirtilen filtrelemeler uygulanarak alınmış olan orijinallik raporuna göre, tezimin benzerlik oranı %8'dir.

Uygulanan filtrelemeler:

1. Kaynakça hariç
2. Alıntılar hariç
3. Beş (5) kelimeden daha az örtüşme içeren metin kısımları hariç

"Başkent Üniversitesi Enstitüleri Tez Çalışması Orijinallik Raporu Alınması ve Kullanılması Usul ve Esaslarını" inceledim ve bu uygulama esaslarında belirtilen azami benzerlik oranlarına tez çalışmamın herhangi bir intihal içermediğini; aksinin tespit edileceği muhtemel durumda doğabilecek her türlü hukuki sorumluluğu kabul ettiğimi ve yukarıda vermiş olduğum bilgilerin doğru olduğunu beyan ederim.

Öğrenci İmzası:

Onay

22/06/2017

Prof. Dr. Mustafa Kocakulak

ACKNOWLEDGEMENTS

First of all, I would like to thank to my thesis advisor Dr. Mustafa Kocakulak for his advices, guidance and patience. He supported me and gave me the opportunity to be independent in my thesis research. About the Ph. D. study he always encouraged me and put me to the right track.

I am eternally grateful to Dr. Utkan Demirci, for giving me the opportunity to join and carry out this thesis work in his laboratory, Bio-Acoustic-MEMS in Medicine (BAMM) Laboratory (Harvard Medical School, Boston, MA, USA). Dr. Demirci shaped my thesis work and he was like a second advisor for me.

I am also grateful to my supervisors in BAMM LABs, Dr. Waseem Asghar, Dr. Hadi Shafiee and Dr. Fatih İnci they taught me a lot about bioengineering concepts, thanks for their fruitful discussions and advices. I appreciate all the help that I have received from the rest of the group, who are also my friends, Dr. Sinan Güven, Michael Zhang, Muntasir Jahangir, Magesh Sadasivam, Jake Rochman, Mert Keser and Adhithi Rajagopalan. Working in Dr. Demirci's BAMM LABs was an invaluable experience also I enjoyed the time I spent in his laboratory.

I would like to thank to my Ph.D. candidacy committee members, Dr. İ. Cengiz Koçum and Dr. Derya Yılmaz, they were always ready to help. Also I would like to acknowledge to Dr. Halil Murat Aydın and Memed Duman for accepting to be the jury members for evaluating this thesis.

I appreciate my undergraduate teacher Dr. Mustafa Karaman who first introduced and encouraged me to be a researcher.

I am grateful to all my Rectors Dr. Mehmet Haberal and Dr. Ali Haberal, Dean Dr. Berna Dengiz, Chairman Dr. Ö. Faruk Elaldı and Director of the Institute Dr. M. Emin Akata in Başkent University for supporting my Ph.D. education.

My research visit to BAMM LABs was funded by TUBITAK (The Scientific and Technological Research Council of Turkey) and supported by Başkent University, I am grateful for their support.

Finally and most importantly, to my family, my father İbrahim, my mother Ayşe Özten, my sister Zekiye Ruken, my brother Barış, my nieces Ayşe Pelin and Dicle and my nephew İbrahim Özgür, they are the real supporters, they have loved me unconditionally, they gave me the opportunity to take the best education and I dedicate this doctoral degree to them. I am forever grateful to my family.

ABSTRACT

MICROFLUIDIC BIOSENSORS FOR POINT OF CARE APPLICATIONS USING ELECTRICAL IMPEDANCE ANALYSIS AND PORTABLE LENSLESS WIDE-FIELD MICROSCOPY IMAGING

Mehmet Yüksekkaya
Başkent University, Institute of Science and Engineering,
Department of Electrical-Electronics Engineering

Diagnosis and treatment monitoring near patient or point of care (POC) is an essential need. POC tests can be robust, accurate, cost effective, user friendly, specific, deliverable and sensitive according to current needs. POC tests can result faster diagnosis and optimize treatment follow up, they are also crucial for infectious diseases.

HIV/AIDS is a global issue with 36 Million infected person. Most of them are living in developing countries with limited health care resources, there is an urgent need for POC diagnosis and treatment monitoring of HIV/AIDS.

In this thesis first a flexible polymer based microfluidic biosensor using electrical impedance detection for POC HIV-1 virus load diagnosis is developed, second, a microfluidic biosensor and POC diagnosis system using lensless wide-field microscopy imaging for POC CD4+T cell counting is developed for HIV/AIDS monitoring and finally a biopreservation method for increasing the shelf life of POC CD4+T cell counting biosensor at room temperature is engineered.

POC HIV virus load diagnosis biosensor using electrical impedance analysis is able to diagnosis 10^6 - 10^8 copies/mL of HIV-1 virus load, it is practical and cost effective, and its electrical model is analyzed in detail.

POC CD4+T cell count system is able to specifically capture and automatically count CD4+T cells in whole blood with the developed novel cell detection and counting algorithm. A lensless wide-field microscope system integrated with a microfluidic cell capturing chip is developed and cell images to be counted are obtained using this microscope.

POC CD4+T cell count biosensor is engineered to increase its shelf life. Biopreservation of multilayer immuno-functionalized surfaces inside a microfluidic chip has been developed using trehalose as a biopreservation agent. That biopreserved biosensors are stored in room temperature and used for tests up two 6 months. Their cell capture accuracy, specificity and precision are almost over 90% and sensitivity is average.

KEYWORDS: Microfluidic biosensor, HIV/AIDS diagnosis, impedance spectroscopy, lensless wide-field microscopy, image processing, biopreservation of microfluidic chips.

Advisor: Prof. Dr. Mustafa Kocakulak, Başkent University, Department of Biomedical Engineering.

ÖZ

YERİNDE BAKIM UYGULAMALARI İÇİN ELEKTRİKSEL EMPEDANS ANALİZİ VE TAŞINABİLİR LENS GEREKTİRMEYEN GENİŞ ALAN MİKROSKOBİK GÖRÜNTÜLEME KULLANAN MİKROAKIŞKAN BİYOSENSÖRLER

Mehmet Yüksekkaya
Başkent Üniversitesi, Fen Bilimleri Enstitüsü,
Elektrik-Elektronik Mühendisliği Anabilim Dalı

Hasta başı ve yerinde bakım günümüzde önemli bir ihtiyaçtır. Yerinde bakım testleri mevcut ihtiyaçlara göre sağlam, doğru, düşük maliyetli, kullanıcı dostu, özgül, duyarlı ve iletilebilir olabilir. Yerinde bakım testleri ile hızlı tanı konabilir ve tedavi takibi en iyileştirilebilir, bu testlerin kullanımı bulaşıcı hastalıklar için de çok önemlidir.

HIV/AIDS küresel bir sorundur, dünyada 36 milyon HIV pozitif kişi vardır. Enfeksiyona sahip kişilerin büyük bir çoğunluğu yeterli sağlık bakım olanakları bulunmayan gelişmekte olan ülkelerdedirler. Bu nedenle HIV/AIDS teşhisi ve tedavisinin takibi için pratik, uygun maliyeti ve efektif yerinde bakım testlerine ihtiyaç vardır.

Bu tez çalışmasında ilk olarak, yerinde HIV-1 virüs yükü teşhisi için elektriksel empedans analizi kullanan esnek polimer tabanlı bir mikroakışkan biyosensör geliştirilmiştir. İkinci olarak, yerinde HIV/AIDS takibi için lens gerektirmeyen geniş alan mikroskobik görüntüleme kullanan CD4+T hücrelerinin sayımını yapabilen mikroakışkan biyosensör geliştirilmiştir, son olarak bu sensörlerin oda sıcaklığında saklanabilmesi ve nakliye edilebilmesi ve raf ömrünün arttırılması için bir biyokoruma yöntemi geliştirilmiştir.

İlk çalışmada, tasarlanan biyosensör, elektriksel empedans analizi kullanarak 10^6 - 10^8 kopya/mL HIV-1 virüs yükü teşhisi yapabilmektedir. Esnek polimer tabanlı olduğu için basit ve uygun maliyetlidir. Elektriksel modeli detaylı incelenmiştir.

İkinci çalışmada, tasarlanan biyosensör, mikroakışkan çip kullanarak kandaki CD4+T hücrelerini yakalar ve lens gerektirmeyen geniş alan mikroskobik görüntüleme kullanarak otomatik sayar. Belirtilen mikroskobik görüntüleme sistemi

uygulanmış ve yeni ve özgün bir hücre belirleme ve sayma algoritması tasarlanmıştır.

Üçüncü çalışmada, ikinci çalışmada tasarlanan mikroakışkan biyosensörün oda sıcaklığında raf ömrü arttırılmıştır. Biyokoruma ajanı olarak trehalose kullanan mikroakışkan kanallar için çoklu tabaka organik yüzey kimyası biyokoruma yöntemi geliştirilmiştir. Bu biyokorunmuş biyosensör 6 ay boyunca test edilmiştir ve hücre yakalama performansları, doğruluk, özgüllük ve hassaslık için yaklaşık %90 oranındadır ve duyarlılık için ortalamadır.

ANAHTAR SÖZCÜKLER: Mikroakışkan biyosensör, HIV/AIDS teşhisi, empedans spektroskopisi, lens gerektirmeyen geniş alan mikroskopi, görüntü işleme, mikroakışkan çiplerin biyokorunması.

Danışman: Prof. Dr. Mustafa Kocakulak, Başkent Üniversitesi, Biyomedikal Mühendisliği Bölümü.

CONTENTS

ABSTRACT i
ÖZ iii
CONTENTS v
LIST OF FIGURES ix
LIST OF TABLES xxvii
LIST OF ABBREVIATIONS xxix
1 INTRODUCTION 1
1.1 Thesis Scope 1
1.1.1 Motivation 1
1.1.2 Objectives 2
1.1.3 Walkthrough 2
1.1.4 Publications 3
1.2 Point of Care Test 4
1.3 Biosensor 12
1.3.1 Microfluidics based biosensors 13
1.3.2 Paper based microfluidic biosensors 15
1.4 Surface Functionalization for Cell and Virus Capturing 17
1.5 Multilayer Immuno-functionalized Surface Stabilization 18
2 HIV – AIDS 21
2.1 HIV Prevalence 22
2.2 Structure of HIV-1 23
2.3 HIV Entry into CD4+T Cell 24
2.4 Significance of gp-120 26
2.5 HIV/AIDS Diagnosis 26
3 IMPEDANCE SPECTROSCOPY 29
3.1 Electrochemical Cell 29
3.2 Electrical Equivalent Modelling of Electrochemical Cell 30
3.2.1 Design of an electrochemical cell 30
3.2.2 Equivalent circuit elements 31
3.2.2.1 Double layer capacitance 32
3.2.2.2 Constant phase element 33
3.2.2.3 Charge transfer resistance 33
3.2.2.4 Warburg impedance 35
3.3 Electrical Equivalent Model of Electrochemical Cell for an Electrode 35

3.4 Electrical Equivalent Circuit Model for a Full Electrode Electrochemical Cell System with Two Identical Electrodes 40
3.5 Capacitance of Coplanar Electrode System 42
3.6 Electrochemical Impedance Spectroscopy Based Biosensors 45
4 FLUORESCENCE AND LENSLESS WIDE-FIELD MICROSCOPY 48
4.1 Fluorescence Microscopy 48
4.2 Lensless Wide-field Microscopy (Shadow Imaging) Principle 49
4.3 Image Processing for Object Counting 51
4.3.1 Contrast stretching 52
4.3.2 Correlation 54
4.3.3 Thresholding 55
4.3.4 Neighborhood pixel detection 56
5 FLEXIBLE POLYMER BASED MICROFLUIDIC BIOSENSOR USING ELECTRICAL IMPEDANCE DETECTION FOR POC HIV VIRUS LOAD DIAGNOSIS 57
5.1 Materials and Methods 57
5.1.1 Flexible polymer based microfluidic chip development 58
5.1.1.1 Electrode layer 58
5.1.1.2 Channel layer 60
5.1.1.3 Inlet layer 61
5.1.2 HIV capturing and lysation 63
5.1.2.1 Magnetic bead surface functionalization 65
5.1.2.2 HIV capturing 66
5.1.2.3 HIV lysate sample preparation 67
5.1.3 Electrical Impedance spectroscopy analysis 68
5.1.3.1 Electrical Impedance spectroscopy analysis setup 68
5.1.3.2 Representation methods of impedance results 69
5.2 Experiments and Results 70
5.2.1 Electrical equivalent model for flexible polymer based microfluidic chip 71
5.2.2 Impedance measurements 71
5.2.2.1 Impedance measurement for empty channel 71
5.2.2.2 Impedance measurement for DI pure water 77
5.2.2.3 Impedance measurements for solutions with already known conductivities 79
5.2.2.4 Impedance measurements for HIV lysate in PBS 84
5.2.2.5 Time dependency test of the method 88

5.2.2.6 Lower concentration of virus diagnosis test using the method 90
5.2.2.7 Specificity test of the method 92
5.2.2.8 Impedance measurements for HIV lysate in plasma 97
5.2.2.9 Impedance measurements for HIV lysate in blood 100
5.3 Conclusion 103
6 MICROFLUIDIC BIOSENSOR USING LENSLESS WIDE FIELD MICROSCOPY IMAGING FOR POC CD4+T CELL COUNTING 106
6.1 Materials and Methods 106
6.1.1 Microfluidic chip development 106
6.1.1.1 Bottom glass layer 107
6.1.1.2 Channel layer 107
6.1.1.3 Inlet and outlet layer 108
6.1.2 Microfluidic channel surface functionalization for cell capture 110
6.1.2.1 Bottom layer glass surface functionalization 112
6.1.2.2 CD4+T cell capturing 115
6.1.3 Obtaining initial amount of CD4+T cells 116
6.1.4 Counting cells inside channels under microscope 119
6.1.4.1 Staining of CD4+T cells 120
6.1.4.2 Manual counting of cells 121
6.1.4.3 Performance Evaluation of CD4+T Cells Counting 121
6.1.5 Counting cells inside channels using lensless wide-field microscopy system 123
6.1.5.1 Lensless wide-field microscopy system development 123
6.1.6 Cell counting program 129
6.1.6.1 Sample image taken by the system 129
6.1.6.2 First program: Obtaining averaged model cell image 132
6.1.6.3 Adaptive linear histogram stretching 134
6.1.6.4 Averaged model cell image 138
6.1.6.5 Second program: Cell detection using correlation 140
6.1.7 Automatic counting of cells 146
6.2 Experiments and Results 146
6.2.1 Testing the microfluidic chip 146
6.2.2 Optimizing surface functionalization 148
6.2.3 Cell capturing performance 149
6.2.4 Cell counting under microscope 152

6.2.5 Cell counting using lensless wide-field microscopy system and cell counting program 155
6.3 Conclusion 160
7 ENGINEERING A METHOD FOR INCREASING SHELF LIFE AT ROOM TEMPERATURE OF A MICROFLUIDIC POC BIOSENSOR 162
7.1 Materials and Methods 162
7.1.1 Functionalized groups stabilization method 162
7.1.2 Microfluidic chip drying methods 163
7.1.3 Microfluidic chip preservation method 168
7.2 Experiments and Results 170
7.2.1 Performance of microfluidic chip drying methods 170
7.2.2 Cell capturing performance of stabilized microfluidic chips 172
7.3 Conclusion 175
8 CONCLUSION AND DISCUSSION 177
REFERENCES 180
APPENDIX 193

LIST OF FIGURES

Figure 1.1 Some commercially available POCT technologies. a) Alere INRatio® 2 PT/INR Monitoring System is used for anticoagulation monitoring and management by measuring Prothrombin Time/International Normalized Ratio (PT/INR) [2]. b) The Clearview® Malaria Combo is a method for testing, the presence of plasmodium falciparum, plasmodium vivax, plasmodium malariae and plasmodium ovale antigens in whole blood [3]. c) Alere Determine™ HIV 1/2 Ag/Ab Combo is used to detect free non immuno-complexed HIV p24 antigen (Ag), and antibodies (Ab) for HIV-1 and HIV-2 in human serum, plasma or whole blood (Alere Inc.) [4]. d) Accu-Chek® Aviva is a compact blood glucose meter (Copyright © F. Hoffmann-La Roche Ltd.) [5]. e) Astute140® Meter and NephroCheck® test card are for detecting biomarkers of acute kidney injury (AKI), TIMP-2 and IGFBP-7 (Astute Medical, Inc.) [6]. f) BD Veritor™ System is and influenza test for detection of Flu A+B (Becton Dickinson and Company. © 2015 BD) [7]. 4

Figure 1.2 Conventional laboratory testing versus point of care testing. a) Ordered test added on the system, b) sample collected by specialist, c) sampled labeled and sent to the laboratory, d) test performed by specialist, e) results reported and archived, f) results send to the patient and clinicians and g) simple point of care test in which the results obtained instantly.6

Figure 1.3 The infrastructure and operation requirements for a microfluidics biological test using a) a research purpose testing device, b) POCT device and c) Central laboratory test device. d) Radar charts compares the instrument cost, size, weight, multiplexing ability, required test time, specialist expertise and cost for the test. [16], [17] 7

Figure 1.4 General trend in biological tests (Adopted from [19]) 8

Figure 1.5 Components of a biosensor. 12

Figure 1.6 The process for traditional labs and microfluidics lab-on-a-chip device. (influenced form [40]) 14

Figure 1.7 An example of microfluidic a lab-on-a-chip device for DNA analysis, it is integrated the microfluidics and electronics. [43] 15

Figure 1.8 An example of a paper based bioassay by Martinez et al. [50] a) The Waterman ink absorbs by capillary action to the photolithography patterned channels in a chromatography paper. b) The assays are filled with reagents, the square is protein test, the circular on the left is glucose test and the other circular on the top is control well. c) As a negative control an artificial urine used. d) The positive assay used with glucose and protein (bovine serum albumin) in an artificial urine solution. e) Colorimetric assay results for different concentrations of glucose and protein..... 16

Figure 1.9 An example of a printed flexible plastic microchip. Silver electrodes are patterned using screen printing and channel is formed using a double sided adhesive (DSA) tape. [49] 17

Figure 1.10 Scanning electron microscope (SEM) images of two examples of affinity chromatography based capturing. In both, surfaces are functionalized by sample specific antibody. a) HIV's are immobilized in glass surface. [53] b) Breast cancer cell is immobilized on graphene oxide surface. [54] 18

Figure 2.1 A scanning electron microscope (SEM) image of an HIV infected lymphocyte (red). After culturing of virus and lymphocyte, virus reproduce itself and the HIV-1 virions (green) are budding from the lymphocyte. (Center for Disease Control and Prevention (CDC), Public Health Image Library (PHIL), ID#:10000) [91]..... 21

Figure 2.2 Adult HIV Prevalence by countries in 2007. (Adopted from [100]) 23

Figure 2.3 The structural representation of HIV virion. (Splettstoesser, Thomas (www.scistyle.com)) [103] 24

Figure 2.4 HIV-1 entry into CD4 T cells and its life cycle (National Institute of Allergy and Infectious Diseases (NIAID)) [108]..... 25

Figure 2.5 Diagnostic markers of HIV. Their levels in blood according to time, start by infection. The timing of the efficiency of the tests from first to fourth generation tests and nucleic acid amplification test (NAAT). (adopted from [109] and [110]) 26

Figure 2.6 The relation of HIV viral load and CD4+T cell count according to the progress of infection. [111]..... 27

Figure 3.1 Simple two electrode electrical impedance measurement system for solutions, V_{AC} is AC voltage source A is an ampere meter. 29

Figure 3.2 Example of a two parallel electrode system for calculation of resistance (Equation (3.1)) and capacitance (Equation (3.2)), *l* is the distance between parallel electrodes, and A is the area of the electrodes..... 30

Figure 3.3 Different electrode configurations, a) forward looking electrode, b) co-planar electrodes, c) Interdigitated electrodes. 31

Figure 3.4 Electrode in contact with an electrolyte. Electrical double layer (Helmholtz plane), and a diffuse layer formation. [124]..... 34

Figure 3.5 The electrode electrolyte interface, ion behaviors and its equivalent electrical circuit model. This electrical equivalent model for an electrode is called Randles electrical equivalent circuit model. C_{DL} is the double layer capacitance, R_{CT} is the charge transfer resistance, Z_W is the Warburg impedance and R_{sol} is the bulk resistance..... 36

Figure 3.6 Bode plot of impedance magnitude against frequency for Randles electrical equivalent circuit model. 38

Figure 3.7 Bode plot of impedance phase against frequency for Randles electrical equivalent circuit model. 39

Figure 3.8 Nyquist plot of Randles electrical equivalent circuit model's frequency response. Z_{re} is real impedance and Z_{im} is imaginary impedance..... 39

Figure 3.9 Randles electrical equivalent circuit model for each interface component in an electrochemical cell with CPE constant phase element instead of

C_{DL} double layer capacitance. R_{CT} is the charge transfer resistance, Z_W is the Warburg impedance and R_{sol} is the bulk resistance. 40

Figure 3.10 Electrical equivalent circuit model for a full electrode electrochemical cell system with two identical electrodes. The circuit model composed of two Randles equivalent circuits. CPE is constant phase element, R_{CT} is the charge transfer resistance, Z_W is the Warburg impedance, R_{sol} is the bulk resistance, C_{sol} is the bulk capacitance and R_{sys} is the ohmic resistance of the electrical wiring. 41

Figure 3.11 A simplified electrical equivalent circuit model representation for full electrode electrochemical cell system with two identical electrodes. . 41

Figure 3.12 The geometry and capacitances for coplanar electrode system. The cross section of electrochemical cell system is shown. The gap between electrodes and width of electrode are 2a and W respectively. The height of top material, inside solution, and bottom material are h_{TM}, h_{IN}, and h_{BM} respectively. The capacitance of top material, inside solution, and bottom material are C_{TM}, C_{IN}, and C_{BM} respectively. 43

Figure 3.13 Electrical field distribution for coplanar electrodes, T is the field penetration depth. 44

Figure 3.14 Electrical field distribution for coplanar electrodes, when channel height is lower than the electrode width (W). 45

Figure 4.1 Principle of fluorescence microscopy. [152] 49

Figure 4.2 A simplified demonstration of lensless wide-field microscopy (Shadow imaging) principle. 50

Figure 4.3 a) A raw shadow images of cells and b) its histogram..... 52

Figure 4.4 Piecewise linear transformation function used for contrast stretching. 53

Figure 4.5 a) Contrast stretched image of the image given in Figure 4.3 a). b) Histogram of the contrast stretch image. The transformation is applied

using the piecewise contrast stretching transformation function given in Figure 4.4 53

Figure 4.6 Cross correlation example. a) Image with objects in it, b) image of the similar object, c) 3D plot of cross correlation results where peaks indicates the center of the objects in image and d) the 2D plot of cross correlation results. x, y Axis are the spatial coordinates of image, z axis in c) and color bar in d) indicates the cross correlation result with an arbitrary unit. 54

Figure 4.7 Piecewise linear transformation function used for thresholding with a threshold value of 150. 55

Figure 5.1 The three layers of flexible polymer based microfluidic chip (FFchip). From to bottom to top: the electrode layer, channel layer and inlet layer. 58

Figure 5.2 The CAD design of mask for screen printing of electrodes. 59

Figure 5.3 The screen printing process for fabricating electrode layer. a) Placing the mask on the flexible polymer film, b) dropping some silver paste mixture, c) spreading the paste, d) after spreading the open spaces in the mask is filled with paste. 59

Figure 5.4 The CAD design of channel. 60

Figure 5.5 The CAD design of inlet layer. 61

Figure 5.6 The fabrication process of flexible polymer based microfluidic chip (FFChip). 62

Figure 5.7 The flexible polymer based microfluidic chip (FFChip). 62

Figure 5.8 The actual dimensions for lateral cross section of FFChip shown in Figure 5.7 after laser cutting of layers and drying of electrodes. 63

Figure 5.9 The model representation of a) Streptavidin coated magnetic bead, b) streptavidin on the surface of the bead, c) Biotinylated anti-gp120 antibody, and d) Human immunodeficiency virus (HIV). 64

Figure 5.10 Washing steps of magnetic beads. a) Bead are in the solution ready to wash, b) tube is stand to the magnetic separator, beads are get together close to magnet, c) solution is pipetted out, d) tube without solution but with beads only, e) tube is removed from the magnetic separator and new solution is pipetted in to the tube, f) new solution and beads are mixed together and g) mixed final solution..... 65

Figure 5.11 The anti gp120 antibody conjugation to streptavidin-coated magnetic bead. a) Incubation of magnetic beads with antibodies, b) The avidin + biotin binding, c) conjugated antibody..... 66

Figure 5.12 HIV capturing, a) the magnetic beads are suspended in HIV media culture for incubation, b) the viral envelope protein gp120 binding with anti gp120 antibody which is conjugated on the magnetic bead surface, c) Magnetics bead with immobilized HIV on its surface. 67

Figure 5.13 The HIV lysate preparation and injection to FFChip. a) Magnetic beads with immobilized HIV in biological model sample is washed 3 times with nonconductive 20% glycerol solution in DI pure water, b) lysation of HIV by suspending the beads in 1% Triton x-100 and incubating for 5 min, c) separation of lysate from beads using magnetic separator and d) injection of lysate in FFChip for impedance spectroscopy measurements. 68

Figure 5.14 Electrical impedance measurement setup for FFChip. a) Solutions, b) LCR meter, c) FFChip..... 69

Figure 5.15 Coplanar electrode configuration and its electrical equivalent circuit representation for flexible polymer based microfluidic chip..... 71

Figure 5.16 Impedance magnitude spectra of FFChips with empty channel for a frequency range between 100 Hz and 1 MHz..... 72

Figure 5.17 Impedance phase spectra of FFChips with empty channel for a frequency range between 100 Hz and 1 MHz. 73

Figure 5.18 Capacitance spectra calculated using the impedance magnitude and phase data of FFChips with empty channel when the equivalent circuit model is just a resistor parallel to a capacitor. 73

Figure 5.19 Impedance magnitude spectra of DI pure water for a frequency range between 100 Hz and 1 MHz..... 77

Figure 5.20 Impedance phase spectra of DI pure water for a frequency range between 100 Hz and 1 MHz..... 78

Figure 5.21 Nyquist plot of impedance value of DI pure water for a frequency range between 100 Hz and 1 MHz..... 78

Figure 5.22 Conductivity values for solutions with different PBS concentration. .. 79

Figure 5.23 Resistivity values for solutions with different PBS concentration..... 80

Figure 5.24 Impedance magnitude spectra of control and solutions with different PBS concentration for a frequency range between 100 Hz and 1 MHz. 80

Figure 5.25 Impedance phase spectra of control and solutions with different PBS concentration for a frequency range between 100 Hz and 1 MHz. 81

Figure 5.26 Nyquist plot of impedance value of control and solutions with different PBS concentration for a frequency range between 100 Hz and 1 MHz. 81

Figure 5.27 Impedance magnitude values of control and solutions with different PBS concentration at 1 kHz. Error bars are STD of the mean of impedance magnitude (n=3)..... 82

Figure 5.28 Normalized impedance magnitude values of solutions with different PBS concentration to the mean of impedance magnitude of control at 1 kHz.

Error bars are STD of the mean of normalized impedance magnitude (n=3). 83

Figure 5.29 Repeatability of normalized impedance magnitude measurements of control and solutions with different PBS concentration at 1 kHz. Error bars are STD of the mean of normalized impedance magnitude (n=3). 83

Figure 5.30 Impedance magnitude spectra of control and lysed HIV subtypes (A, B, C, D, E, G and Panel) for a frequency range between 100 Hz and 1 MHz. 84

Figure 5.31 Impedance phase spectra of control and lysed HIV subtypes (A, B, C, D, E, G and Panel) for a frequency range between 100 Hz and 1 MHz. 85

Figure 5.32 Nyquist plot of impedance value of control and lysed HIV subtypes (A, B, C, D, E, G and Panel) for a frequency range between 100 Hz and 1 MHz. 86

Figure 5.33 Impedance magnitude values of control and lysed HIV subtypes (A, B, C, D, E, G and Panel) at 1 kHz. Error bars are STD of the mean of impedance magnitude (n=3). 86

Figure 5.34 Normalized impedance magnitude values of lysed HIV subtypes (A, B, C, D, E, G and Panel) to the mean of impedance magnitude of control at 1 kHz. Error bars are STD of the mean of normalized impedance magnitude (n=3)..... 87

Figure 5.35 Repeatability of normalized impedance magnitude measurements of control and lysed HIV subtypes (A, B, C, D, E, G and Panel) at 1 kHz. Error bars are STD of the mean of repeatability (n=3). 88

Figure 5.36 Impedance magnitude spectra of control at different time interval after prepared (0, 20, 40, 60 and 80 min). 89

Figure 5.37 Impedance magnitude values of control at different time interval after prepared (0, 20, 40, 60 and 80 min) at 1 kHz. Error bars are STD of the mean of impedance magnitude (n=3). 89

Figure 5.38 Impedance magnitude values of control and lysed HIV subtype D with a concentration of 2.9 × 10^6 copies/mL at 1 kHz. Error bars are STD of the mean of impedance magnitude (n=3). 90

Figure 5.39 Normalized impedance magnitude values of lysed HIV subtype D with a concentration of 2.9 × 10^6 copies/mL to the mean of impedance magnitude of control at 1 kHz. Error bars are STD of the mean of normalized impedance magnitude (n=3)..... 91

Figure 5.40 Repeatability of normalized impedance magnitude measurements of control and HIV subtype D with a concentration of 2.9 × 10^6 copies/mL at 1 kHz. Error bars are STD of the mean of repeatability (n = 3)..... 92

Figure 5.41 Impedance magnitude spectra of control, HIV subtype A, EBV and HIV subtype A + EBV, for a frequency range between 100 Hz and 1 MHz. 93

Figure 5.42 Impedance phase spectra of control, HIV subtype A, EBV and HIV subtype A + EBV, for a frequency range between 100 Hz and 1 MHz. 94

Figure 5.43 Nyquist plot of impedance value of control, HIV subtype A, EBV and HIV subtype A + EBV, for a frequency range between 100 Hz and 1 MHz. 94

Figure 5.44 Impedance magnitude values of control, HIV subtype A, EBV and HIV subtype A + EBV, at 1 kHz. Error bars are STD of the mean of impedance magnitude (n=3). 95

Figure 5.45 Normalized impedance magnitude values of HIV subtype A, EBV, and HIV subtype A + EBV, to the mean of impedance magnitude of control at 1 kHz. Error bars are STD of the mean of normalized impedance magnitude (n=3)..... 96

Figure 5.46 Repeatability of normalized impedance magnitude measurements of control, HIV subtype A, EBV and HIV subtype A + EBV, at 1 kHz. Error bars are STD of the mean of repeatability (n=3). 96

Figure 5.47 Impedance magnitude spectra of control and lysed HIV subtype C spiked in plasma, for a frequency range between 100 Hz and 1 MHz. 98

Figure 5.48 Impedance magnitude values of control and lysed HIV subtype C spiked in plasma, at 1 kHz. Error bars are STD of the mean of impedance magnitude (n=3)..... 99

Figure 5.49 Normalized impedance magnitude values of lysed HIV subtype C spiked in plasma to the mean of impedance magnitude of control at 1 kHz. Error bars are STD of the mean of normalized impedance magnitude (n=3). 99

Figure 5.50 Repeatability of normalized impedance magnitude measurements of control and lysed HIV subtype C spiked in plasma at 1 kHz. Error bars are STD of the mean of repeatability (n=3). 100

Figure 5.51 Impedance magnitude spectra of control and lysed HIV subtype C spiked in whole blood, for a frequency range between 100 Hz and 1 MHz. 101

Figure 5.52 Impedance magnitude values of control and lysed HIV subtype C spiked in whole blood, at 1 kHz. Error bars are STD of the mean of impedance magnitude (n=3)..... 101

Figure 5.53 Normalized impedance magnitude values of lysed HIV subtype C spiked in whole blood to the mean of impedance magnitude of control at 1 kHz. Error bars are STD of the mean of normalized impedance magnitude (n=3). 102

Figure 5.54 Repeatability of normalized impedance magnitude measurements of control and lysed HIV subtype C spiked in whole blood at 1 kHz. Error bars are STD of the mean of repeatability (n=3). 103

Figure 6.1 The three layers of microfluidic chip. From to bottom to top: the glass layer, channel layer and inlet layer. 107

Figure 6.2 The CAD design of a channel. 107

Figure 6.3 The CAD design of channel layer (3 channels together). 108

Figure 6.4 The CAD design of inlet and outlet layer. 109

Figure 6.5 3D schematic of channel with physical dimensions. 109

Figure 6.6 Actual image of microfluidic chip. First and second channels are filled with green and yellow food dye respectively and third channel is filled with whole blood. 110

Figure 6.7 The model representation of materials from top left to bottom right, Sulfur (S), Silicon (Si), Oxygen (O), Nitrogen (N), Carbon (C), Hydrogen (H), N-g-Maleimidobutyryloxy succinimide ester (GMBS), Neutravidin, Biotinylated Anti-CD4 Antibody, Hydroxyl group, 4'-6-diamidino-2-phenylindole (DAPI), (3-Mercaptopropyl) trimethoxysilane (3-MPS), lyophilized bovine serum albumin (BSA), Trehalose and CD4+T cell. 111

Figure 6.8 Surface functionalization after cleaning of glass slide. a) Plasma treatment, b) hydroxyl (OH) groups are formed, and c) covalent binding of 3-MPS. 112

Figure 6.9 Surface functionalization after covalent binding of 3-MPS. a) GMBS binding, b) Neutravidin binding, and c) biotinylated anti-CD4 antibody conjugation to Neutravidin. 113

Figure 6.10 Surface functionalization after conjugation of biotinylated anti-CD4 antibody. a) BSA blocking, b) final groups of functionalization on glass slide. 114

Figure 6.11 Whole blood incubation in channels of microfluidic chips. 115

Figure 6.12 CD4+T cell capturing. a) Whole blood is pipetted into channel. b) CD4 antigen on the surface of the cell is bind to the anti-CD4 antibody conjugated to the surface of glass slide. 116

Figure 6.13 Cells in hemocytometer used for obtaining initial white blood cell and CD4+T cell count. Neubauer hemocytometer is used. There are 48 bright field images with 100x magnification..... 118

Figure 6.14 DAPI stained cells in hemocytometer used for obtaining initial white blood cell and CD4+T cells concentration. Neubauer hemocytometer is used. There are 48 UV fluorescent images with 100x magnification.119

Figure 6.15 Staining of captured and fixed cells on glass slide. a) DAPI and AF-488 conjugated anti-CD4 antibody stains are pipetted to the channels b) after staining. 120

Figure 6.16 LED light source for lensless wide-field microscope. The LED has its heat sink. 124

Figure 6.17 10 MP monochrome CMOS camera used as an image sensor for lensless wide-field microscope, a) view of sensor side, b) back side, and c) sensor stand horizontal. 124

Figure 6.18 CAD design for image sensor stand. Colored parts are engraved on 3mm PMMA. Black lines are cut trough. 125

Figure 6.19 Parts of light way a) lens tube b) tube to LED adaptor, c) tube to box adaptor..... 125

Figure 6.20 CAD design of box part of light way. One side is open for sensor stand and the cross side has an open circle for lens tube connection where the light will shine..... 126

Figure 6.21 Laser cutter used in that thesis work. VLS2.3, Universal Laser Systems Inc. 126

Figure 6.22 Image sensor stand with mounted image sensor. 127

Figure 6.23 lensless wide-field microscopy system. 127

Figure 6.24 Sample in a microfluidic channel on top of image sensor. Whole blood is in the channel in order to show the coverage of sensor area and channel. 128

Figure 6.25 lensless wide-field shadow imaging principle for counting of captured CD4+T cells. 128

Figure 6.26 Sample image taken by the lensless wide-field microscopy system. The image is a part of a channel in the microfluidic chip. In this channel CD4+T cells are captured. In order to image whole channel 5 of this 6.4 mm × 4.6 mm images are required. This image is 3840 × 2748 pixels (10MP) with a pixel size 1.67 μm ×1.67 μm. Two straight lines are the edges of the channel. On the top and bottom of the right side there are the shadow of pen markings. 129

Figure 6.27 Sample image of captured CD4+T cells taken by the lensless wide-field microscopy system. Wide field image of the part of a channel includes inside and some outside part of the channel shown Figure 6.26. The outside part of channel in that image is cropped and only inside of part the channel is shown in b). A small portion from that image is zoomed and shown in figure a), where shadow images of cells are visible. The image in a) is the 1 to 40 portion of the wide-field image in Figure 6.26. 130

Figure 6.28 Histogram of above image in Figure 6.27 b). 131

Figure 6.29 a) Sample image for a single cell, b) histogram of that image. 131

Figure 6.30 Sample cell images for averaging to give a shadow model for a cell. 132

Figure 6.31 Continued of Figure 6.30. From left to right, first image is the square 33x33 pixel image of a cell, second one is the round shape extracted form of the cell image, and third is the histogram of round shape. Total 30 images. 133

Figure 6.32 Pixel value statistics of single cell images given in Figure 6.30 and Figure 6.31. Minimum is the average of minimum pixel values of images. Maximum is the average of maximum pixel values of images. Mean is mean of the expected value of histogram pixel values to total pixel count in an image. Error bars are standard deviations of minimum, mean and maximum values. 134

Figure 6.33 Contrast centering algorithm. 135

Figure 6.34 Histogram (contrast) stretching algorithm..... 136

Figure 6.35 Adaptive histogram stretching of a single cell. a) A sample image of a single cell, b) histogram of that image, c) contrast centered image, d) histogram of contrast centered image, e) histogram stretched image, f) histogram of final image..... 137

Figure 6.36 a) Averaged model cell image, b) histogram of that image. 138

Figure 6.37 2D colored representation of averaged model cell image. The axes are row and column index of pixels and color bar defines the gray color codes. 138

Figure 6.38 3D colored representation of averaged model cell image. The x and y axis's are row and column index of pixels and z and color bar defines the gray color codes. 139

Figure 6.39 Pixel value statistics of the averaged model cell. 139

Figure 6.40 Sample image of cells to be counted..... 140

Figure 6.41 Sample image of cells to be counted..... 141

Figure 6.42 Adaptive histogram stretching for image to be counted. a) A sample image, b) histogram of that image, c) contrast centered image, d) histogram of contrast centered image, e) histogram stretched image, f) histogram of final image..... 142

Figure 6.43 3D representation of cross correlation result of sample image and averaged model cell. x and y axis are the pixel index values for sample image and z and color bar indicates the cross correlation output value, arbitrary unit. 143

Figure 6.44 2D representation of cross correlation result of sample image and averaged model cell. x and y axis are the pixel index values for sample image and z and color bar indicates the cross correlation output value, arbitrary unit. 144

Figure 6.45 Thresholding output of cross correlation white objects indicate the cells. The image is a binary image. 144

Figure 6.46 The pixels in white objects are grouped together and numbered. The colors codes are given to differentiate each group of pixels. Each group of pixels are corresponds to a cell. 145

Figure 6.47 Counted cells and sample image to be counted are overlapped. 145

Figure 6.48 Washing test of channels, a) the microfluidic chip channels filled with yellow and green food dye and blood from top to bottom. b), c) and d) are first, second and third washing steps respectively. For each washing step 50 µL of PBS is used. 147

Figure 6.49 Washing test of channels, a) the microfluidic chip channels filled with yellow and green food dye and blood from top to bottom. b), c) and d) are first, second and third washing steps respectively. For each washing step 100 µL of PBS is used. 148

Figure 6.50 A captured CD4+T cell in a channel, image taken by a high quality 3D fluorescence microscope. Blue indicates the nucleus and green stains outside wall of the cell. The images are for different angles, one side of the cell is flat because this side is attached to the functionalized surface of the glass slide. (1000x magnification, UV and GFP fluorescent light for different zoom levels, overlapped to give 3D image) 149

Figure 6.51 A captured CD4+T cell in a channel image taken by fluorescence microscope. Blue indicates the nucleus and green stains outside wall of the cell. a) Bright field image of a cell, b) UV and c) GFP fluorescence image for same cell, d) merge of all 3 images. (1000x magnification) 150

Figure 6.52 CD4+T cells and some WBC in a channel, 100x magnified images. a) Bright field, b) UV filter, c) GFP filter. 151

Figure 6.53 A sample image of captured CD4+T cells ate the edge of a channel. Image taken by fluorescence microscope with UV filter. The nucleus of the cell are visible. The edge also very visible, DSA seems to be visible at UV filter. 152

Figure 6.54 Bright field and fluorescence microscope images taken for manual cell counting for a channel. Each group of image is for the same channel and is composed of 31 x 7 = 217 (100x magnified) images. a) Bright field, b) UV filter, c) GFP filter. 153

Figure 6.55 CD4+T cell capture performance evaluation results for freshly prepared samples, error bars are standard deviation results. 154

Figure 6.56 Full channel images gathered using lensless wide-field microscopy system. a) Connected images, b) they are cropped to get only the channel, c) the active area where the manual and automatic cell count is applied, is highlighted. 155

Figure 6.57 Examples of empirically defining threshold process. 3 different location inside a channel is used for detecting cells. 1) Original image, 2), 3), and 4) are showing detected cells (red) for different threshold values of 750 (a.u.), 1000 (a.u.) and 1250 (a.u.), respectively. Cell counts are given in Table 6.4. 156

Figure 6.58 Examples of empirically defining threshold process. 3 different location inside a channel is used for detecting cells. 1) Original image, 2), 3), and 4) are showing detected cells (red) for different threshold values of 750

(a.u.), 1000 (a.u.) and 1250 (a.u.), respectively. Cell counts are given in Table 6.4. 157

Figure 6.59 One out of five part of a channel is counted using proposed algorithm. 920 cells (red) are counted when threshold was 1000 (a.u.). 159

Figure 7.1 Functional groups stabilization, a) trehalose injection to channels b) after drying of DI water trehalose crystallization..... 163

Figure 7.2 Microfluidic chip drying by heating experiment set up. Slide warmer is used as a heather. Thermometer is placed in order to measure exact temperature on the surface. 164

Figure 7.3 Drying chips images for the method of heating at 37ºC. a) Chip image at second hour of heating b) the areas showing the dry and wet parts of channels. c) Chip image at fourth hour of heating d) the areas showing the dry and wet parts of channels. Black is dry, white is wet. 165

Figure 7.4 The desiccator for drying of chips using vacuum..... 166

Figure 7.5 The vacuum oven for drying of chips, vacuum pressure is set to 600 mmHg and temperature is set to 37ºC. 166

Figure 7.6 Drying chips images for the method of heating at 37ºC and vacuuming with a pressure of -600 mmHg together and just vacuuming. a) Chip image at second hour of heating and vacuuming together b) the areas showing the dry and wet parts of channels. c) Chip image at fourth hour of just vacuuming d) the areas showing the dry and wet parts of channels. Black is dry, white is wet. 167

Figure 7.7 Benchtop centrifuge used for removing excessive fluid inside the channels. a) Side view and b) top view of chip inside the centrifuge and c) chamber is closed for centrifuging. 168

Figure 7.8 Vacuum sealer, vacuuming and sealing a bag with a chip and a bag of drying agent. 169

Figure 7.9 A functionalized chip, vacuum sealed with a bag of drying agent, ready for storing. 169

Figure 7.10 Drying the channels by heating. Dried channel area according to time, error bars are standard deviation results (n=3). 170

Figure 7.11 Drying the channels by vacuuming. Dried channel area according to time, error bars are standard deviation results (n=3). 171

Figure 7.12 Drying the channels by heating and vacuuming together. Dried channel area according to time, error bars are standard deviation results (n=3). 171

Figure 7.13 Drying the centrifuged channels by heating and vacuuming together. The excessive amount of fluid is already removed from the channel by centrifuging. Dried channel area according to time, error bars are standard deviation results (n=3). 172

Figure 7.14 CD4+T cell capture shelf life performance evaluation results of accuracy for stabilized samples over time. Error bars are standard deviation results. 173

Figure 7.15 CD4+T cell capture shelf life performance evaluation results of specificity for stabilized samples over time. Error bars are standard deviation results. 173

Figure 7.16 CD4+T cell capture shelf life performance evaluation results of sensitivity for stabilized samples over time. Error bars are standard deviation results. 174

Figure 7.17 CD4+T cell capture shelf life performance evaluation results of precision for stabilized samples over time. Error bars are standard deviation results. 174

LIST OF TABLES

Table 1.1 Examples of used, not common, emerging and expectations of POC Tests..... 9

Table 1.2 Advantages of POCT [20-22] 10

Table 1.3 Economic Outcomes of POCT [21, 22]..... 10

Table 1.4 The ideal rapid test: ASSURED criteria. [25] 11

Table 2.1 Summary of HIV/AIDS prevalence statistics 2015. [89, 94]..... 23

Table 3.1 The equivalent circuits' elements for a bio electrochemical system, phase angles and frequency dependence are also given. α is representing the behavior of the CPE (Adopted from [113, 117])..... 32

Table 5.1 The repeatability conditions. [161]..... 70

Table 5.2 The parameters for capacitance value of coplanar electrode system... 74

Table 5.3 Material cost for FFChip biosensor..... 104

Table 6.1 Binary classification test for CD4+T cell counting performance..... 122

Table 6.2 Binary classification test for CD4+T cell counting performance for a sample channel. Green and blue stained cells are counted from microscope images and initial WBC and CD4+T cells pipetted inside the channel are obtained. Other values in the table can be calculated from those values. 153

Table 6.3 CD4+T cell counting performance results for the sample channel. 154

Table 6.4 Manual and automatic cell count from lensless wide-field microscope images in Figure 6.57 and Figure 6.58. Different threshold values are tested in terms of detection performance. Actual cell count is performed by user and cells are counted manually. 158

Table 6.5 Automatic cell count using the developed algorithm from lensless wide-field microscope images of captured CD4+T cells in developed

microfluidic chips channel. Actual cell count is the manual count of blue stained cells under fluorescence microscope. 160

LIST OF ABBREVIATIONS

µPAD	Microfluidic paper-based analytical device
3-MPS	(3-Mercaptopropyl) trimethoxysilane
AC	Alternative current
AF	Alexa Fluor
AIDS	Acquired immune deficiency syndrome
ART	Antiretroviral therapy
ASSURED	Affordable, sensitive, specific, user friendly, robust/rapid, equipment free and deliverable
BSA	Bovine serum albumin
CAD	Computer aided design
CCD	Charge-coupled device
CMOS	Complementary metal oxide semiconductor
CPE	Constant phase element
DAPI	diamidino-2-phenylindole
DI	Deionized water
DMSO	dimethyl sulfoxide
DNA	Deoxyribonucleic acid
DSA	Double sided adhesive
EBV	Epstein-Barr virus
EIS	Electrochemical impedance spectroscopy
FFChip	Flexible polymer based microfluidic chip
GFP	Green Fluorescent Protein
GMBS	N-g-Maleimidobutyryloxy succinimide ester
HIV	Human immunodeficiency virus
INR	International normalized ratio
LED	Light-emitting diode
LOC	Lab-on-a-chip
MEMS	Micro electro mechanical systems
MEMS	Microelectromechanical systems
min	Minutes

NAAT	Nucleic acid amplification test
OH	Hydroxyl
PBS	Phosphate buffered saline
PFA	Paraformaldehyde
PMMA	Poly(methyl methacrylate)
POC	Point of care
POCT	Point of care testing
RNA	Ribonucleic acid
rpm	Revolutions per minute
SEM	Scanning electron microscope
SEM	Scanning electron microscope
USFDA	United States Food and Drug Administration
UV	Ultraviolet
WBC	White blood cell
WHO	World Health Organization

1 INTRODUCTION

This section defines the scope of the thesis and gives some introductory concepts used in the thesis.

1.1 Thesis Scope

Scope of thesis presents 4 main parts, motivation, objectives, walkthrough and publications.

1.1.1 Motivation

Infectious diseases are one of the leading causes of death. Millions of people every year die because of infectious diseases. Human immunodeficiency virus (HIV) / Acquired immune deficiency syndrome (AIDS) is an infectious disease and It has caused 35 million total dead globally, only in 2015 1.1 million people died because of AIDS and related diseases. Diagnostics is a crucial tool for preventing, treating and monitoring infection and infection related diseases. Efficient, fast, reliable, cost effective and deliverable diagnosis of HIV/AIDS is essential worldwide.

Traditional trend for diagnostics uses centralized laboratory tests. Centralized laboratories are in clinics and they need infrastructure, moreover centralized laboratory tests require many progression steps since they are slow. After the development on microfluidics, bioengineering, and nanotechnology complex tests can be done in small sized, mobile and easy to use devices at point of care (POC), those devices are called Lab-on-a-chip (LOC). Point of care test (POCT) can be fast, cost effective, easy to use and easy to access.

There is a crucial need on HIV/AIDS POC diagnosis, current approaches use HIV antibody as a target molecule. This approach is a symptom based, indirect detection approach. POC HIV virus load quantification is still on research and development level. A POC for HIV virus load detection can diagnose HIV in very early stage.

HIV infects CD4+T cells, and in order to monitor AIDS progression CD4+T cell count is mainly used. Counting of those cells is expensive, slow and needs centralized laboratory infrastructure. A POC CD4+T counting test which can be fast, cost effective, reliable and deliverable, is also crucial.

LOC devices requires receptors and usually those receptors have degradable organic molecules. Due to having degradable molecules there should be a shelf life and obligatory storage conditions of the LOC devices. There are many research on designing POC LOC devices but few of them are interested in the storage and shelf life conditions of devices. POC HIV/AIDS diagnosis LOC tests should have a certain shelf life and can be delivered to the POC easily without requirement to be stored in low temperatures.

1.1.2 Objectives

The objectives of this PhD study are three fold:

First, the development of a flexible polymer based microfluidic biosensor using electrical impedance detection for POC HIV virus load diagnosis. It is composed of, the production of a flexible polymer based microfluidic chip for electrical impedance detection, functionalization of magnetic beads for HIV capturing, construction of impedance detection system, analysis of impedance data and testing the performance of the biosensor.

Second, the development of a microfluidic biosensor and POC diagnosis system using lensless wide field microscopy imaging for POC CD4+T cell count. It is composed of, the production of a microfluidic biosensor with functionalized surface for selective capturing of CD4+T cells, implementing a POC platform for imaging of cells, developing an image processing algorithm for automatic counting of cells and testing the performance of the system.

Third, to engineering a method for increasing shelf life at room temperature of a microfluidic POC biosensor. It is composed of, the engineering and development of a method to stabilize the multilayer immuno-functionalized surface of a microfluidic chip and testing the performance of the efficiency of the method for 6 months.

1.1.3 Walkthrough

In Chapter 1, the background information of POCT, microfluidics and paper based biosensor, surface functionalization for cell and virus capturing, and functionalized group stabilization are presented.

In Chapter 2, the mechanism, diagnosis and treatment follow up of HIV/AIDS are reviewed.

In Chapter 3, and Chapter 4 the background information for impedance spectroscopy and cell microscopy techniques used in this work are explained respectively.

In Chapter 5, development, tests and performance analysis of “Flexible polymer based microfluidic biosensor using electrical impedance detection for POC HIV virus load diagnosis” is explained.

In Chapter 6, development, tests and performance analysis of “Microfluidic biosensor using lensless wide field microscopy imaging for POC CD4+T cell counting” is explained.

In Chapter 7, development, tests and performance analysis of “Engineering a method for increasing shelf life at room temperature of a microfluidic POC biosensor” is explained.

In Chapter 8, the results are discussed. Potential developments of thesis work is explained.

1.1.4 Publications

a. H. Shafiee, W. Asghar, F. Inci, M. Yuksekkaya, M. Jahangir, M. H. Zhang, et al., "Paper and flexible substrates as materials for biosensing platforms to detect multiple biotargets," Scientific Reports, volume 5, page 8719, 2015. (SCI)

b. W. Asghar, M. Yuksekkaya, H. Shafiee, M. Zhang, M. O. Ozen, F. Inci, et al., "Engineering long shelf life multi-layer biologically active surfaces on microfluidic devices for point of care applications," Scientific Reports, volume 6, page 21163, 2016. (SCI), (First two authors contributed equally to this work)

1.2 Point of Care Test

Diagnostics in health care are important tools globally. They influence more than 70% of health care decisions. Diagnostics provide proper and well-timed care to patients, satisfy the safety of blood banking, help to obtain significant data for public health and are crucial to limit health care spending. [1] One of the rising diagnostic technology is point of care (POC) technology. It allows cost effective and fast results also it does not require dedicated laboratory environment.

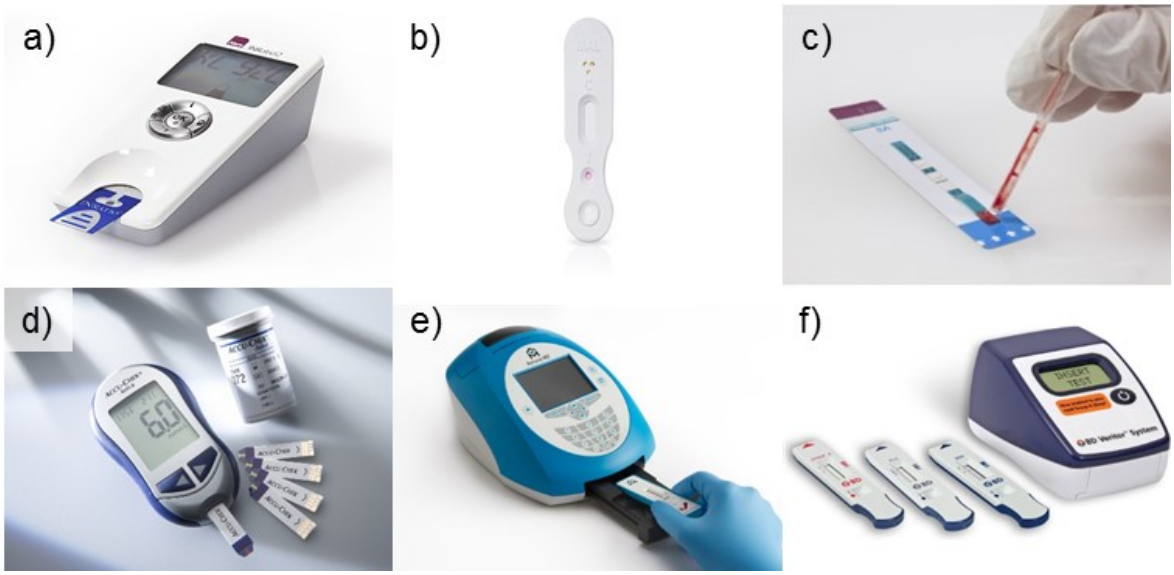

Figure 1.1 Some commercially available POCT technologies. a) Alere INRatio® 2 PT/INR Monitoring System is used for anticoagulation monitoring and management by measuring Prothrombin Time/International Normalized Ratio (PT/INR) [2]. b) The Clearview® Malaria Combo is a method for testing, the presence of plasmodium falciparum, plasmodium vivax, plasmodium malariae and plasmodium ovale antigens in whole blood [3]. c) Alere Determine™ HIV 1/2 Ag/Ab Combo is used to detect free non immuno-complexed HIV p24 antigen (Ag), and antibodies (Ab) for HIV-1 and HIV-2 in human serum, plasma or whole blood (Alere Inc.) [4]. d) Accu-Chek® Aviva is a compact blood glucose meter (Copyright © F. Hoffmann-La Roche Ltd.) [5]. e) Astute140® Meter and NephroCheck® test card are for detecting biomarkers of acute kidney injury (AKI), TIMP-2 and IGFBP-7 (Astute Medical, Inc.) [6]. f) BD Veritor™ System is and influenza test for detection of Flu A+B (Becton Dickinson and Company. © 2015 BD) [7].

Point-of-Care Testing (POCT) is defined as medical tests performed at or near the patient. POCT does not need dedicated space so there is no need for a specific medical laboratory. POCT instruments are usually hand-carried, bench top or portable cart devices which can perform immediate test with minimum complexity. They can be transported to the location of patient or they can be used as an immediate and simple testing device in operating room or intensive care unit. [8] The synonyms for POCT are bedside testing, near-patient testing, alternate-site testing and extra laboratory testing. [9]

Although the name and concepts seem new, bedside testing like urine test has been used for a long time. In last few years because of technological developments in micromachining, bioengineering and nanotechnology many diagnostic tests can be performed as POCT. [10] Some examples of currently commercial available tests are depicted in Figure 1.1.

The main purpose of POCT is to obtain the test result immediately. Immediate results can improve the efficiency of treatment and by the immediate results rapid precautions can be applied. This can guide for efficient and low cost health care. [10] POCT helps to reduce patient acuteness, morbidity, criticalness, and mortality. In life threatening emergency situations POCT can save life. POCT is effective because it helps fast diagnosis, and because diagnosis is fast the appropriate treatment can be applied faster, also monitoring of treatment can be effective and changes in treatment can be applied faster and patients and physicians are more satisfies because there is event based evidence of diagnosis and treatment monitoring. [11]

Conventional laboratory tests require many steps: first ordered test should be filed, second the sample should be obtained by the specialist in a sample collection room, third samples should be labeled and sent to the laboratory, fourth test should be applied by another specialist at a specific laboratory center, fifth results should be filed and added to archive system finally the test results are forwarded to the clinicians and patient. The progress is time and money consuming. POCT is an alternative to all of these steps. In Figure 1.2 this process is descried.

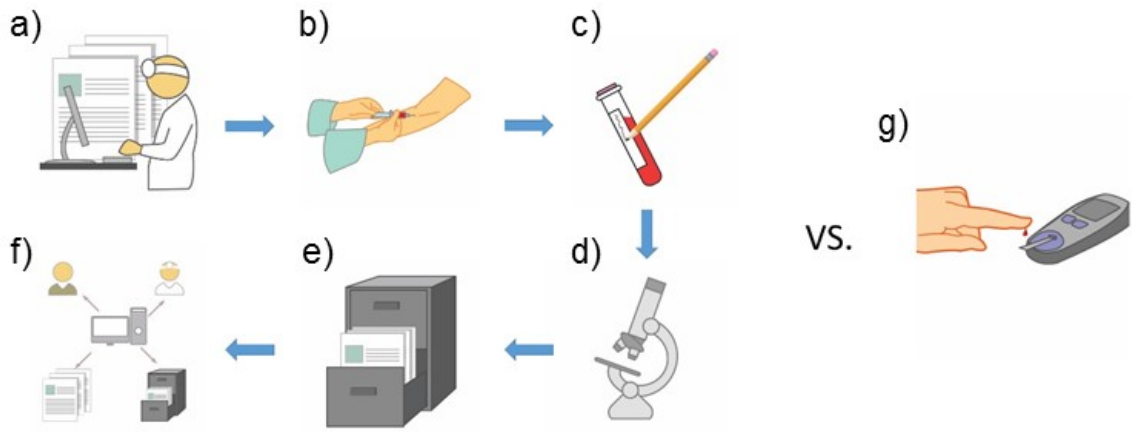

Figure 1.2 Conventional laboratory testing versus point of care testing. a) Ordered test added on the system, b) sample collected by specialist, c) sampled labeled and sent to the laboratory, d) test performed by specialist, e) results reported and archived, f) results send to the patient and clinicians and g) simple point of care test in which the results obtained instantly.

Recently support and attention on using diagnostic technologies are increased. There are three main factors for that. First is the rise of antibiotic resistance and pandemic diseases. Second scientific and technological advances on genome sequencing and antigen screening which allows unraveling of pathogenesis on a molecular level and identifies pathogen and disease biomarkers. Third the development on microfluidics, bioengineering and nanotechnology led to bring solutions for sample processing, increased assay performance and analyte detection. These factors also led to the development of POC [12-15]. They become accurate and sensitive. [1]

POCT can be divided in to two main types: hand-carried and bench top or portable cart devices. The blood gas and electrolyte analyzers are common examples for bench top or portable cart devices, these devices are like the smaller versions laboratory analyzers whereas urine albumin, blood glucose and coagulation test analyzers are examples for hand-carried devices. They are usually micro-fabricated with a simple look but they are complex systems. Some of them have the ability to do electrochemical test, optical test and immunoassay analyses. [10]

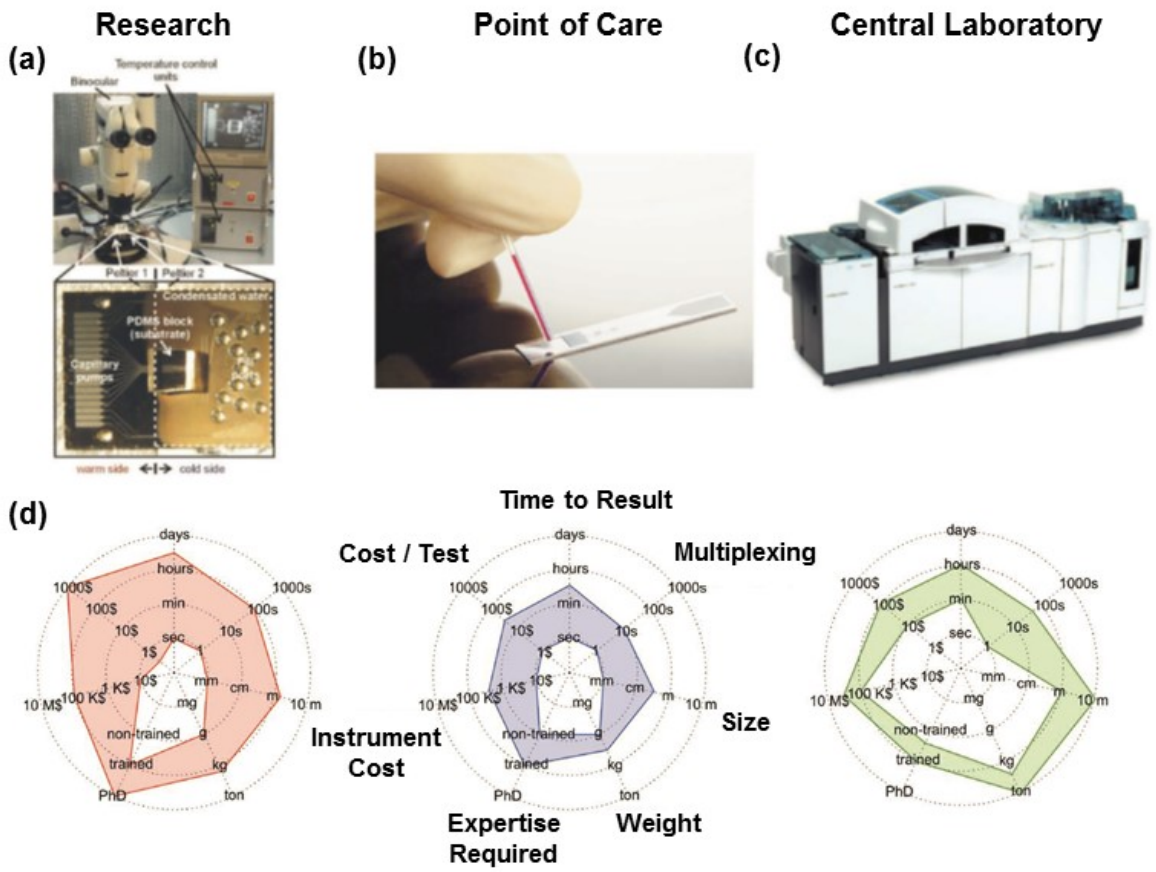

Figure 1.3 The infrastructure and operation requirements for a microfluidics biological test using a) a research purpose testing device, b) POCT device and c) Central laboratory test device. d) Radar charts compares the instrument cost, size, weight, multiplexing ability, required test time, specialist expertise and cost for the test. [16], [17]

Samples for POCT can be urine, blood, eye drop, saliva and other bodily fluids. The targets in those samples can be proteins, drugs, cells, pathogens, nucleic acids, gases and metabolites. [18]

The microfluidics biological tests are first applied as research purpose then central laboratory and POCT devices are developed. They need different requirements which are illustrated in Figure 1.3. The radar charts shows that for POCT devices, the overall requirements are lower compared to research purpose testing devices and central laboratory test devices. For POCT devices the instrument cost, test cost, expertise required for the test, time required for test results, weight and size are lower.

According to the developments in micromachining, bioengineering and nanotechnology the POC tests become highly adequate as biological test. In both developed and developing countries the trend is obtaining fast and accurate results by simple and cost efficient tests that can be applied by non-specialist in the location of patient. This general trend is depicted in Figure 1.4.

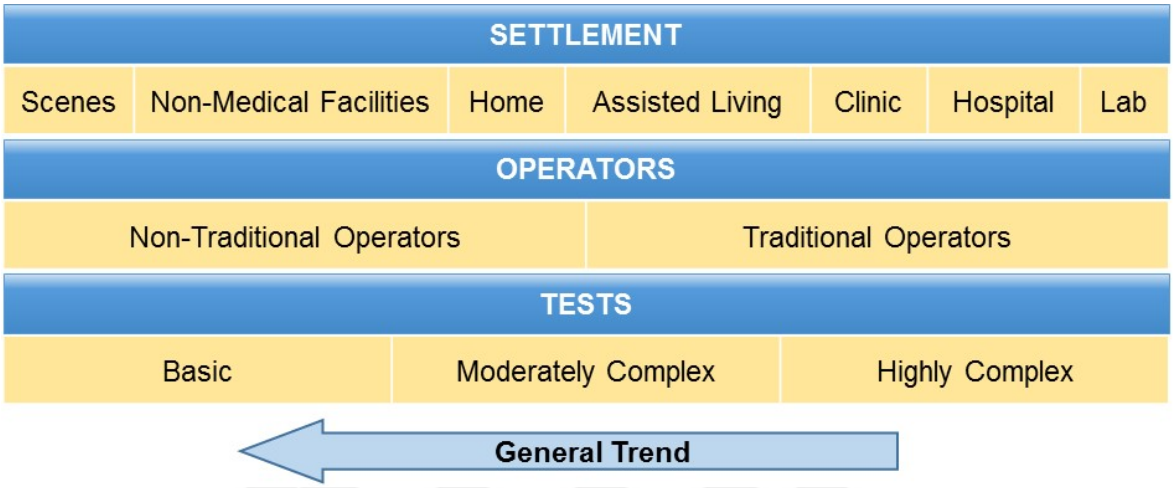

Figure 1.4 General trend in biological tests (Adopted from [19])

The technological advances bring new POC tests. By new POC tests patient-doctor counseling can be more effective. Due to immediate test results, rapid evidence based diagnosis can be possible and treatment can be prescribed immediately. So patient care process can be optimized and outcomes becomes higher. [19]

According the general trend in biological tests POCT research are growing. Some of the common, available but not common, emerging and future expectations of POC tests are shown in Table 1.1.

Because of the advantages, there is a significant increase in the development of POC tests. The advantages of POC tests are shown in Table 1.2. The most important advantage of the POCT is the faster test results which leads to faster decision and advising faster treatment plan. POCT are faster because of the reasons described in Figure 1.2, the sample does not need to transport and approval of the test is at the location of the patient. For the treatment follow up tests are needed in order to determine the efficiency of the treatment, therefore faster test results bring optimized treatment follow up.

Table 1.1 Examples of used, not common, emerging and expectations of POC Tests.

Common Use	**Available but not Common (not usually practical)**		**Emerging**	**Future Expectations**
Blood gas analysis	D dimer for thromboem-bolism	Transcutaneous bilirubin	White blood cell count	Parathyroid hormone
Electrolytes	Drug / toxicology	Influenza antigen	Complete blood count	Growth hormone
Activated clotting time for high dose heparin monitoring	Coagulation for hemostasis assessment (TEG)	Micro albumin creatinine	Coagulation for transfusion algorithms	Adrenocortico-tropic Hormone (ACTH)
Pregnancy	Heparin	Hemoglobin A1c	HIV virus	Gastrin
Occult blood	INR	HIV antibody and antigen	CD4+T cells count	Sepsis markers
Hemoglobin	Cardiac markers	Lipids		Stroke markers
Bacterial pharyngitis	Magnesium	Helicobacter pylori		DNA testing
	Lactate	Other bacteria		Microbiology
	ABO typing, crossmatch	Basic metabolic panel		

Usually POC tests requires less amount of sample compared to traditional laboratory tests because most of the tests require 25-125 mL volume of whole blood sample but for POCT the devices are usually microfluidics so 40-100μL volume of sample is enough.

POC tests are user friendly because they do not require expertise to use, maintenance, and usually they use disposable test strips/cartridges. Fast diagnosis, fast assigning of treatment plan brings patient appreciation. Immediate reports and results makes communication with patient easier. Those are some of the factors which increase patient and clinician satisfaction. [20-22]

Table 1.2 Advantages of POCT [20-22]

Faster test results
Faster treatment prescription
Optimized treatment follow up
Less precious sample volume
User friendly devices
Economic advantages
Patient and clinician satisfaction

In addition to many clinical and general health care outcomes POCT has many economical outcomes which are listed in Table 1.3. The economic outcomes are obvious if patient spend less time in clinic which can be satisfied by fast diagnosis and fast treatment follow up. When diagnosis is fast misusing of drugs are reduced. Fast healing and less spending time in clinics results in efficient use of workforce and patients will not be idle for longer time. The overall impacts are improved health quality and health care. [21, 22]

Table 1.3 Economic Outcomes of POCT [21, 22]

Short length of stay for diagnosis in clinic
Early discharge from clinic
Less clinic visit for diagnosis and treatment follow up
Less misusing of drugs
Reduced need for clinic facilities and clinicians
Improved health care

There is a higher demand in POCT, in both developing and already developed countries. The worldwide market value in 2015 was 15,743.6 Million $ and expected to be 27,507.2 Million $ in 2022. [23, 24] So in 6-7 years the market is expected to

be almost doubled worldwide. According to this higher market expectations there has been a considerable increase in research in POCT.

Although there has been a remarkable need for POCT an ideal test should have some limitations and properties. World Health Organization (WHO) defined those limitations and properties as the ideal characteristic for rapid test and announce the acronym ASSURED at 2003 WHO Special Program for Research and Training in Tropical Diseases (WHO/TDR). According to that criteria an ideal rapid test should be affordable, sensitive, specific, user friendly, robust/rapid, equipment free and deliverable to those who need. [25] This becomes as a dominant definition for POCT but since the most critical advantage of POCT is rapid diagnosis and rapid application of treatment the ideal characteristics for POCT can be reconfigured. Pai and his friends offered importance of clear and actionable decision taking within the same clinic visit. Although the test is not very user friendly or affordable in some circumstances rapid results are more important. [26] So ideal criteria's for a POCT can be "ASSURED" under the requirement of rapid and clear diagnosis and rapid beginning of treatment according to test results.

Table 1.4 The ideal rapid test: ASSURED criteria. [25]

A	Affordable
S	Sensitive
S	Specific
U	User-friendly
R	Robust and rapid
E	Equipment-free or minimal equipment that can be solar-powered
D	Deliverable to those who need them

POCT can be used and crucial for infectious diseases as well. The management of infectious diseases depend on regular and rapid testing so reliable, cost effective and sensitive tests are produced, developed and still developing for infectious diseases. POCT are able to diagnose HIV and AIDS and can be used for monitoring the status of AIDS. [27]

The needs for reliable diagnostic and treatment monitoring tests for global health are critical. [1] The crucial requirement for those tests is they should be “ASSURED” under the condition of rapid and reliable decision and initializing of treatment. The POCT can satisfy those needs, there are remarkable research on it, and future market expectations of POCT are high.

1.3 Biosensor

In order to understand the definition of biosensor one should understand the transducer and sensor. Transducer is a device capable of converting one form of energy to another form. Sensor is a device which can measure physical quantities. Biosensor is a sensor which can measure biological quantity or signal and has a transducer which can convert the biological quantity or signal into an electrical signal. [28, 29]

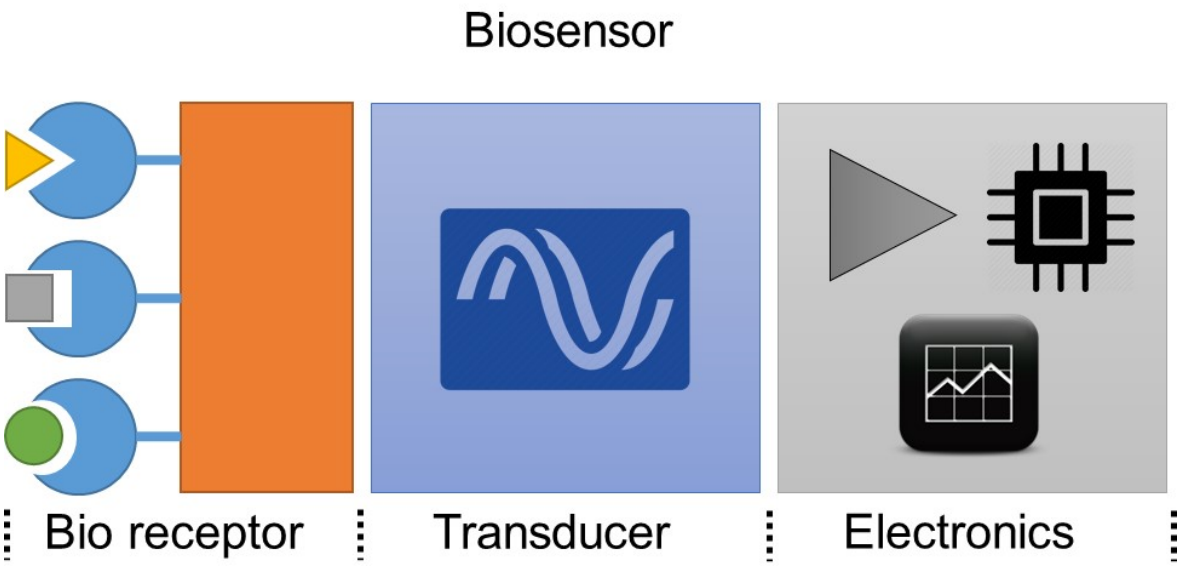

Figure 1.5 Components of a biosensor.

A typical biosensor has three main parts, bio receptor, transducer and electronics Figure 1.5. The biological quantity detected by the bio receptor is converted to electrical signal by transducer and finally this electrical signal is modified and displayed by the electronic system.

Biological samples or analytes are the target components that can be bio chemicals, molecules, proteins, pathogens, cells and tissues. Bio receptors are the bio

recognition elements that recognize the sample and can be micro-organisms, antibodies, nucleic acids, tissue, enzymes, organelles, etc. They also can be bio mimetics. [30]

The transducers are the detectors, and with bio receptor they can be called bio transducers. The detection mechanism can be optical, mechanical, electronical, electrochemical, and calorimetrical. Those detection mechanisms can be used as classification properties for biosensors.

Biosensors are used for medical diagnostics, agricultural, drug discovery, environmental monitoring, drug research, defense research, etc.[31]

1.3.1 Microfluidics based biosensors

Microfluidics is the science and technology of systems studying and analyzing of fluid flow in microscale. The flow structures which are designed less than 1 mm and large than 1 μm is called microfluidic devices. Those devices usually have channels, valves and reservoirs in microscale and fluids behavior is different compared to macroscale. [32, 33]

At microscale force due to the surface effects are higher than inertial forces. When the device is smaller electrostatic forces, viscous effects and friction becomes more effective. [33, 34] This phenomenon is explained by Galileo's "squared-cube law". [35]

$$\frac{Area}{Volume} \propto \frac{L^2}{L^3} = \frac{1}{L} \tag{1.1}$$

where, L is the main dimension of the microfluidics device. This law indicated that decrease in dimension cause faster degrease in volume properties than area properties. [33, 35]

For general laboratory type biosensing applications, manipulations of samples and reagents are done by macroscale machines. In microfluidics all those manipulations and also transducer attractions can be performed in micro devices. Microscale devices has many advantageous. Samples and reagents could be in microliter

volumes which saves the precious biological samples and reduces the costs and waste products. By using microfabrication techniques devices can be fabricated economically also integration of these devices with MEMS (Micro electro mechanical systems) electronics is possible. Using microfluidics for biosensors increased sensitivity, selectivity and repeatability also faster results become available. [36-38] Microfluidics consist of valves, channels, mixers, reservoirs, filters, and reaction, detection, storage and waste chambers.

Biosensors with microfluidics are usually designed to do laboratory functions in a single chip which is called lab-on-a-chip (LOC). [39] LOCs are cost effective, specific and detection limit is higher compared to conventional detection methods. They are also used as POCT devices. [31] Figure 1.6 illustrates the process of traditional laboratory analysis vs. Microfluidics lab-on-a-chip analysis. The process in lab-on-a-chip is faster, less samples and reagents are needed, and can be POC.

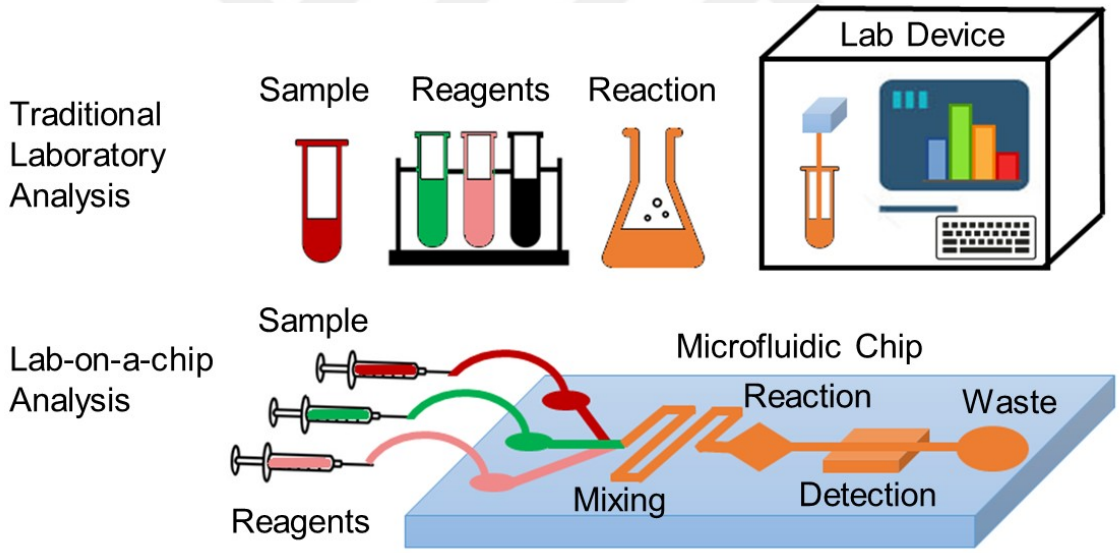

Figure 1.6 The process for traditional labs and microfluidics lab-on-a-chip device. (influenced form [40])

There are several microfluidic biosensors based point of care tests which are approved by USFDA (United States Food and Drug Administration) and used in clinic. Those tests includes, blood chemistry, urine, flu diagnostics, pathogen detection, blood coagulation etc. [41, 42]

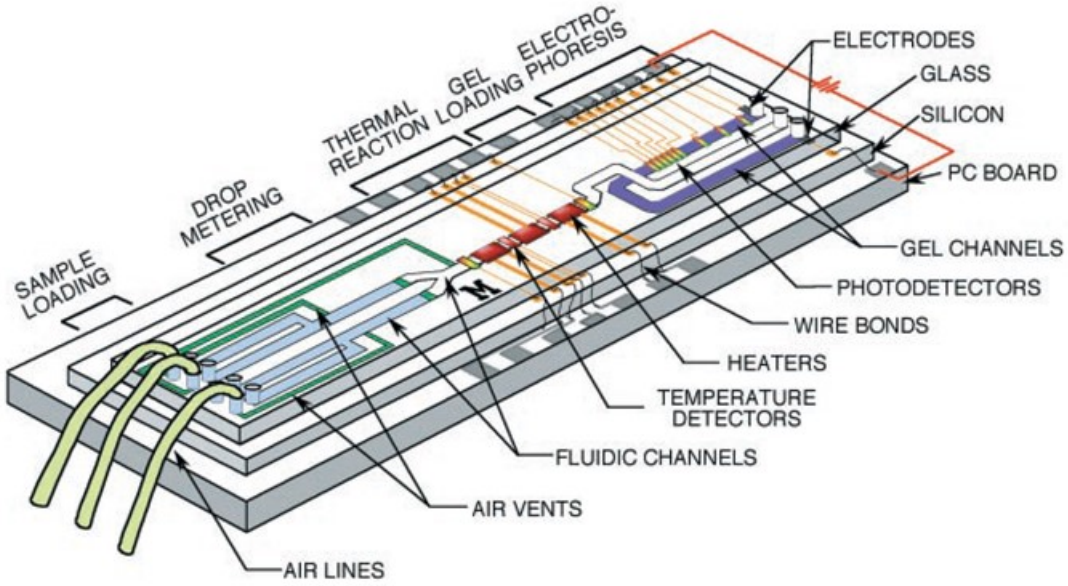

Figure 1.7 An example of microfluidic a lab-on-a-chip device for DNA analysis, it is integrated the microfluidics and electronics. [43]

In Figure 1.7 an example of a lab-on-a-chip device is shown, it is fabricated using photolithography. The device has microfluidics channels, temperature sensors, heaters, fluorescence detectors, and it is capable of performing DNA amplification and sequencing. [43]

1.3.2 Paper based microfluidic biosensors

Cellulose paper and flexible polymer paper can be used as a material for microfluidics because paper wicks liquids, porous, flexible and biocompatible. By using paper as a material for microfluidics fabrication, devices can be easy to use, low cost and easy to dispose. Microfluidic paper-based analytical devices (µPADs) is an adequate name in order to describe those kind of microfluidics. [44-47]

In paper microfluidics fluid movements are mostly passive and depends on capillarity and evaporation, hence, there is a little or no need for active fluid flow supporting equipment. Paper is made of cellulose or polymer which are biocompatible. These materials are highly compatible with a wide variety of functional groups like organic materials, DNA, protein and reagents. Paper is easy to fabricate and modify so fabrication and modification cost and complexity is lover.

Paper is flexible and foldable, which can be used to manipulate the fluid flow. Paper is flammable so easy to dispose. [47]

There are many ways to fabricate paper based microfluidic devices. It is possible to make micro-channels, reservoirs, and detection chambers on paper. Whiteside's group published the methods used for patterning paper, these methods are photolithography, plotting, inkjet etching, plasma etching, cutting and wax printing. [47] Also there is one more method which can be used for making channels, electrodes and reservoirs which is screen printing and it is used in these thesis and related publications. [48, 49]

In Figure 1.8 an example of a paper based millimeter size bioassay as a colorimetric glucose and protein detector in urine by Martinez et al. [50] is shown. In this study chromatography paper is patterned by photolithography and millimeter size channels and reservoirs are formed. The assay has the capability to detect glucose and protein. The assay is disposable, practical, small, needs no extra equipment.

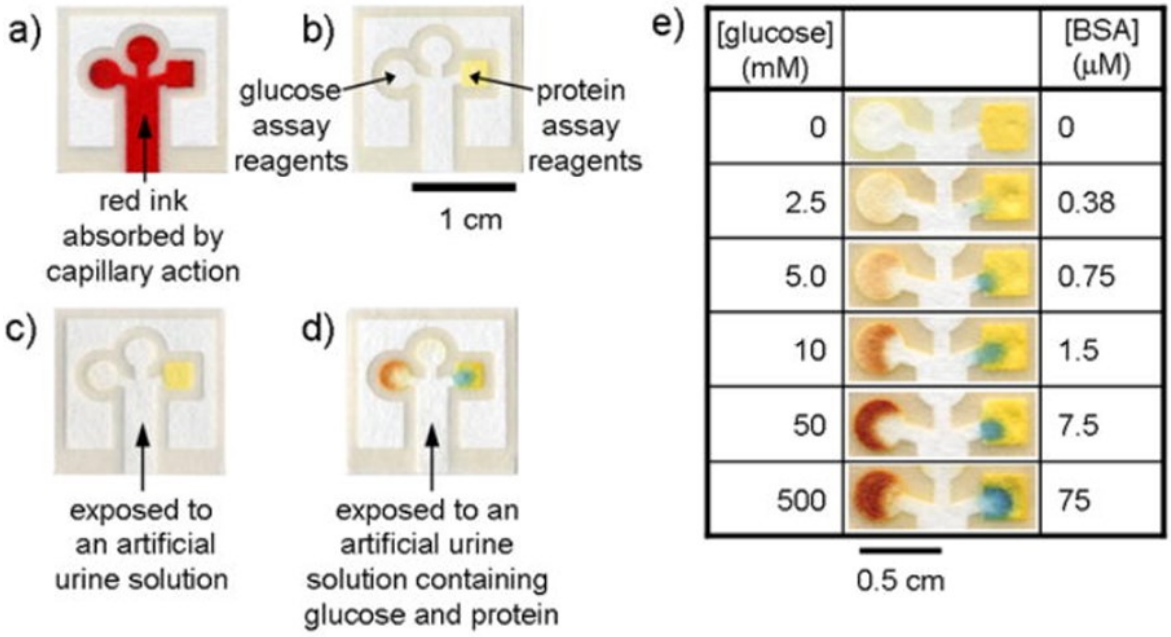

Figure 1.8 An example of a paper based bioassay by Martinez et al. [50] a) The Waterman ink absorbs by capillary action to the photolithography patterned channels in a chromatography paper. b) The assays are filled with reagents, the square is protein test, the circular on the left is glucose test and the other circular on the top is control well. c) As a negative control an artificial urine used. d) The positive

assay used with glucose and protein (bovine serum albumin) in an artificial urine solution. e) Colorimetric assay results for different concentrations of glucose and protein.

In Figure 1.9 an example of printed flexible plastic microchip for detection of virus is shown. In that study electrodes on a plastic paper were screen printed, and using a 50µm thickness double sided adhesive (DSA) tape, microchannel was constructed. In this study HIVs had been captured using an affinity based coating of magnetic microbeads, and captured viruses lysed and the electrical capacitance change of the concentration correlated with the amount of virus. The measurement was done in the flexible paper channel. [49]

Figure 1.9 An example of a printed flexible plastic microchip. Silver electrodes are patterned using screen printing and channel is formed using a double sided adhesive (DSA) tape. [49]

1.4 Surface Functionalization for Cell and Virus Capturing

The technique in order to separate a target molecule using the specific attraction between enzyme and substrate, antigen and antibody or ligand receptor is called affinity chromatography. [51]

Affinity chromatography can be used to immobilize cell and virus in a surface. In order to capture a molecule on a surface, it should be activated and functionalized so a specific molecule can be attached to the surface and the partner one can be

attracted with it and immobilize in the location. This technique is simple and used for many years. Detection becomes easier because of capturing. The partner molecule immobilized on a surface can be detected, because it is localized and concentration becomes higher. [52]

In order to immobilize the molecule on a surface usually surface is functionalized. This functionalization can be physical, chemical, and/or biological. After functionalization surface is ready to attract the target molecule.

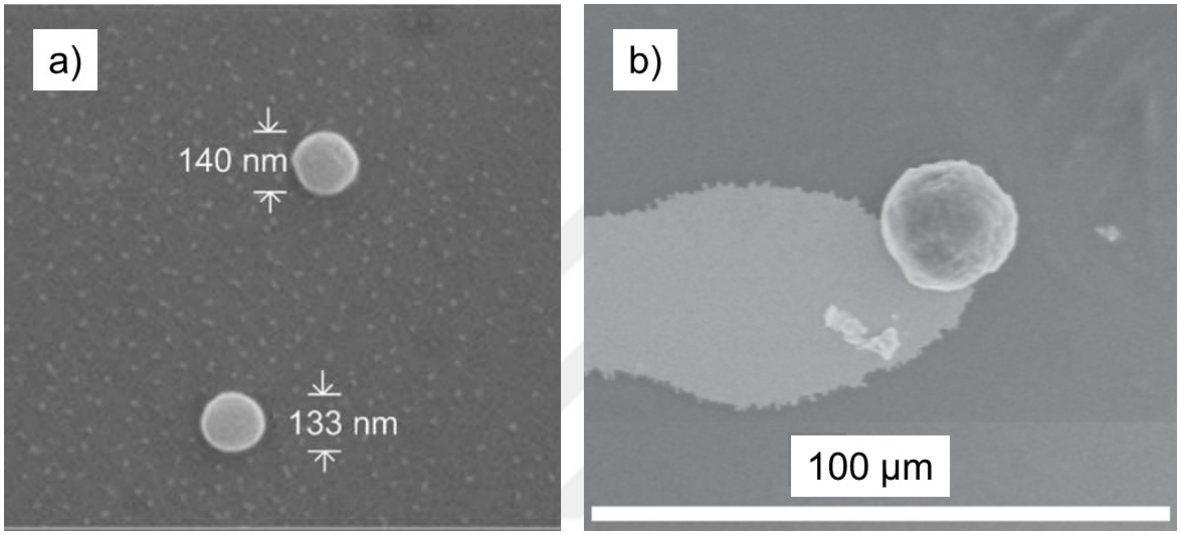

Figure 1.10 Scanning electron microscope (SEM) images of two examples of affinity chromatography based capturing. In both, surfaces are functionalized by sample specific antibody. a) HIV's are immobilized in glass surface. [53] b) Breast cancer cell is immobilized on graphene oxide surface. [54]

1.5 Multilayer Immuno-functionalized Surface Stabilization

Organic structures tend to lose their stability according to catalyzers or environmental effects. Also for antibody-antigen coated surfaces stabilization of the structure of protein is an issue. The biopreservation methods of proteins using sugar solutions (sorbitol, maltitol, glycerol, etc.) and polymers are well described and used. [55-60] However, it is still a challenge to keep the multi-layer immuno-functionalized surface of microfluidic devices stable. [61, 62] Better antibody orientation and higher capture efficiency can be ensured with the help of the multi-layer surface chemistry methods. [63] Multilayer immuno-functionalized microfluidic devices need to be stabilized in order to deliver to point of care. However for resource-constraint

settings where electricity and refrigeration are not available or not reliable, delivering and storing of those microfluidic devices are a challenge. [27, 64-67]

There are various methods such as freezing, drying, dilution and lyophilization to protect antibodies dry or in solution. [68, 69] However, immuno-functionalized microfluidic devices stabilization has recently been investigated. [13, 70, 71] In lateral flow and dipstick assays single antibodies can be stabilized. For microfluidic devices multiple antibodies and proteins which are possibly conjugated and immobilized should to be stabilized inside channels.

Sugar solutions such as trehalose can be used as a bio-preservative. Trehalose is a stress-responsive factor and it can be found in unicellular organisms in nature and trehalose is synthesized in these organisms in order to maintain the integrity of cells under stress conditions such as heat, desiccation, and cold. [72-74] Trehalose has been studied extensively related to the issues such as stabilization and preservation of biological molecules and cells. [75-79]

Trehalose can stabilize proteins via various mechanisms such as preferential exclusion, vitrification and water replacement. [80, 81]

In vitrification theory, a glassy cocoon is formed by trehalose in order to protect the protein from abiotic stresses. In this mechanism, stabilizing agent should have higher glass transition temperature (Tg) compared to storage temperature. Trehalose has the Tg as 117 ^{o}C which is higher than the room temperature. Trehalose has a better protein stabilizing ability because it has a higher Tg compared to other sugars such as maltose and sucrose. [82]

According to preferential exclusion mechanism, trehalose removes water molecules away from protein and thus reduces the protein radius, and increases the stability and compactness of the protein. In this exclusion theory, no direct interaction between protein and trehalose molecules can be observed. [80, 81]

On the other hand, water replacement theory proposed that trehalose makes hydrogen bounds with protein while drying. Due to that water molecules around protein are replaced by trehalose so stabilization is ensured because the three-dimensional structure of protein can be preserved while protein is dry. [83-86]

Stabilizing ability of trehalose (such as preserving biomolecules, proteins and cells) can be explained by these mechanisms.

Trehalose is used as a cryoprotective agent to preserve the mammalian cells and protein/antibody suspensions. [75-79] However, it has not yet been studied that trehalose can preserve functionalized microfluidic devices with immobilized antibodies and proteins at refrigeration-free conditions. There are problems in protecting a protein or a cell in a suspension and these issues are different than those related to preserving the biological surface with multiple layers of surface chemistry. For a multilayer surface chemistry diagnostic performance parameters of a device should also be maintained. [87]

2 HIV – AIDS

Virus is an infectious life form with its own genetic structure. Viruses can reproduce themselves only in a living cell. [88] The Human Immunodeficiency Virus (HIV) is a virus that effects the immune system of humans. A HIV infected person is called HIV positive (HIV+). HIV attacks immune cells. The virus infect immune cell, reproduce inside them and destroy them. Infected individuals become immunodeficient. Due to the immunodeficiency individual become vulnerable to diseases, which a healthy individual can manage. HIV positive (HIV+) individual eventually develops this immunodeficiency and it is called as Acquired Immunodeficiency Syndrome (AIDS). [89, 90]

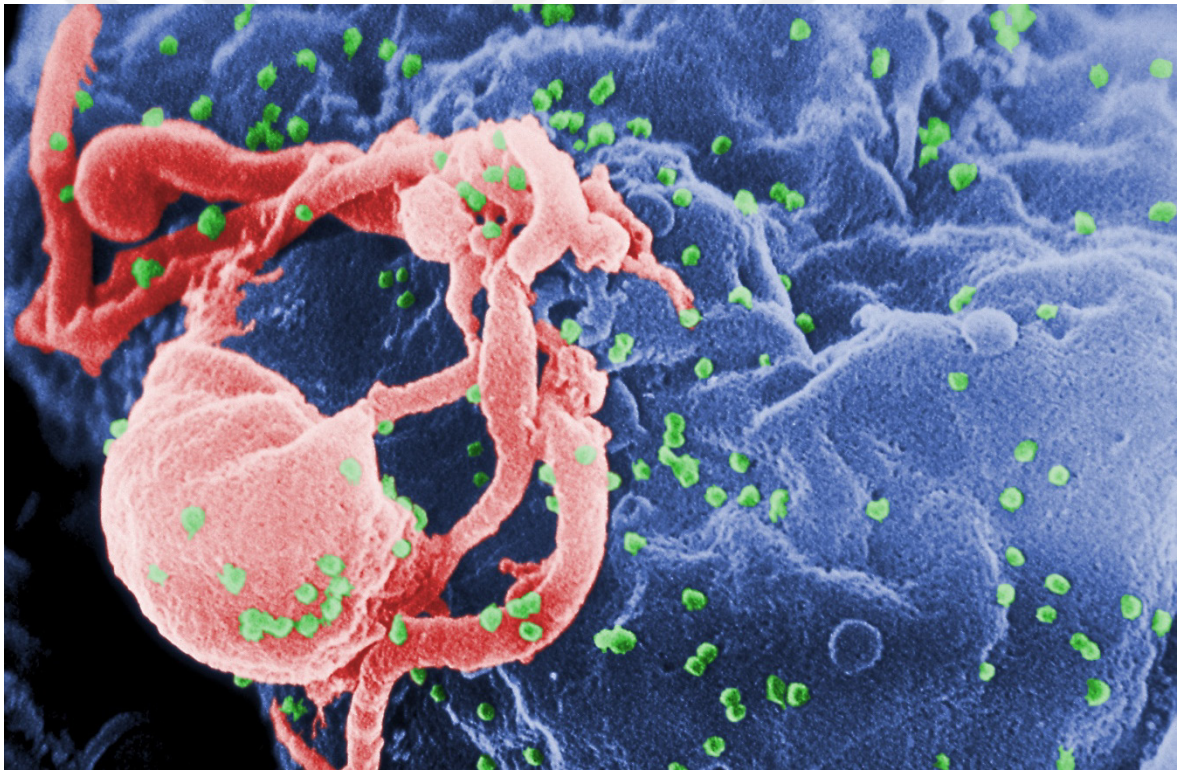

Figure 2.1 A scanning electron microscope (SEM) image of an HIV infected lymphocyte (red). After culturing of virus and lymphocyte, virus reproduce itself and the HIV-1 virions (green) are budding from the lymphocyte. (Center for Disease Control and Prevention (CDC), Public Health Image Library (PHIL), ID#:10000) [91]

HIV infects, T helper cells, dendritic cells, and macrophages. HIV especially infects CD4+T helper lymphocyte cells. CD4+T cells count is used as an indication for AIDS, if CD4+T cell count are low the immunity may lost. [92] In Figure 2.1 an SEM

image of HIV infected lymphocyte is shown. The HIV-1 virions are budding from the cytoplasm of lymphocyte.

2.1 HIV Prevalence

HIV/AIDS is a major public health issue globally. 36.7 million people globally were living with HIV. 1.1 million of them are children. [93, 94] According to population reference bureau USA world overall population is 7.2 billion [95] so almost 5 out of 1000 people have HIV/AIDS globally. In 2015 over than 2.1 million people newly infected from HIV globally and 1.1 million people with HIV died from AIDS related illnesses. [94]

70% of people living with HIV are in sub-Sharan African countries. The majority of people living with HIV are in low and medium income countries. 40% of the people are not aware of having the infection. [96] Even in an already developed country USA, in 2008, 20% of HIV-infected individuals are unaware of their diagnosis [97] and in 2013, 1.2 million people are HIV-infected and 13% of them are unaware of their diagnosis [98]. In 2015, 39,513 people were newly diagnosed with HIV. [98]

The investment to HIV infection treatment and prevention is rising every day. In 2015, US$ 19 billion was invested to AIDS in low and middle income countries which estimated to be US$ 26.2 billion in 2020 and US$ 23.9 billion in 2030. [94]

The late diagnosis of HIV is a big problem because of the increasing mortality rate and costs even in developing countries. Late diagnosis is also an important reason for spreading infection. [87, 99]

Late diagnosis means that the diagnosis is after the CD4+T cell count is dropped to 350 cells/μL (or lower) or it is dropped to that number within 91 days after diagnosis. [99]

Although the infection is widespread people who are in treatment is still low. In 2015 Around 54% of HIV-infected people did not have access to treatment and 23% of HIV-infected pregnant women did not have access to antiretroviral medicines in order to prevent infection of HIV to their fetuses. [94]

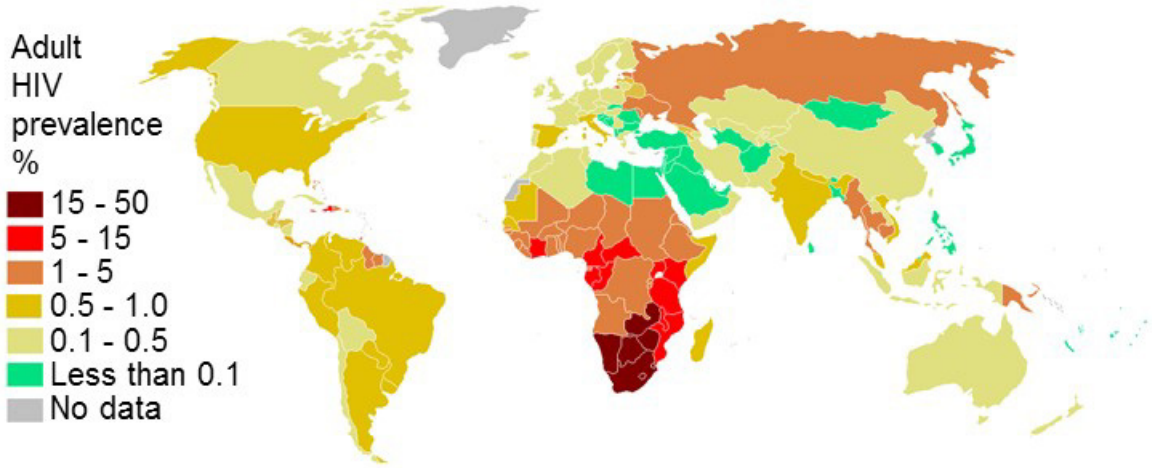

Figure 2.2 Adult HIV Prevalence by countries in 2007. (Adopted from [100])

HIV prevalence in 2017 by countries is given in Figure 2.2 and summary of HIV/AIDS prevalence statistics is given in Table 2.1.

Table 2.1 Summary of HIV/AIDS prevalence statistics 2015. [89, 94]

People living with HIV	36.7 Million
HIV prevalence globally	5 out of 1000
Percent of people living with HIV in sub-Sharan African countries compared to all people living with HIV.	70%
People on antiretroviral therapy (ART)	18.2 Million
Percent of HIV infected individuals who have not receiving antiretroviral treatment	54%
Mother-to-child transmission ratio	7 out of 10
Percent of HIV infected individuals not aware of their infections	40%
Percent of HIV infected individuals not aware of their infections in USA	20%
Investments on diagnosis and treatment in low and middle income countries	US$ 19 Billion

2.2 Structure of HIV-1

HIV-1, the predominant type of retrovirus causative of HIV, is about 120nm in diameter, and approximately spherical [101]. The structural envelope enclosing the

RNA genetic component of the virus contains important proteins that facilitate host cell-virus interactions. The surface protein which has an important function on binding of virions to cells are noncovalent trimer complex pf glycoproteins, external gp120 and transmembrane gp41. They are produced by gp160 precursor protein. They are called the env viral glycoproteins [102]

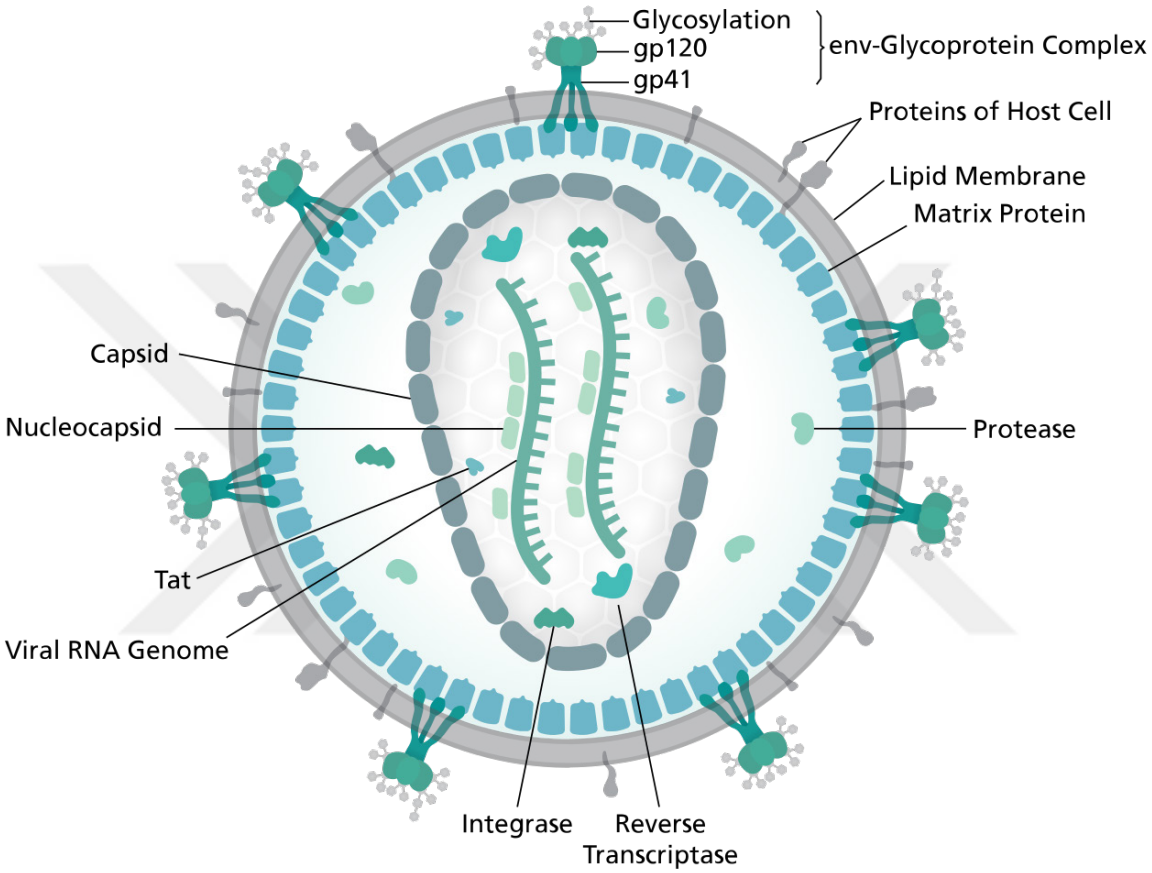

Figure 2.3 The structural representation of HIV virion. (Splettstoesser, Thomas (www.scistyle.com)) [103]

2.3 HIV Entry into CD4+T Cell

CD4 (cluster of differentiation 4) is a glycoprotein found on the surface of immune cell class CD4+T. The surface gp120 contains binding site for CD4 receptor, and other chemokine co-receptors that facilitate entry of HIV virus into the cell and fusion with cell membrane. [104] Upon entry, further intracellular signaling downstream of chemokine receptors such as CCR5 [105] and CXCR4 [106] causes the HIV viral nuclear migration and synthesis of additional virus particles thus effectively spreading the infection.

Further the virus deleteriously infects CD4+T cell activation and proliferation, thus leading to depleted levels of CD4+T cells. The human immune system is severely compromised due to depletion of CD4+T cells (cytoxic) which identify and destroy other pathogens in the blood stream. This depletion of vital immune cells leads to Acquired Immuno-Deficiency Syndrome (AIDS), where the patient is vulnerable to opportunistic infections, further weakening the immune system. [107]

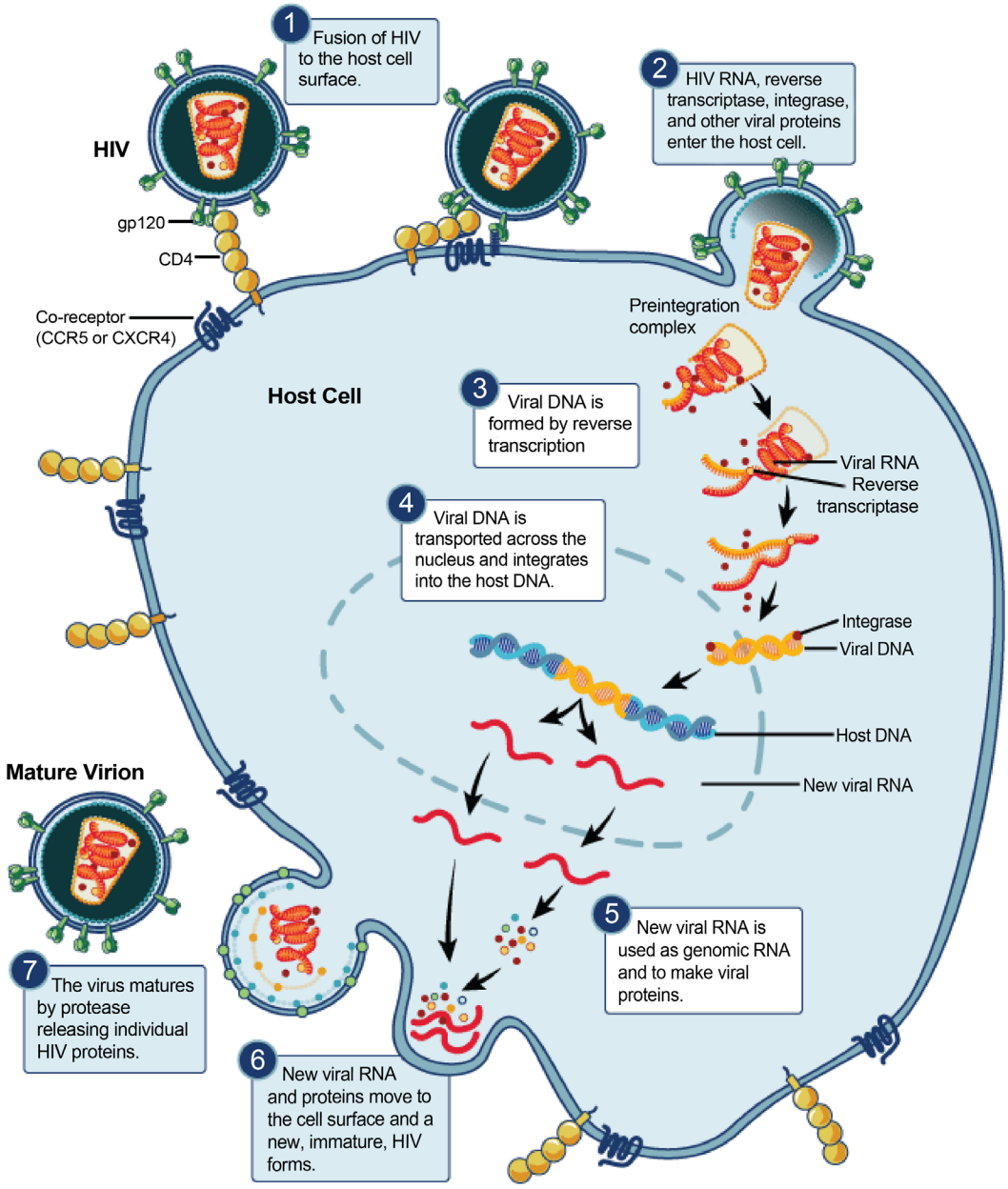

Figure 2.4 HIV-1 entry into CD4 T cells and its life cycle (National Institute of Allergy and Infectious Diseases (NIAID)) [108]

2.4 Significance of gp-120

The viral envelope protein, gp120, can be conveniently used for viral detection purposes due to its position on the viral surface and loose binding with the transmembrane gp41. Upon viral lysis, it is released from the viral surface, giving access to antibody-binding domains. [102]

2.5 HIV/AIDS Diagnosis

The infection of HIV is determined by blood or body fluids tests. The early detection is very important in order to start treatment earlier and in order not to spread the infection.

The diagnostic markers for HIV diagnosis are immunoglobulin G (IgG), immunoglobulin M (IgM), HIV ribonucleic acid (RNA) and HIV p24 antigen.

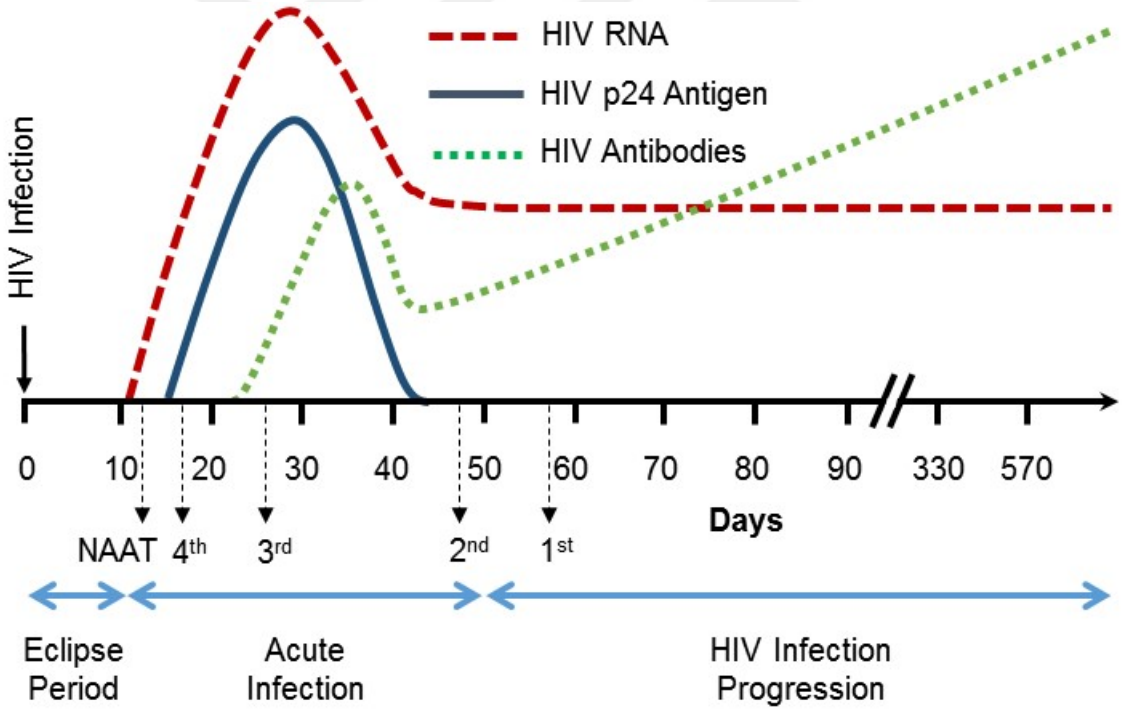

Figure 2.5 Diagnostic markers of HIV. Their levels in blood according to time, start by infection. The timing of the efficiency of the tests from first to fourth generation tests and nucleic acid amplification test (NAAT). (adopted from [109] and [110])

HIV tests can be grouped as first to fourth generation tests and nucleic acid amplification test (NAAT). First generation assays are immunoassays for detecting

IgG antibodies which are response for HIV-1 lysates as the antigens. Second generation assays are more specific compared to first generation assays, specificity is increased by producing viral antigens using peptides or recombinant proteins. Third generation assays are able to detect both HIV-1/2 IgG and IgM. The fourth generation assays can simultaneously detect HIV-1/2 IgG, IgM and p24 antigen. NAAT is the test for HIV RNA. [109, 110] The time when the tests can be applied is related to method and diagnostic markers. Timing is depicted in Figure 2.5.

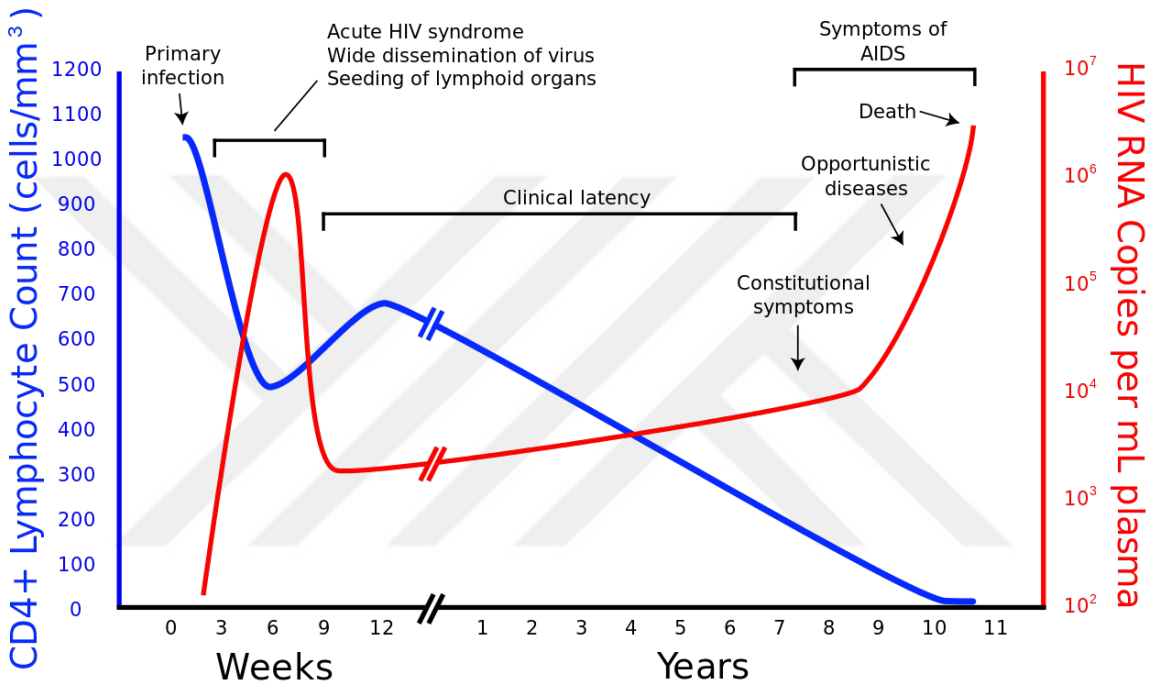

Figure 2.6 The relation of HIV viral load and CD4+T cell count according to the progress of infection. [111]

For the diagnosis and treatment monitoring of AIDS HIV viral load and CD4+T cell count are used. The therapy for AIDS is antiretroviral therapy (ART). [48] ART suppresses the viral load so infected CD4+T cells can be lower. ART is applied when CD4+T cell count falls down. According to World Health Organization (WHO) the treatment should start when CD4+T cell count is below 500 cells/µL, but for pregnant woman treatment should start immediately after HIV infection diagnosis. [64, 112] In low income settlings 1 of 4 people starts ART when CD4+T cell count falls below 100 cells/µL this is because of lack of access to HIV monitoring. Initiating ART when CD4+T cell count is below 100 cells/µL is considered as late diagnosis. Late diagnosis may result illness, less comfort of living and early death. [87, 112]

The HIV viral load relation with CD4+T cell count according to time after HIV infection is given in Figure 2.6.

3 IMPEDANCE SPECTROSCOPY

Electrical Impedance spectroscopy or electrochemical impedance spectroscopy (EIS) studies the electrical response of a system to a periodic small amplitude alternative current (AC) signal. The measurements are carried out at different frequencies, hence, the name spectroscopy. Media with the sample which is used for EIS, is usually connected to electrodes. After EIS measurements, impedance results are obtained. Those results contains information about the interface, structure and reactions taking place in the media. [113]

3.1 Electrochemical Cell

Basic EIS measurement system with two electrode setup and electrolyte solution is shown in Figure 3.1. AC voltage with different frequencies is applied to electrodes and current is measured for each frequency. When voltage is applied to the electrodes an electrical field is formed between electrodes and because of ion migration, free electrons in the solution and capacitive response of electrode system a current passes through electrodes. [114] The system with AC voltage source is called electrolytic cell or electrochemical cell. [115]

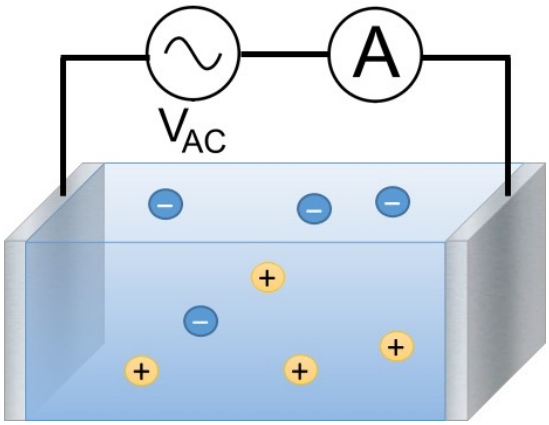

Figure 3.1 Simple two electrode electrical impedance measurement system for solutions, V_{AC} is AC voltage source A is an ampere meter.

The impedance value in two electrode system depends on bulk resistivity and permittivity of solution, geometric positing of electrodes, electrode-solution interface, electrochemical reactions taking place on the electrode and electrolysis. [115]

3.2 Electrical Equivalent Modelling of Electrochemical Cell

The EIS data is usually the impedance versus frequency data. After analyzing this data one can understand the structure of the materials in the electrochemical cell and reactions taking place in the system of an electrochemical cell. An electrical equivalent model of an electrochemical system helps to analyze the data better. The electrical equivalent model depends on the geometry/design of the system and equivalent circuit elements.

3.2.1 Design of an electrochemical cell

The geometric positioning of electrodes and the resistivity and permittivity of solution defines simple bulk resistance and capacitance of an electrical equivalent model in an electrochemical cell.

Resistivity is related to the amount and mobility of free electrons in a material, permittivity is related the polarization of the material according to an electrical field applied to material. Resistivity and permittivity of solution can be changed according to the ingredient of the solution.

The electrical field and the distribution of electrical charge on an electrode are related to the geometric positioning of electrodes which effects resistance and capacitance of the electrode system so it is effecting the impedance.

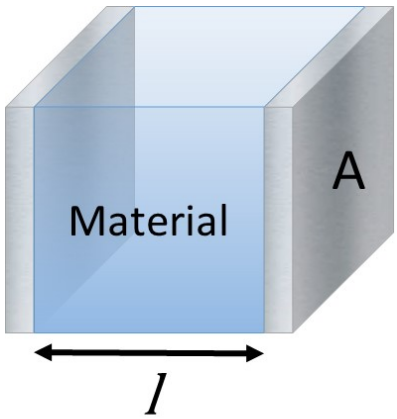

Figure 3.2 Example of a two parallel electrode system for calculation of resistance (Equation (3.1)) and capacitance (Equation (3.2)), *l* is the distance between parallel electrodes, and A is the area of the electrodes.

In Figure 3.2 a parallel electrode system is shown. The resistance and capacitance values according to the material properties are given in Equation (3.1) and (3.2) respectively. [113]

$$R = \rho \frac{l}{A} \tag{3.1}$$

$$C = \varepsilon \frac{A}{l} \tag{3.2}$$

where, *R* is resistance, *ρ* is resistivity, *l* is the distance between parallel electrodes, *A* is area of the electrode, *C* is the capacitance and ε is the permittivity. [113]

Two electrode systems can have different geometric configurations; forward looking electrodes, co-planar electrodes and interdigitated electrodes as shown in Figure 3.3. Different electrode configurations can be used to emphasize different properties of electrical information. For forward looking electrode, capacitance of the system is more effective than co planar electrode and interdigitated electrode. And between co-planar electrode and interdigitated electrode usually contact resistance is low in interdigitated one.

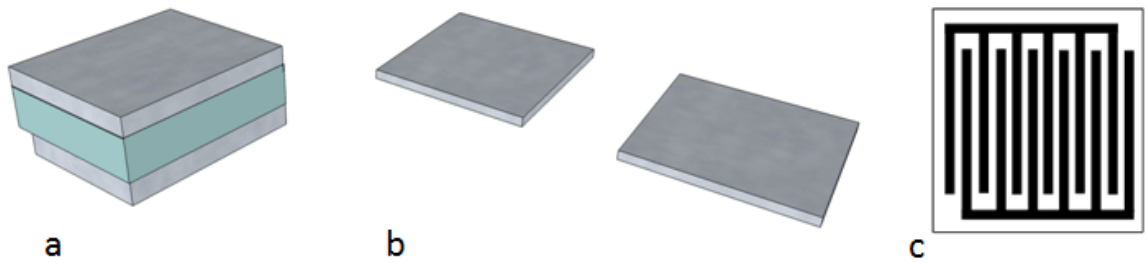

Figure 3.3 Different electrode configurations, a) forward looking electrode, b) co-planar electrodes, c) Interdigitated electrodes.

3.2.2 Equivalent circuit elements

Electrical equivalent circuit modelling is simply fitting the experimental data to an equivalent circuit model output data. Equivalent circuits and circuit's elements should be estimated on the basis of analyzing and understanding the chemical and

physical properties of the electrochemical system. [116] Table 3.1 lists some of the equivalent circuit elements, their phase angle behavior and frequency decencies.

Table 3.1 The equivalent circuits' elements for a bio electrochemical system, phase angles and frequency dependence are also given. α is representing the behavior of the CPE (Adopted from [113, 117])

Circuit Elements	Symbol	Phase Angle	Frequency Dependence
Resistance of solution	R_{sol}	0^0	No
Capacitance of solution	C_{sol}	90^0	Yes
Double layer capacitance	C_{DL}	90^0	Yes
Constant phase element	CPE	0^0 - 90^0	Yes for $\alpha \neq 0$
Charge transfer resistor	R_{CT}	0^0	No
Warburg impedance	W	45^0	Yes

Resistance and capacitance of the solution and their dependencies are described before and the rest is described further in this section. In the literature electrical equivalent circuit can have more circuit elements like sorption resistance and inductance, which usually do not exist for bio electrochemical system cells, they appear more in battery cells so they are not described.

3.2.2.1 Double layer capacitance

When an electrical voltage applied to an electrode in an ionic solution the ions are transported according to the charges on the electrodes. [118] Eventually a double layer of charge is formed on the surface of electrode given in Figure 3.4. Because of the ions onto the electrode, and electrons in the electrode this double layer is formed. This two layer of charge is separated from each other with a very thick dielectric, so it forms a capacitor and is called a double layer capacitor. The factors which are effecting the value of double layer capacitance are; electrode potential, temperature, types of ions, ionic concentrations, impurity adsorption, oxide layers, electrode roughness, electrode potential etc. [119]

3.2.2.2 Constant phase element

The double layer capacitance is modeled as an ideal capacitor and this model is adequate for homogeneous surfaces. When the surface is inhomogeneous, rough and/or porous the ideal capacitor model is not exactly fit to the experimental data. A frequency dependency in the data is observed. This phenomenon is modeled by an empirical formula and a distributed circuit element name Constant Phase Element (CPE). [120, 121] CPE is a measure of the actual double layer capacitance for inhomogeneous, rough and/or porous interfaces. [122] The formula defines CPE, is given in Equation (3.3) and (3.4).

$$Z_{CPE} = \frac{1}{Q(jw)^{\alpha}}, \qquad 0 \leq \alpha \leq 1 \tag{3.3}$$

$$Z_{CPE} = \frac{1}{Q} w^{-\alpha} \left(\cos\frac{\alpha\pi}{2} - \sin\frac{\alpha\pi}{2}\right) \tag{3.4}$$

where Z_{CPE} is the impedance of CPE (Ω), Q is the admittance of an ideal capacitance ($Fs^{\alpha-1}$ or $\Omega^{-1}s^{\alpha}$), α is an empirical constant representing the behavior of the CPE and ω is the angular frequency (Hz). [123]

The name CPE is used because the phase coefficient is assumed to be frequency independent. For α=0, CPE behaves as a resistor and for α=1, it behaves as a pure capacitor. When α= 0.5, the CPE's phase response is equivalent to the so-called Warburg element, which will be described further. α= 0.5 means that the diffusion is homogenous, other values of α represents that the diffusion is inhomogeneous. [116]

3.2.2.3 Charge transfer resistance

The electrolyte cell system allows electrochemical reactions in the solution and on the electrode surface, one of the reactions is electronically dissolving of the metal on the electrode into the solution. When metal ions dissolve in to the solution the charge moves to the electrode, this is simply a charge transfer. A current flow occurs as a result of the charge transfer. This current depends on the concentration of ions being transferred, the potential due to electrochemical reactions and the products

of the reaction. The ratio of the applied voltage to the current occurred as a result of the charge transfer is called the charge transfer resistance. The equation of charge transfer resistance is given in Equation (3.5). [113, 119]

$$R_{CT} = \frac{R_G T}{zFi_0} \tag{3.5}$$

where: R_{CT} is the charge transfer resistance (Ω), R_G is the gas constant (8.31 J/(Kmol)), T is the absolute temperature (K), z is the number electron charges involved, F is the Faraday constant (96500 C/mol) and i_0 is the exchange current density. [113, 119]

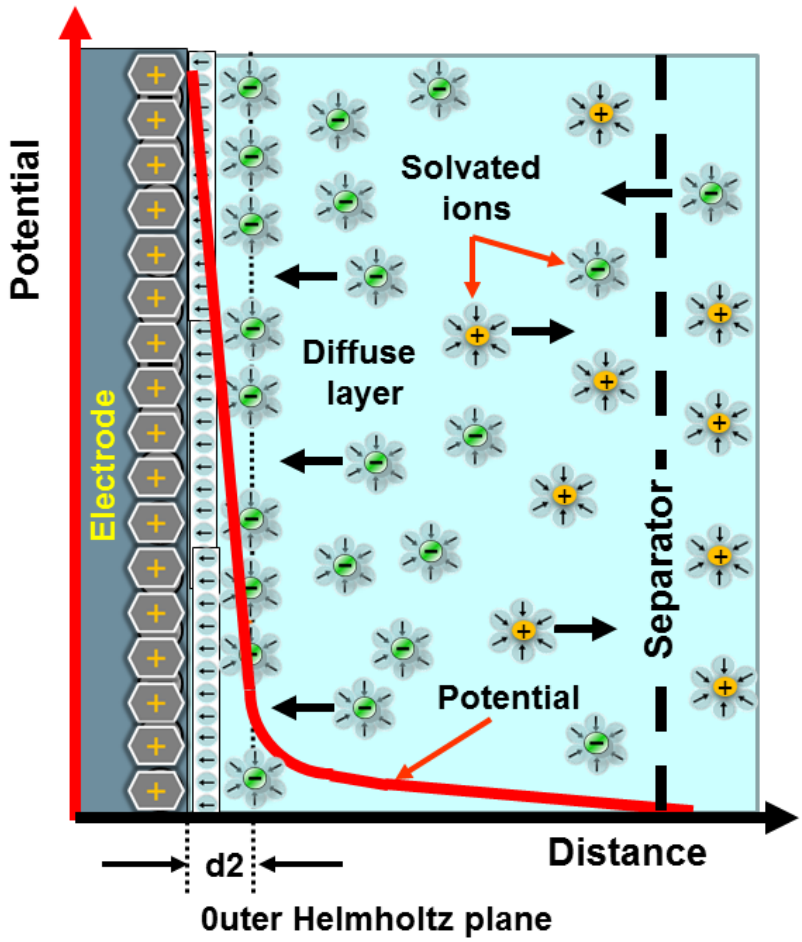

Figure 3.4 Electrode in contact with an electrolyte. Electrical double layer (Helmholtz plane), and a diffuse layer formation. [124]

3.2.2.4 Warburg impedance

The mass transport impedance is related to the migration, convection and diffusion. It is said transport because it is about the transport of reactants and species. Migration and convection can happen in the bulk solution inside the diffusion layer as shown in Figure 3.4. The diffusion is about ion migration and diffusion in the diffusion layer. The impedance occurs because of this diffusion is called Warburg impedance.

Warburg impedance is highly dependent on the frequency of applied voltage because ion movement is slow and when the polarity changes frequently there would not be a real ion movement. For lower frequencies Warburg impedance is higher and for higher frequencies it is lower. The value of Warburg impedance is proportional to Warburg coefficient and inversely proportional to square root of frequency. Warburg impedance has a 45º constant phase shift. The Warburg impedance and coefficient is given in equation (3.6) and (3.7) respectively. [113, 119]

$$Z_W = \frac{\sigma_D\,(1-j)}{\sqrt{w}} \tag{3.6}$$

$$\sigma_D = \frac{R_G T}{z^2 F^2 A\sqrt{2}}\left(\frac{1}{C^*_{OX}\sqrt{D_{OX}}} + \frac{1}{C^*_{RED}\sqrt{D_{RED}}}\right) \tag{3.7}$$

where: Z_W is the Warburg impedance (Ω), σ_D is the Warburg coefficient ($\Omega \cdot \sqrt{\mathrm{Hz}}$), w is the angular frequency (Hz), R_{CT} is the charge transfer resistance (Ω), R_G is the gas constant (8.31 J/(Kmol)), T is the absolute temperature (K), z is the electron valance number of the involved charge, F is the Faraday constant (96500 C/mol), A is the surface area of the electrode, D is the diffusion coefficient and C* is the bulk concentration. OX means oxidized and RED means reductant. [113, 119]

3.3 Electrical Equivalent Model of Electrochemical Cell for an Electrode

The electrical equivalent model of electrochemical cell at an electrode has 4 main elements: double layer capacitance, charge transfer resistance, Warburg

impedance and bulk resistance as shown in Figure 3.5. This model is called Randles electrical equivalent circuit model. [125-127]

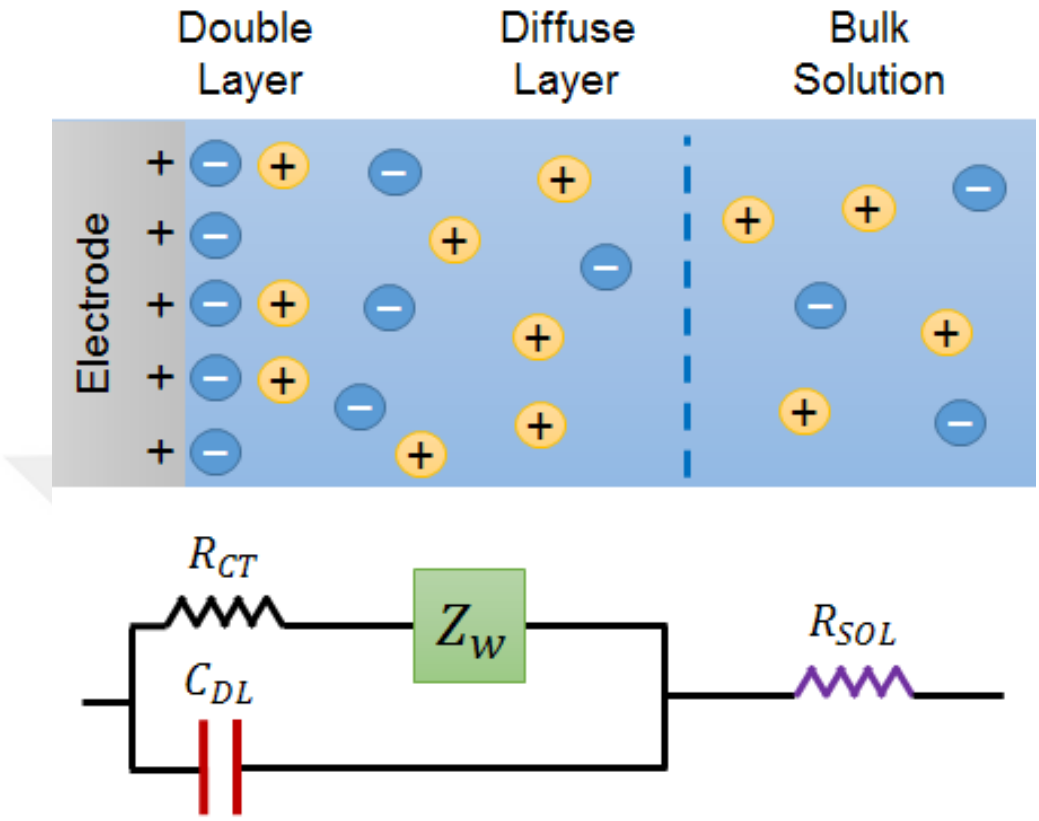

Figure 3.5 The electrode electrolyte interface, ion behaviors and its equivalent electrical circuit model. This electrical equivalent model for an electrode is called Randles electrical equivalent circuit model. C_{DL} is the double layer capacitance, R_{CT} is the charge transfer resistance, Z_W is the Warburg impedance and R_{sol} is the bulk resistance.

In Randles electrical equivalent circuit model the properties of bulk solution is simply represented by R_{sol} resistance of bulk solution and partly by Z_W Warburg Impedance, R_{CT} and C_{DL} are charge transfer resistance and capacitive double layer respectively and they are related to the electrode-electrolyte interface and reactions takes place around there. Those reactions are semi-infinite linear diffusion of electroactive particles in between electrolyte and electrodes.

The impedance value derivation for the Randles electrical equivalent circuit model is given in Appendix A and the final impedance result is given in Equation (3.8).

$$Z_{RM} = R_{sol} + \frac{R_{CT} + \sqrt{w^{-1}}\sigma_D}{\left(1+\sqrt{w}\sigma_D C_{DL}\right)^2 + \left(wR_{CT}C_{DL} + \sqrt{w}\sigma_D C_{DL}\right)^2} - j\frac{\sqrt{w^{-1}}\sigma_D + 2{\sigma_D}^2 C_{DL} + w{R_{CT}}^2 C_{DL} + 2\sqrt{w}\sigma_D R_{CT} C_{DL}}{\left(1+\sqrt{w}\sigma_D C_{DL}\right)^2 + \left(wR_{CT}C_{DL} + \sqrt{w}\sigma_D C_{DL}\right)^2} \quad (3.8)$$

The Warburg impedance is highly dependent on frequency, for higher frequencies Warburg impedance and Warburg coefficient are small. For higher frequencies the Randles electrical equivalent circuit model equation can be simplified to (3.9).

$$w \to \infty;$$

$$Z_{RM} = R_{sol} + \frac{R_{CT}}{1+(wR_{CT}C_{DL})^2} - j\frac{w{R_{CT}}^2 C_{DL}}{1+(wR_{CT}C_{DL})^2} \quad (3.9)$$

For lower frequencies the Warburg impedance becomes dominant and the Randles electrical equivalent circuit model equation can be simplified to the Equation (3.10).

$$w \to 0;$$

$$Z_{RM} = R_{sol} + R_{CT} + \sqrt{w^{-1}}\sigma_D - j\left(\sqrt{w^{-1}}\sigma_D + 2{\sigma_D}^2 C_{DL}\right) \quad (3.10)$$

In Bode plots of Randles electrical equivalent circuit model, for higher frequencies the bulk solution resistance can be observed clearly and for lower frequencies the Warburg impedance can be observed as a the difference above the line of bulk resistance plus the charge transfer resistance, which is shown in Figure 3.6. [128]

The impedance value is the ratio of AC voltage to AC current and it is a complex number. A complex number has two components real and imaginary components ($Z = Z_{re} + j * Z_{im}$). Real components can be plotted against imaginary components which is called Nyquist plot, and for Randles electrical equivalent circuit model one example is shown in Figure 3.8. The Nyquist plot give information about both the phase and magnitude of impedance in one graph.

Nyquist plot and Bode Plots are the best ways to visualize and describe Randles electrical equivalent circuit model. Bode plots are the frequency response in terms of magnitude and phase of impedance. Examples of Bode plots are shown in Figure 3.6 for the magnitude of impedance magnitude and in Figure 3.7 for phase of impedance. [129-131]

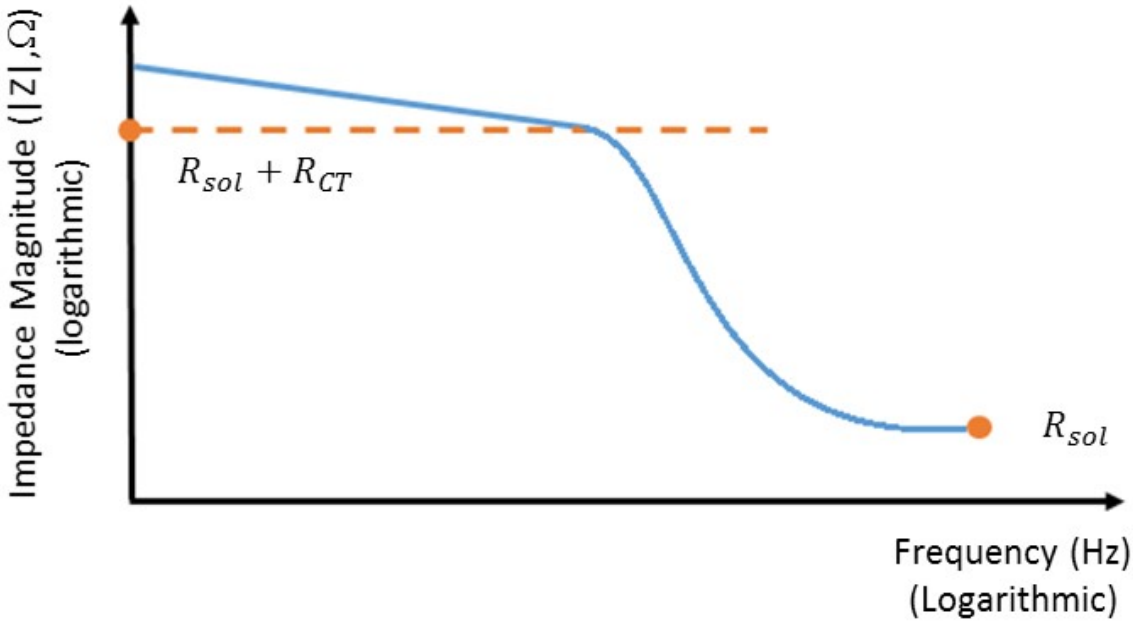

Figure 3.6 Bode plot of impedance magnitude against frequency for Randles electrical equivalent circuit model.

The Nyquist plot of Randles electrical equivalent circuit model has a semicircle and a linear part as in Figure 3.8. Semicircle which is observed for high frequencies is related to the electron transfer limited process. Linear part which is observed at lower frequencies related to the diffusion limited process. R_{CT} is charge transfer and is roughly expressed the diameter of the circle. C_{DL} is double layer capacitance and can be determined from maximum impedance value of semicircle. Both charge transfer resistance and double layer capacitance form the semicircle. R_{sol} is the bulk resistance of solution and can be obtained for higher frequencies. Warburg impedance is the reason for linear part of Nyquist plot and it appears visible for only lower frequencies. Warburg coefficient can be identified by extrapolating the liner line to the real impedance axis. [126, 129, 130]

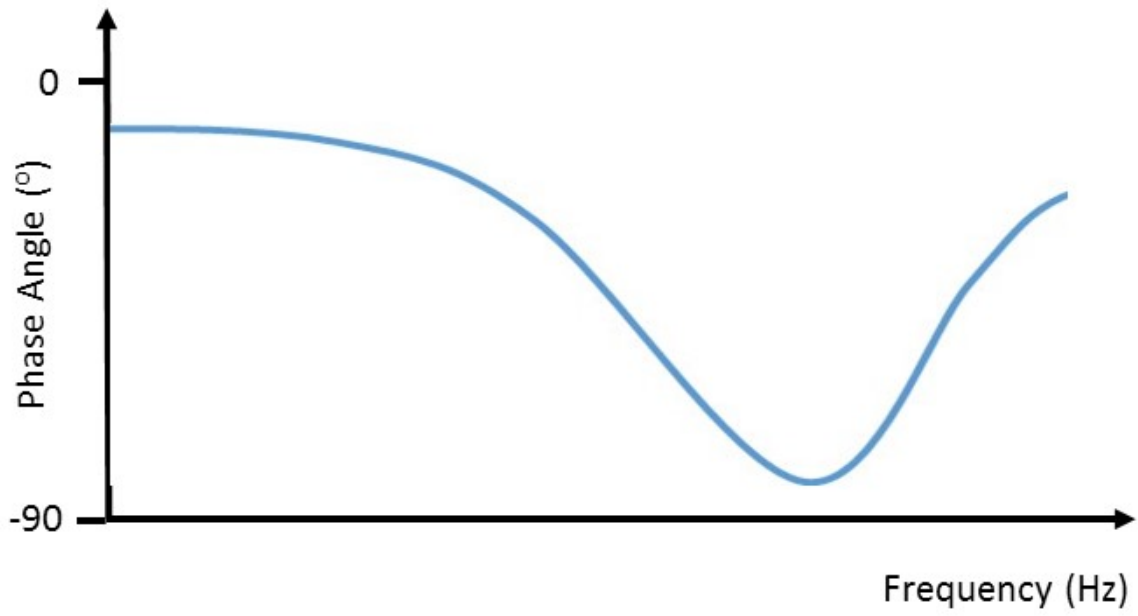

Figure 3.7 Bode plot of impedance phase against frequency for Randles electrical equivalent circuit model.

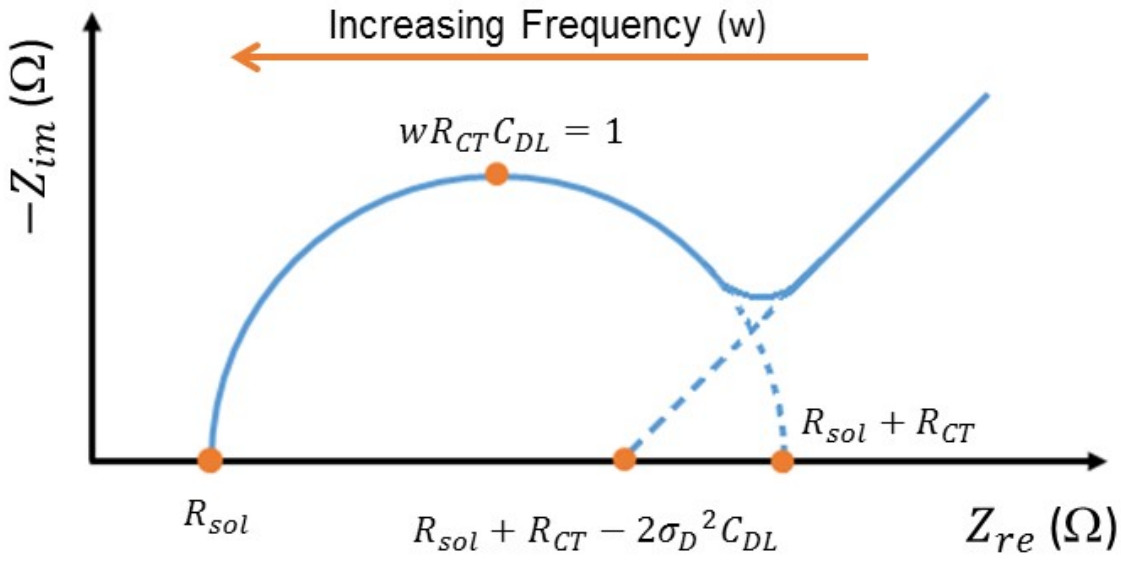

Figure 3.8 Nyquist plot of Randles electrical equivalent circuit model's frequency response. Z_{re} is real impedance and Z_{im} is imaginary impedance.

If the surface of the electrode is inhomogeneous, rough and/or porous the double layer capacitance should be replaced by constant phase element CPE. CPE is frequency dependent and more adequate to represent the impedance data. [116] The equivalent circuit with CPE replaced by C_{DL} is given in Figure 3.9.

When C_{DL} is replaced with CPE the semicircle shown in Nyquist impedance plot of Randles equivalent circuits in Figure 3.8 is suppressed according to the value of α. [116] There are several approaches for defining the value of α in an electrochemical system. α can be a function of surface roughness, the pour size distribution and fractal dimensions. α can also be related to electrochemical processes' time constants in the porous electrode. [132] CPE can be used to define the porosity of the electrode. [133]

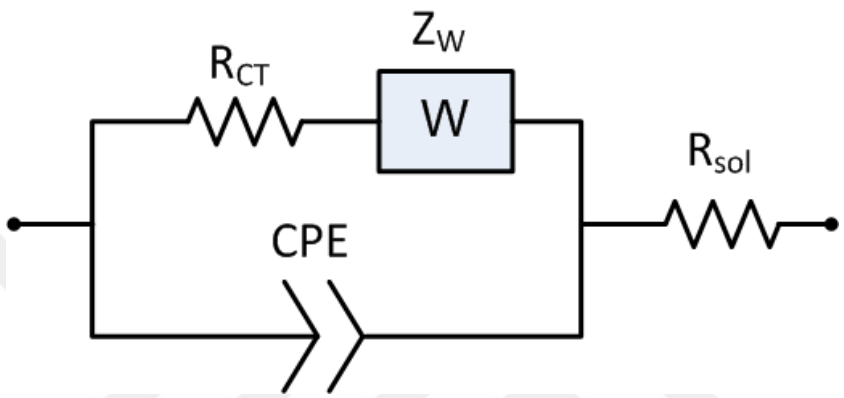

Figure 3.9 Randles electrical equivalent circuit model for each interface component in an electrochemical cell with CPE constant phase element instead of C_{DL} double layer capacitance. R_{CT} is the charge transfer resistance, Z_W is the Warburg impedance and R_{sol} is the bulk resistance.

Surface roughness and porosity of the electrodes depends on the material of electrode and process of fabricating the electrode.

3.4 Electrical Equivalent Circuit Model for a Full Electrode Electrochemical Cell System with Two Identical Electrodes

The electrodes in an electrochemical system can be either two electrode system or tree electrode system. In two electrode system when one of the electrode area is so small than the other this system is called a monopolar electrode system, and when the electrodes are same it is called bipolar electrode system. [115]

The monopolar electrode system can be defined by Randles electrical equivalent model because the surface of one electrode is so small and it can negligible from equations. However when the electrodes have same surface area the equivalent

circuits should be different and that system is called a full electrode electrochemical system.

A full electrode electrochemical system with two identical electrode can be represented by series combination of two Randles circuits, a parallel capacitor for bulk solution and a series resistor for ohmic resistance because of wiring. [113]

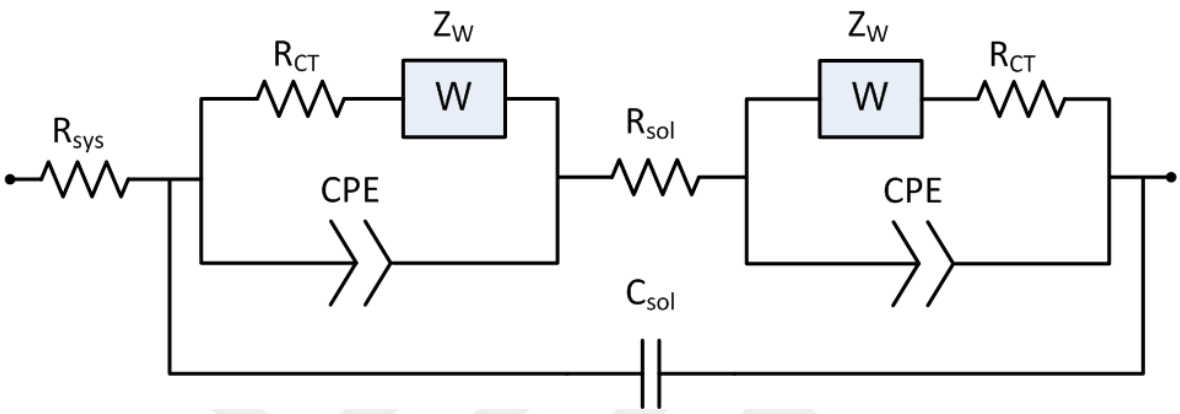

Figure 3.10 Electrical equivalent circuit model for a full electrode electrochemical cell system with two identical electrodes. The circuit model composed of two Randles equivalent circuits. CPE is constant phase element, R_{CT} is the charge transfer resistance, Z_W is the Warburg impedance, R_{sol} is the bulk resistance, C_{sol} is the bulk capacitance and R_{sys} is the ohmic resistance of the electrical wiring.

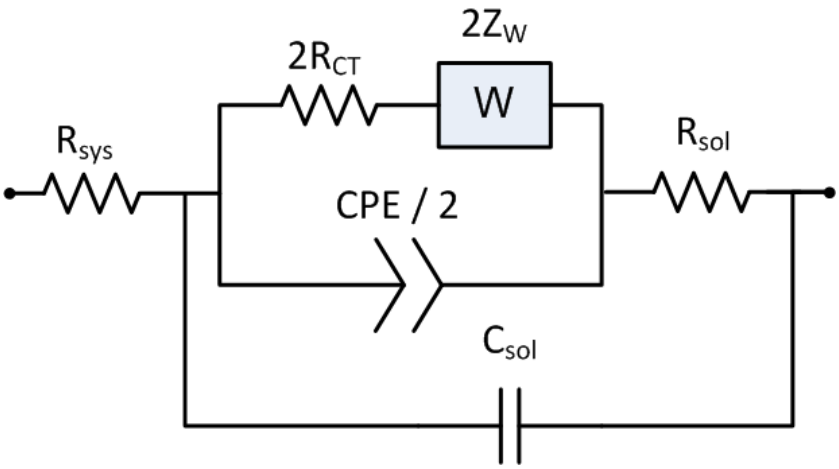

Figure 3.11 A simplified electrical equivalent circuit model representation for full electrode electrochemical cell system with two identical electrodes.

The equivalent circuit for a full electrode system is shown in Figure 3.10 and since the electrodes are identical the circuit can be simplified as in Figure 3.11. The equations are given in Equation (3.11) and (3.12).

$$Z_{FM} = R_{sys} + \frac{1}{\mathrm{jw}C_{sol} + \frac{1}{R_{sol} + \frac{1}{\frac{1}{\frac{CPE}{2}} + \frac{1}{2R_{CT} + 2Z_W}}}} \tag{3.11}$$

$$Z_{FM} = R_{sys} + \frac{1}{\mathrm{jw}C_{sol} + \frac{1}{R_{sol} + \frac{1}{\frac{1}{2}\,Q(jw)^{\alpha} + \frac{1}{2R_{CT} + 2\frac{\sigma_D\,(1-j)}{\sqrt{w}}}}}} \tag{3.12}$$

3.5 Capacitance of Coplanar Electrode System

In electrical equivalent circuit model for a full electrode electrochemical cell system with two identical electrodes C_{sol} can be very important. It is composed capacitance of the material which the coplanar electrode system is made and the capacitance depends to the geometry of system and permittivity of the solution. If this capacitance value is higher, the system impedance is highly effected and even if it is lover the system impedance is still effected for higher frequencies. The studies [134-136] about understanding the capacitance value of coplanar electrodes showed that the capacitance value is dependent on the geometry and the solution permittivity.

In order to understand the capacitance of coplanar electrode system the geometry of the system should be defined. In Figure 3.12 the geometry of the coplanar electrode is system is defined. There are tree capacitance values to define the resultant capacitance. The capacitance of top material, inside solution, and bottom material are C_{TM}, C_{IN}, and C_{BM} respectively, they are in parallel to each other, so the total capacitance will be the sum of all.

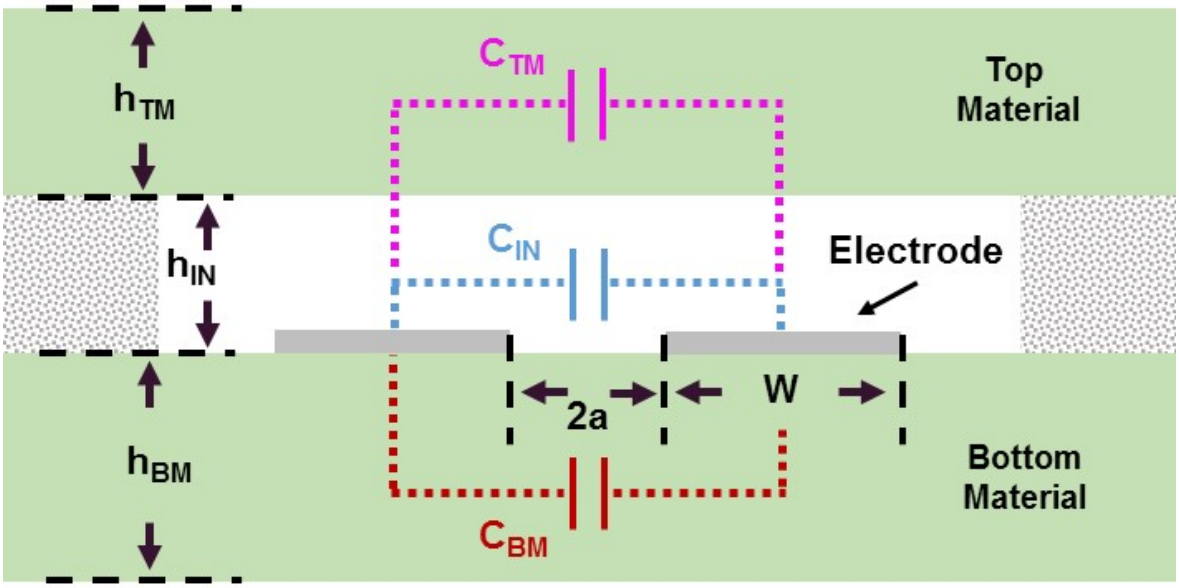

Figure 3.12 The geometry and capacitances for coplanar electrode system. The cross section of electrochemical cell system is shown. The gap between electrodes and width of electrode are 2a and W respectively. The height of top material, inside solution, and bottom material are h_{TM}, h_{IN}, and h_{BM} respectively. The capacitance of top material, inside solution, and bottom material are C_{TM}, C_{IN}, and C_{BM} respectively.

When the electrodes are placed in coplanar geometry the capacitance becomes lower in comparison with parallel plate electrodes, however it has a value. The capacitance for two coplanar electrode system calculated by Chen et. al [135] and given in Equation (3.13).

$$C = \frac{2\varepsilon_r \varepsilon_0 l}{\pi} \cdot ln\left[\left(1 + \frac{W}{a}\right) + \sqrt{\left(1 + \frac{W}{a}\right)^2 - 1} \right] \tag{3.13}$$

where; C is capacitance (F), ε_r relative permittivity of material, ε_0 permittivity of free space (8.85×10^{-12} F/m), l is the length of the electrodes (m), W is the width of the electrodes (m) and a is the half of the gap between electrodes (m).

Equation (3.13) is defined for W/a >> 1, but it is also a good approximation for W ≈ a. [135, 136] The electrical field distribution for coplanar electrodes are important when determining the capacitance value. The distance of those fields can effectively reach is called field penetration depth. The electrical field lines for the coplanar electrodes has a finite field penetration depth, which is dependent to the electrode

width and gap between electrodes. Electrical field lines distribution and field penetration depth is depicted in Figure 3.13 and the formula for penetration is given in Equation (3.14).

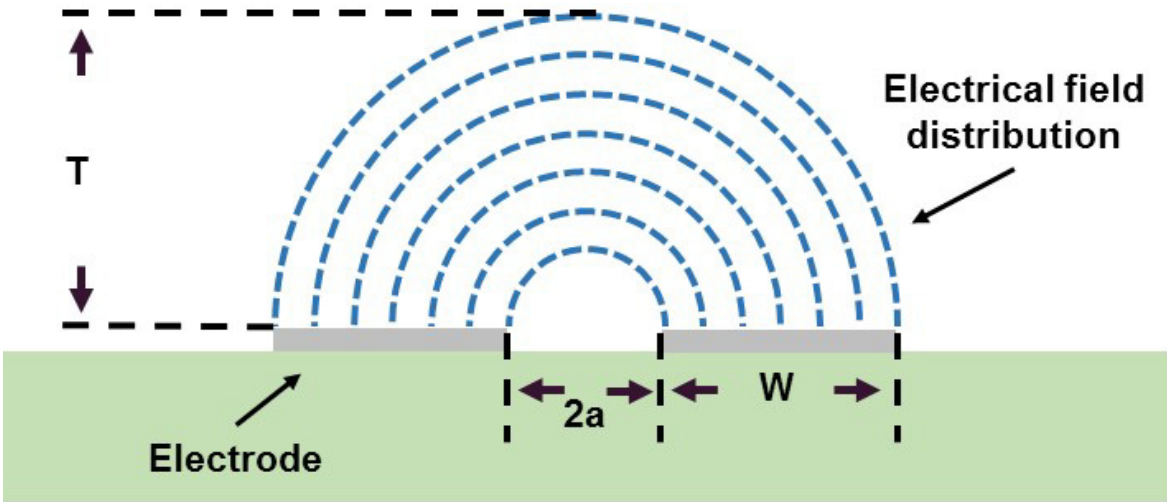

Figure 3.13 Electrical field distribution for coplanar electrodes, T is the field penetration depth.

$$T = a\sqrt{\left(1+\frac{W}{a}\right)^2 - 1} \tag{3.14}$$

where; T is the field penetration depth (m).

Field penetration depth and the height of channel and the relation between them is also effected the capacitance value. If the height of channel is higher than the field penetration depth then effective width of electrode is full width of electrode however if the height of channel is lower than the field penetration depth then effective width of electrodes is different than the width of electrodes and should be calculated. The case and the electric field lines is depicted in Figure 3.14 .If the channel depth (h_{IN}) is so lower compared to field penetration depth (T) and the liquid permittivity is much higher than the permittivity of the top cover, the capacitance is highly dependent to electrical field lines inside the channel. Because of this effect only some portion of the channel width is effectively contributed to the capacitance value which is defined in Equation (3.15). [135, 136]

$$\frac{W_{eff}}{a} = \sqrt{1 + \left(\frac{h_{IN}}{a}\right)^2} - 1 \tag{3.15}$$

where; W_{eff} is effective electrode width (m), h_{IN} is channel depth (m).

After the effective electrode width is calculated the calculated the effective capacitance between electrodes can be calculated and it is given in Equation (3.16).

$$C_{eff} = \frac{2\varepsilon_r \varepsilon_0 l}{\pi} \cdot ln\left[\frac{h_{IN}}{a} + \sqrt{1 + \left(\frac{h_{IN}}{a}\right)^2}\right] \tag{3.16}$$

where; C_{eff} is effective capacitance (F).

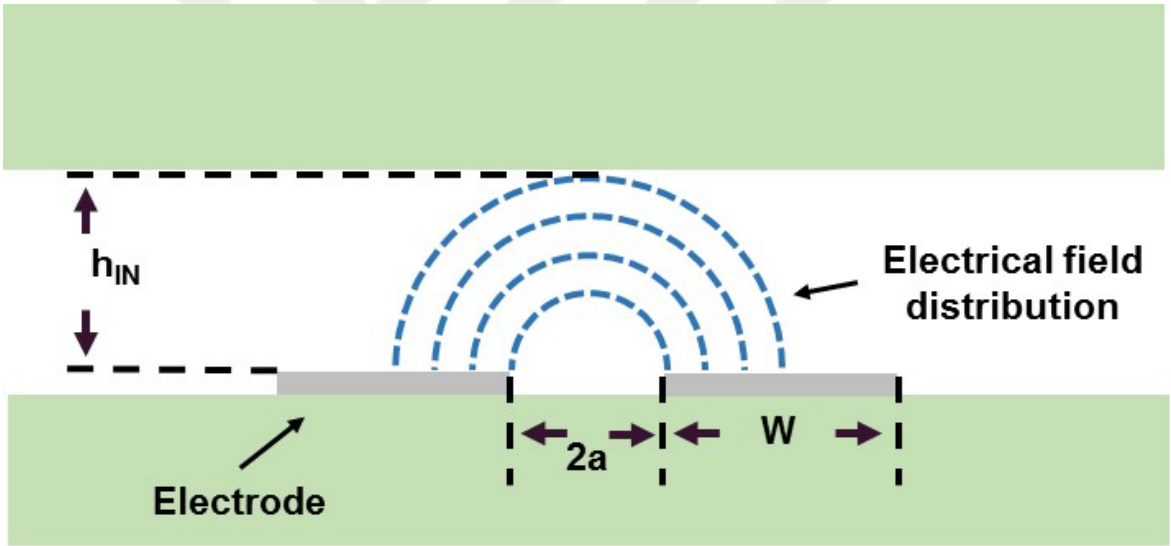

Figure 3.14 Electrical field distribution for coplanar electrodes, when channel height is lower than the electrode width (W).

3.6 Electrochemical Impedance Spectroscopy Based Biosensors

EIS can be used as a detector in biosensors. Those types of biosensor are usually called electrochemical biosensors. Electrochemical biosensors can be divided to three types according to the sensing techniques as impedimetric, amperometric, and potentiometric. EIS can take a part of all those techniques but mainly used for impedimetric sensing technique. [131]

EIS based biosensors can be portable, rapid, sensitive, low cost, label free, used in POC and miniaturized easily. [126] EIS can be used to analyze structural properties of solutions/materials or electrochemical reactions on the surface of modified electrodes or in the solution. Electrochemical reactions can be enzyme catalyzed reactions, specific binding reactions of receptors, proteins, lectins, nucleic acids, whole cells, antibodies or related substances. [137] Structural properties of solutions/materials can be changed according to the conductivity and permittivity change due to the amount of the biomolecules changes in the substance.

There are many reviews in the literature about applications of EIS based biosensors. Grieshaber et al. [138] and Niina et. al. [139] reviewed electrochemical biosensors in general. Edward et al. [130] and Lisdat et al. [117] reviewed the EIS with an overview of bioanalytical applications. Bahadır et al. [137] and Guana et al. [140] reviewed the impedimetric biosensors, Bahadır et al. divided them to 4 subtypes such as antibody-antigen based impedimetric immunosensors, cell based impedimetric biosensors, aptamer-based impedimetric biosensors and Enzyme based impedimetric biosensors. Brosel-Oliu et al. [126] presented the recent publications and future trends of impedimetric sensors for bacteria detection. Ahmed et al. [131] also reviewed electrochemical biosensors for bacterial whole cell detection. Varshney et al. [141] have also review the impedance biosensors for detection of bacterial cells with only focusing on interdigitated array microelectrodes based sensors.

One of the scope of thesis is about HIV detection using EIS. The literature about virus detection using EIS is growing. Abdelghani [142] reviewed the electrochemical biosensors for virus detection and Krejcova et al. [143] reviewed the electrochemical biosensors for especially for influenza virus detection.

There are 4 papers so far in the literature about impedance spectroscopy based detection and counting of cell and virus using cell and virus lysate. In the study of Cheng et al. [144] specifically captured CD4+T cells are lysate, and the impedance spectroscopy is applied to the solution and CD4+T cells are enumerated according to impedance change in the bulk solution. In the following three studies of Shafiee et al. [145], [49] and [48]; isolated HIV virus is lysate and according to the presence of HIV the impedance of the bulk solution is changed. Last one is included to the

thesis scope and will be described further. Also there are 2 patents about cell detection [146] and pathogen detection [147] using impedance spectroscopy. Last one is a similar approach used in this thesis.

4 FLUORESCENCE and LENSLESS WIDE-FIELD MICROSCOPY

Imaging of microorganisms opened a new world, it helped scientist to understand living organisms. The traditional ways to monitor microorganisms is light and electron microscopy. Fluorescence is a physical phenomenon which is absorption and re-radiation of light. Florescence microscope is an optical microscope which uses fluorescence phenomenon to generate an image. Fluorescence microscope is massively used in life science and health care. There is an alternative to optical light microscopy which is lensless wide field microscopy or microscopic shadow imaging.

This chapter explains the principle of fluorescence microscopy, microscopic shadow imaging and several image processing techniques that are used in this thesis.

4.1 Fluorescence Microscopy

Fluorescence microscopy visualize the microscopic source of light. The specimen can be already be fluorescent or can be fluorescent after exciting. Certain materials emits light energy and excites that energy as light with a specific wavelength. One of those materials is fluorophore, which is a fluorescent chemical. The light radiation with the desired wavelength collides with the atoms in fluorophore and electrons in atoms are jump to an excited state. After excitation electrons relax to lower state while relaxing they emits light with a specific wavelength. There is usually less than a microsecond delay between excitation and emission. Fluorescence microscopes are able to detect the emitted light specifically. [148-150]

In fluorescence microscopy white light is used as the light source, that light is filtered by excitation filter to get the specific wavelength to excite fluorophores in the specimen. The wavelengths passes form the excitation filter is reflected by a dichroic mirror to the specimen with fluorophores. Than the fluorophores emits light with emission wavelength, that light goes through the objective to the dichroic mirror which lets the emission wavelength while reflecting excitation wavelength. After dichroic mirror the light is filtered with an emission filter. Emission filter filtered the unwanted wavelengths. Then filtered emission light shining exactly from the specimens goes to ocular and to the observer. Since all the components of light microscope are also used in fluorescence microscopy, microscopic lights become

visible. [148, 149, 151] The principle of fluorescence microscopy is shown in Figure 4.1. [152]

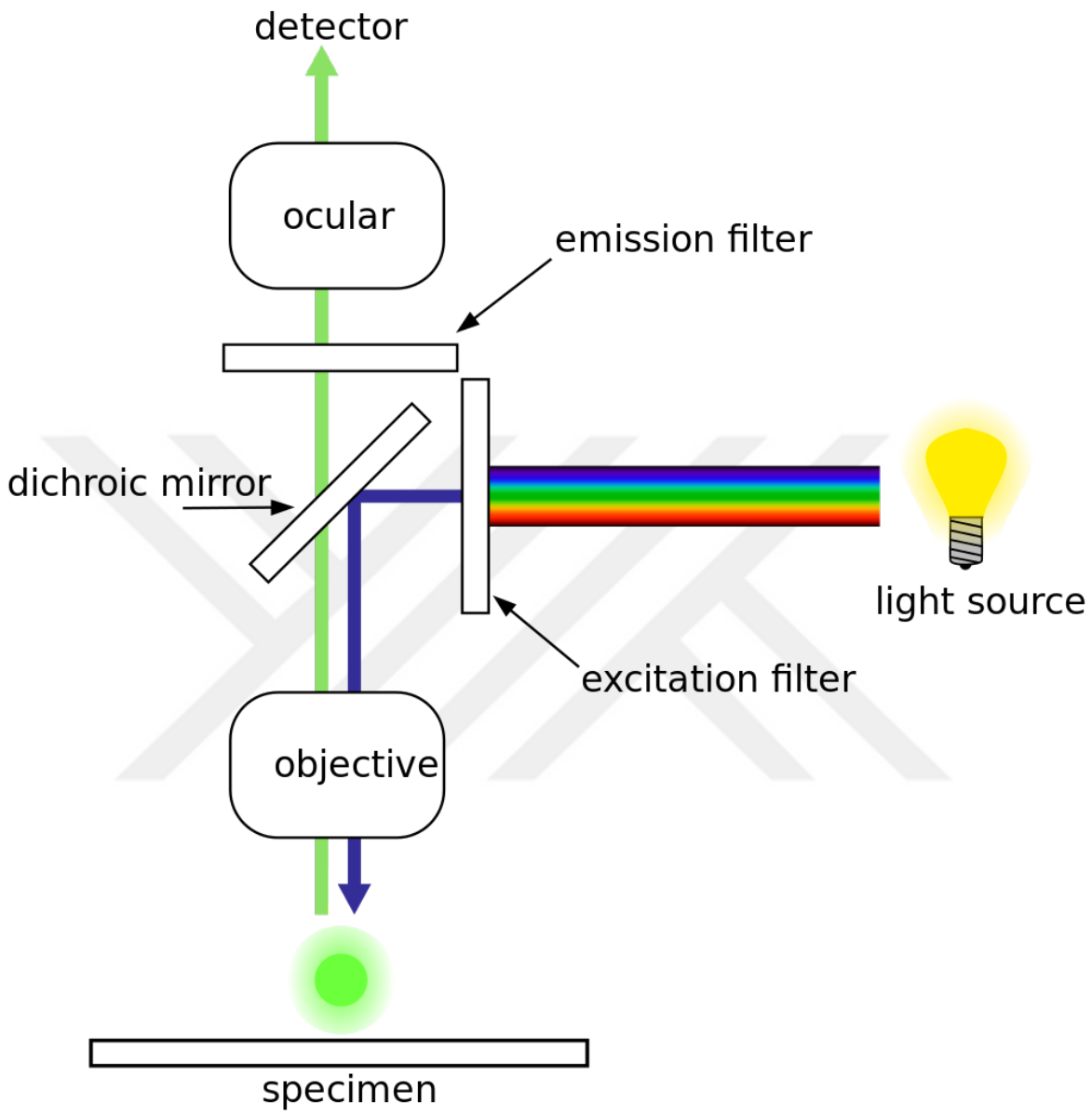

Figure 4.1 Principle of fluorescence microscopy. [152]

4.2 Lensless Wide-field Microscopy (Shadow Imaging) Principle

Optic light microscopes and electron microscopes are costly, requires optical instruments and advance infrastructures, in order to operate them they need highly trained personnel and they are difficult to miniaturize. For POC care their use are limited. [65, 153, 154]

There is a demand for a microscope for POC which is inexpensive, easy to operate, reliable, robust and can be integrated with microfluidics and MEMS. Shadow imaging can be an answer to this need. [154] Ozcan & Demirci [155] proposed lensless wide-field cell imaging platform that uses the idea of monitoring shadows of cells.

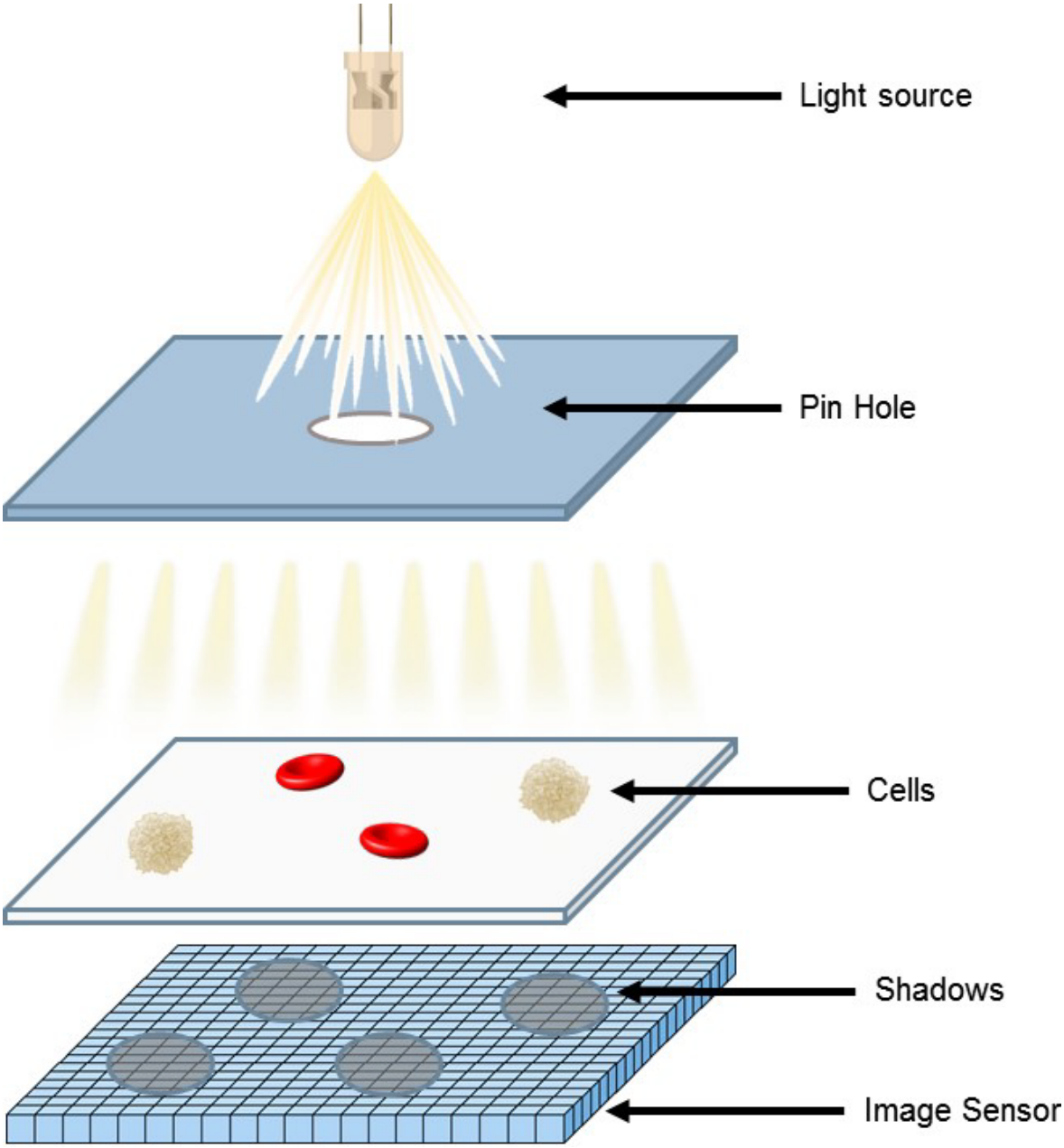

Figure 4.2 A simplified demonstration of lensless wide-field microscopy (Shadow imaging) principle.

Lensless wide-field microscopy can be portable, battery operated and very small size. It can be built simply and can be low cost. It does not require lenses or high

cost optical devices. Nowadays imaging sensor are highly advanced. Their pixel size can be as small as 1.1 µm x 1.1 µm which increases the shadow imaging resolution. The developments in CMOS or CCD imaging sensors can also improve the shadow imaging. Since it is small and compact, it can be integrated with microfluidics, MEMS and nano-micro designs. [65, 154]

The principle of microscopic shadow imaging relies on receiving shadow images of micro structures on an imaging sensor. There is light source which can be white LED. A pin hole which will simply focuses the light. Sample, in this case cells. And an image sensor which can be CCD or CMOS image sensor. The light shines on cells and their shadows appears on image sensor. [155] Depiction of shadow imaging principle is given in Figure 4.2.

The field of view depends on the area of image sensor which can be very large compared to a light microscope with a similar view of image. The resolution of image depends on the pixel size, lower pixel size increase the quality of the image. For cell counting applications wide field imaging increased the number of counted cells. Usually in cell counting applications cell solution is suspended and counted under light microscope. Usually only small area of sample is counted. But using this wide-field system cell can be counted for a larger view, which increases accuracy. 2D scanning of samples under light microscope can be an alternative for wide field imaging but it need special equipment's and auto focusing property for microscope and scanning all the sample takes time. However using shadow imaging, gathering wide field images take seconds.

4.3 Image Processing for Object Counting

Object counting is the process of defining an object and retrieving the number of that object in an image. The process of object counting starts with enhancing the image, detecting object in the image and counting. In this thesis, for enhancing the image contrast stretching is used and for object detection cross correlation, thresholding and neighborhood pixel detection methods are used. This section explains the theoretical aspects of those methods.

4.3.1 Contrast stretching

Contrast is the color or luminance difference of the objects in an image. In a low contrast image it is hard to distinguish objects. An image contrast is the difference between minimum and maximum pixel values. It is not only the pixel values but the number of pixels with lower values and higher values. The best way to understand contrast of an image is to analyze the histogram of the image. Histogram is the pixel value distribution in an image. If the histogram is not spread the contrast is low. One of the way of enhancing contrast is contrast stretching. [156]

Contrast stretching can be performed using piecewise linear transformation. The transformation functions can be used for this operation. Which is a spatial domain method. [157]

In the below Equation (4.1) a spatial domain transform function is defined.

$$G(x,y) = T\big(F(x,y)\big) \tag{4.1}$$

where, F is the input image, and G is the output image. x and y are the spatial coordinate of a pixel in an image. T is the transformation function. [157]

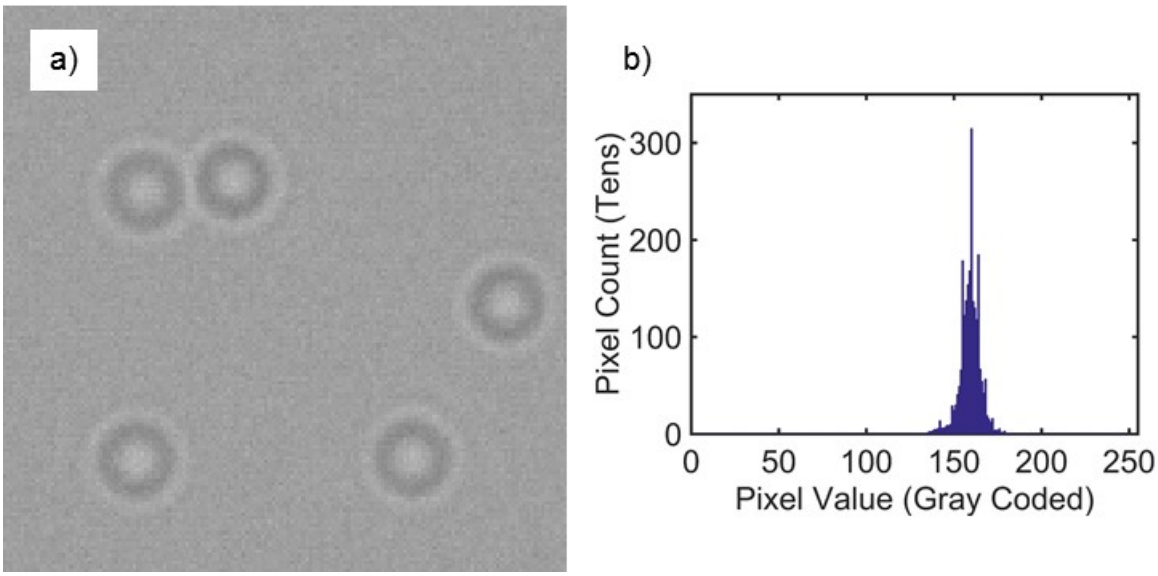

Figure 4.3 a) A raw shadow images of cells and b) its histogram.

The raw data from shadow imaging system is an example of a low contrast image as in Figure 4.3 a), its histogram is squeezed in a very narrow band as in Figure 4.3 b). In order to increase the contrast, a histogram transfer function can be defined as in Figure 4.4. After transform function is applied to the raw image the output image and its histogram are in Figure 4.5. Simply histogram is stretched and spread. The contrast is enhanced. This method is called linear contrast stretching.

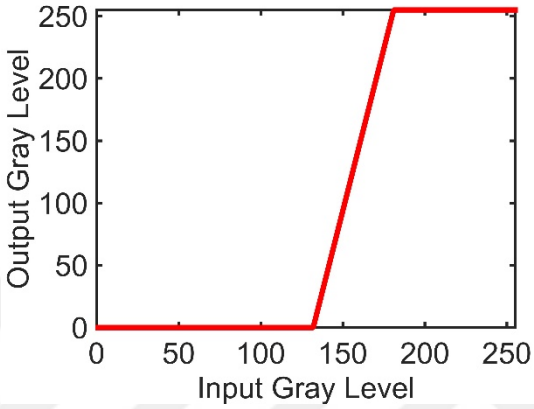

Figure 4.4 Piecewise linear transformation function used for contrast stretching.

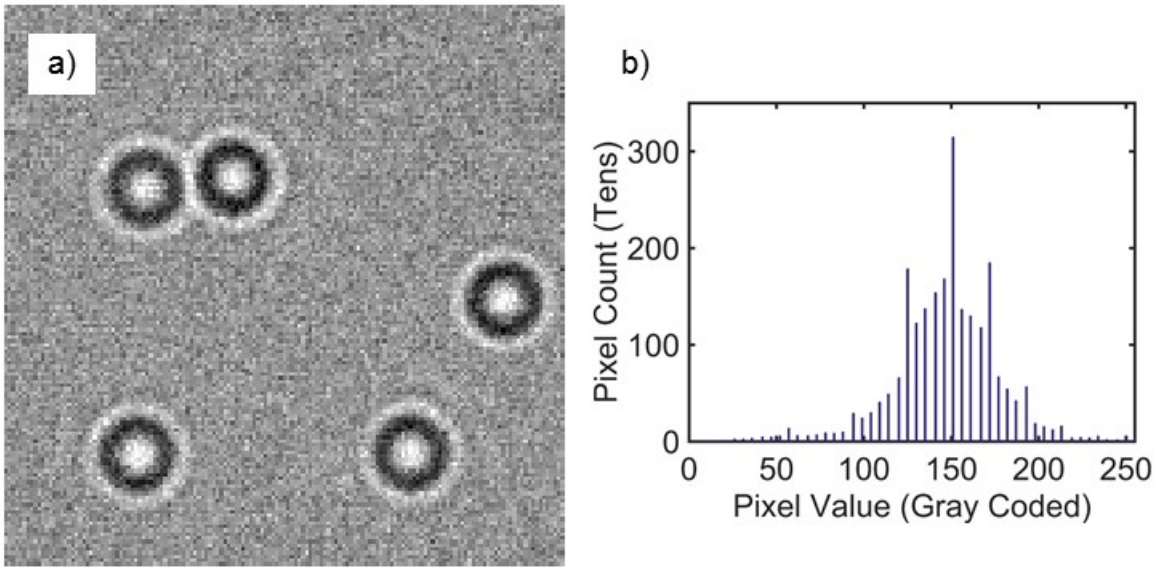

Figure 4.5 a) Contrast stretched image of the image given in Figure 4.3 a). b) Histogram of the contrast stretch image. The transformation is applied using the piecewise contrast stretching transformation function given in Figure 4.4.

4.3.2 Correlation

Cross correlation is used to find similarity of an object inside of an image. It is also called sliding dot product. While sliding inside of an image, if for a location there is a similarity in the image at that object, cross correlation result is maximized. The formula for cross correlation is given in Equation (4.2). [157]

$$F(x,y) \circ H(x,y) = \frac{1}{MN} \sum_{m=0}^{M-1} \sum_{n=0}^{N-1} F^*(m,n) H(x+m, y+n) \tag{4.2}$$

where, F is the image, F* the complex conjugate of F, H is the template, and x and y are the coordinates of the image pixels. The cross correlation will get a maximum value where the template H is located in F. It can be used for detecting template H in F. Auto correlation is the cross correlation of an image with itself. [157]

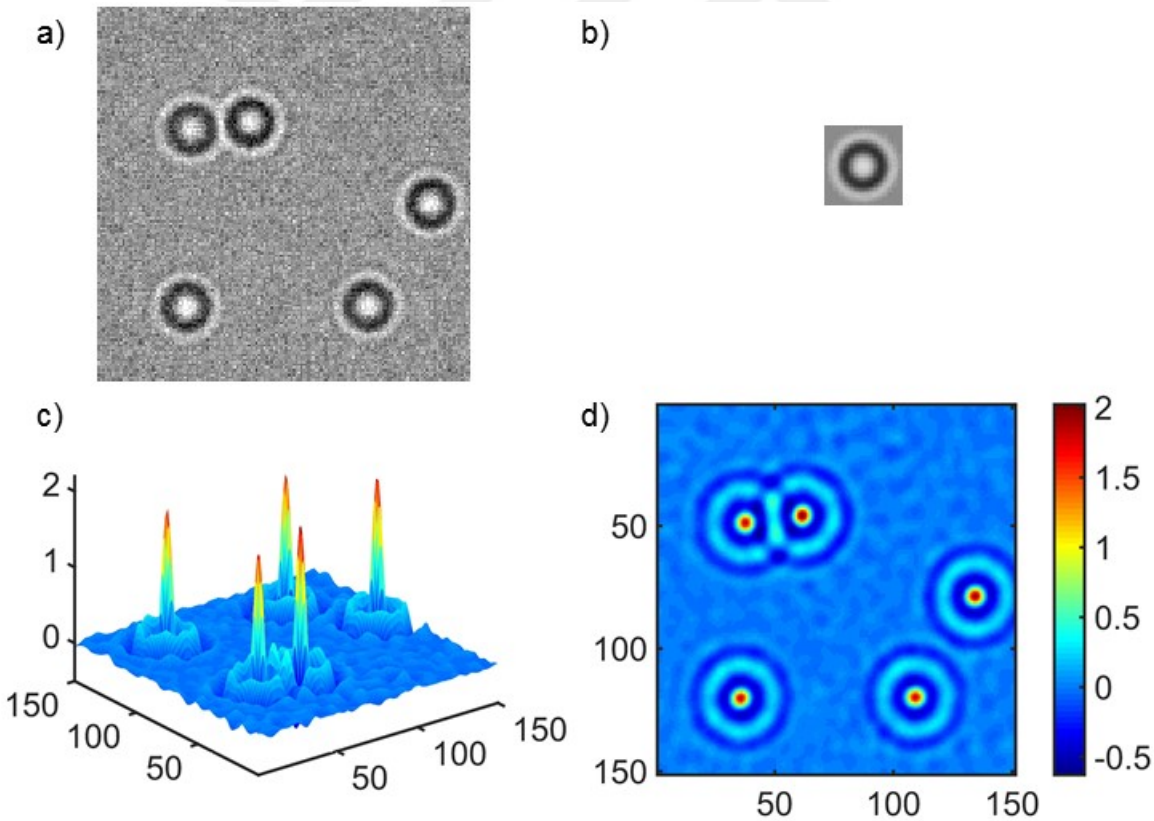

Figure 4.6 Cross correlation example. a) Image with objects in it, b) image of the similar object, c) 3D plot of cross correlation results where peaks indicates the center of the objects in image and d) the 2D plot of cross correlation results. x, y Axis are

the spatial coordinates of image, z axis in c) and color bar in d) indicates the cross correlation result with an arbitrary unit.

Cross correlation can be an effective tool to detect and determine the location of one particular shape, in an image. If the shape is repeating in the image the correlation result will have local maximums. An example of cross correlation is given in Figure 4.6.

4.3.3 Thresholding

Thresholding is usually used for image segmentation. After getting a high contrast difference between an object in an image and the image, thresholding used to segment the object. The result of thresholding is usually just black and white pixels, so it can be binary. For thresholding there should be a threshold level. The transform for thresholding is applied by changing every pixel above this threshold value to white and every pixel below that threshold value to black. [157]

If the spatial domain transformation function in Equation (4.1) is used, a transformation function for thresholding can be the function given in Figure 4.7, where the threshold value is 150. Simply every pixel below 150 turns to black and every pixel above and equal to that level turns to white.

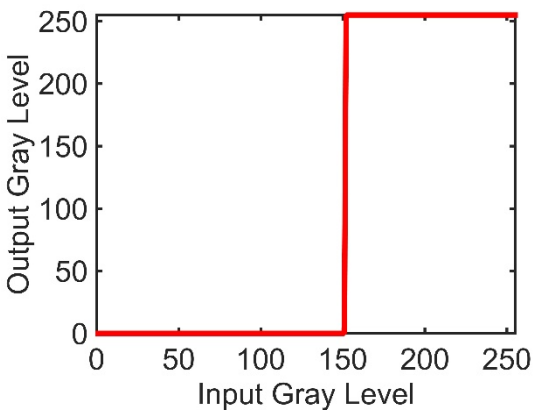

Figure 4.7 Piecewise linear transformation function used for thresholding with a threshold value of 150.

4.3.4 Neighborhood pixel detection

Neighborhood pixel detection is a form of segmentation. In a binary image it can be used for segmenting and numbering group of white pixels. The simplest form of neighborhood pixel detection is applied for binary images. White pixels and their neighborhoods are checked in an image, if they are in neighborhood they get the same number, at the end highest number is the number of total group of white pixels. [158]

5 FLEXIBLE POLYMER BASED MICROFLUIDIC BIOSENSOR USING ELECTRICAL IMPEDANCE DETECTION FOR POC HIV VIRUS LOAD DIAGNOSIS

Diagnosis of infectious diseases are crucial for a healthy life. Many infectious diseases are preventable of transmission and some of them are curable after diagnosis. POC diagnostics of infectious diseases are becoming more available and have many advantages described in Section 1.2.

HIV infection and AIDS disease are major public health issues. The statistics about HIV/AIDS are reviewed in detain in section 2.1. Those statistics show that early, accessible, practical and rapid diagnosis of HIV infection is necessary because 40% of infected people are unaware their situation and HIV screening is expensive and required well equipped facilities.

NAAT is a golden approach to early and effective diagnosis of HIV infection but it is not a POC approach. Current POC HIV diagnosis methods depend on HIV antibodies and it can be used after acute state, which can be considered as a late diagnosis.

Due to those reasons there is a demand for a practical, economic and rapid HIV viral load diagnosis test. A POC biosensor with a flexible polymer based material is a potential solution of this need. These materials are light, flexible, thin, inexpensive and easily shaped or modified. Biosensors using paper or paper like flexible polymer based materials are mass producible, easy to fabricate and easy to dispose. [47, 48, 159]

In this part of the thesis the design and tests of a POC flexible polymer based microfluidic biosensor using electrical impedance detection for HIV diagnosis is explained.

5.1 Materials and Methods

In this section the designed and used materials and methods are explained.

5.1.1 Flexible polymer based microfluidic chip development

Impedance measurements of lysate HIV solutions are performed in the flexible polymer based microfluidic chips (FFChip). Those FFchips are fabricated by assembling three layers. Electrodes on a flexible polymer is the bottom layer. Medium layer is the layer formed with a double sided adhesive and patterned to form the channel. Top layer is a flexible polymer layer with patterned inlet and outlet. The simple depiction is in Figure 5.1.

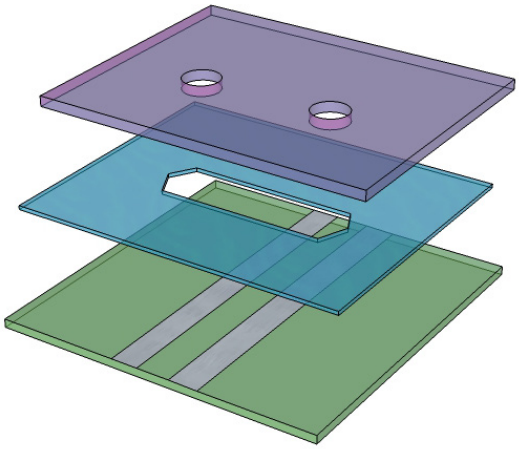

Figure 5.1 The three layers of flexible polymer based microfluidic chip (FFchip). From to bottom to top: the electrode layer, channel layer and inlet layer.

5.1.1.1 <u>Electrode layer</u>

Electrode layer is formed by screen printing of silver paste mixture on the flexible polymer surface. The silver paste mixture is composed of highly conductive silver ink (CI-1001) purchased from Engineered Materials System Delaware, OH, USA) and silicon adhesive (All-Purpose 100% Silicone Adhesive Sealant, 00688) purchased from DAP (Baltimore, MD, USA). The composition of silver paste mixture is 1 silver ink to 4 silicon adhesive in weight. The conductivity of silver ink is 0.015Ω/□ (ohms/square) @ 25.4 microns.

In order to form the electrode layer using screen printing; first a mask (mesh or mold) is patterned on a flexible hydrophobic polymer film from the protective film of a double sided adhesive (DSA). DSA (8113) was purchased from 3M (St. Paul, MN, USA). The mask is patterned using laser cutter (Universal Laser Systems Inc.,

VLS2.3, Scottsdale, AZ, USA). For the pattern of electrode a computer aided design (CAD) is formed using Corel Draw® Software. The design is shown in Figure 5.2.

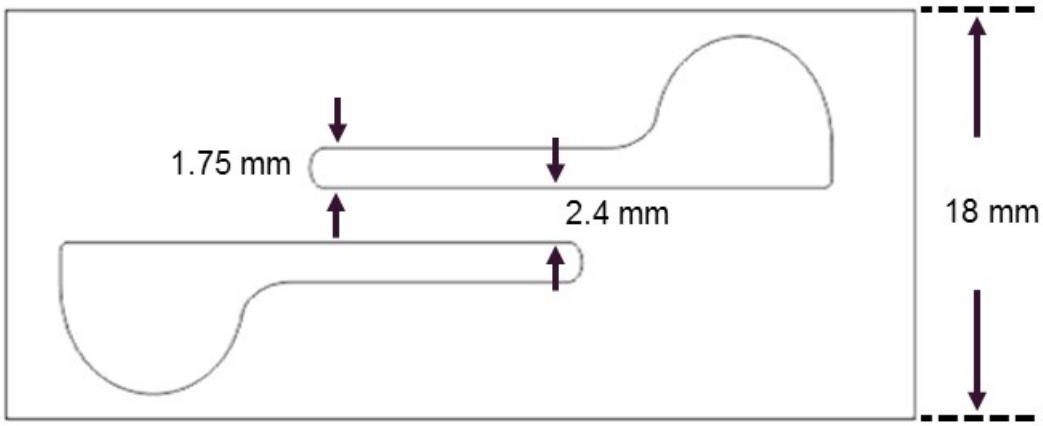

Figure 5.2 The CAD design of mask for screen printing of electrodes.

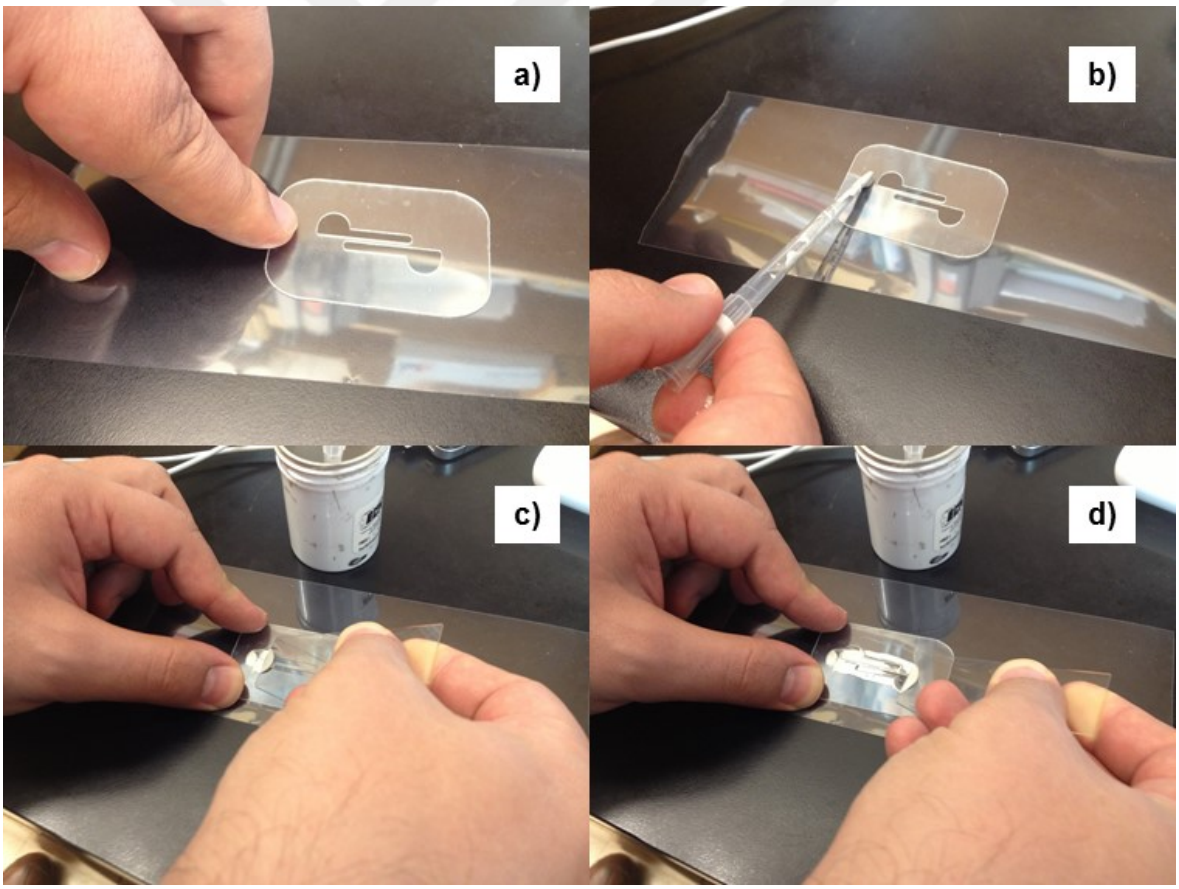

Figure 5.3 The screen printing process for fabricating electrode layer. a) Placing the mask on the flexible polymer film, b) dropping some silver paste mixture, c) spreading the paste, d) after spreading the open spaces in the mask is filled with paste.

For the screen printing of the electrode first the mask is placed on a flexible hydrophilic polymer; Dual-Purpose Transparency Film (CG5000) purchased from 3M (St. Paul, MN, USA). Then the silver paste mixture is placed on one side of the mask. After that a microscope glass slide is used as a squeegee in order to spread the paste on the mask, so the paste filled the open space in the mask. The process is shown in Figure 5.3. Finally the mask is removed and the film with patterned wet silver paste is baked at 80 °C for an hour. After this process the electrodes on flexible polymer film is ready. Since the laser cutter cuts the polymer by applying laser light and burning the film the actual dimensions of electrodes are changed a little and also the silver paste mixture is spread a small amount while baking that also causes a small change in the dimensions of electrodes. The final thickness of electrodes and gap between electrodes becomes almost 2mm. The thickness of the flexible hydrophilic polymer film is around 120µm.

5.1.1.2 Channel layer

The channel layer is used to form a chamber for solution to be filled. It is very important to use a constant volume of solution for impedance measurements. The channel layer is patterned on DSA (8212CL), which was purchased from 3M (St. Paul, MN, USA).

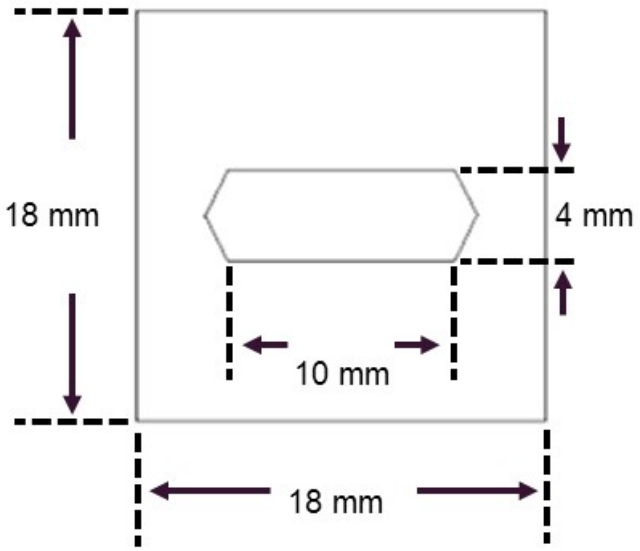

Figure 5.4 The CAD design of channel.

The adhesive thickness is 50µm which is define the depth of channel. The pattern is CAD designed and patterning is performed by laser cutter. The CAD design is shown in Figure 5.4.

5.1.1.3 Inlet layer

Inlet layer is the top layer where the inlet and outlet is patterned. The flexible hydrophilic polymer; Dual-Purpose Transparency Film (CG5000) is used and patterned using laser cutter. The CAD design is shown in Figure 5.5.

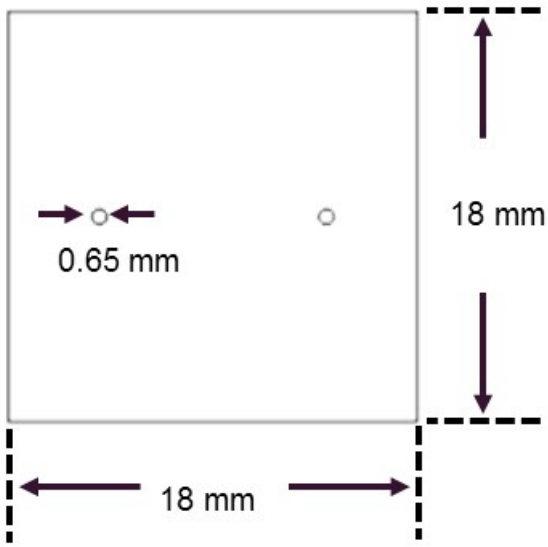

Figure 5.5 The CAD design of inlet layer.

The hole diameter is 0.65mm in the CAD design but since laser cutter cuts the polymer by burning the actual diameter becomes like 1mm. After fabricating three layers are assembled together. Protective film of one side of DSA is removed and DSA is laminated on the electrodes, then the other protective film is removed and top layer is laminated on that side. The fabrication process is shown in Figure 5.6 and the final FFChip is in Figure 5.7.

Screen printing technique is used for many applications, it can be done using a silk on the mask, by using the silk mask can be intact, however small dimension design are almost not possible by silk printing. Due to that reason screen printing without using silk is used for printing of electrodes.

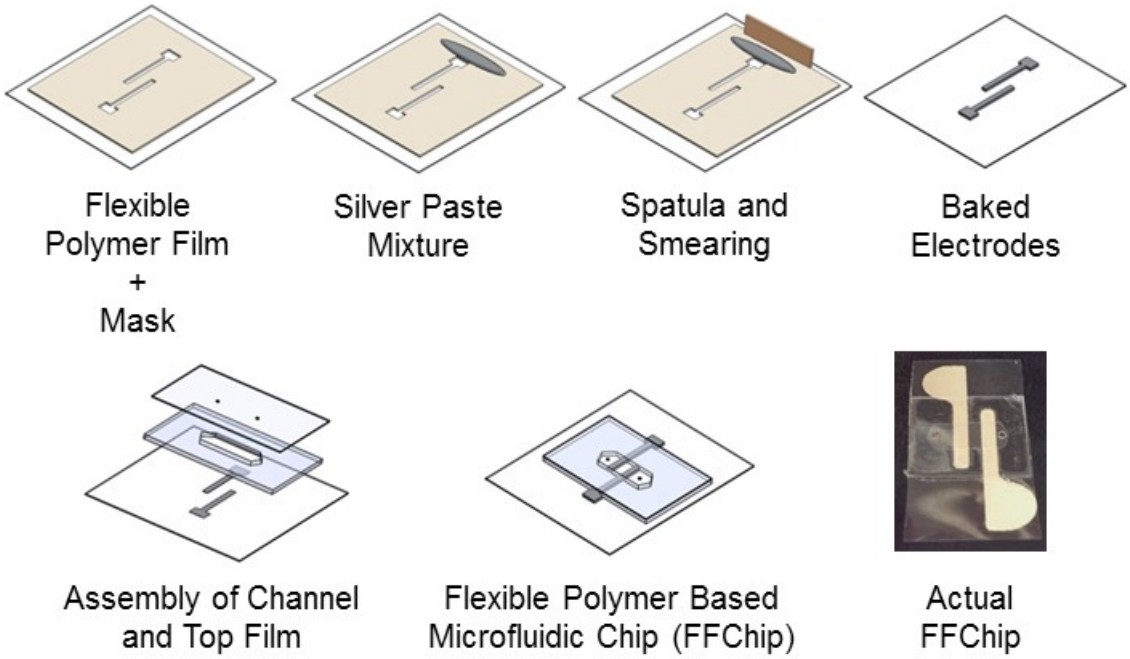

Figure 5.6 The fabrication process of flexible polymer based microfluidic chip (FFChip).

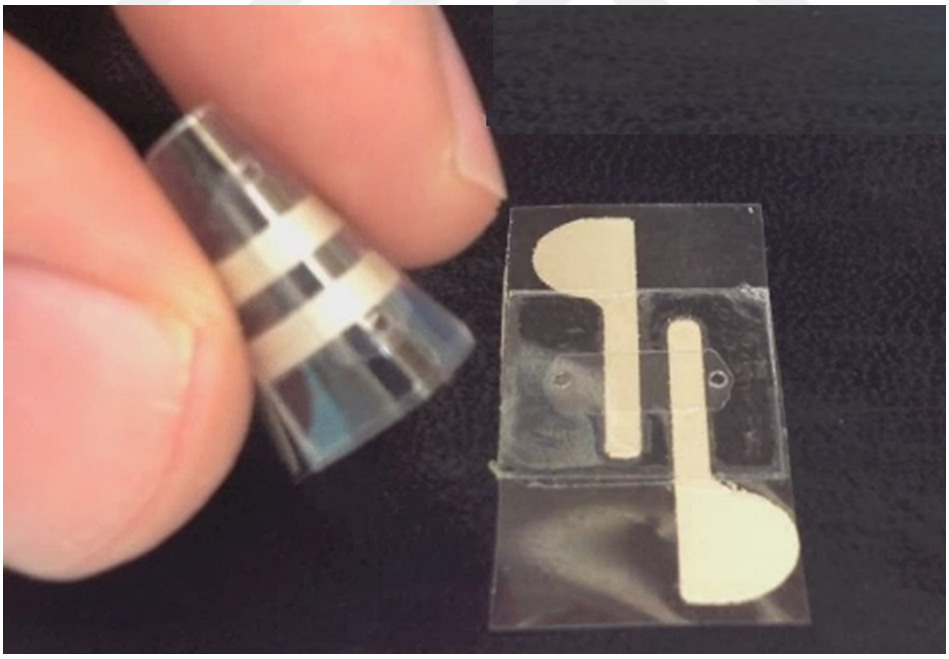

Figure 5.7 The flexible polymer based microfluidic chip (FFChip).

Laser cutting process usually does not give the exact dimensions in CAD design because laser patterns the polymer and DSA by burning, also the dimension of wet silver paste mixture becomes different after drying. So the actual micro dimensions can be different from the planned one. Due to these reasons after many fabrications

CAD dimensions are set to give desired final dimensions. In Figure 5.8 the measured dimension after FFChip fabrication are depicted. The scheme is the lateral cross section of FFChip in Figure 5.7.

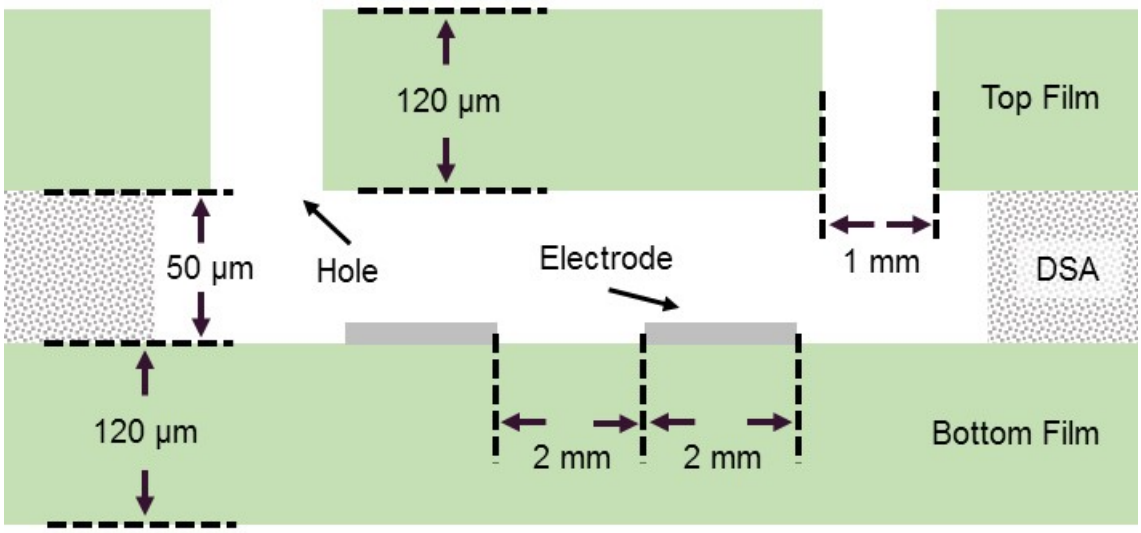

Figure 5.8 The actual dimensions for lateral cross section of FFChip shown in Figure 5.7 after laser cutting of layers and drying of electrodes.

The fabrication of FFChip does not require complex and expensive device dependent lithography techniques, it can be produced in any environment. Baking of electrodes should not be at a certain temperature. If the temperature is low it should be baked longer or if it is more that it should be baked shorter. The baking does not change the measurement parameters a lot. Also since FFChips are mostly produced by polymers and can be burned, disposing of them is very simple. FChips are cheap to fabricate and the materials are also cheap.

5.1.2 HIV capturing and lysation

In order to detect viruses, viruses should be specifically captured and lysed. Affinity chromatography based method is used to immobilize HIV specifically from the sample medium. Sample medium can be phosphate buffer saline (PBS), plasma or whole blood. HIV in those sample mediums are clinical models for HIV infection. The surface functionalization, virus capturing and virus lysing have been described in this section, models representations used to explain the methods are described in Figure 5.9 and will be used further.

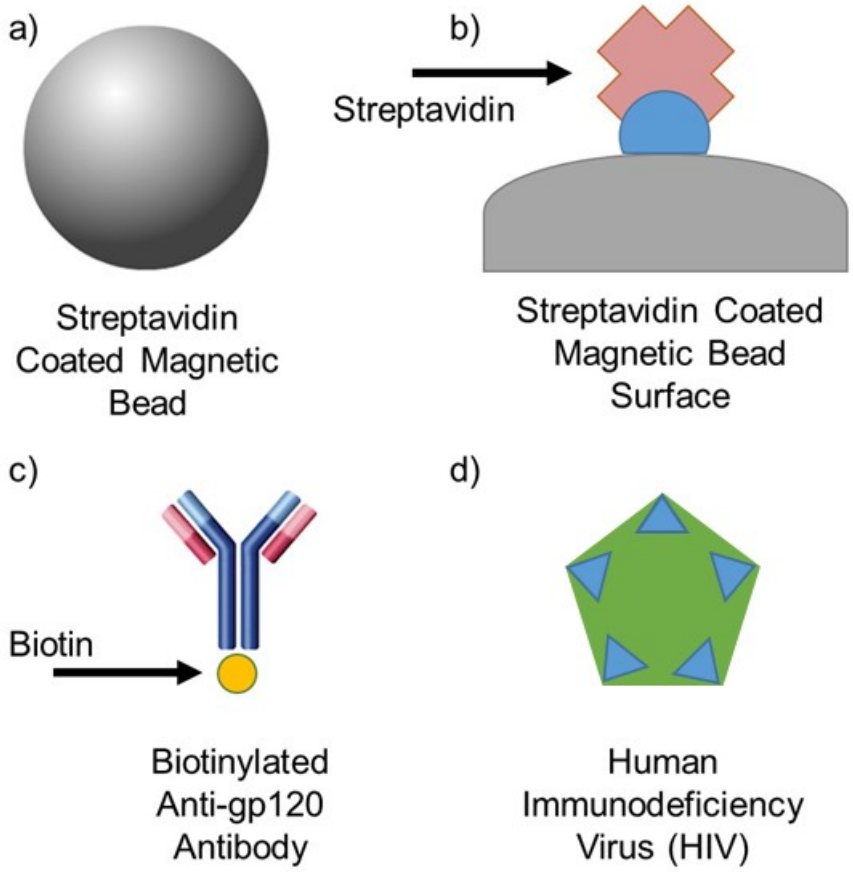

Figure 5.9 The model representations of a) streptavidin coated magnetic bead, b) streptavidin on the surface of the bead, c) biotinylated anti-gp120 antibody, and d) Human Immunodeficiency Virus (HIV).

Virus samples are HIV-1 subtypes A, B, C, D, E, G, and panel. Panel is simply a mixture of subtypes A, B, C, D, and circulating recombinant forms, CRF01_AE and CRF02_AG. The viral loads of the HIV-1 subtypes A, B, C, D, E, G, and panel were 1.74×10^8, 1.2×10^8, 1.17×10^8, 2.9×10^8, 8.39×10^8, 6.53×10^8 and 1.48×10^9 copies/mL, respectively.

Dulbecco's Phosphate Buffered Saline (DPBS, 1X) was bought from Life Technologies ® (Grand Island, NY, USA). Triton X-100 (100%), glycerol (100%), Bovine Serum Albumin (BSA, 10%) and Ethanol (200 proof) were purchased from Sigma-Aldrich® (St Louis, MO, USA). HyPure® Molecular Biology Grade Water was obtained from Fisher Scientific® (Agawam, MA, USA). Biotinylated polyclonal goat anti-gp120 antibody (4g/mL) was obtained from Abcam® (ab53937, Cambridge, MA, USA). Streptavidin-coated magnetic beads (1 µm diameter) were purchased from Thermo Scientific®, (88816, Rockford, IL, USA).

The main reason to use magnetic beads is their ability of effectively washing. Washing of magnetic beads are done on a stand, multistep magnetic separator purchased from BioMag® (Polyscience Inc., Warrington, PA). Diluted bead solution in tube, stands on the magnetic separator which has a magnet close to the tube. The beads get together close to the magnet in tube wall. The remaining solution in the tube is pipetted out from the tube while beads are standing on the side wall of tube. Finally tube is removed from magnet and new solution is pipetted in to the tube and mixed. The steps are depicted in Figure 5.10.

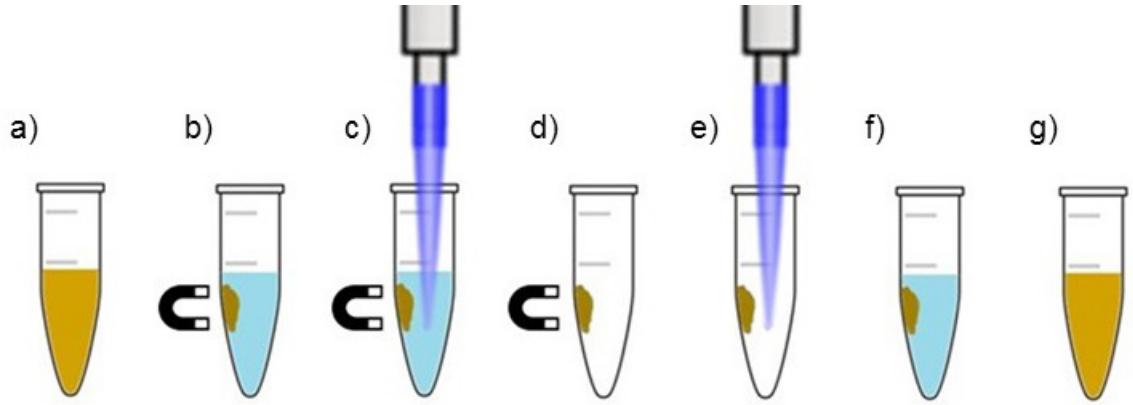

Figure 5.10 Washing steps of magnetic beads. a) Bead are in the solution ready to wash, b) tube is stand to the magnetic separator, beads are get together close to magnet, c) solution is pipetted out, d) tube without solution but with beads only, e) tube is removed from the magnetic separator and new solution is pipetted in to the tube, f) new solution and beads are mixed together and g) mixed final solution.

5.1.2.1 Magnetic bead surface functionalization

The streptavidin-coated magnetic beads and biotinylated anti-gp120 antibody and their avidin + biotin binding is used for conjugation of antibody to the beads. The protocol for conjugation of anti gp120 antibody to magnetic beads has 3 main steps. First streptavidin-coated magnetic beads are diluted 1:10 (v/v) in PBS and washed 3 times by PBS. Second biotinylated anti-gp120 antibodies (15 µg/mL) are added to the solution and incubated in a rotator at a speed of 30 rpm for 2 hours at 4°C. The conjugation depends on the relation between avidin and biotin binding represented in Figure 5.11. This binding is the strongest non-covalent interaction of ligand and

protein ever known. [160] Third the remaining antibodies are removed from the solution by washing 3 times with PBS.

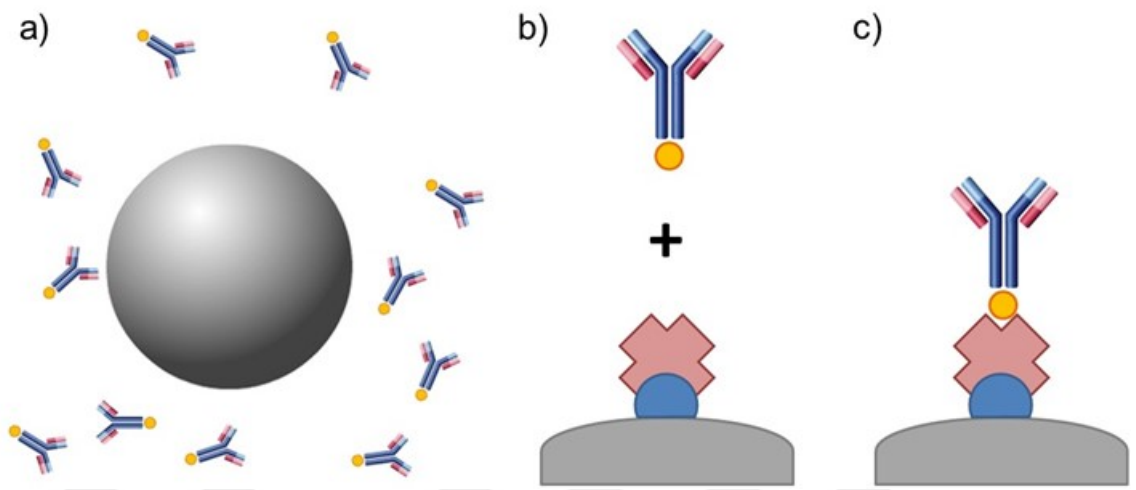

Figure 5.11 The anti gp120 antibody conjugation to streptavidin-coated magnetic bead. a) Incubation of magnetic beads with antibodies, b) The avidin + biotin binding, c) conjugated antibody.

5.1.2.2 HIV capturing

Anti gp120 antibody conjugated magnetic beads are suspended in HIV culture medium. They were incubated at room temperature for 30 minutes. The incubation is done on a rotator at 15 revolutions per minute (rpm). The HIV capturing is depicted in Figure 5.12. The binding results with capturing of HIV on surface of magnetic bead is because of the viral envelope protein gp120 on surface of HIV binding with anti gp120 antibody conjugated on magnetic beads.

In this step the control samples also started to prepare, by suspending magnetic beads with biological model sample without virus. Those samples can be PBS, plasma or whole blood which are used further for experiments. The control samples will be further prepared for experiments.

After incubation the beads are washed using a low conductive glycerol solution. Washing performed using magnetic stands and manual pipetting. The sample is ready for lysing of HIV.

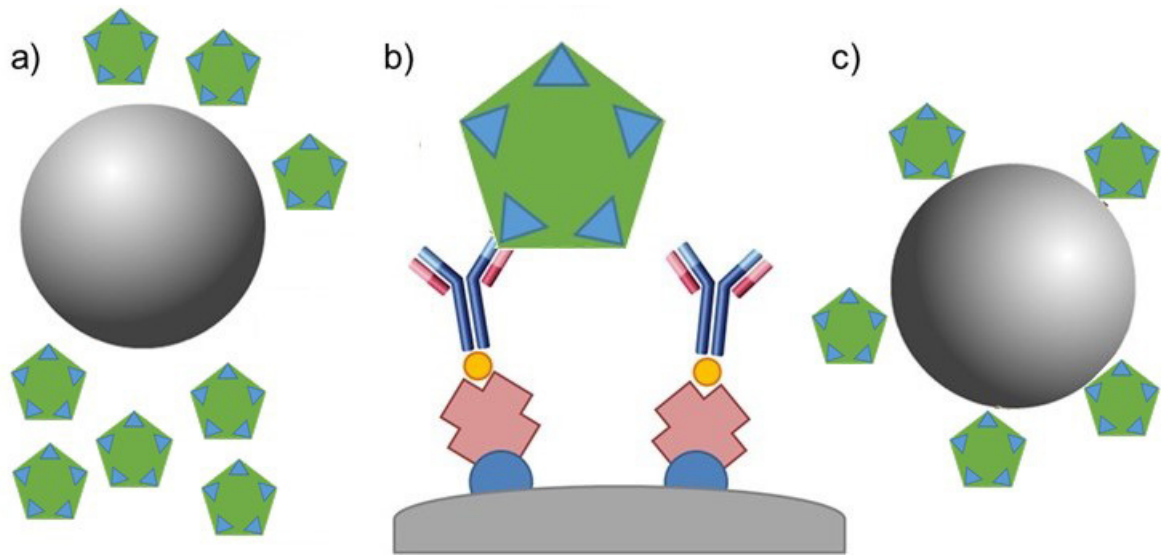

Figure 5.12 HIV capturing, a) the magnetic beads are suspended in HIV media culture for incubation, b) the viral envelope protein gp120 binding with anti gp120 antibody which is conjugated on the magnetic bead surface, c) Magnetics bead with immobilized HIV on its surface.

5.1.2.3 HIV lysate sample preparation

Impedance spectroscopy of biological sample lysate can be used as a detection method [144-147]. In the proposed method in order to detect the existence of HIV, immobilized viruses on magnetic beads should be lysed than impedance spectroscopy of the lysate should be obtained.

The magnetic beads with immobilized viruses suspended in biological model sample is the sample ready to be lysed. First the sample is washed 3 times with electrically nonconductive 20% glycerol in deionized (DI) pure water. Second the beads are suspended in 1% Triton x-100 and incubated for 5 minutes. In that 5 minutes the immobilized virus are ruptured and their ingredients which are enzymes, proteins, ions, antigens, and similar biological substance are suspended in to the solution. These biological samples are expected to change the impedance of the solution. Third the lysate is extracted from magnetic beads using magnetic separator. Finally the lysate is injected to the FFChip to be measured. The whole process is depicted in Figure 5.13.

The control sample which is virus free anti gp-120 antibody conjugated magnetic beads in biological model sample is also washed 3 times with 20% glycerol in DI

pure water, then bead are suspended and incubated for 5 min in 1% Triton x-100, finally pipetted to FFChip in order to perform impedance measurements.

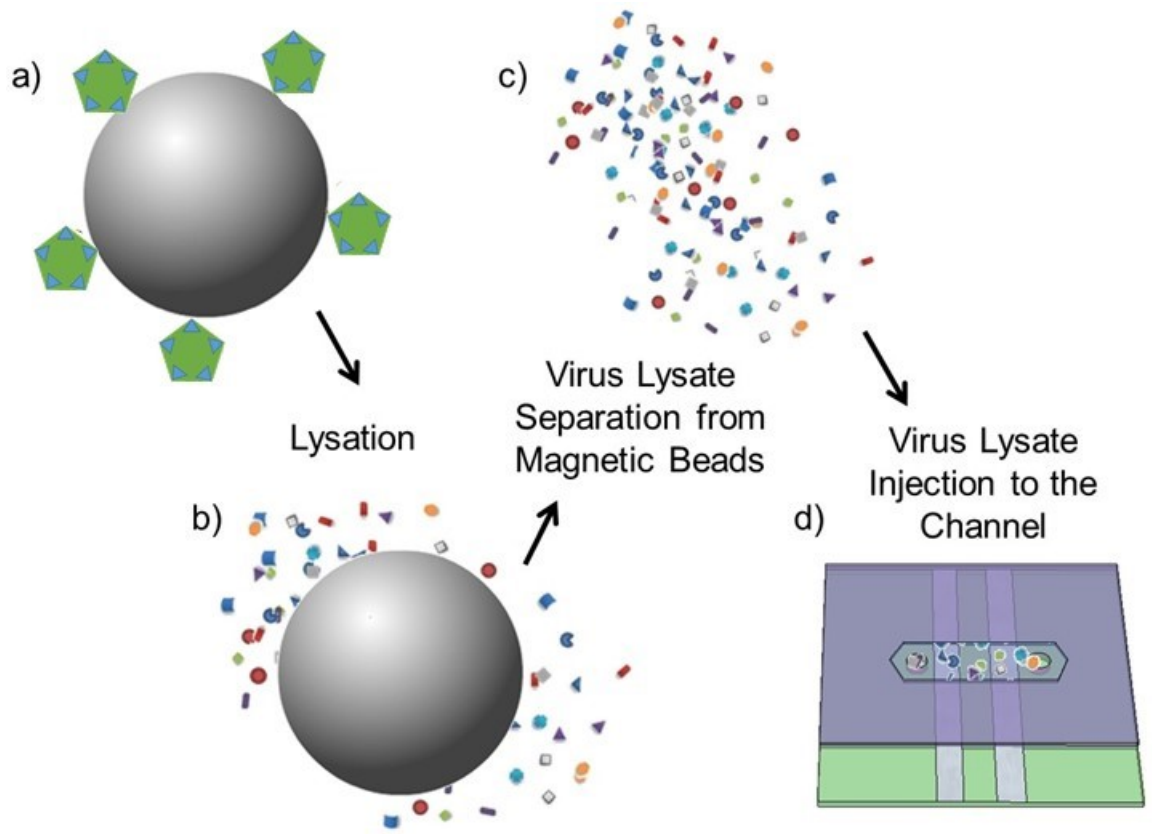

Figure 5.13 The HIV lysate preparation and injection to FFChip. a) Magnetic beads with immobilized HIV in biological model sample is washed 3 times with nonconductive 20% glycerol solution in DI pure water, b) lysation of HIV by suspending the beads in 1% Triton x-100 and incubating for 5 min, c) separation of lysate from beads using magnetic separator and d) injection of lysate in FFChip for impedance spectroscopy measurements.

5.1.3 Electrical Impedance spectroscopy analysis

Electrical impedance spectroscopy setup design and data analysis methods are explained in this section.

5.1.3.1 Electrical Impedance spectroscopy analysis setup

Impedance measurements are applied using an LCR meter (Inductance L, Capacitance C, Resistance R meter). Probes of LCR meter is connected to the

electrodes of flexible polymer based microfluidic chip, then sample solution is applied into the channels of the chip, finally magnitude and phase of impedance of the solution are obtained using input AC signal with 1 Volt peak-peak and over a range of AC frequency 100Hz to 1MHz. The LCR meter used in experiments is a precision LCR Meter LCR-8101G of GW INSTEK®.

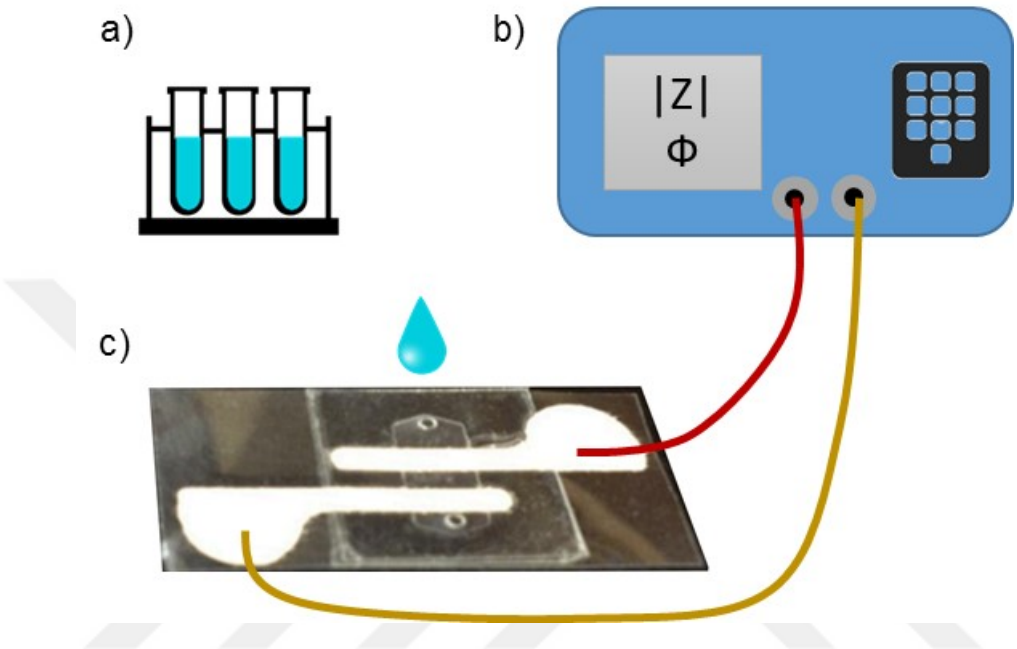

Figure 5.14 Electrical impedance measurement setup for FFChip. a) Solutions, b) LCR meter, c) FFChip.

5.1.3.2 Representation methods of impedance results

Electrical impedance results can be represented in many ways. Impedance value is a complex value, it can be represented as magnitude and phase value. So in this report impedance values are represented as magnitude versus frequency change and phase versus frequency change which are bode plots. In this report frequency range is 100 Hz to 1 MHz. A complex value has its real and imaginary components so it can be represented using Nyquist plots as imaginary value versus real value. Also the magnitude of impedance can be shown according to a frequency value. In this report the highest difference value for impedance change is almost observed around 1 kHz, so impedance magnitude for 1 kHz is shown.

For impedance magnitude plots at 1 kHz the standard deviation for different samples are shown as error bars. Also at 1 kHz the impedance change compared to control

values are plotted and standard deviation also plotted as error bars. The impedance magnitude change according to control value is calculated using Equation (5.1).

$$I.M.Change\Big|_{1\ kHz} = \frac{I.M.Value\ for\ a\ Sample\Big|_{1\ kHz}}{I.M.Value\ for\ Control\Big|_{1\ kHz}} \tag{5.1}$$

where, I.M. is impedance magnitude.

In order to understand the consistency of measurement repeatability is calculated. Repeatability is the closeness of the successive measurements results under repeatability conditions. [161]

Table 5.1 The repeatability conditions. [161]

Same observer
Same measurements procedures
Same instruments
Same location
Same repetition

After repeatability conditions are satisfied repeatability is calculated using Equation (5.2).

$$Repeatability = \frac{I.M.Change\Big|_{1\ kHz} \cdot 100}{I.M.Change\Big|_{1\ kHz} + \begin{matrix} Standard\ Error\ of \\ I.M.Change \end{matrix}\Big|_{1\ kHz}} \tag{5.2}$$

5.2 Experiments and Results

Impedance measurement based HIV detection system using FFChip is designed and explained in section 5.1. After the system is ready measurements are applied in order to evaluate the performance of the method.

5.2.1 Electrical equivalent model for flexible polymer based microfluidic chip

One of the electrical equivalent model for FFChip can be the Randles model with CPE for two identical electrodes as defined in Section 3.4. The configuration of coplanar electrodes for the chip and its electrical equivalent is depicted in Figure 5.15. The electrical equivalent circuit model equation can be the one in Equation (3.12).

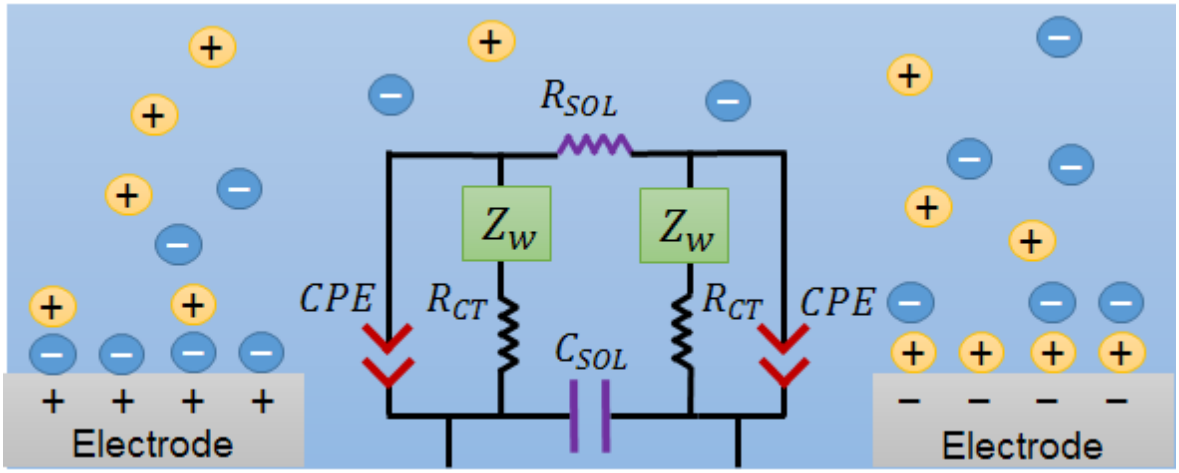

Figure 5.15 Coplanar electrode configuration and its electrical equivalent circuit representation for flexible polymer based microfluidic chip.

5.2.2 Impedance measurements

Impedance measurement experiments are applied using the setup in Figure 5.14. Different solutions filled to the channel in the FFchip. The main aim is to detect HIV, however in order to better understand the system and impedance results, solutions with already known conductance are measured first. Then HIV measurements are applied. After that in order to understand the specificity of the detection Epstein-Barr Virus (EBV) measurements are applied. The EBV is used in order to test the capture specificity of the immobilization process. Finally time dependency and high concentrated virus measurements are done.

5.2.2.1 <u>Impedance measurement for empty channel</u>

Empty channel measurements for FFChip is applied in order to better understand the capacitance response of geometric shape of design and intrinsic resistance

between electrodes. All measurements are taken for frequencies between 100 Hz and 1 MHz. Empty channel is actually air filled channel.

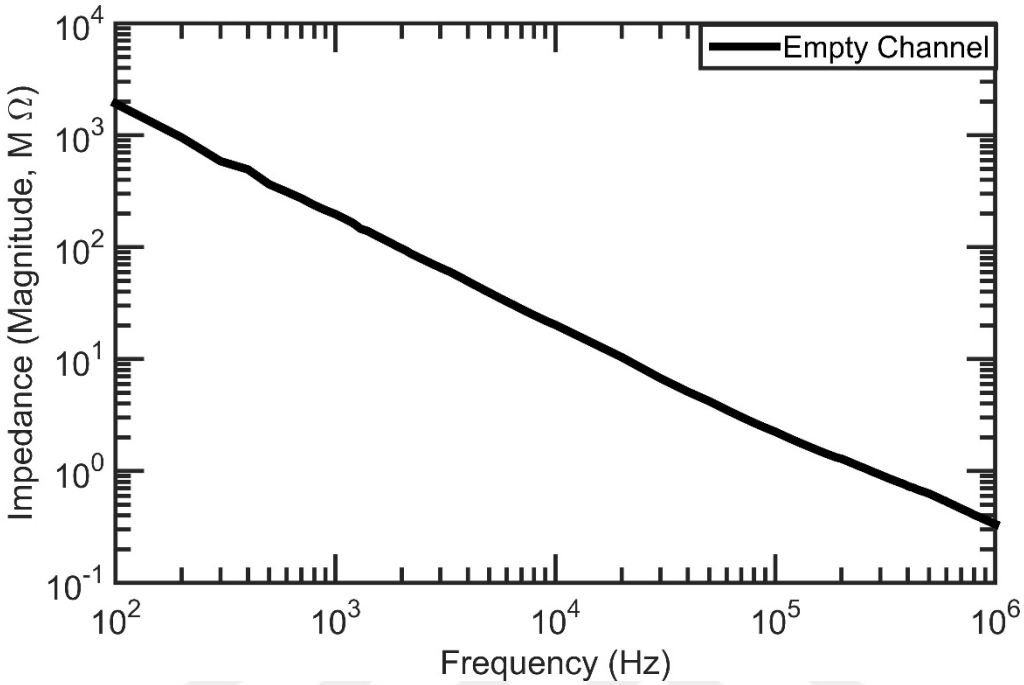

Figure 5.16 Impedance magnitude spectra of FFChips with empty channel for a frequency range between 100 Hz and 1 MHz.

The magnitude and phase spectra results of the measurements are shown in Figure 5.16 and Figure 5.17, respectively. The phase spectra seems to show that the impedance is highly dependent on imaginary components so the system should be highly capacitive which should be the case because the channel is air filled. The resistive component should be very high so the dominant impedance is because of capacitive component. When we assume the channel is highly capacitive the equivalent circuit should be just a capacitor parallel to a very high value of resistance. So the capacitance can be calculated from the formula given in Equation (5.3) as explained in Appendix B.

$$C = -\frac{Z_{im}}{wZ^2} \tag{5.3}$$

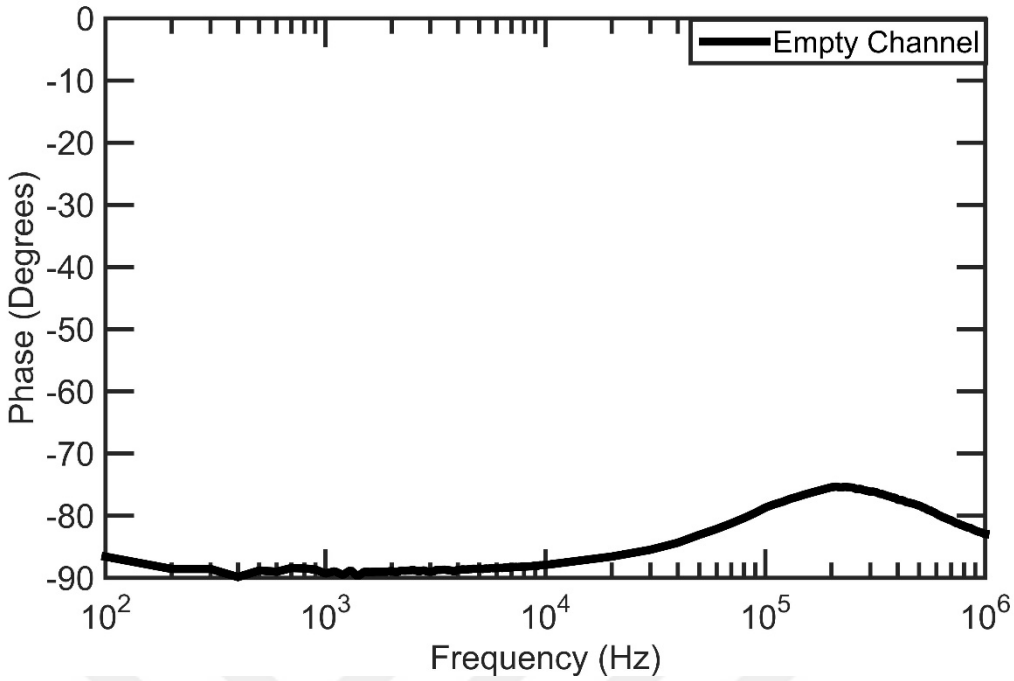

Figure 5.17 Impedance phase spectra of FFChips with empty channel for a frequency range between 100 Hz and 1 MHz.

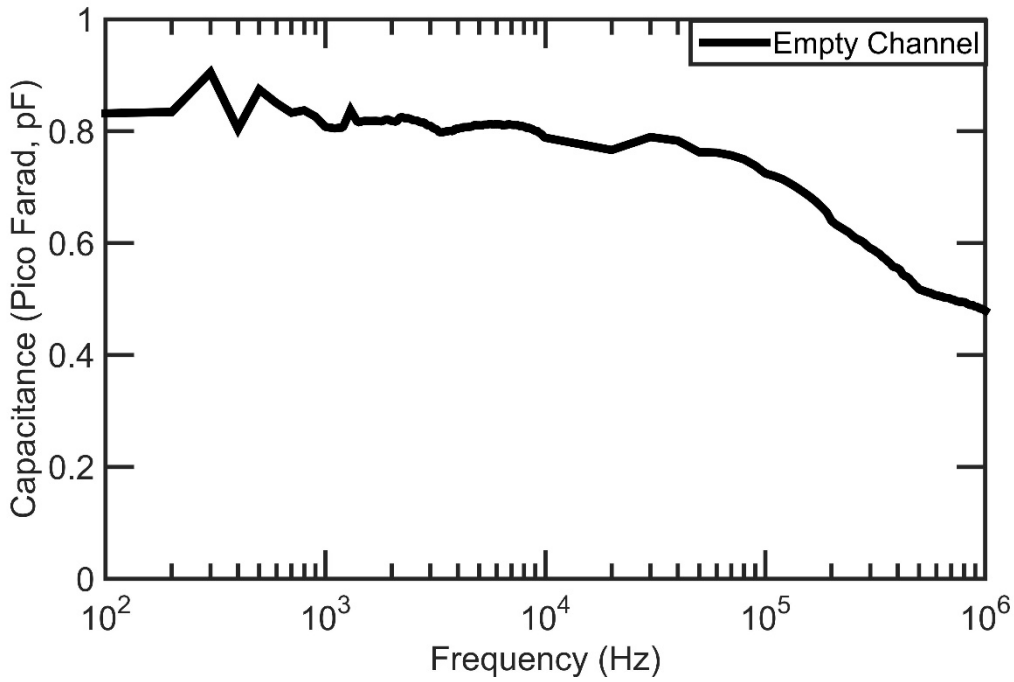

Figure 5.18 Capacitance spectra calculated using the impedance magnitude and phase data of FFChips with empty channel when the equivalent circuit model is just a resistor parallel to a capacitor.

From Figure 5.18, capacitance value of air filled FFChip is between 0.9 pF and 0.5 pF for frequency range 100 Hz to 1 MHz. This capacitance value should be constant, or not dependent to frequency in definition but it seem that it is slightly dependent to the frequency. This may be because of the electrodes are made from a silver ink + silicon paste, and the material is polymer and those materials may respond differently to different frequencies. Also for very high Impedance values, the accuracy of LCR meters might be lower. But the capacitance is very low and in between a close range of 0.5 pF to 0.9 pF.

For the coplanar electrode geometry capacitance values can be calculated theoretically using Equation (3.14), (3.15) and (3.16). The parameters and their values used in equations are given in Table 5.2. Since the electrodes are produced using wet paste and DSA and transparency films are cut by laser cutter some of the dimensions are approximated as explained in Section 3.5.

Table 5.2 The parameters for capacitance value of coplanar electrode system.

Parameter	Symbol	Value
Relative permittivity of air	ε_{ra}	1.00059
Relative permittivity of transparency film	ε_{rf}	≈ 3
Permittivity of vacuum	ε_0	8.854×10^{-12} F/m
Electrode width	W	≈ 2 mm
Electrode length	l	≈ 4 mm
Channel height	h_{IN}	50 µm
Top transparency film height	h_{TM}	≈ 120 µm
Bottom transparency film height	h_{BM}	≈ 120 µm
Half gap between electrodes	a	≈ 1 mm

The 3M transparency film CG5000 is used for electrode film and for top cover film. CG5000's relative permittivity is not given exactly. But from the material sheet of film, it is composed of more than 94% Acrylate Copolymer, 5% of Urea-Formaldehyde Polymer and less than 1% of Ammonium. Acrylate Copolymer is a

group name and real material is not given by the producer, but according to [162] and measurements using LCR meter its relative permittivity is around 3.

The penetration depth T in Equation (3.14) is calculated for FFChip.

$$T = a\sqrt{\left(1+\frac{W}{a}\right)^2 - 1} = 1mm\sqrt{\left(1+\frac{2mm}{1m}\right)^2 - 1} = 2.83 \cdot 10^{-3} = 2.83mm \quad (5.4)$$

The penetration depth T = 2.83 mm is larger than all heights (channel height, bottom cover, and top cover) so for the effective capacitance calculation the effective width formulation should be used, as the width of electrode should be the one in Equation (3.15).

There are 4 capacitor values; capacitance of top and bottom cover, capacitance of inside channel and intrinsic capacitance, C_{TM}, C_{IN}, C_{BM} and C_N respectively. First three is explained in Section 3.5 and shown in Figure 3.12. The intrinsic capacitance can be assumed as noise capacitance. The LCR meter cables and the crocodile clips in the tip of cables generate a capacitance also because the penetration depth is higher compared to the height of FFChip, material under the FFChip, and air above it creates a medium for additive capacitance. The total capacitance will be the parallel resultant of all four as shown in Equation (5.5).

$$C = C_{IN} + C_{BM} + C_{TM} + C_N \quad (5.5)$$

where; C_N is the intrinsic or noise capacitance.

The total capacitance value is 17.33 fF plus the intrinsic capacitance. The measured capacitance is between 0.5 pF to 0.9pF so the intrinsic capacitance may be dominant and it may be the reason for measured capacitance for empty channel. One other possibility is that the permittivity of transparency film may be almost 30 times higher around 100, which can be also possible because conjugated polymers can have higher permittivities [163].

$$C_{eff} = \frac{2\varepsilon_r \varepsilon_0 l}{\pi} \cdot ln\left[\frac{h_{IN}}{a} + \sqrt{1 + \left(\frac{h_{IN}}{a}\right)^2} \right] \tag{5.6}$$

$$C_{IN} = \frac{2\varepsilon_{ra} \varepsilon_0 l}{\pi} \cdot ln\left[\frac{h_{IN}}{a} + \sqrt{1 + \left(\frac{h_{IN}}{a}\right)^2} \right] = 1.13\ fF \tag{5.7}$$

$$C_{BM} = \frac{2\varepsilon_{rf} \varepsilon_0 l}{\pi} \cdot ln\left[\frac{h_{BM}}{a} + \sqrt{1 + \left(\frac{h_{BM}}{a}\right)^2} \right] = 8.1\ fF \tag{5.8}$$

$$C_{TM} \cong \frac{2\varepsilon_{rf} \varepsilon_0 l}{\pi} \cdot ln\left[\frac{h_{TM}}{a} + \sqrt{1 + \left(\frac{h_{TM}}{a}\right)^2} \right] \cong 8.1\ fF \tag{5.9}$$

For C_{TM} the same formula as in other capacitance values is used however top cover is not connected with electrodes so this formula is only an approximation, the actual value should be lesser than this value.

$$\begin{gathered} C = C_{IN} + C_{BM} + C_{TM} + C_N \\ C \cong 1.13\ fF + 8.1\ fF + 8.1\ fF + C_N \\ C \cong 17.33\ fF + C_N \end{gathered} \tag{5.10}$$

The capacitance value of the channel is very low for the empathy channel. This shows that even if it is field with a higher permittivity solution in water the capacitance of bulk solution cannot be very high compared to that value. This indicated that even for lower frequency values this bulk solution capacitance will be very big, so it may not affect the total impedance because it is parallel to the whole system. This response will be observed further in Nyquist plots of HIV lysate measurements.

5.2.2.2 Impedance measurement for DI pure water

After empty channel measurements, deionized (DI) pure water filled to the channel of FFChip and impedance measurements are taken. Before measurements, DI pure water conductivity is measured with Elcometer® 138 Conductivity Meter and the value is less than 1μS/cm, which is out of the range for the device. However the DI pure water generator specification defines that the resistivity is 18 MΩcm around 0.2μS/cm so actual conductivity of DI pure water should be around 0.2μS/cm - 1μS/cm. All measurements are applied for frequencies between 100 Hz and 1 MHz.

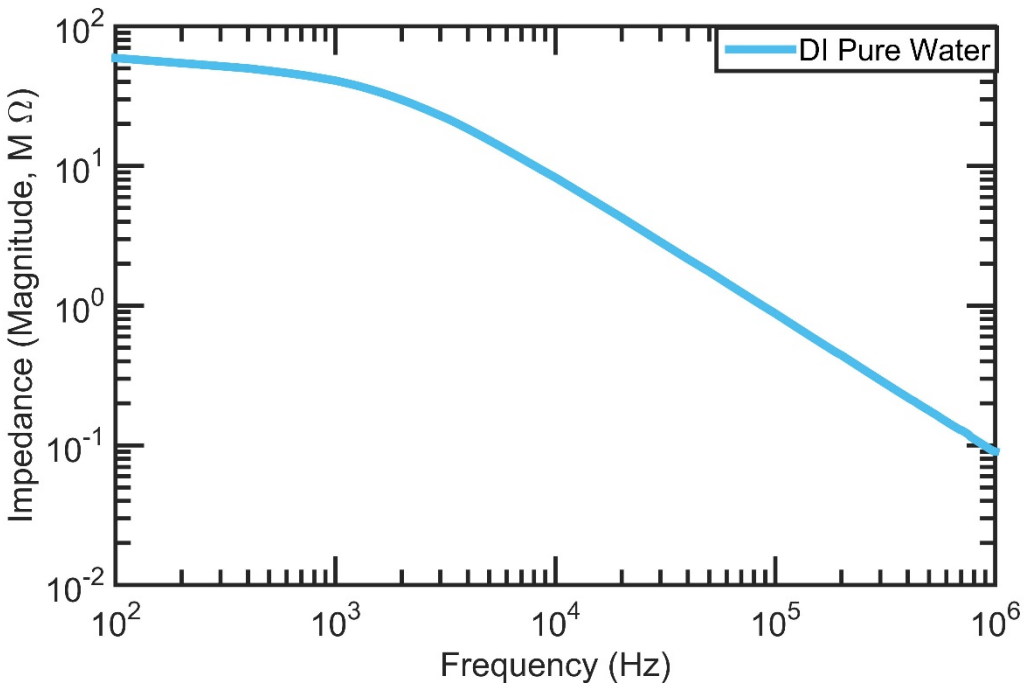

Figure 5.19 Impedance magnitude spectra of DI pure water for a frequency range between 100 Hz and 1 MHz.

The conductivity of DI pure water is constant and it is assumed that there is no or not many ions in the solution so the impedance response is highly dependent on the capacitive response of the water filled FFChip plus resistivity of the DI pure water. Also the resistive response should be constant and equivalent for all frequencies. For non-ionic solution the circuit model should be a capacitor parallel to a resistor which seems to be the case. From the phase spectra graphs in Figure 5.20, for lower frequencies, the impedance value is a result of resistive response and for higher frequencies it is as a result of capacitive response.

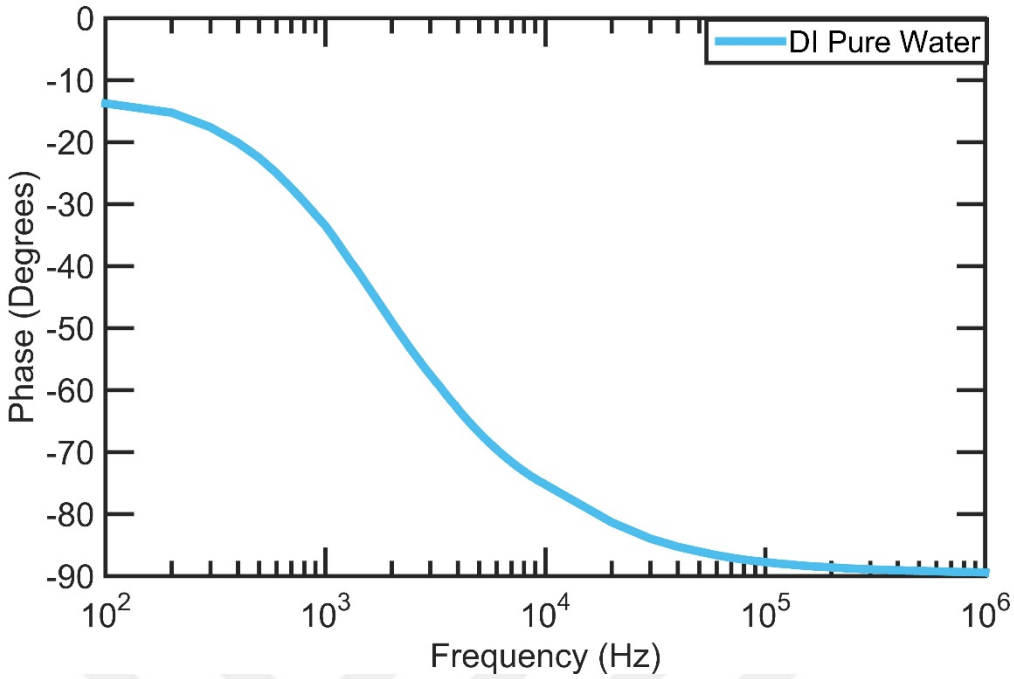

Figure 5.20 Impedance phase spectra of DI pure water for a frequency range between 100 Hz and 1 MHz.

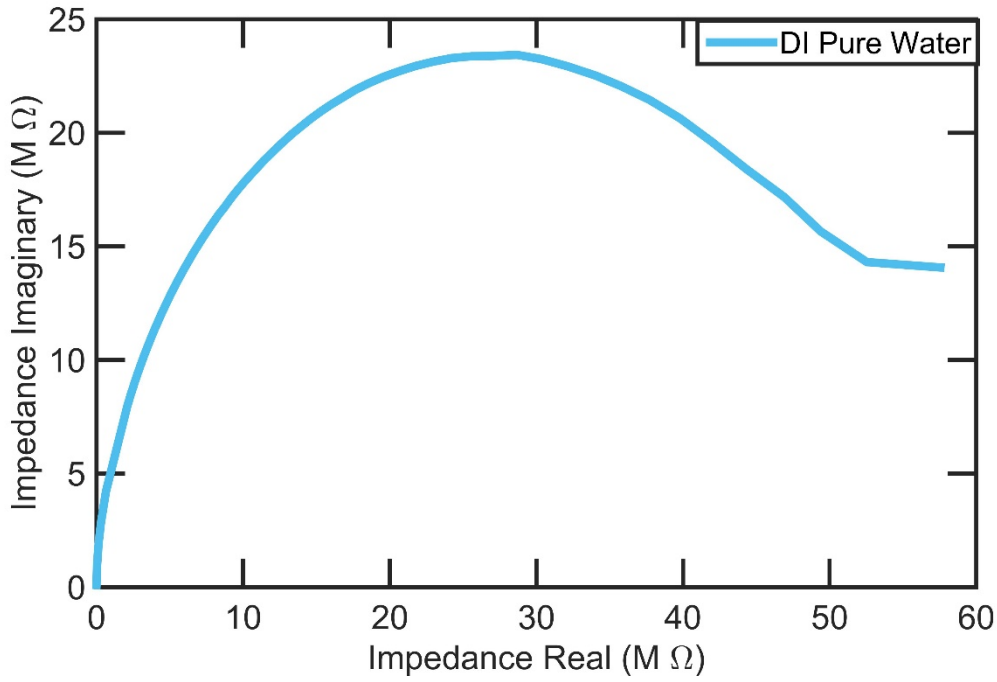

Figure 5.21 Nyquist plot of impedance value of DI pure water for a frequency range between 100 Hz and 1 MHz.

5.2.2.3 Impedance measurements for solutions with already known conductivities

After empty and deionized (DI) pure water filled channel measurements, solutions with different conductivities are measured. As a control 1% Triton 100-X solution in DI pure water is prepared. For test samples 0.05%, 0.1%, 0.25%, 0.50%, 1.0% and 5.0% PBS in DI pure water solutions are prepared. First solutions conductivities are measured with Elcometer® 138 Conductivity Meter and the values are shown in Figure 5.22.

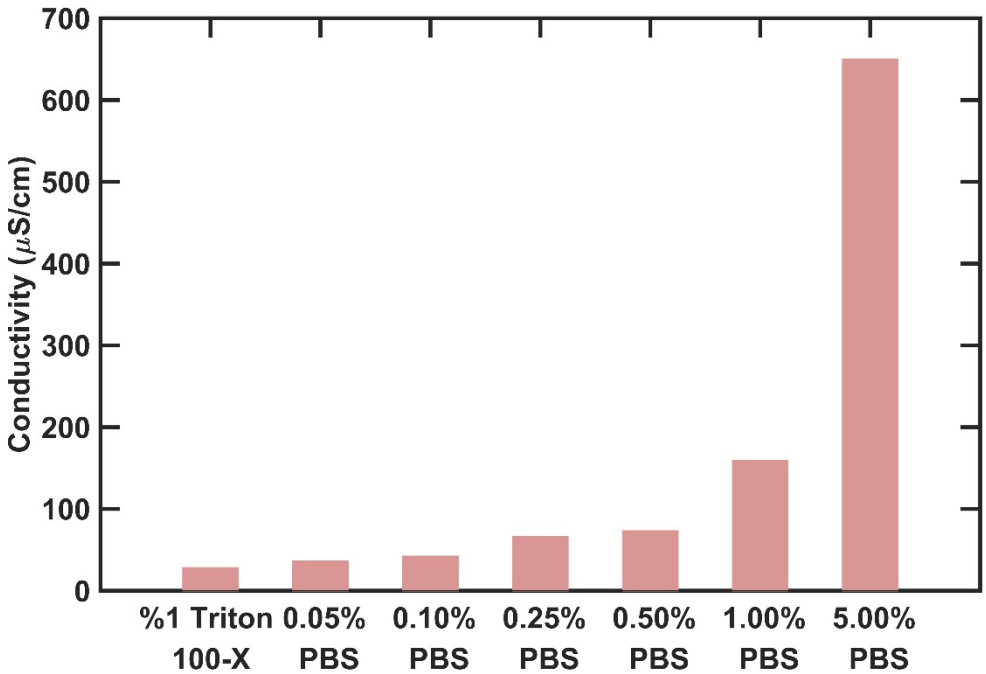

Figure 5.22 Conductivity values for solutions with different PBS concentration.

The measured conductivities show that solutions with different conductivities are obtained. And resistivity is calculated by one over conductivity values as in Equation (5.11) and shown in Figure 5.23.

$$\rho = \frac{1}{\sigma} \tag{5.11}$$

where, ρ is resistivity (Ω cm) and σ is conductivity (S/cm).

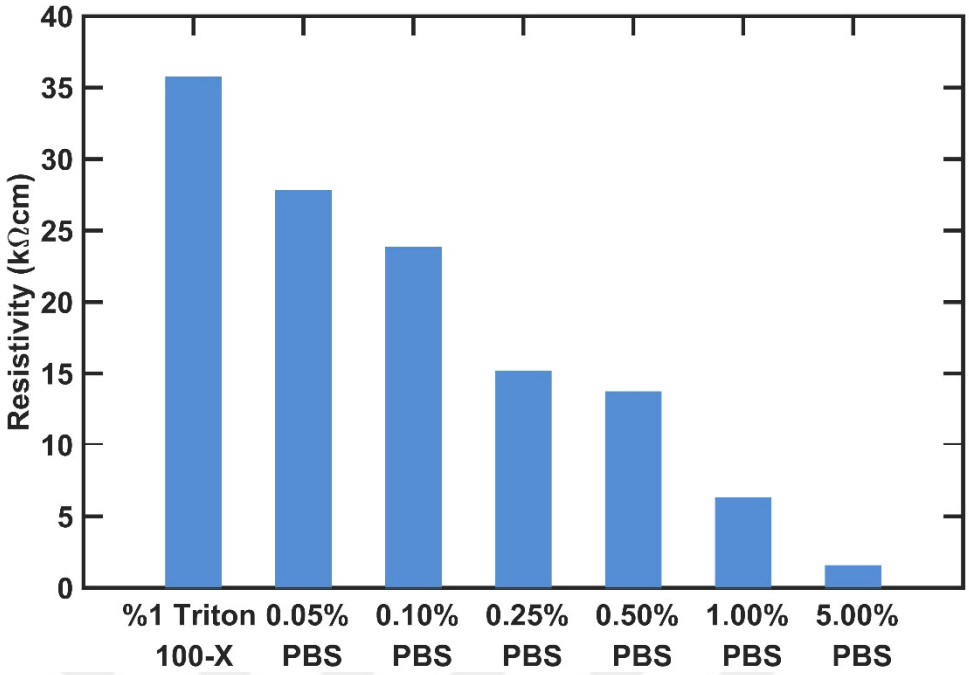

Figure 5.23 Resistivity values for solutions with different PBS concentration.

After determining the resistivities of control and PBS solutions impedance spectra measurements are applied for a frequency range between 100 Hz and 1 MHz.

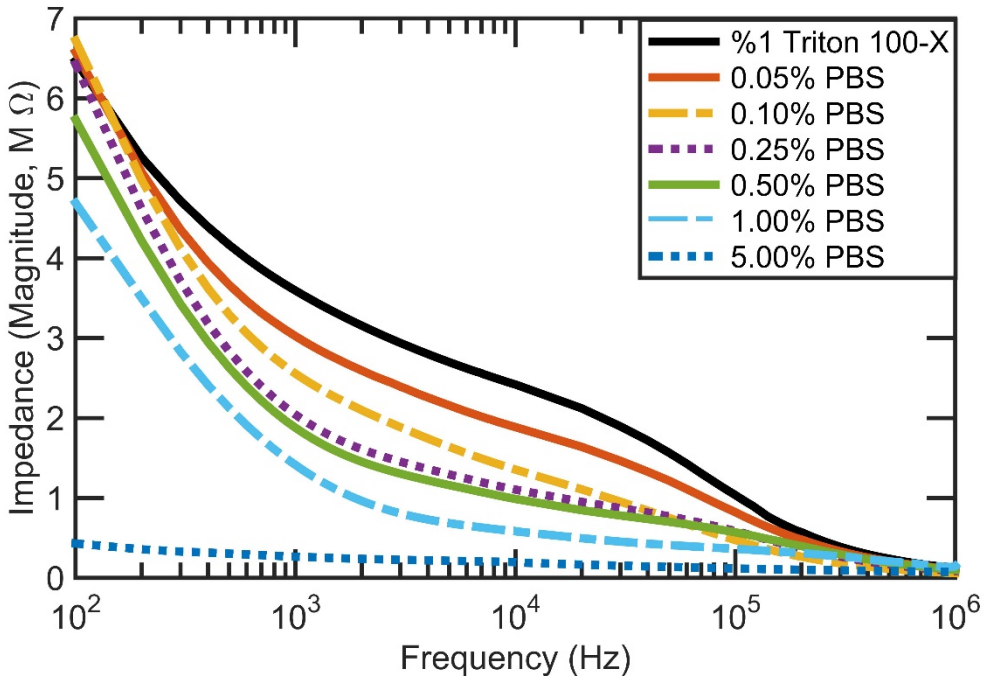

Figure 5.24 Impedance magnitude spectra of control and solutions with different PBS concentration for a frequency range between 100 Hz and 1 MHz.

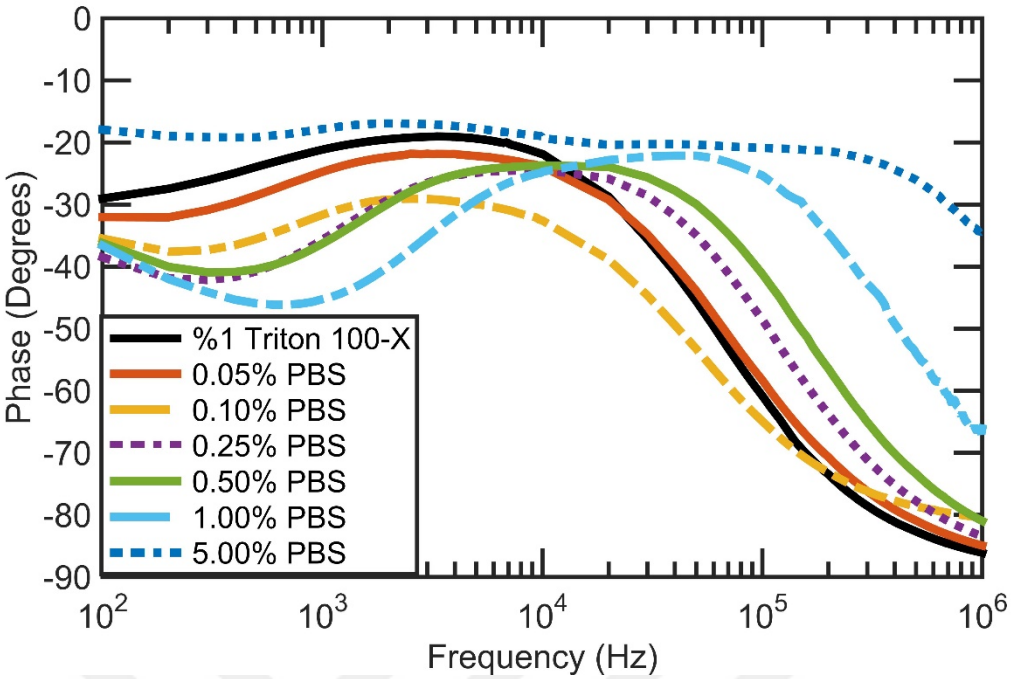

Figure 5.25 Impedance phase spectra of control and solutions with different PBS concentration for a frequency range between 100 Hz and 1 MHz.

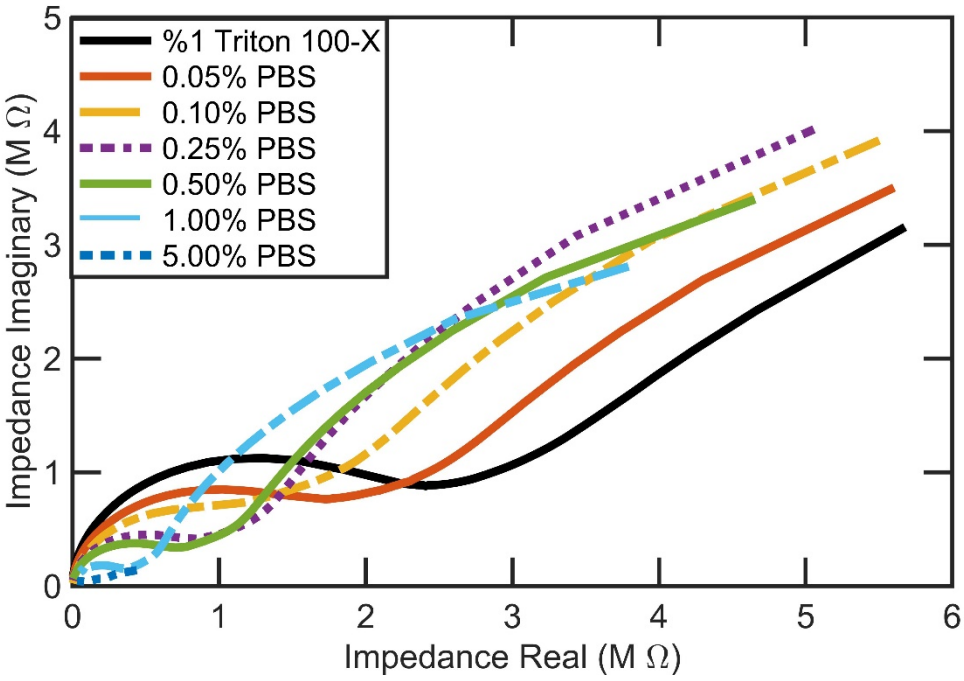

Figure 5.26 Nyquist plot of impedance value of control and solutions with different PBS concentration for a frequency range between 100 Hz and 1 MHz.

10uL of Control and PBS solutions are pipetted to channel in FFChip and corresponding impedance measurements has been applied. For each solution 3 different samples are used. The long curves are the electrical impedance magnitude spectra, phase spectra and Nyquist plot for different PBS concentration and control, which are represented in Figure 5.24, Figure 5.25 and Figure 5.26 respectively. Since there are 3 samples of each solutions, 3 measurements has been applied and the curves are the average of those 3 measurements results.

The impedance magnitudes for solutions at a certain frequency (1 kHz) are given in Figure 5.27 and the impedance magnitude change with respect to average control value is given in Figure 5.28. In order to see the difference in the impedance magnitude change, it has been calculated by dividing all impedance magnitude results to the average of control impedance magnitude at the certain 1 kHz. Also at that frequency the repeatability is also calculated and shown in Figure 5.29.

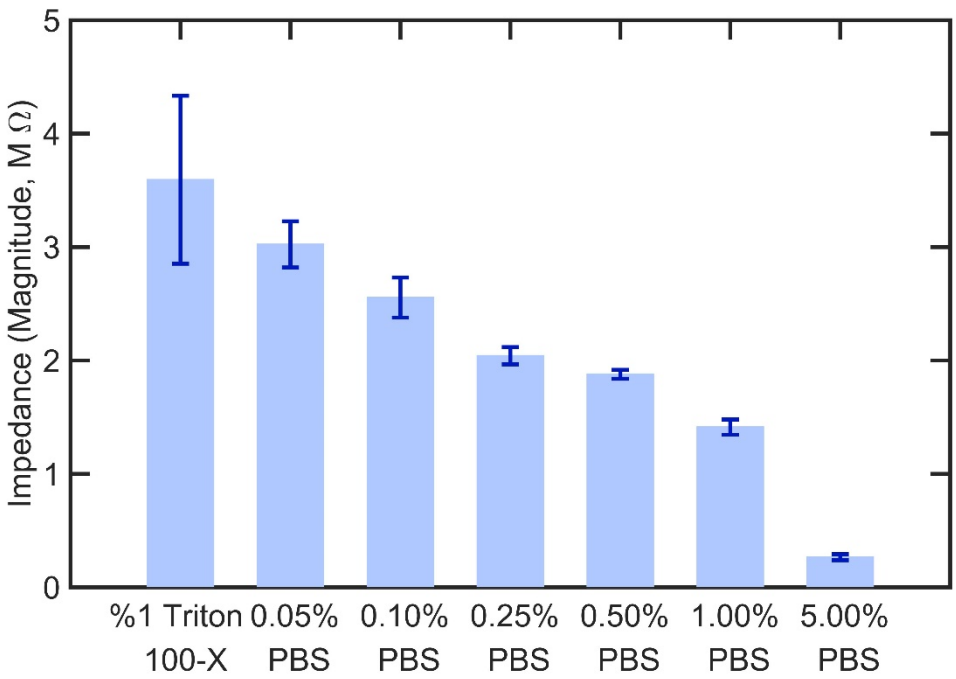

Figure 5.27 Impedance magnitude values of control and solutions with different PBS concentration at 1 kHz. Error bars are STD of the mean of impedance magnitude (n=3).

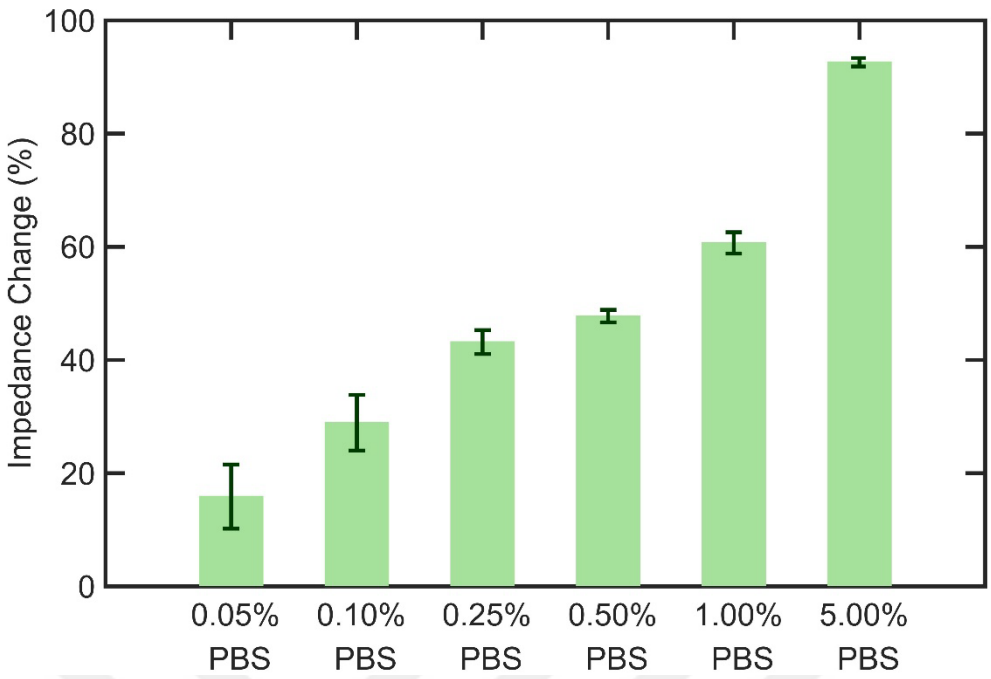

Figure 5.28 Normalized impedance magnitude values of solutions with different PBS concentration to the mean of impedance magnitude of control at 1 kHz. Error bars are STD of the mean of normalized impedance magnitude (n=3).

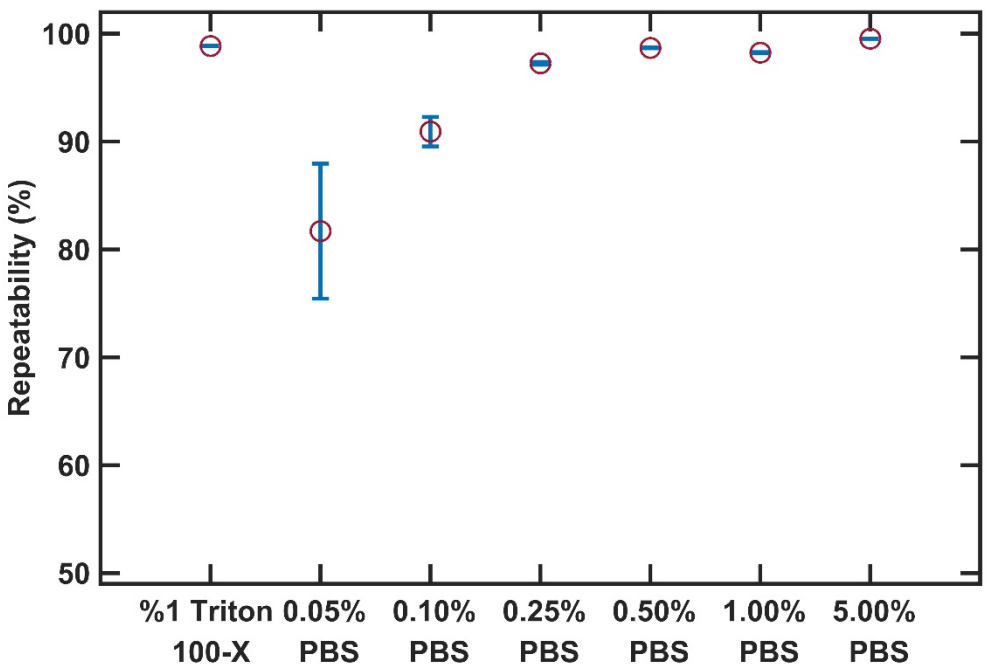

Figure 5.29 Repeatability of normalized impedance magnitude measurements of control and solutions with different PBS concentration at 1 kHz. Error bars are STD of the mean of normalized impedance magnitude (n=3).

There is a correlation between the conductivity and impedance magnitude results for different concentrations of PBS in DI pure water solutions which is expected. Also the repeatability of the measurements are over 80%. The electrodes are fully functional and ready to use for lysed HIV impedance measurements.

5.2.2.4 Impedance measurements for HIV lysate in PBS

The samples with lysed HIV are prepared for different subtypes (A, B, C, D, E, G, and pane), the preparation of those samples and control are explained in section 5.1.2.3. In this experiment HIV subtypes are spiked in PBS as a clinical disease model. After that proposed detection method for diagnosis of HIV is applied, using FFChip. 10uL of HIV lysate and control are pipetted to FFChip and impedance measurements are applied using the analysis setup described in section 5.1.3.1.

The viral loads of HIV-1 subtypes A, B, C, D, E, G, and the panel are 1.74×10^8, 1.2×10^8, 1.17×10^8, 2.9×10^8, 8.39×10^8, 6.53×10^8, and 1.49×10^9 copies/mL, respectively. All measurements are applied for frequencies between 100 Hz and 1 MHz.

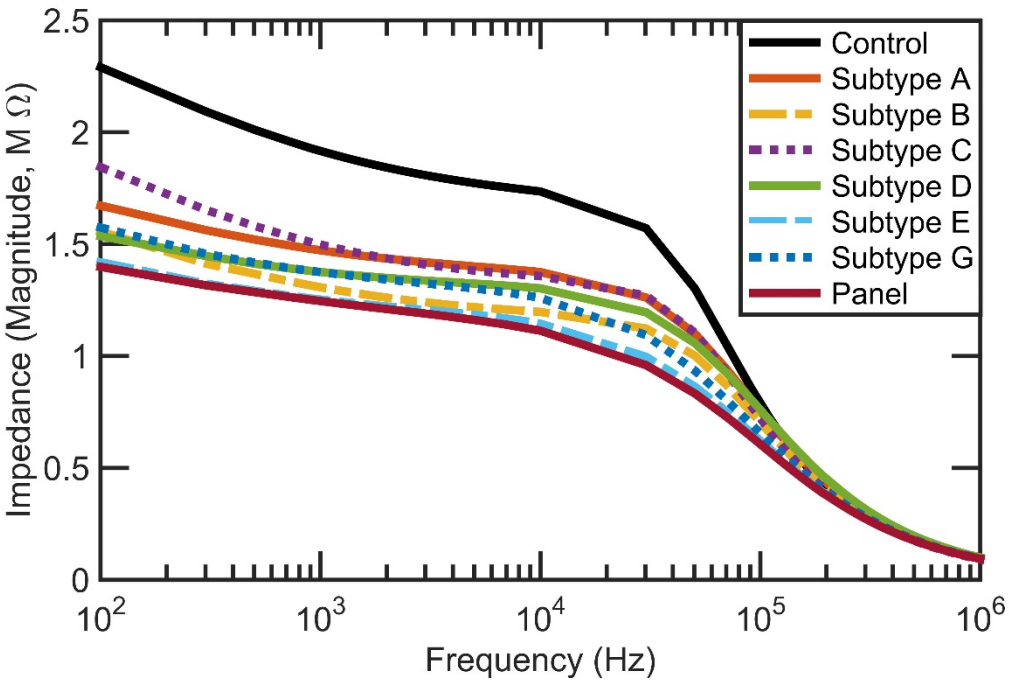

Figure 5.30 Impedance magnitude spectra of control and lysed HIV subtypes (A, B, C, D, E, G and Panel) for a frequency range between 100 Hz and 1 MHz.

The impedance of lysed solution is changed compared to the impedance of non-virus control. The detection is applied by impedance measurement of solution in FFChip. Mean impedance magnitude values of all subtypes compared to control are different for frequencies lower than around 50 kHz as shown in Figure 5.30. Between frequencies 100 Hz and 30 kHz the difference between mean impedance magnitude values of subtypes and control is almost 0.5 MΩ. Mean phase values are almost not distinguishable from each other as shown in Figure 5.31. From Nyquist plot in Figure 5.32, it can be seen that the time constant of control is obviously different from all subtypes.

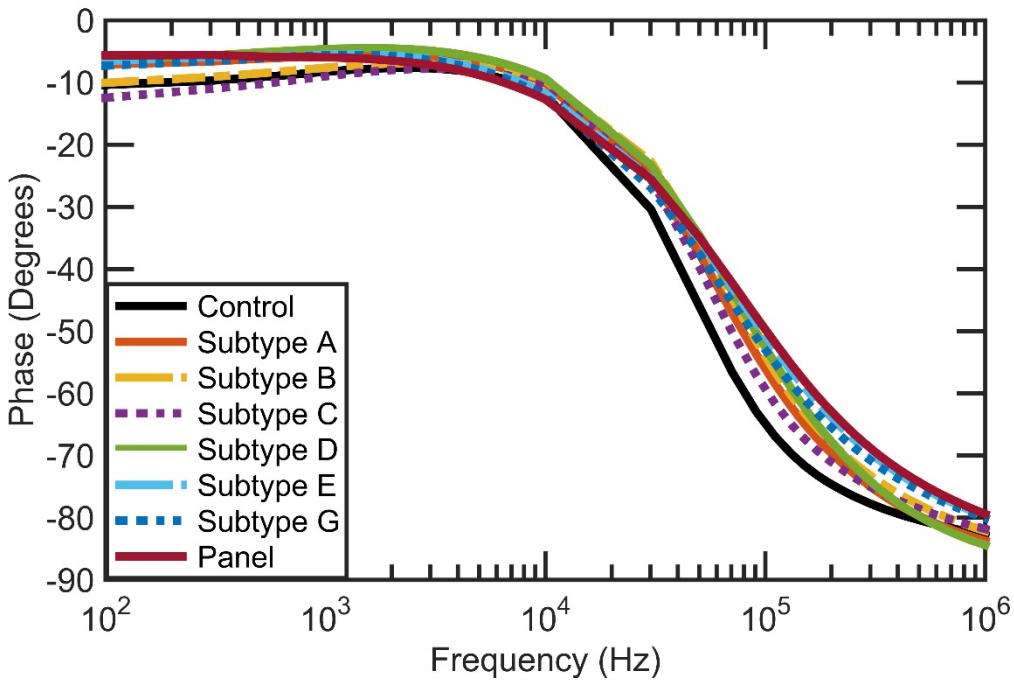

Figure 5.31 Impedance phase spectra of control and lysed HIV subtypes (A, B, C, D, E, G and Panel) for a frequency range between 100 Hz and 1 MHz.

The mean impedance magnitude for panel is the lowest one compared to all others and control, it may be because there are more viruses in panel virus solution, since there are more viruses the captured and lysed virus may be more and the impedance degrease can be higher because of more ions in the solution from lysed viruses.

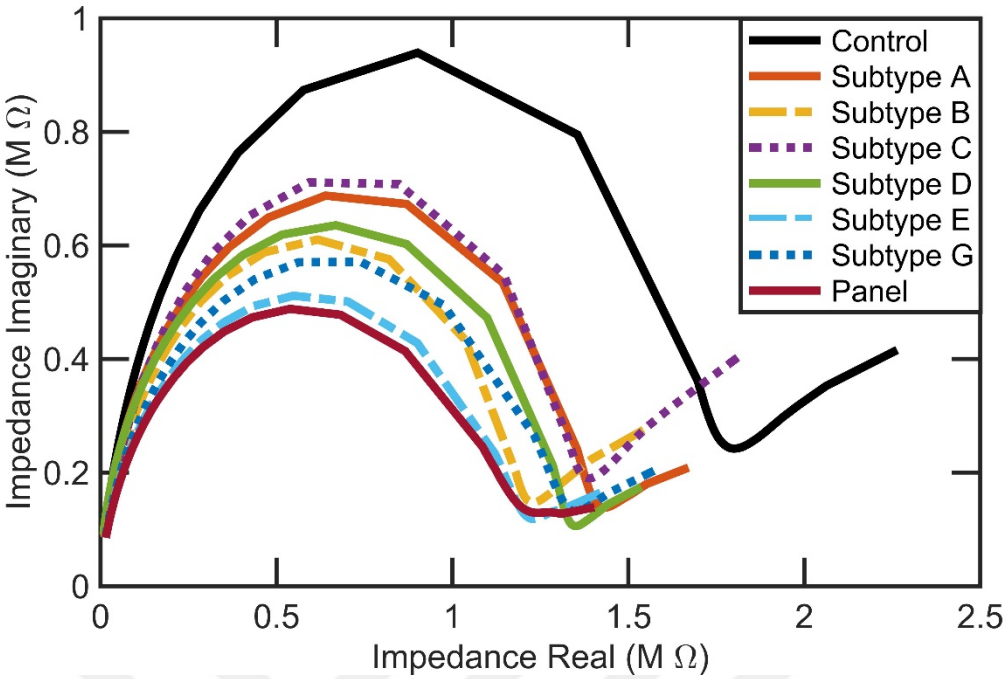

Figure 5.32 Nyquist plot of impedance value of control and lysed HIV subtypes (A, B, C, D, E, G and Panel) for a frequency range between 100 Hz and 1 MHz.

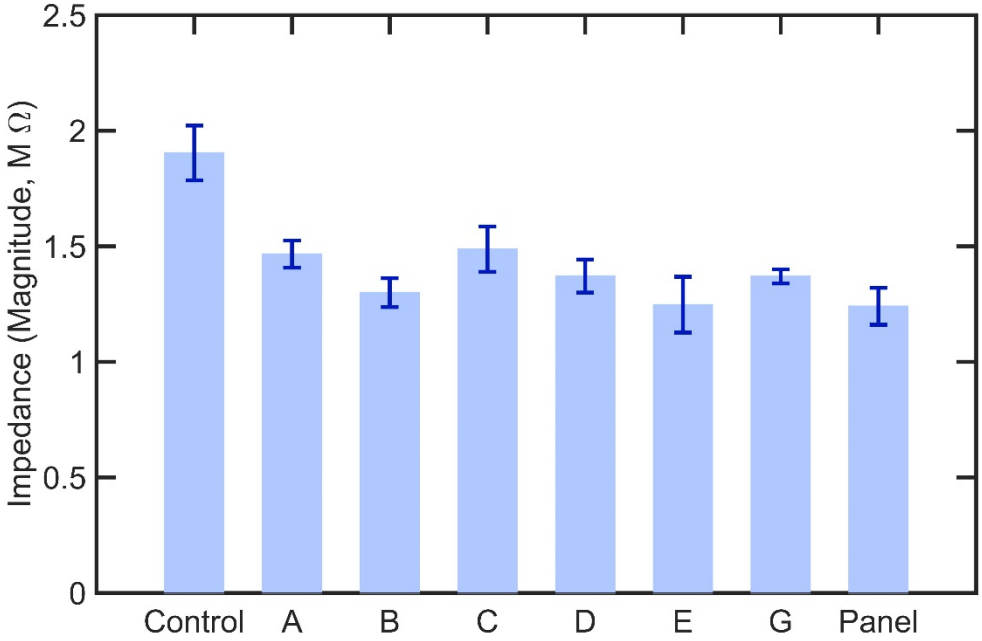

Figure 5.33 Impedance magnitude values of control and lysed HIV subtypes (A, B, C, D, E, G and Panel) at 1 kHz. Error bars are STD of the mean of impedance magnitude (n=3).

The maximum difference in mean impedance magnitude is observed at around 1 kHz. So at that frequency the impedance magnitudes are obtained for all samples and results are reported in Figure 5.33. Mean impedance magnitude value is plotted with error bars which indicates the standard deviation of impedance magnitude (n=3). Statistical analysis of the results was performed using ANOVA with Tukey post hoc test for multiple comparisons.

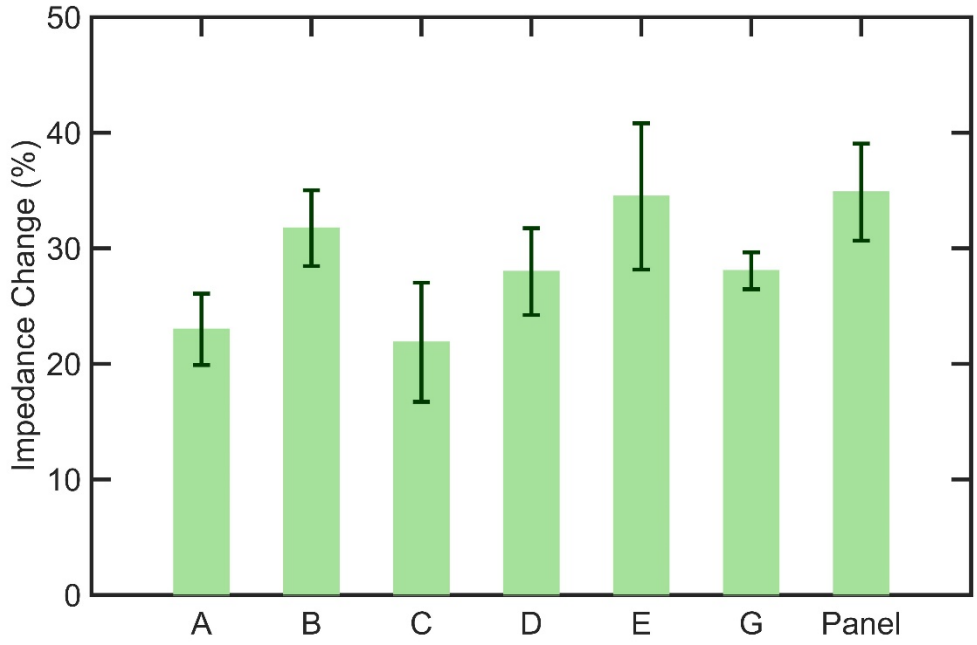

Figure 5.34 Normalized impedance magnitude values of lysed HIV subtypes (A, B, C, D, E, G and Panel) to the mean of impedance magnitude of control at 1 kHz. Error bars are STD of the mean of normalized impedance magnitude (n=3).

Statistical significance threshold is set to 0.05, ($p < 0.05$). It has been observed that impedance magnitude of control is significantly higher than HIV subtypes ($n = 3$, $p < 0.05$). Between HIV subtypes in terms of the impedance magnitudes there are no statistically significant difference ($n = 3$, $p > 0.05$). The diagnosis method can detect multiple subtypes of HIV.

The impedance magnitudes of HIV subtypes are normalized according to the mean impedance magnitude of control at 1 kHz. The results are plotted in Figure 5.34. It has been observed that HIV subtypes impedance magnitudes are changed between 20% - 35%.

Repeatability of the measurements is calculated according to the method given in section 5.1.3.2 and given in Figure 5.35. The minimum and maximum values for repeatability are around 87% and 99%, respectively. This indicates that the measurements are at least 87% repeatable.

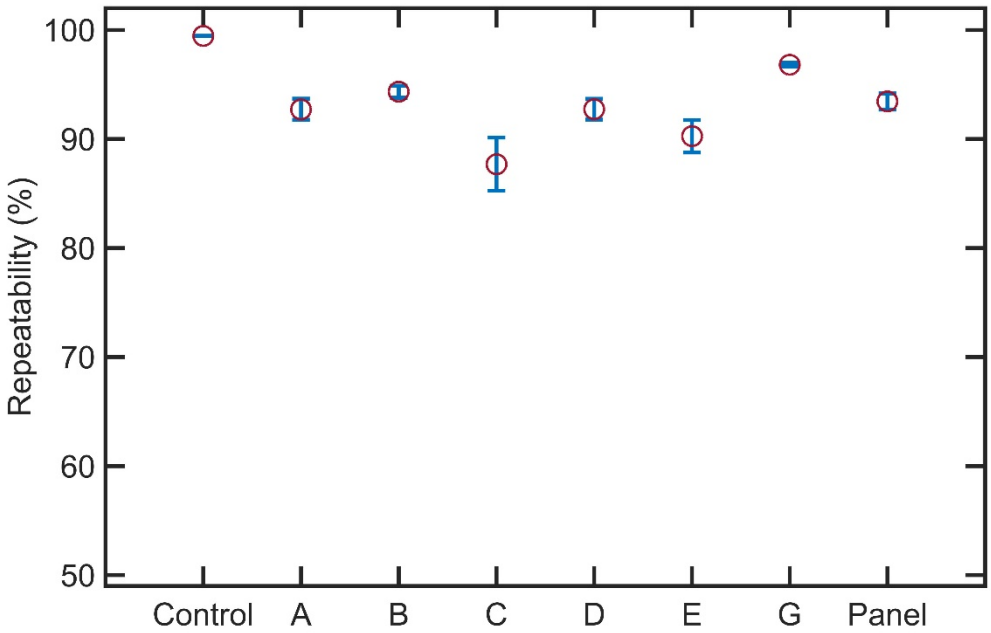

Figure 5.35 Repeatability of normalized impedance magnitude measurements of control and lysed HIV subtypes (A, B, C, D, E, G and Panel) at 1 kHz. Error bars are STD of the mean of repeatability (n=3).

5.2.2.5 Time dependency test of the method

In order to understand the effect of time on lysate solution, time dependency test is performed. Triton 100-X is used for lysing the viruses and control solution is the same lysing solution as explained in section 5.1.2.3. After the solution is prepared the effect of time on this solution is tested for 80 min with intervals of 20 mins. All measurements are applied for frequencies between 100 Hz and 1 MHz.

The Impedance magnitude spectra of control at different time interval after prepared (0, 20, 40, 60 and 80 min) are shown in Figure 5.36. The impedance values seem similar. Also at 1 kHz frequency values of the impedance magnitudes are obtained and results are reported in Figure 5.37.

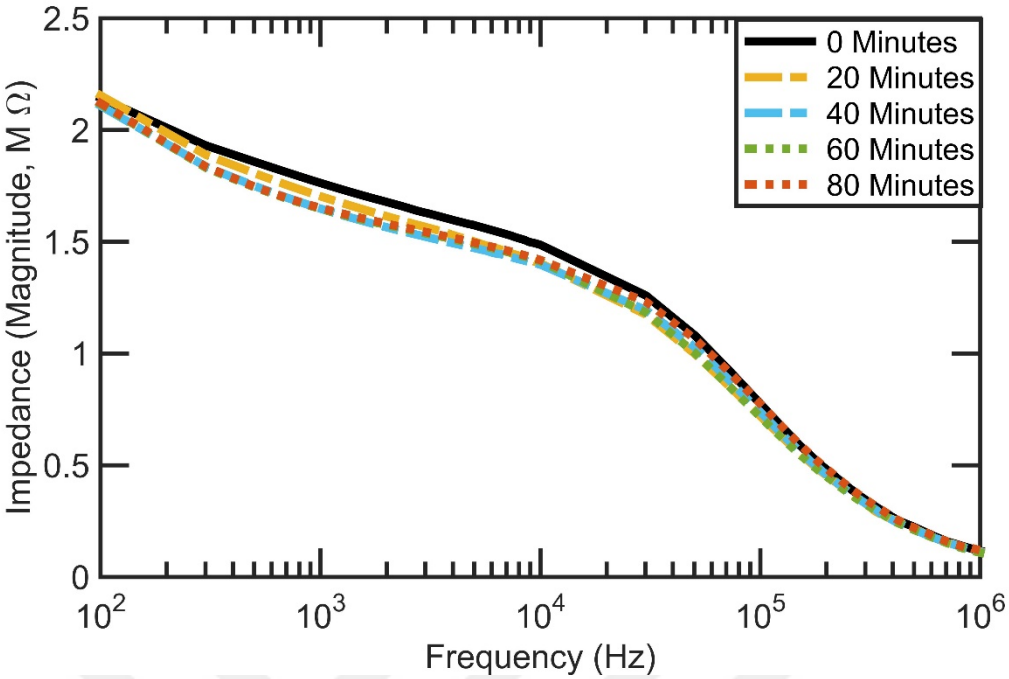

Figure 5.36 Impedance magnitude spectra of control at different time interval after prepared (0, 20, 40, 60 and 80 min).

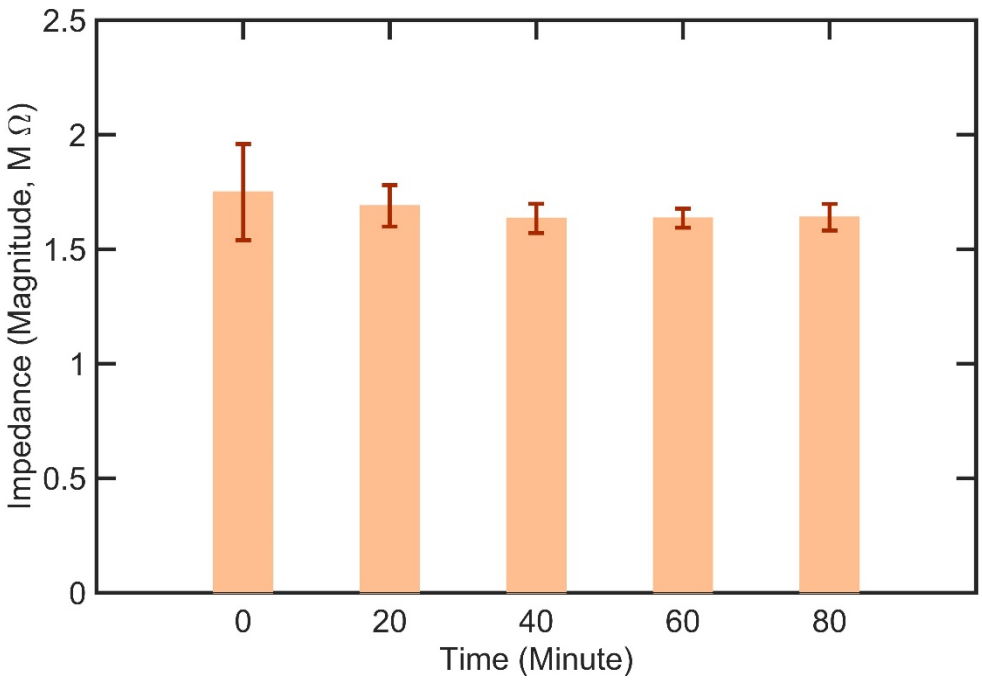

Figure 5.37 Impedance magnitude values of control at different time interval after prepared (0, 20, 40, 60 and 80 min) at 1 kHz. Error bars are STD of the mean of impedance magnitude (n=3).

It has been observed that there is not a statistically significant difference between impedance magnitude dependence of on time until 80 mins of control samples (n = 3, $p > 0.05$). Statistical analysis of the results was performed using ANOVA with Tukey post hoc test for multiple comparisons. Lyse and control samples are not time dependent.

5.2.2.6 Lower concentration of virus diagnosis test using the method

In the measurements the viral loads of HIV-1 subtypes A, B, C, D, E, G, and the panel with 1.74×10^8, 1.2×10^8, 1.17×10^8, 2.9×10^8, 8.39×10^8, 6.53×10^8, and 1.49×10^9 copies/mL, respectively are used. The diagnosis method is able to detect viruses around this concentrations, in order to test methods efficiency for lower concentration, HIV subtype D is diluted to get 2.9×10^6 copies/mL and tested.

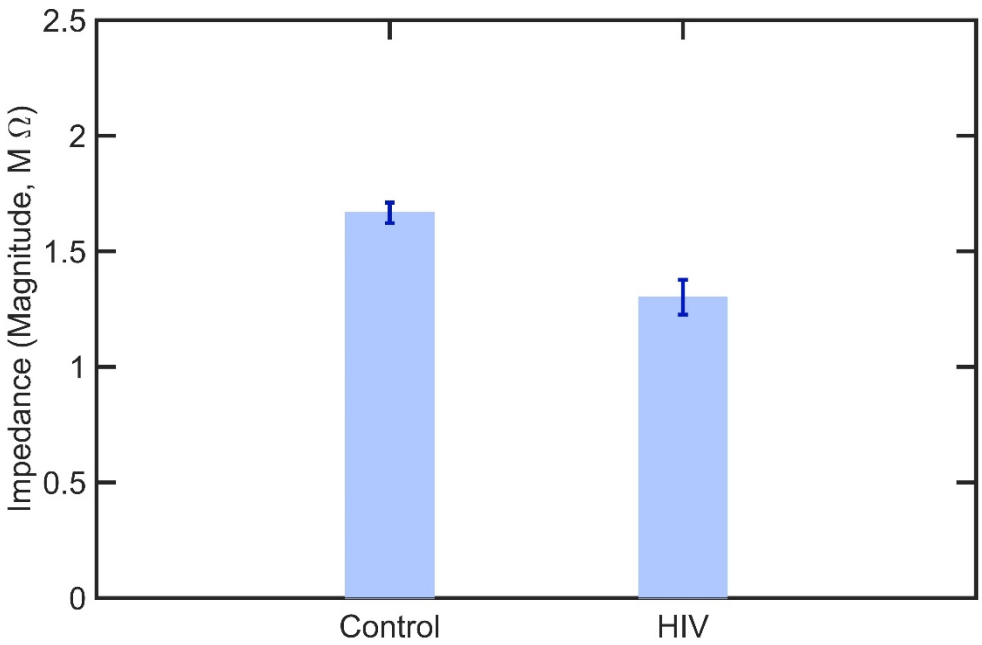

Figure 5.38 Impedance magnitude values of control and lysed HIV subtype D with a concentration of 2.9×10^6 copies/mL at 1 kHz. Error bars are STD of the mean of impedance magnitude (n=3).

The maximum difference in mean impedance magnitude is observed at around 1 kHz. So at that frequency the impedance magnitudes are obtained for control and HIV subtype D of lower concentration (2.9×10^6 copies/mL) and results are reported

in Figure 5.38. Mean impedance magnitude value is plotted with error bars which indicates the standard deviation of impedance magnitude (n=3). The impedance difference between control and virus is almost 0.3 MΩ.

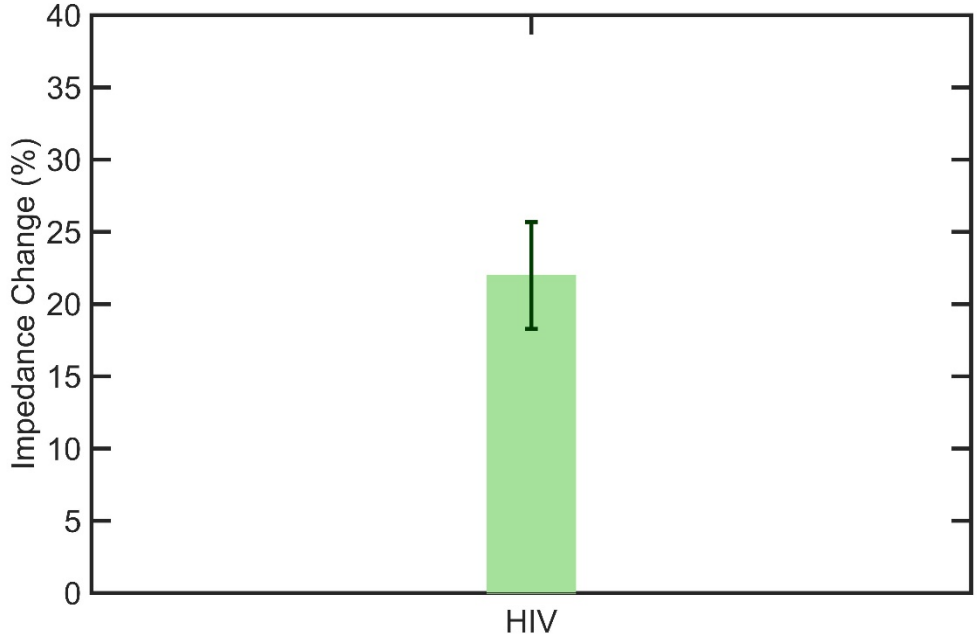

Figure 5.39 Normalized impedance magnitude values of lysed HIV subtype D with a concentration of 2.9 × 10^6 copies/mL to the mean of impedance magnitude of control at 1 kHz. Error bars are STD of the mean of normalized impedance magnitude (n=3).

Statistical analysis of the results was performed. Statistical significance threshold is set to 0.05, ($p < 0.05$). It has been observed that impedance magnitude of control is significantly higher than HIV subtypes D with a concentration of 2.9 × 10^6 copies/mL ($n = 3$, $p < 0.05$).

The impedance magnitudes of HIV subtype D with a concentration of 2.9 × 10^6 copies/mL is normalized according to the mean impedance magnitude of control at 1 kHz. The result is plotted in Figure 5.39. It has been observed that the impedance magnitude change is 22%. So the proposed diagnosis method is able to detect even 10^6 copies/mL of HIV spiked in PBS.

Repeatability of the measurements is calculated according to the method given in section 5.1.3.2 and given in Figure 5.40. The minimum and maximum values for repeatability are around 90% and 99%, respectively. This indicates that the measurements are at least 90% repeatable.

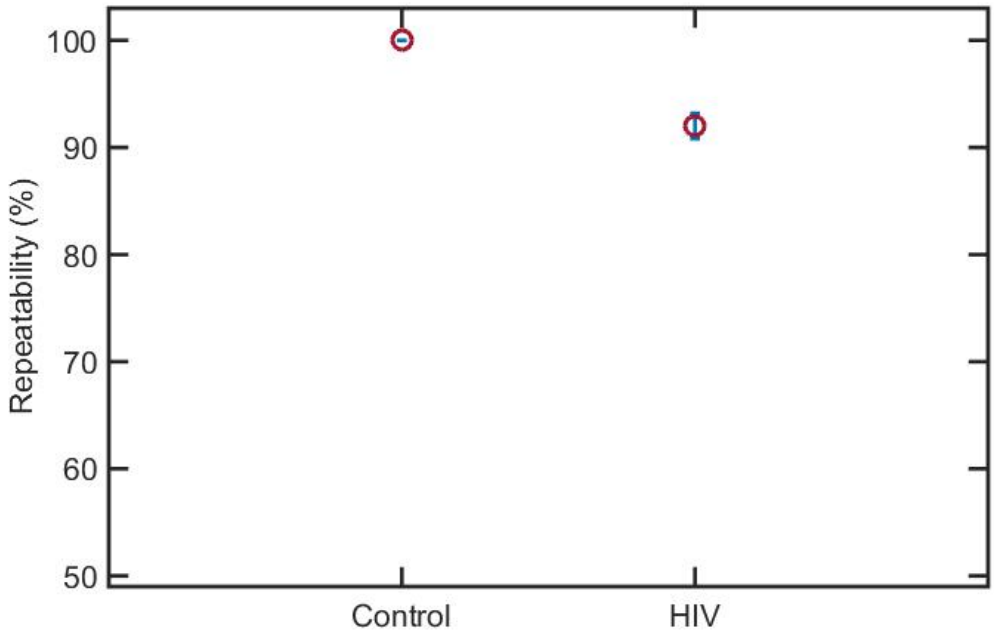

Figure 5.40 Repeatability of normalized impedance magnitude measurements of control and HIV subtype D with a concentration of 2.9 × 10^6 copies/mL at 1 kHz. Error bars are STD of the mean of repeatability (n = 3).

5.2.2.7 Specificity test of the method

In order to determine the specificity of the proposed diagnosis method, the method is tested using a different virus. In this experiment Epstein-Barr virus (EBV) is used to test specificity. Three solutions in PBS are prepared for HIV subtype A, EBV and a mix of them. Those three solutions are clinical examples of target virus, non-target virus, and mix of them. For detection and lysing processes which were explained in section 5.1.2.3 those solutions are used as sample mediums. Lysate solution of three samples and control are ready for impedance measurements using FFChip. Control is simply virus free lysis solution. All measurements are applied for frequencies between 100 Hz and 1 MHz.

The impedance analysis can be evaluated by defining 2 groups, first group is control and EBV samples, second group is HIV subtype A and HIV subtype A + EBV samples. Further discussions will be made according to groups.

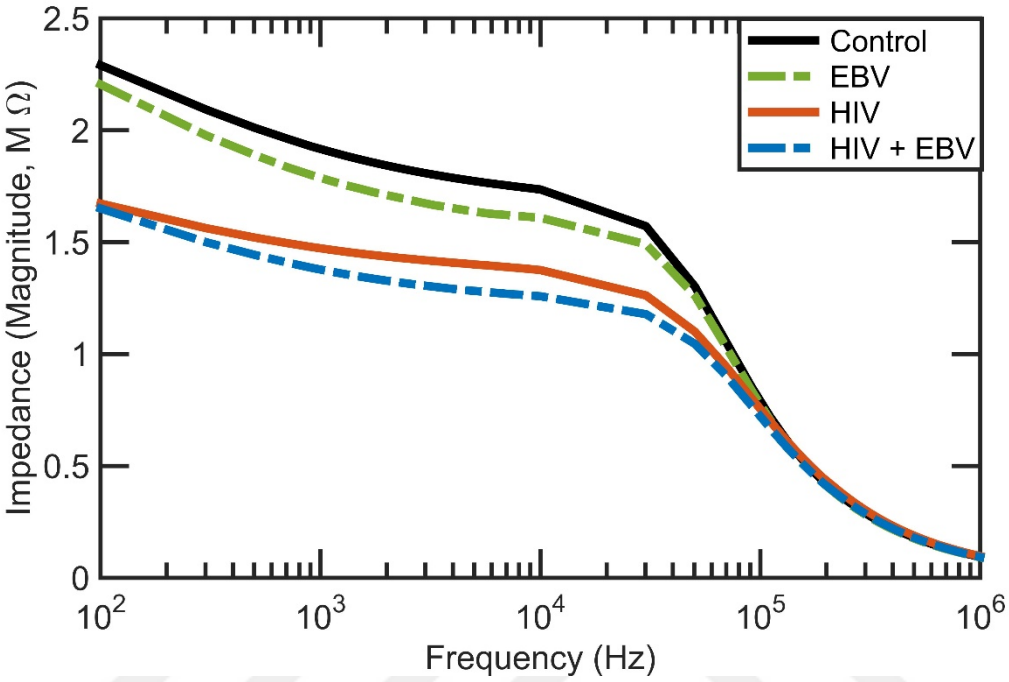

Figure 5.41 Impedance magnitude spectra of control, HIV subtype A, EBV and HIV subtype A + EBV, for a frequency range between 100 Hz and 1 MHz.

Impedance magnitude spectra of control, HIV subtype A, EBV and HIV subtype A + EBV, are given in Figure 5.41. Control and EBV samples (first group) impedance magnitude spectra's are almost equal to each other, also HIV subtype A and HIV subtype A + EBV (second group) samples impedance magnitude spectra's are almost equal to each other but impedance magnitude of first group and second group is different from each other. Mean impedance magnitude values of first group is different from second group for frequencies lower than around 50 kHz. Between frequencies 100 Hz and 30 kHz the difference between mean impedance magnitude values of first group and second group is almost 0.4 MΩ.

Mean impedance phase values are almost not distinguishable from each other for all samples as shown in Figure 5.42. From Nyquist plot in Figure 5.43 it is can be seen that the time constant of first group is obviously different from second group.

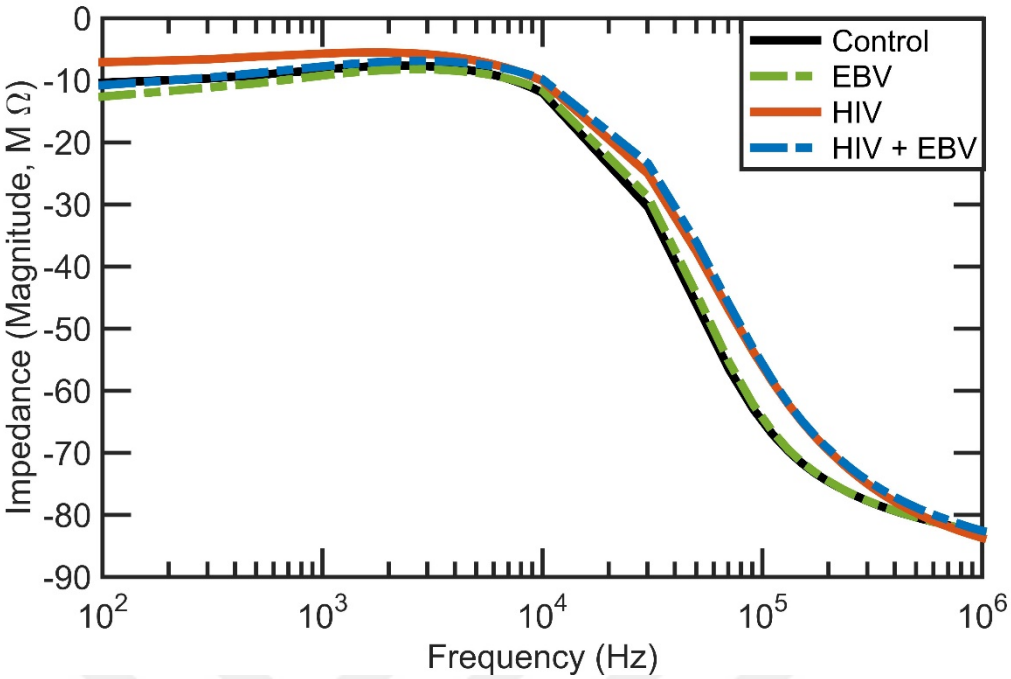

Figure 5.42 Impedance phase spectra of control, HIV subtype A, EBV and HIV subtype A + EBV, for a frequency range between 100 Hz and 1 MHz.

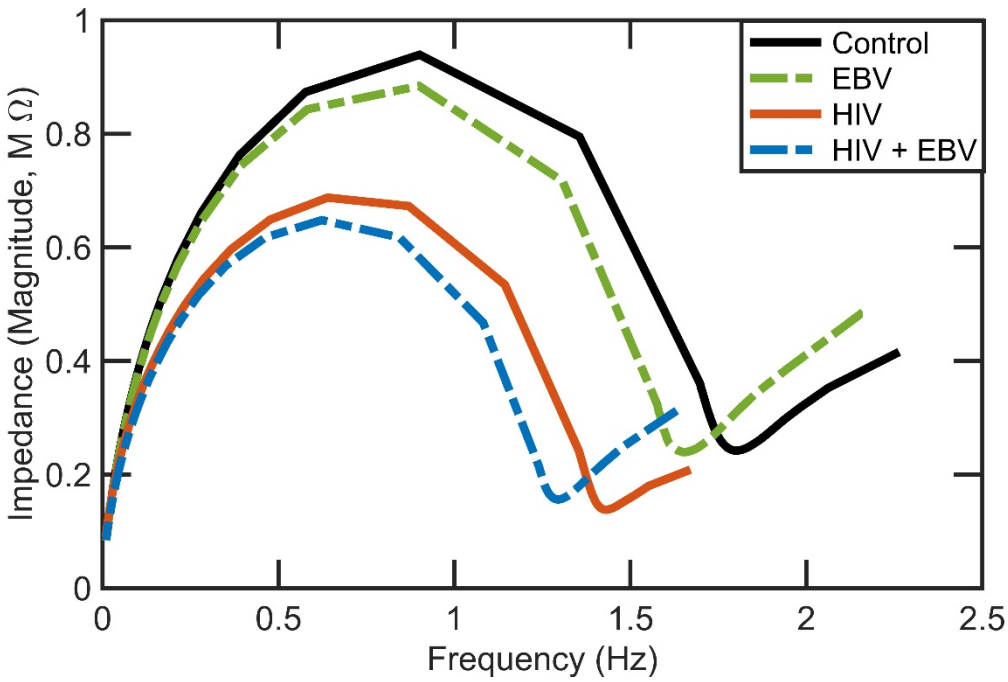

Figure 5.43 Nyquist plot of impedance value of control, HIV subtype A, EBV and HIV subtype A + EBV, for a frequency range between 100 Hz and 1 MHz.

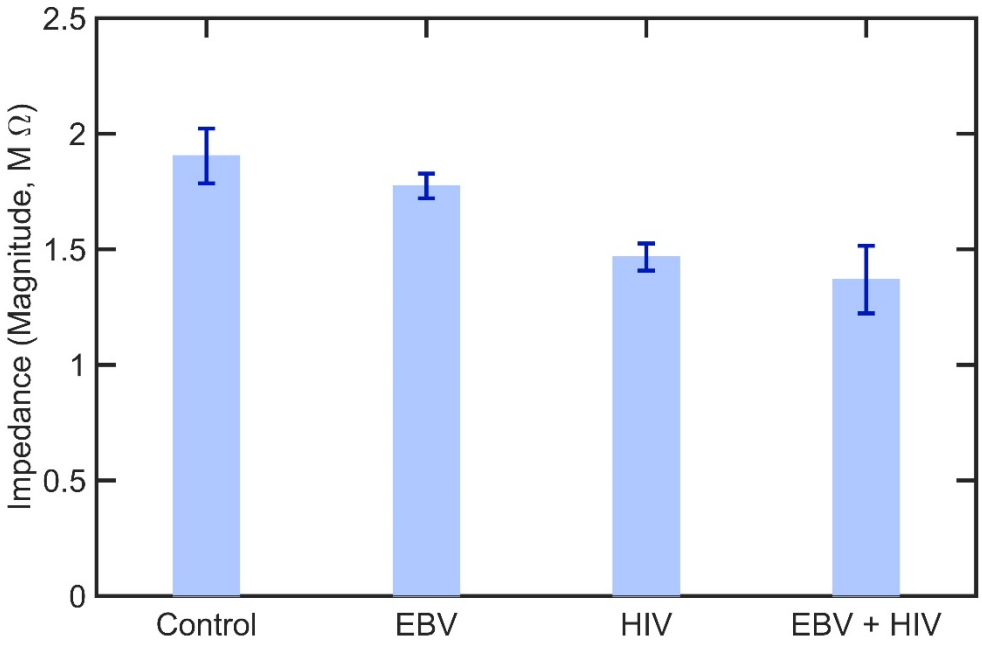

Figure 5.44 Impedance magnitude values of control, HIV subtype A, EBV and HIV subtype A + EBV, at 1 kHz. Error bars are STD of the mean of impedance magnitude (n=3).

The maximum difference in mean impedance magnitude of groups are observed at around 1 kHz. So at that frequency the impedance magnitudes are obtained for all samples and results are reported in Figure 5.44. Mean impedance magnitude value is plotted with error bars which indicate the standard deviation of impedance magnitude (n=3). Statistical analysis of the results was performed using ANOVA with Tukey post hoc test for multiple comparisons.

Statistical significance threshold is set to 0.05, ($p < 0.05$). It has been observed that impedance magnitude of first group is significantly higher than second group ($n = 3$, $p < 0.05$). In first group between control and EBV samples in terms of the impedance magnitudes there are no statistically significant difference ($n = 3$, $p > 0.05$). Also in first group between HIV subtype A and HIV subtype A + EBV samples in terms of the impedance magnitudes there are no statistically significant difference ($n = 3$, $p > 0.05$). These results indicate that the diagnosis method is specific to HIV.

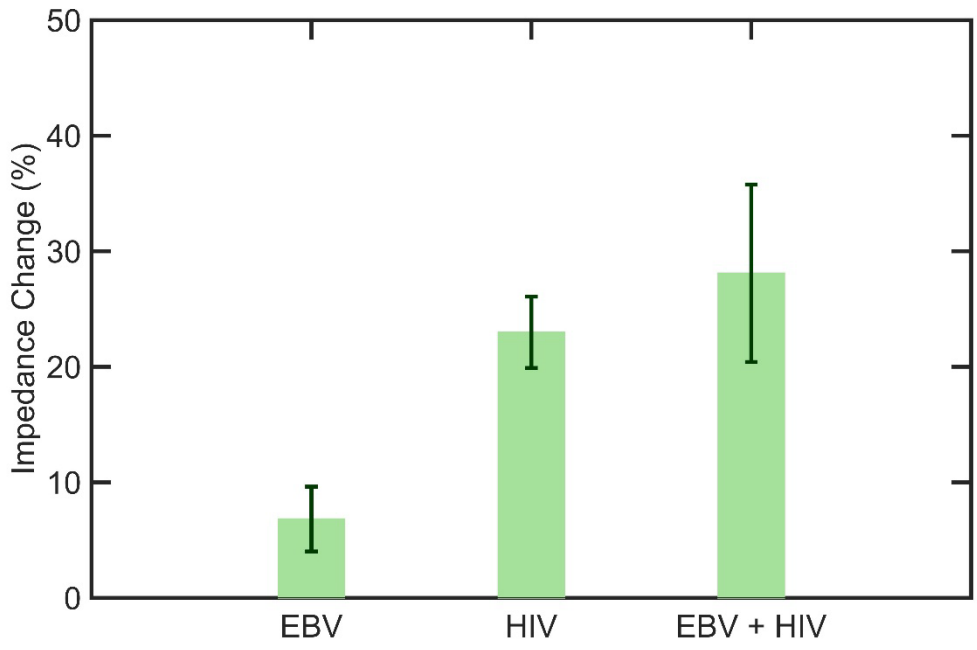

Figure 5.45 Normalized impedance magnitude values of HIV subtype A, EBV, and HIV subtype A + EBV, to the mean of impedance magnitude of control at 1 kHz. Error bars are STD of the mean of normalized impedance magnitude (n=3).

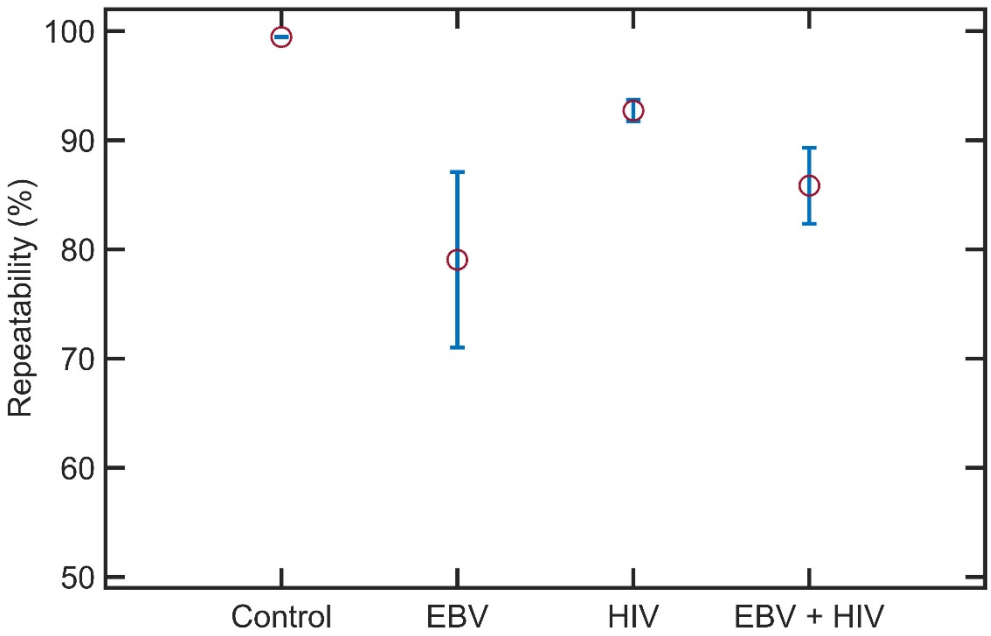

Figure 5.46 Repeatability of normalized impedance magnitude measurements of control, HIV subtype A, EBV and HIV subtype A + EBV, at 1 kHz. Error bars are STD of the mean of repeatability (n=3).

The impedance magnitudes of EBV, HIV subtype A and HIV subtype A + EBV are normalized according to the mean impedance magnitude of control at 1 kHz. The results are plotted in Figure 5.45. It has been observed that the change in impedance magnitudes of HIV subtype A is around 25% and HIV subtype A + EBV the change is around 28%. The change of EBV is statistically negligible and also the difference between HIV and HIV subtype A + EBV is statistically negligible.

Repeatability of the measurements is calculated according to the method given in section 5.1.3.2 and given in Figure 5.46. The minimum and maximum values for repeatability are around 80% and 99%, respectively. This indicates that the measurements are at least 80% repeatable.

5.2.2.8 Impedance measurements for HIV lysate in plasma

In the analysis for HIV lysate in PBS, the HIV samples are in PBS solution and in order to capture them anti-gp120 antibody conjugated magnetic beads are added to PBS solution with HIV. In this part and in the next part in order to see the sensibility of the diagnosis method in biological samples, HIV is spiked to plasma and blood, and the test was performed to detect virus in plasma and blood.

In this experiment HIV subtype C is spiked in plasma. The sample preparation for HIV lysate and control are done exactly as explained in section 5.1.2.3, except plasma is used as a medium for viruses. After that HIV diagnosing method using FFChip by impedance spectroscopy is applied. 10uL of HIV lysate and control are pipetted to FFChip and impedance measurements are applied using the analysis setup described in section 3.5.

The impedance of lysed solution is changed compared to the impedance of non-virus control in plasma medium. Mean impedance magnitudes of HIV subtype C lysate compared to control is different for frequencies lower than around 50 kHz as shown in Figure 5.47. Between frequencies 100 Hz and 30 kHz the difference between mean impedance magnitude values of subtype A and control is almost 0.2 MΩ.

The maximum difference in mean impedance magnitude is observed at around 1 kHz. So at that frequency the impedance magnitudes are reported for subtype A

and control in Figure 5.48. Mean impedance magnitude value is plotted with error bars which indicates the standard deviation of impedance magnitude (n=3). Statistical analysis of the results is performed. Statistical significance threshold is set to 0.05, ($p < 0.05$). It has been observed that impedance magnitude of control is significantly higher than HIV subtype C spiked in plasma ($n = 3$, $p < 0.05$). The diagnosis method can detect HIV in plasma.

The impedance magnitudes of HIV subtype C is normalized according to the mean impedance magnitude of control at 1 kHz. The results are plotted in Figure 5.49. It has been observed that HIV subtype C impedance magnitude change is 18% according to control sample.

Repeatability of the measurements are calculated according to the method given in section 5.1.3.2 and given in Figure 5.50. The minimum and maximum values for repeatability are around 70% and 99%, respectively. This indicates that the measurements are at least 70% repeatable.

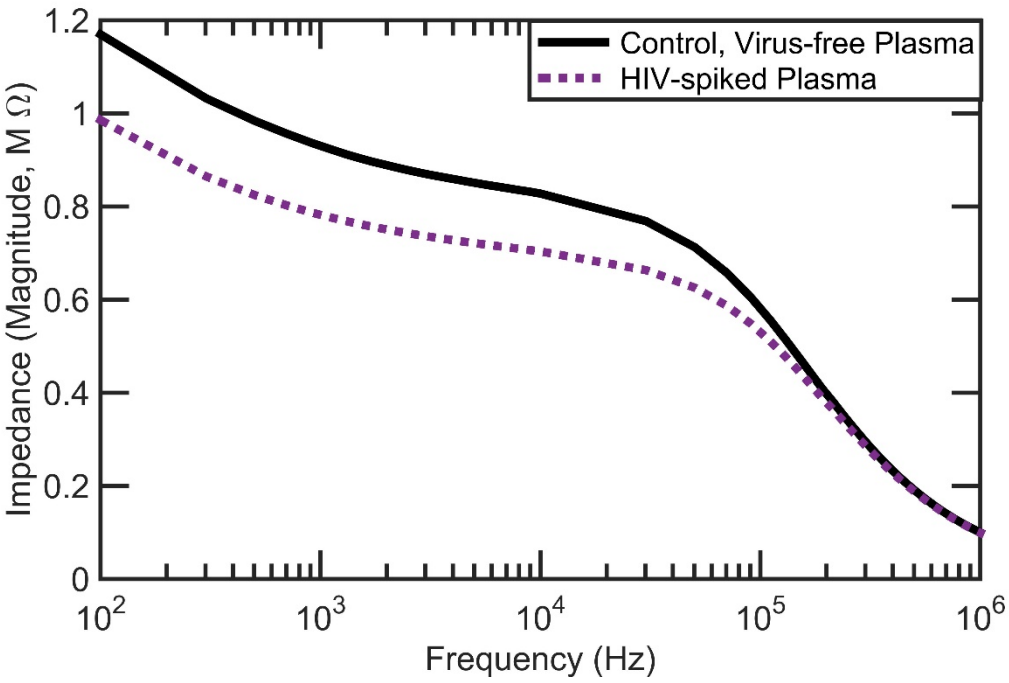

Figure 5.47 Impedance magnitude spectra of control and lysed HIV subtype C spiked in plasma, for a frequency range between 100 Hz and 1 MHz.

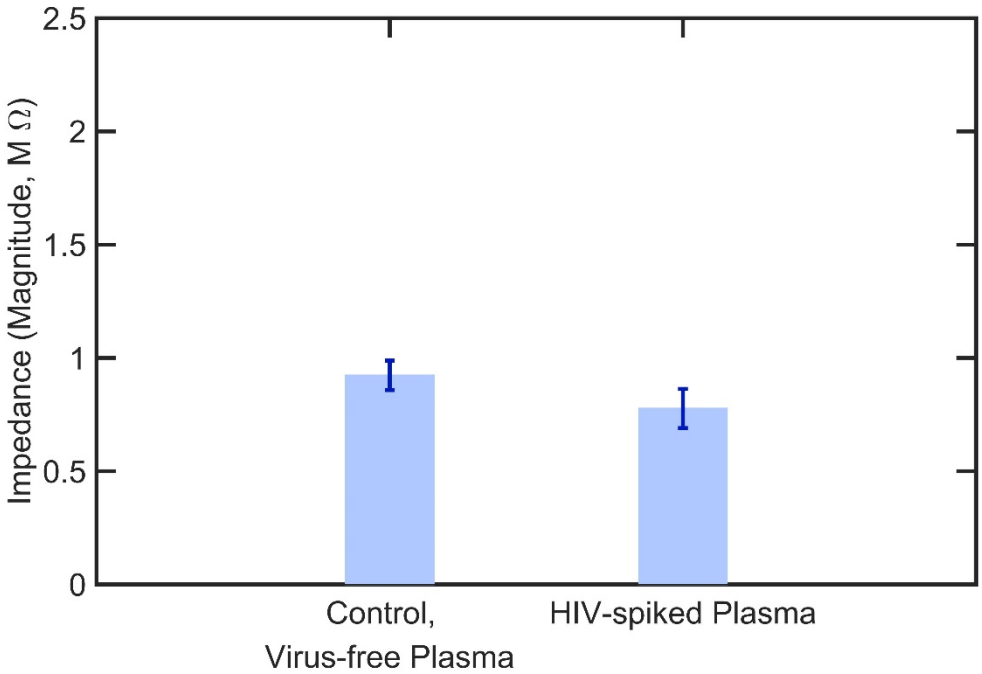

Figure 5.48 Impedance magnitude values of control and lysed HIV subtype C spiked in plasma, at 1 kHz. Error bars are STD of the mean of impedance magnitude (n=3).

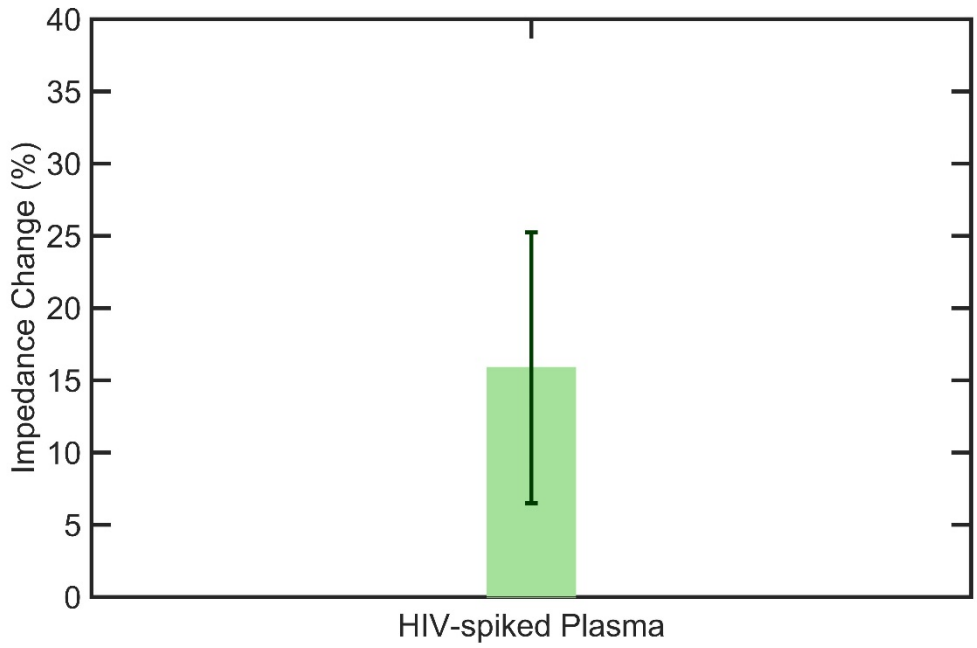

Figure 5.49 Normalized impedance magnitude values of lysed HIV subtype C spiked in plasma to the mean of impedance magnitude of control at 1 kHz. Error bars are STD of the mean of normalized impedance magnitude (n=3).

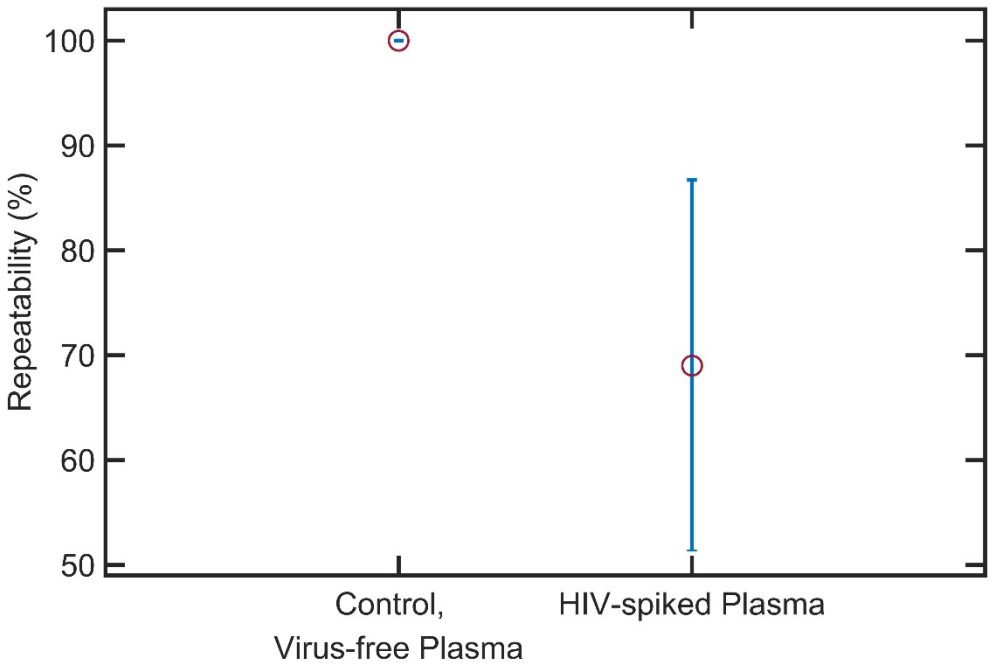

Figure 5.50 Repeatability of normalized impedance magnitude measurements of control and lysed HIV subtype C spiked in plasma at 1 kHz. Error bars are STD of the mean of repeatability (n=3).

5.2.2.9 Impedance measurements for HIV lysate in blood

In this experiment HIV subtype C is spiked in whole blood in order to see the sensibility of the diagnosis method in biological samples. Also this case, virus in whole blood, is the actual case. The sample preparation for HIV lysate and control are done exactly as explained in section 5.1.2.3, except whole blood is used as a medium for viruses. After that HIV diagnosing method using FFChip by impedance spectroscopy is applied. 10uL of HIV lysate and control are pipetted to FFChip and impedance measurements are applied using the analysis setup described in section 3.5.

The impedance of lysed solution is changed compared to the impedance of non-virus control in whole blood medium. Mean impedance magnitudes of HIV subtype C lysate compared to control is different for frequencies lower than around 50 kHz as shown in Figure 5.51. Between frequencies 100 Hz and 30 kHz the difference between mean impedance magnitude values of subtype A and control is almost 0.2 MΩ.

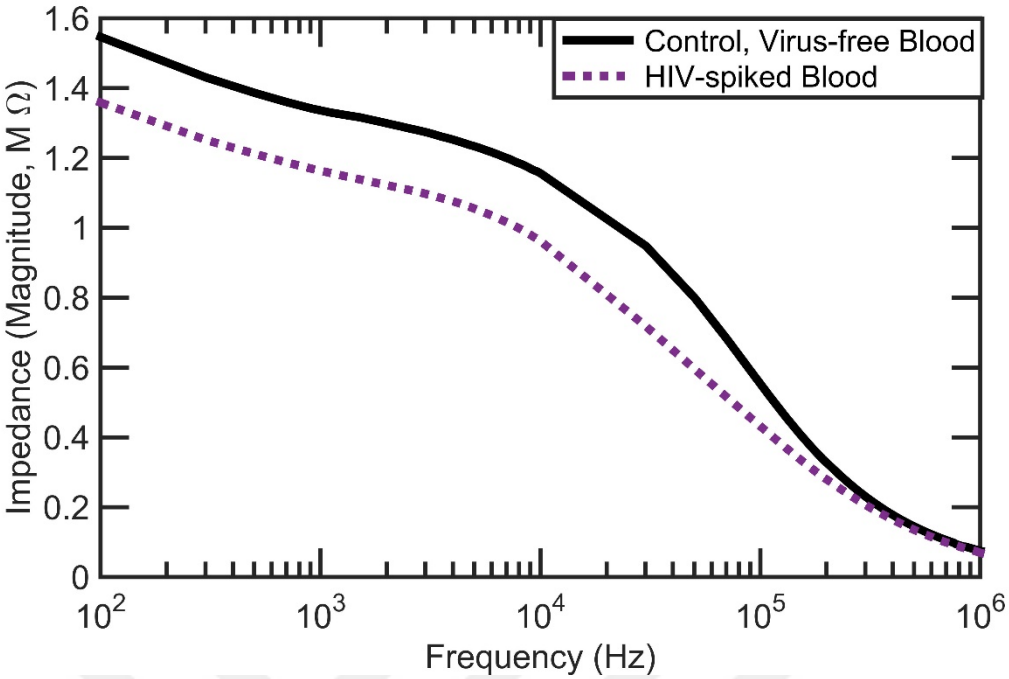

Figure 5.51 Impedance magnitude spectra of control and lysed HIV subtype C spiked in whole blood, for a frequency range between 100 Hz and 1 MHz.

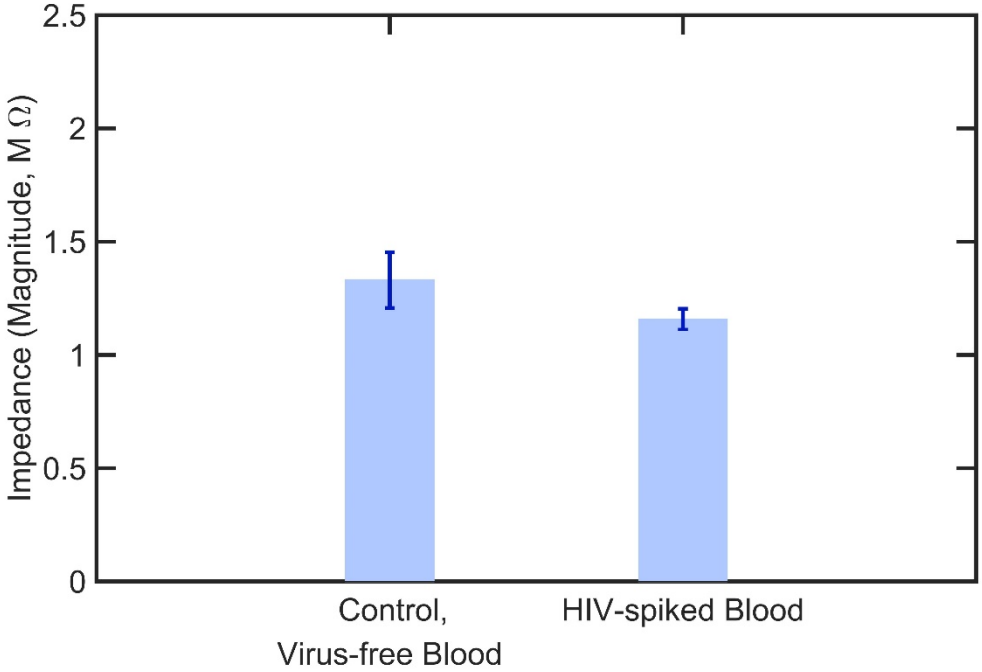

Figure 5.52 Impedance magnitude values of control and lysed HIV subtype C spiked in whole blood, at 1 kHz. Error bars are STD of the mean of impedance magnitude (n=3).

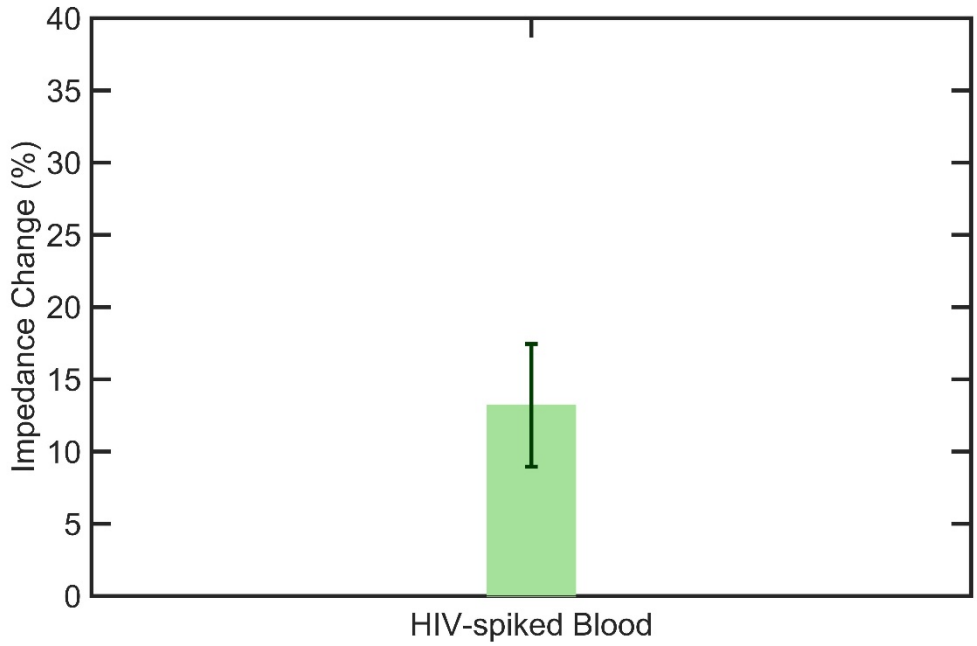

Figure 5.53 Normalized impedance magnitude values of lysed HIV subtype C spiked in whole blood to the mean of impedance magnitude of control at 1 kHz. Error bars are STD of the mean of normalized impedance magnitude (n=3).

The maximum difference in mean impedance magnitude is observed at around 1 kHz. So at that frequency the impedance magnitudes are reported for subtype A and control in Figure 5.52. Mean impedance magnitude value is plotted with error bars which indicates the standard deviation of impedance magnitude (n=3). Statistical analysis of the results is performed. Statistical significance threshold is set to 0.05, ($p < 0.05$). It has been observed that impedance magnitude of control is significantly higher than HIV subtype C spiked in whole blood ($n = 3$, $p < 0.05$). The diagnosis method can detect HIV in whole blood.

The impedance magnitudes of HIV subtype C is normalized according to the mean impedance magnitude of control at 1 kHz. The results are plotted in Figure 5.53. It has been observed that HIV subtype C impedance magnitude change is 18% according to control sample.

Repeatability of the measurements are calculated according to the method given in section 5.1.3.2 and given in Figure 5.54. The minimum and maximum values for

repeatability are around 83% and 99%, respectively. This indicates that the measurements are at least 83% repeatable.

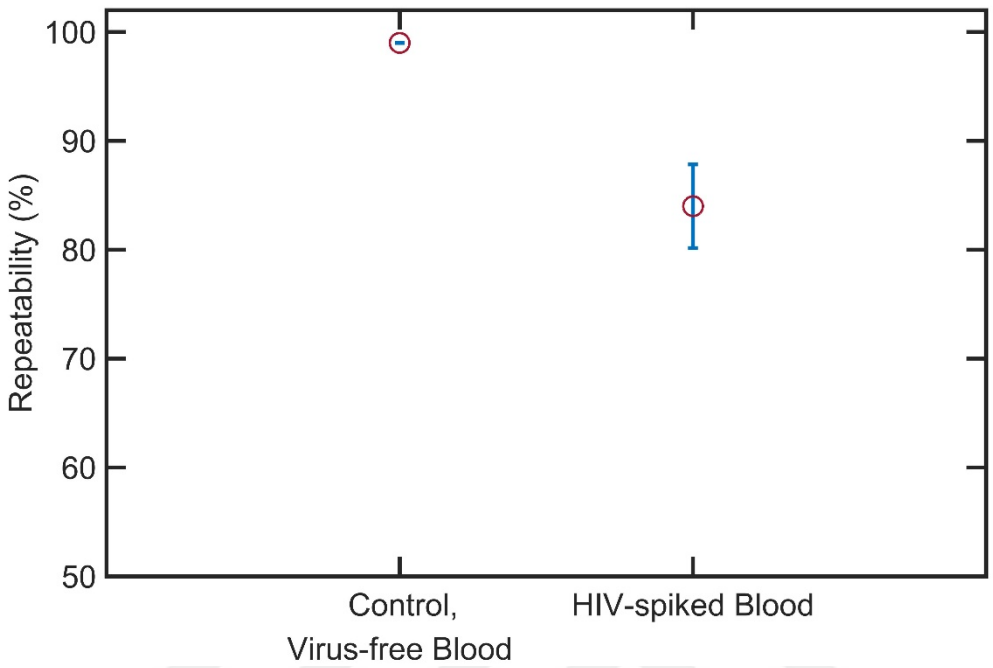

Figure 5.54 Repeatability of normalized impedance magnitude measurements of control and lysed HIV subtype C spiked in whole blood at 1 kHz. Error bars are STD of the mean of repeatability (n=3).

5.3 Conclusion

In this part of the thesis a flexible polymer film based microfluidic biosensor using electrical impedance detection for POC HIV virus load diagnosis is designed and tested.

The need for a POC diagnostic tool is reviewed and main objective is designing a POC diagnostic tool to detect HIV-1 infection in the acute period.

The flexible polymer film based microfluidic chips were produced using simple, inexpensive and accessible materials using non-lithographic fabrication techniques which made the chip inexpensive and not complex. The production step of FFChip explained in detail. The material cost for the chip given in Table 5.3 is lower than US$ 0.2. The final product is flexible, light, thin and inexpensive.

Electrical impedance spectroscopy analysis system and its background was explained, one of the electrical equivalent model of FFChip was defined. In order to evaluate the performance of the biosensor system, empty channel and DI water filled channel measurements were applied and very high impedances were obtained and system was more capacitive without any ions in the solution after that solutions with already known conductance were tested and results showed that system is able to distinguish even kΩ of differences.

Table 5.3 Material cost for FFChip biosensor.

Materials	Amount Per Test	Cost (US$)
Magnetic beads	5 µL	0.80
Antibody	0.25 µL	0.87
Silver ink + Silicon	0.05 grams	0.06
Polyester film	2 cm × 1 cm × 2	0.004
Double sided adhesive	2 cm × 1 cm	0.006
Water, Triton 100-X, Glycerol	Very small amounts	≈ 0.06
	Total	0.180

In order to capture different subtypes of HIV-1 an affinity chromatography based method is developed and applied. As a clinical model viruses were suspended in PBS, plasma and whole blood. Than captured viruses were lysed. Lysate was pipetted to FFChip and impedance measurements were applied. At first clinical model is viruses in PBS. The results showed that impedance of virus lysates were statistically different than control. The performance of the system is tested for lower concentrations of viruses as 10^6 copies/ml, the results showed that impedance of virus lysate was statistically different than control. In order to evaluate the specificity of the test samples a different virus was used. EBV was tested. And specificity was proved statistically.

The capacitance value for empty channel measurements range around 0.5 pF - 0.9 pF is quite small (Figure 5.18), which may be indicated that bulk solution capacitance can be neglected for lower frequencies. The effect can be observed

from Nyquist plots of HIV lysates (Figure 5.30), for the higher frequency all plots for subtypes and control go to an impedance value, which may be indicate that there is a parallel capacitance to all other components similar as shown in full electrode model in Figure 3.11 and Equation (3.12). And for lower frequencies the Nyquist plot is similar to Randles model which can be indicated that this capacitance value quite small as obtained from empty channel measurements.

Finally plasma and whole blood were used as a clinical model. And the results showed that HIV can be detected in those mediums. For all measurements repeatabilities are also tested and the repeatability's are over 70%.

It has been proved that the method is able to capture and detect 10^6-10^8 copies/ml of HIV-1 in PBS, and 10^8 copies/ml of HIV-1 in plasma and whole blood, specifically. Measurements are at least 70% repeatable.

6 MICROFLUIDIC BIOSENSOR USING LENSLESS WIDE FIELD MICROSCOPY IMAGING FOR POC CD4+T CELL COUNTING

Practical, low cost and reliable HIV diagnosis and AIDS treatment monitoring are a challenge for resource limited settling. In already developed countries antiretroviral therapy (ART) is accessible and affordable. However only less than half of the people with HIV infection are able to access ART and for developing countries due to the lack of infrastructure this ratio is even lower. [94] The most efficient way of monitoring ART is retrieving CD4+T cell count. So there is an urgent need for a POC CD4+T cell counting system.

POC CD4+T cell counting systems are proposed over last 10 years. [66, 164-166] In this thesis similar approaches are used. Main differences in this thesis are proposing a novel cell counting algorithm for images obtained from lensless wide-field microscopy and slight different approaches on the fabrication of microfluidic chip.

Microfluidic biosensor using lensless wide-field microscopy imaging for POC CD4+T cell counting has 4 main designs, microfluidic chip, surface functionalization, lensless wide-field microscope and cell counting algorithm. In order to test the performance of biosensor statistical binary classification is applied using fluorescence microscope images for captured cells.

6.1 Materials and Methods

In this section the designed and used materials and methods are explained.

6.1.1 Microfluidic chip development

Microfluidics chips are developed to capture CD4+T cells specifically. Those captured cells can be enumerated. Counting of cells can be applied by using either fluorescence microscope or lensless wide field microcopy. Microfluidic chips are produced by using non-lithographic techniques. Microfluidic chips are fabricated by assembling three layers. Glass surface is the bottom layer. Medium layer is the layer formed with a double sided adhesive and patterned to form the channel. Top layer is a PMMA layer with patterned inlet and outlet. The simple depiction is in Figure 6.1.

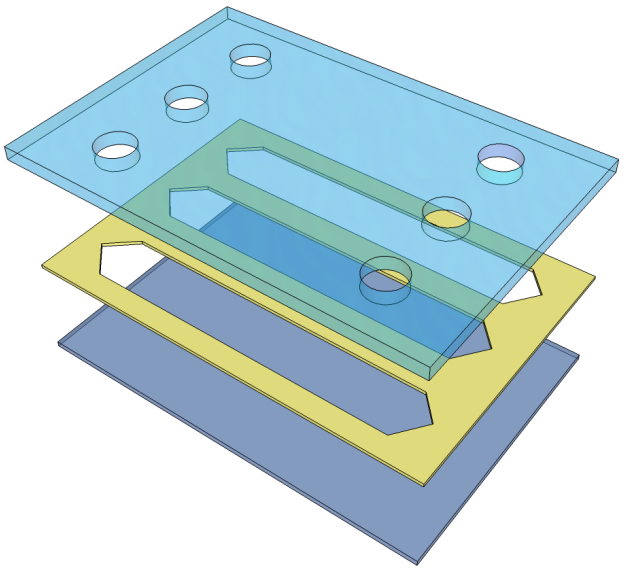

Figure 6.1 The three layers of microfluidic chip. From to bottom to top: the glass layer, channel layer and inlet layer.

6.1.1.1 Bottom glass layer

The bottom layer is simply microscope cover slip glass slide. Cover slip glass slides (Gold Seal Cover glass 24 mm × 40 mm) were purchased from Fisher Scientific (Fair Lawn, NJ, USA).

6.1.1.2 Channel layer

The channel layer is used to form a chamber wall for solution to be filled. The channel layer is patterned on DSA (8113), which was purchased from 3M (St. Paul, MN, USA).

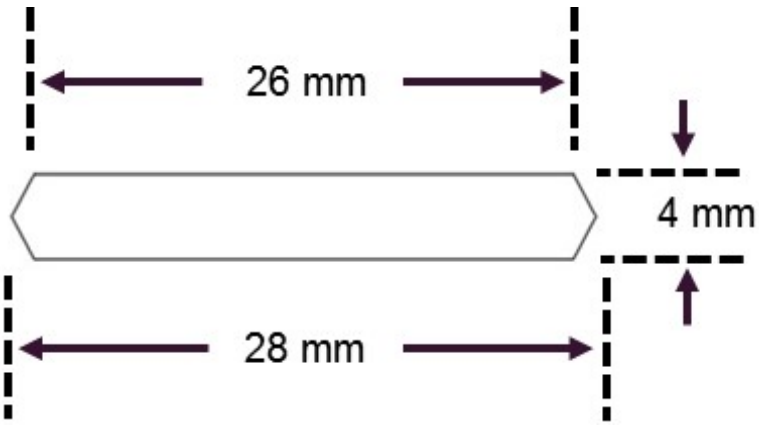

Figure 6.2 The CAD design of a channel.

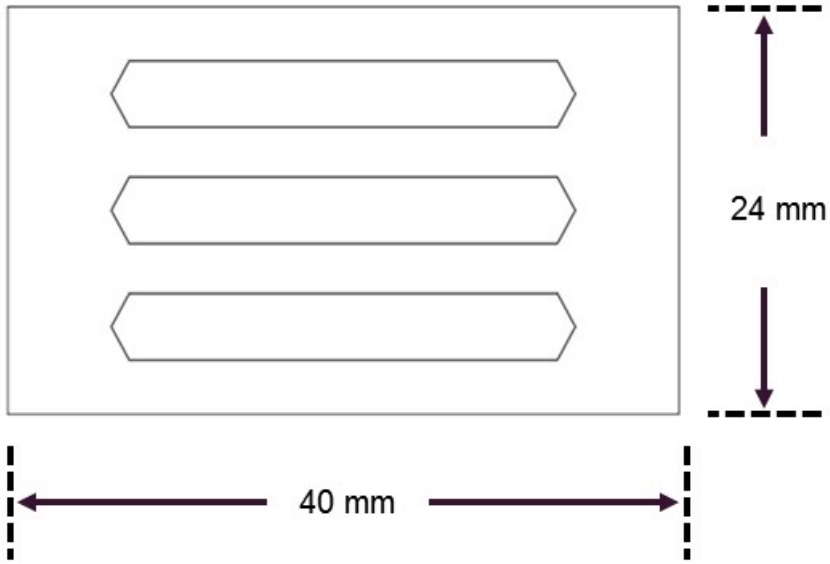

Figure 6.3 The CAD design of channel layer (3 channels together).

The adhesive thickness is 80µm which defines the height of the channel. The pattern is CAD designed and patterning is performed by laser cutter. The CAD design of a channel is shown in Figure 6.2 and channel layer in which 3 channels are together is shown in Figure 6.3.

6.1.1.3 Inlet and outlet layer

Inlet and outlet layer is the top layer where the inlet and outlet is patterned using laser cutter. This layer is patterned on Poly(methyl methacrylate) (PMMA). PMMA is known as acrylic glass and it has a thickness of 3.175 mm, it is easy to process using laser cutter. It is transparent. PMMA (Polymethymetacrylate, 8560K239)) is purchased from McMaster Carr Supply Co. Inc. (Los Angeles, CA, USA). The CAD design is shown in Figure 6.4.

The hole diameter is 0.65mm in the CAD design but since laser cutter cuts the PMMA by burning the actual diameter becomes bigger like 0.9mm.

After fabricating channel layer and inlet and outlet layer, there layers are assembled together. First protective film of one side of DSA is removed and DSA is laminated on the inlet and outlet layer (PMMA), than the other protective film is removed from DSA and cover slip glass slide is laminated on that side.

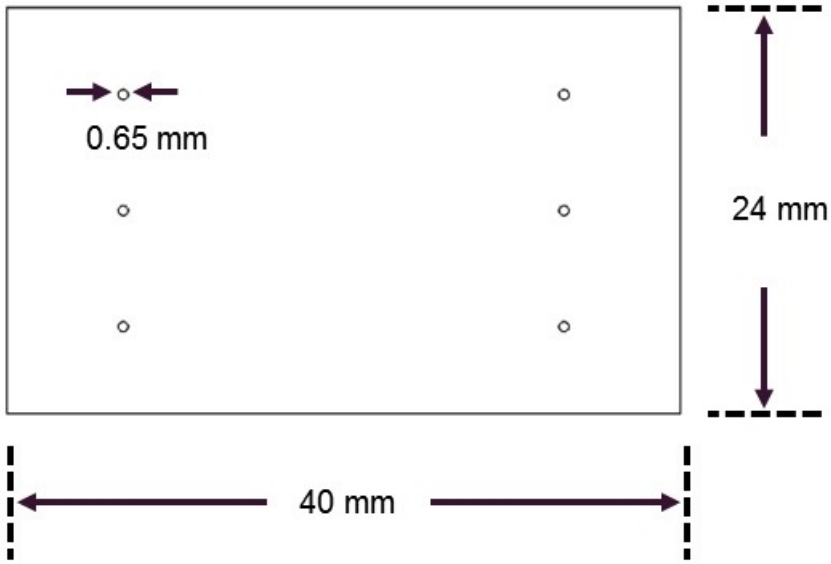

Figure 6.4 The CAD design of inlet and outlet layer.

One of the channel's 3D schematics and its physical dimensions are given in Figure 6.5 and the actual fabricated microfluidic chip with food dyes and whole blood in channels is in shown in Figure 6.6.

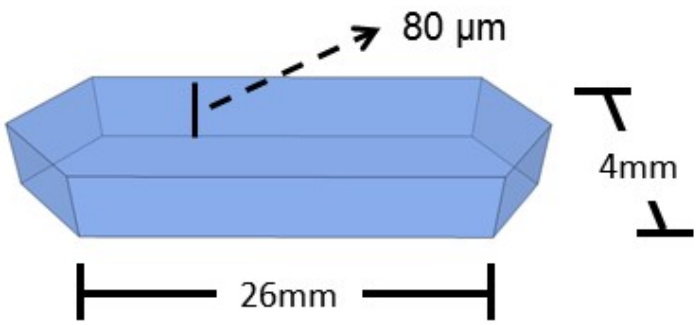

Figure 6.5 3D schematic of channel with physical dimensions.

The volume is calculated where the channel floor is assumed as an exact rectangular with dimensions of 4 mm × 26 mm. So the total volume is calculated as 4 mm × 26 mm × 80 µm and is equal to 8.32 mm^3 which is equal to 8.32 µL. The rectangular cross section volume can take 8.32 µL of solution.

Holes in the chip are adequate for pipetting solution manually. While pipetting solutions from one hole (inlet) remaining solution inside channel can ejected from opposite hole (outlet). In order to clean the channels, they are washed 3 times with

required amount of adequate solution. Washing the channels is characterized and will be explained in the experiment section.

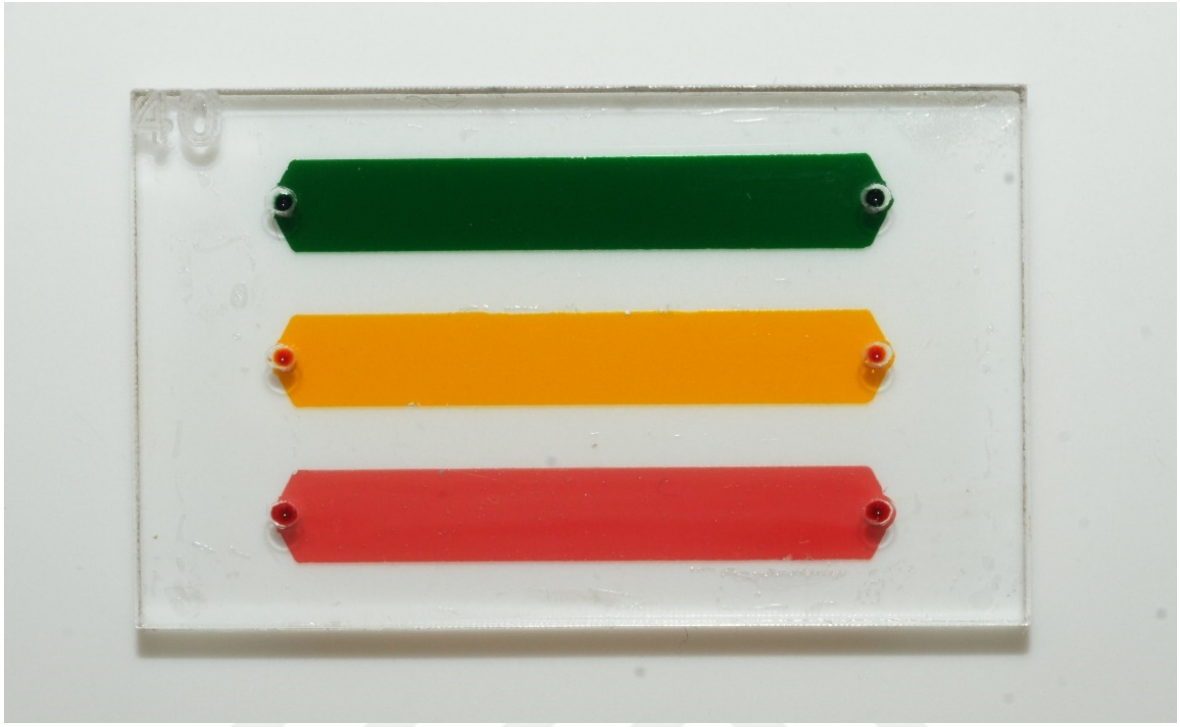

Figure 6.6 Actual image of microfluidic chip. First and second channels are filled with green and yellow food dye respectively and third channel is filled with whole blood.

6.1.2 Microfluidic channel surface functionalization for cell capture

In order to count cells, they should be specifically captured on the surface of the bottom layer of the microfluidic chip. Affinity chromatography based method is used to capture CD4+T cells specifically from whole blood. The surface functionalization and cell capturing have been described in this section, models representations used to explain the methods are described in Figure 6.7 and will be used further. Also control samples should be prepared in order to understand the capture specificity.

(3-Mercaptopropyl) trimethoxysilane (3-MPS, 175617), lyophilized bovine serum albumin (BSA, A2153), and dimethyl sulfoxide (DMSO), are obtained from Sigma-Aldrich Corp. (Saint Louis, MI, USA). Phosphate buffered saline (PBS) is purchased from Gibco (Grand Island, NY, USA). NeutrAvidin protein and N-g-Maleimidobutyryloxy succinimide ester (GMBS) are obtained from Pierce

Biotechnology (Rockford, IL, USA). Biotinylated anti-CD4 antibody (Clone 13B8.2, COIM0704) was purchased from Fisher Scientific (Fair Lawn, NJ, USA). A 4'-6-diamidino-2-phenylindole (DAPI) is obtained from Invitrogen (Carlsbad, CA, USA). Alexa Flour 488 (AF488) conjugated Anti-CD4 antibody (Clone RPA-T4, 557695) and BD FACS Lysing Solution (349202) were purchased from BD Bioscience (Becton, Dickinson and Company, San Jose, CA, USA). 1X RBC Lysis Buffer (00-4333-57) was purchased from eBioscience (San Diego, CA, USA).

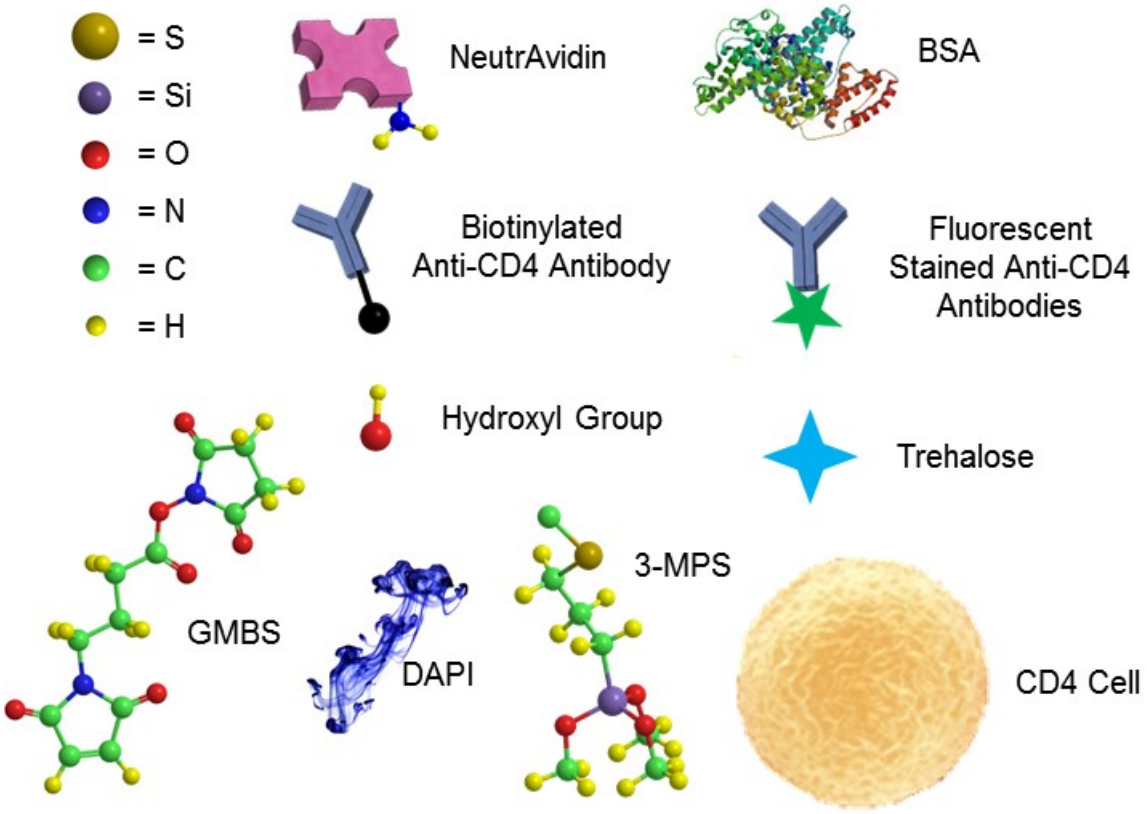

Figure 6.7 The model representation of materials from top left to bottom right, Sulfur (S), Silicon (Si), Oxygen (O), Nitrogen (N), Carbon (C), Hydrogen (H), N-g-Maleimidobutyryloxy succinimide ester (GMBS), Neutravidin, Biotinylated Anti-CD4 Antibody, Hydroxyl group, 4'-6-diamidino-2-phenylindole (DAPI), (3-Mercaptopropyl) trimethoxysilane (3-MPS), lyophilized bovine serum albumin (BSA), Trehalose and CD4+T cell.

6.1.2.1 Bottom layer glass surface functionalization

CD4+T cells should be specifically captured and immobilized to the surface of glass slide and counted using microscope. Neutravidin and biotinylated anti-CD4 antibody and their avidin + biotin binding is used for conjugation of antibody to functionalized surface. This anti-CD4 antibody can specifically capture CD4 cells in whole blood. Surface functionalization protocol has 8 main steps.

First, glass slide is cleaned by dipping in to ethanol solution (70% (v/v) ethanol in DI pure water) in a baker and placing in ultrasonic bath for 15 min at around 30W. Cleaned class slide is dried by nitrogen gas using an air gun.

Second, glass slide is treated by plasma. Oxygen plasma is applied at 100 W using 1% oxygen for 2 minutes. Plasma device is PX-250 chamber (March instruments, Concord, MA, USA). After oxygen plasma hydroxyl (OH) groups are formed on the top surface of glass slide. Plasma treatment and hydroxyl (OH) groups are shown in Figure 6.8, a) and b).

Third, glass slide is placed in a petri dish and incubated for 30 min in silanization solution (4% (v/v) 3-MPS in ethanol) while covered by para film at room temperature. 3-MPS is covalently bind to the hydroxyl groups on the surface of glass slide. This process is shown in Figure 6.8, c).

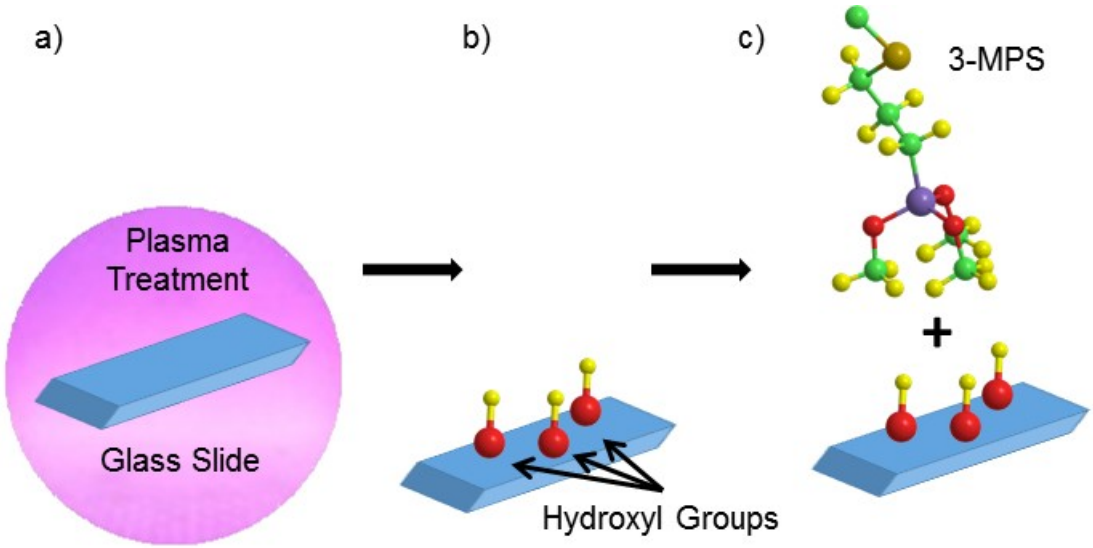

Figure 6.8 Surface functionalization after cleaning of glass slide. a) Plasma treatment, b) hydroxyl (OH) groups are formed, and c) covalent binding of 3-MPS.

Forth, glass slide is leaned on 45º to a petri dish wall and washed using pipet by dropping ethanol on top of it. After washing glass slides left for drying for 3-4 minutes at room temperature. At that point glass slide is assembled to DSA + PMMA as explained in section 6.1.1.3 and as shown in Figure 6.1. Microfluidic chip and channels are formed. Channels are washed 3 times with PBS in order to remove remaining ethanol.

Fifth, GMBS solution is pipetted to the channel. GMBS solution is 4% (w/v) GMBS in DMSO solution and DMSO solution is 10% DMSO in PBS. GMBS solution is incubated for 30 minutes at room temperature. After incubation channels are washed 3 times with PBS in order to remove GMBS solution. This process is shown in Figure 6.9, a).

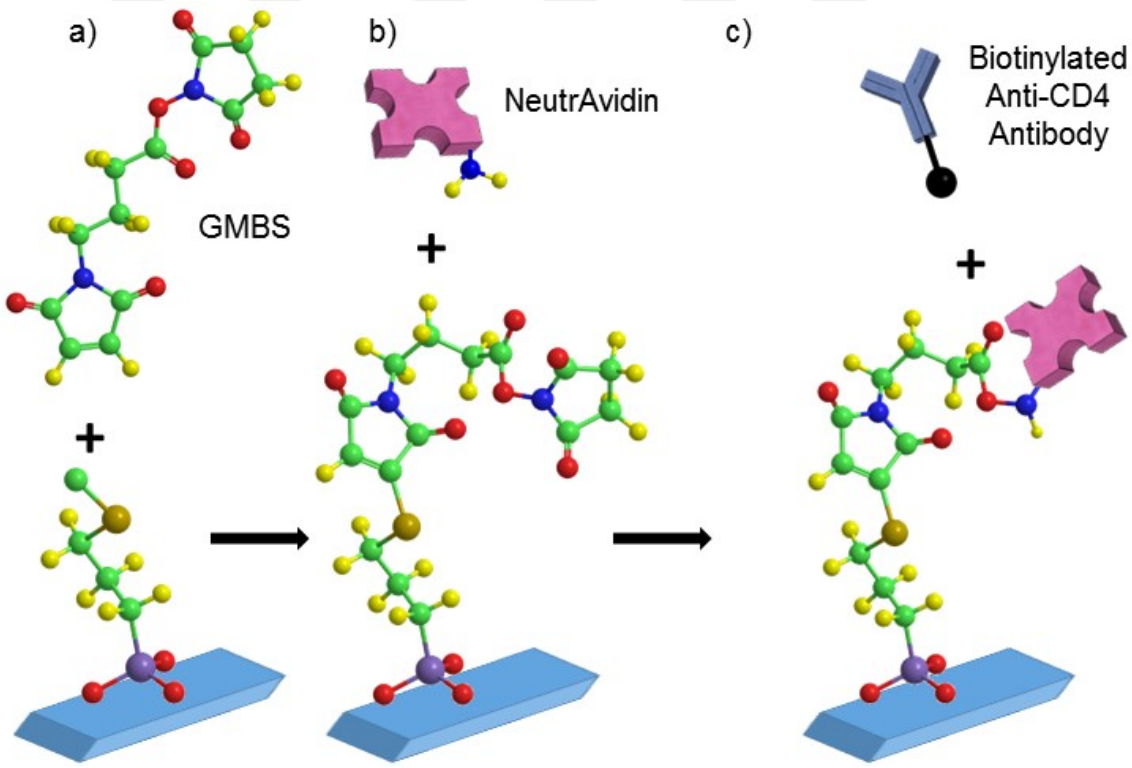

Figure 6.9 Surface functionalization after covalent binding of 3-MPS. a) GMBS binding, b) Neutravidin binding, and c) biotinylated anti-CD4 antibody conjugation to Neutravidin.

Sixth, Neutravidin solution is pipetted and incubated for 2 hours at 4 °C. Neutravidin solution is 0.1 mg/mL in PBS. After incubation channels are washed 3 times with

PBS in order to remove remaining Neutravidin solution. Process is shown in Figure 6.9, b).

Seventh, biotinylated anti-CD4 antibody solution is incubated for 30 minutes at room temperature. Biotinylated anti-CD4 antibody solution is 20 µg/mL in PBS. After incubation channels are washed 3 times with PBS in order to remove remaining biotinylated anti-CD4 antibody solution. This process is shown in Figure 6.9, c). This step is not applied for control samples.

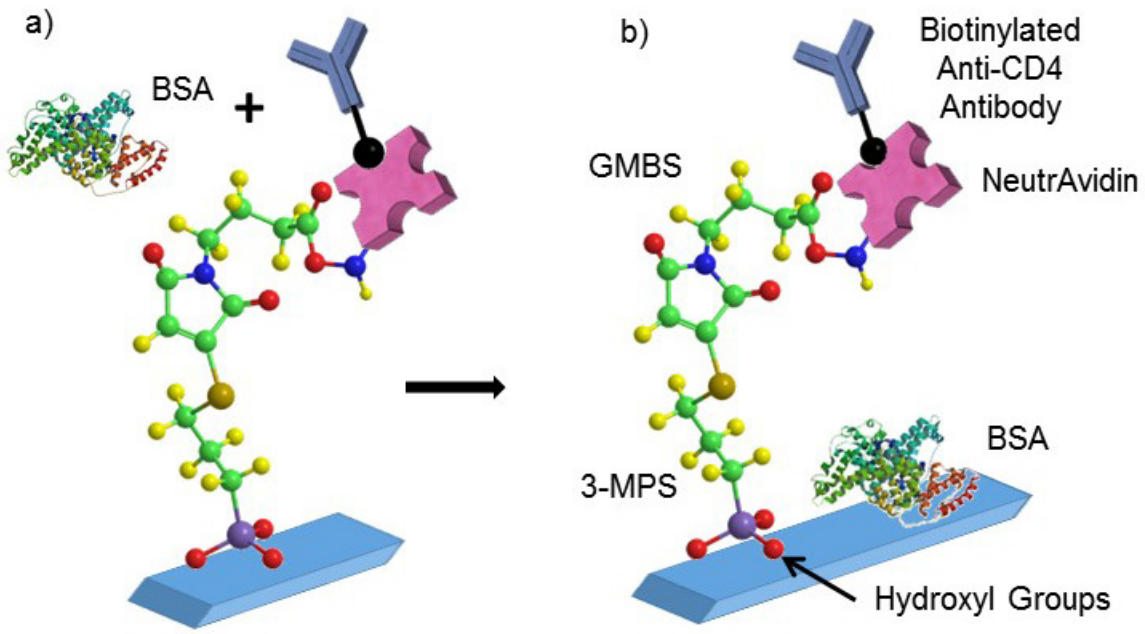

Figure 6.10 Surface functionalization after conjugation of biotinylated anti-CD4 antibody. a) BSA blocking, b) final groups of functionalization on glass slide.

Eighth, BSA solution is incubated for 30 minutes at room temperature. BSA solution is 1% (w/v) BSA in PBS. This step is used to block unspecific binding. After incubation channels are washed 3 times with PBS in order to remove biotinylated anti-CD4 antibody solution. Process is shown in Figure 6.10, a).

The microfluidic chip is ready to capture and immobilize CD4+T cells. Final groups on glass slide are depicted in Figure 6.10, b).

Control samples are samples without anti-CD4 antibody, all of the other functionalization described above are applied except step seven.

6.1.2.2 CD4+T cell capturing

There is antigen-antibody interaction between anti-CD4 antibody and CD4 proteins on CD4+T cells. So when whole blood suspended on the surface of glass slide CD4 proteins on cells are attracted to the immobilized anti-CD4 antibody on the surface and then CD4+T cells become captured.

In order to immobilize CD4+T cells on glass surface, whole blood is pipetted to channels and incubated at room temperature for 25 minutes. In this 25 minutes samples are shaken 2 times gently. The cells fall down to the bottom of channel and antibody and antigen reaction immediately occurs. The CD4+T cell capturing is depicted in Figure 6.12.

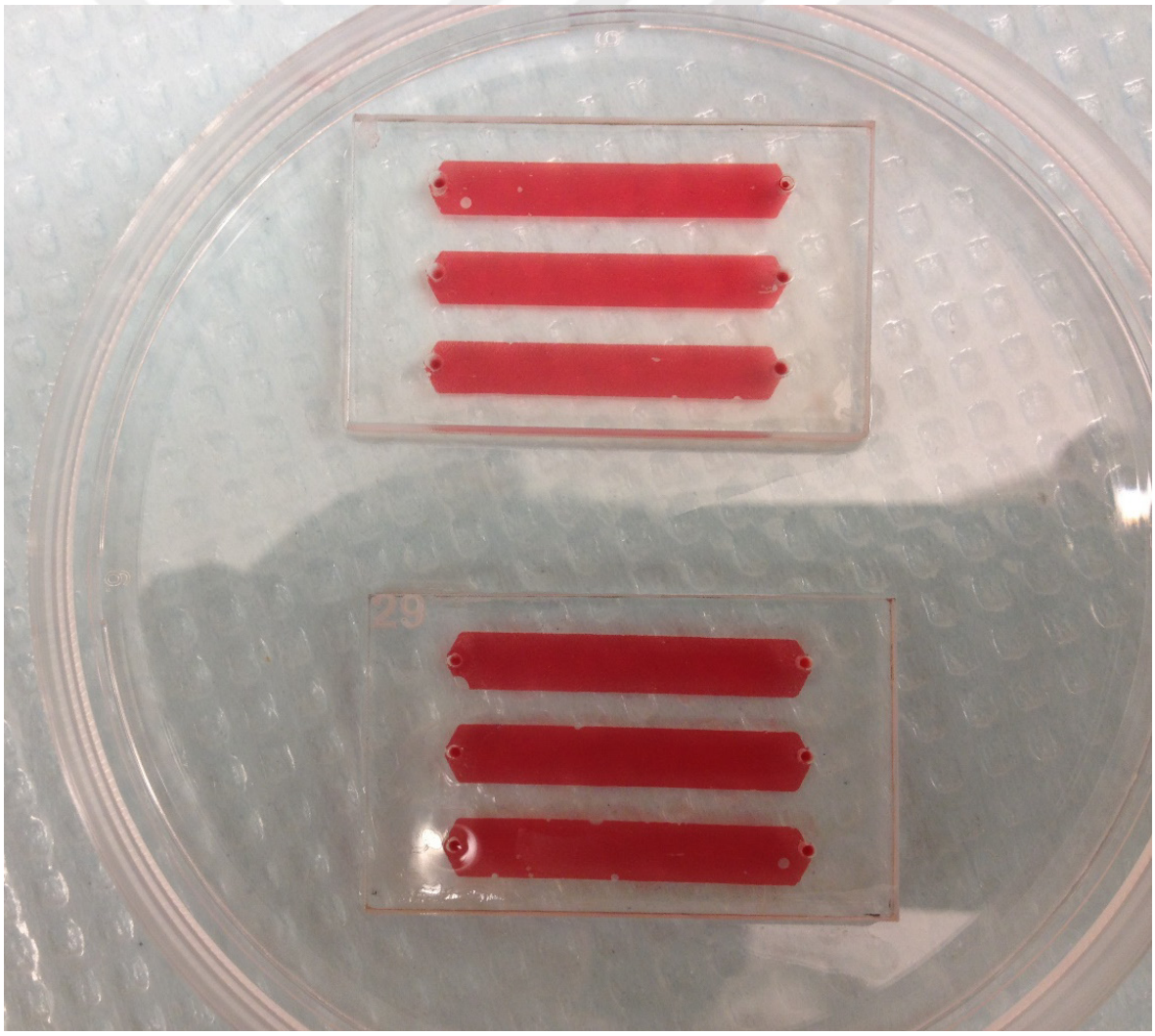

Figure 6.11 Whole blood incubation in channels of microfluidic chips.

In this step the control samples are also prepared. Whole blood is pipetted to channels of control sample and incubated at room temperature for 25 minutes. In this 25 minutes samples are shaken 2 times gently. Whole blood incubation in channels of microfluidic chips is shown in Figure 6.11.

After incubations samples are washed 3 times by pipetting PBS into the channel to remove whole blood.

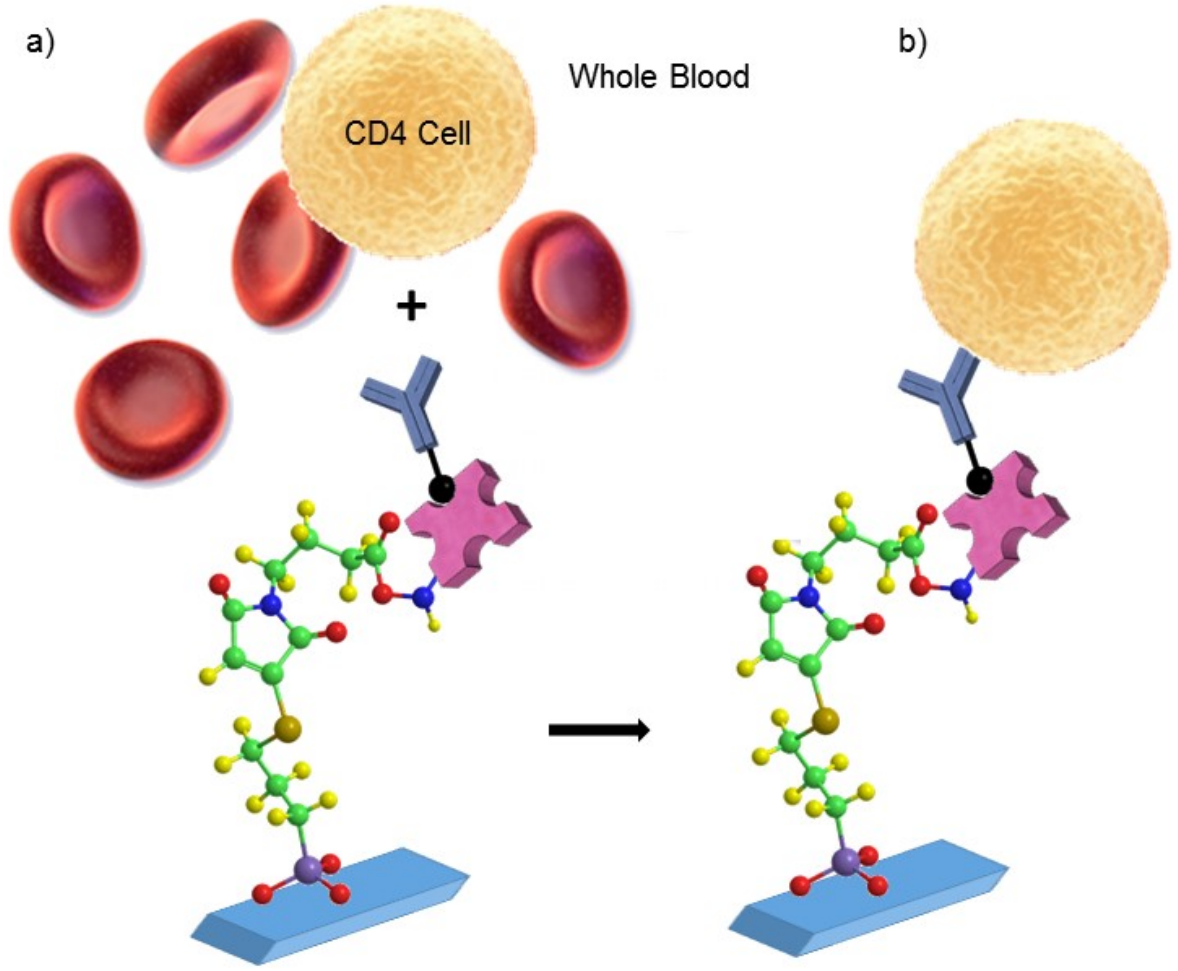

Figure 6.12 CD4+T cell capturing. a) Whole blood is pipetted into channel. b) CD4 antigen on the surface of the cell is bind to the anti-CD4 antibody conjugated to the surface of glass slide.

6.1.3 Obtaining initial amount of CD4+T cells

To compare the capture efficiency the initial number of CD4+T cells in solution is needed. In order to get this number white blood cells (WBC) are removed from the

same whole blood sample pipette to the channel. And then CD4+T cells in those WBC's are stained and counted in hemocytometer under microscope.

The protocol is as follows, first, whole blood is suspended in 10% red blood cell (RBC) lysis solution and incubated for 3 minutes. In the meantime RBC's are lysed and only WBC's are in the cell suspension. Cell suspension is centrifuged at 150 Gauss (G) for 5 minutes in order to separate WBC's and debris of RBC. Than the supernatant is removed and cell pellet at the bottom of tube is resuspended in PBS. The PBS amount is chosen to get the initial blood volume.

Second, the isolated WBCs are fixed with 4% PFA. PFA incubation takes 10 minutes. Than cell suspension is centrifuged at 150 Gauss (G) for 5 minutes, supernatant is removed and cells are resuspended in PBS in order to stop fixing. This process is done 2 times and final suspension was around 100 µL, it has to be this amount because staining markers are in very less amounts.

Third, staining of CD4+T cells. In order to stain the cells DAPI and Alexa Fluor 488 conjugated anti-CD4 antibody solutions are used. DAPI stock concentration is 5mg/mL DAPI in DI water. And DAPI solution is 0.2% (v/v) DAPI stock solution in DI water. AF-488 conjugated anti-CD4 antibody stock concentration is 100 µg/mL AF-488 conjugated anti-CD4 antibody in PBS. And AF-488 conjugated anti-CD4 antibody solution is 1% (v/v) AF-488 conjugated anti-CD4 antibody stock solution in PBS. Those staining solutions are added to cell suspension and incubated 90 min at 4 °C. Then cell suspension is centrifuged at 150 Gauss (G) for 5 minutes, supernatant is removed and cells are resuspended in PBS in order to stop staining. The PBS amount is chosen to get the initial blood volume.

Finally, stained CD4+T cells are counted using hemocytometer under microscope. In the microscope UV and GFP fluorescent images and bright field images are obtained for 100x magnification. Green cells are CD4+T cells and blue cells are white blood cells. Green dived blue gives the ratio of CD4+T cells in all WBC's. The hemocytometer count gives the total number of WBC's. Mosaic image is an image with 48 100x magnified images get together for bright field and UV. They are shown in Figure 6.13 and Figure 6.14 respectively. Cells are counted using those images. Neubauer hemocytometer is used for counting.

Initial amount of CD4+T cells and white blood cells are obtained in 1 mL. The effective volume of channel is almost 4 mm x 26 mm x 80 μm = 8.32 μL. So the initial amount of cells pipetted into a channel can be calculated.

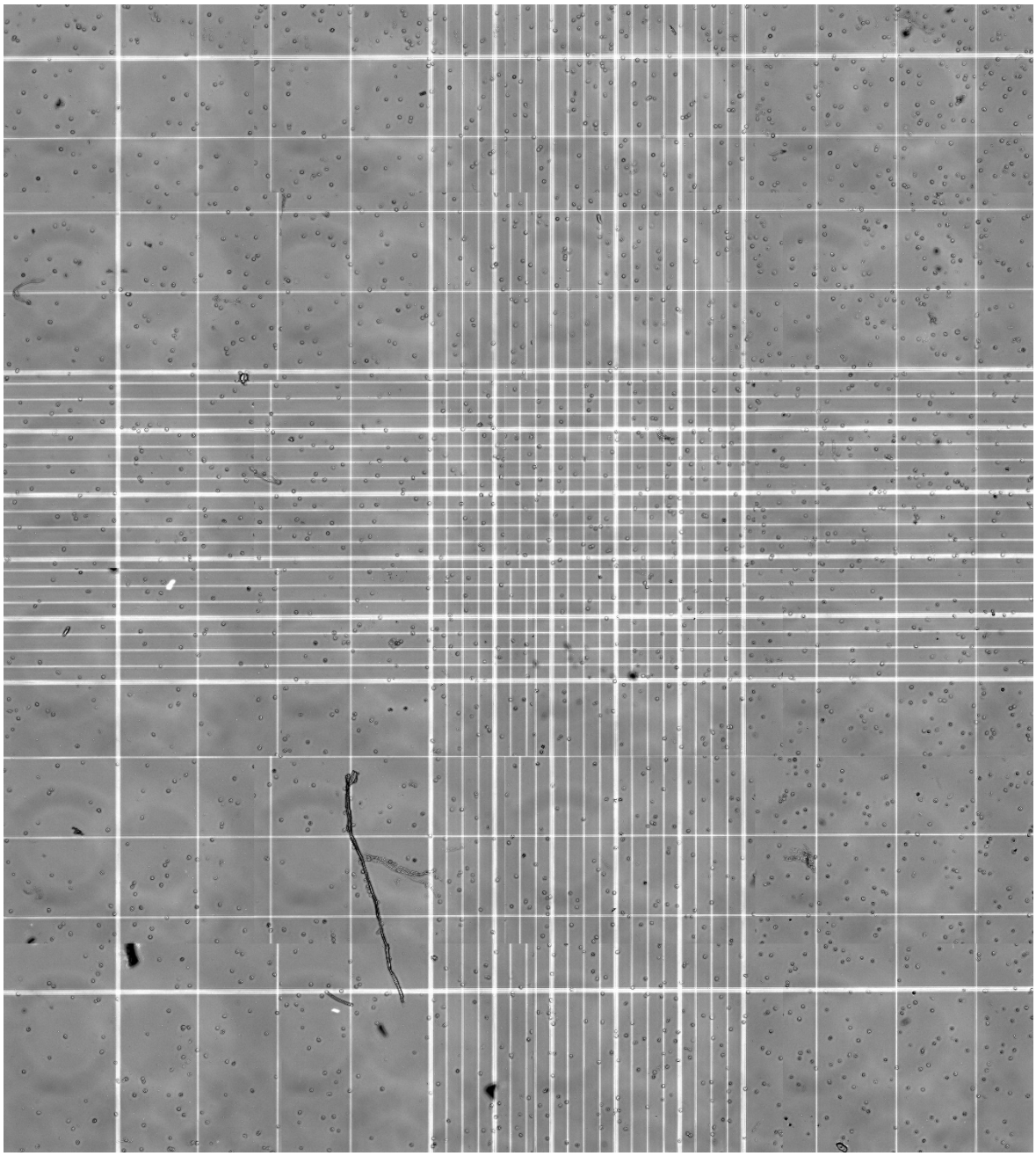

Figure 6.13 Cells in hemocytometer used for obtaining initial white blood cell and CD4+T cell count. Neubauer hemocytometer is used. There are 48 bright field images with 100x magnification.

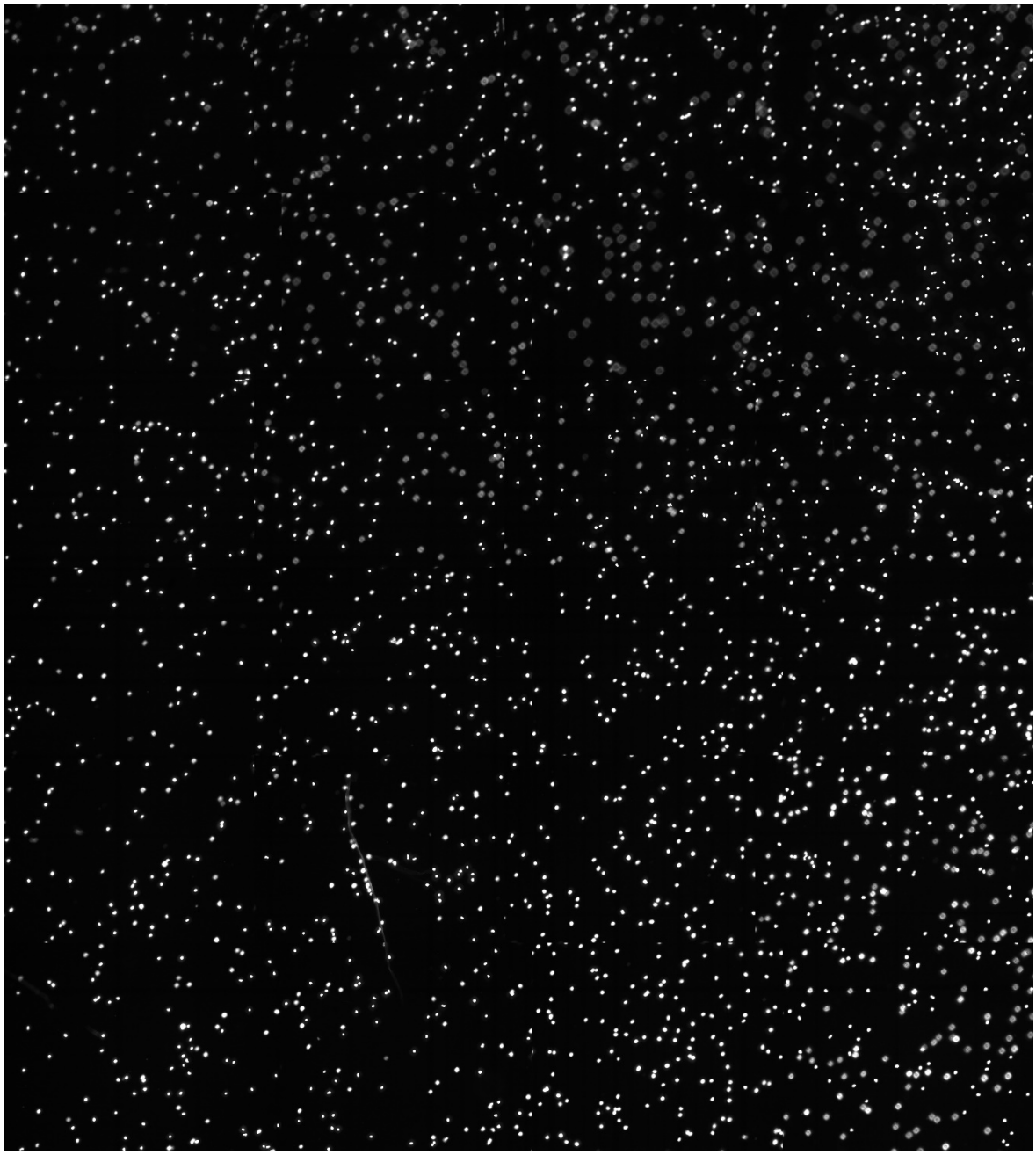

Figure 6.14 DAPI stained cells in hemocytometer used for obtaining initial white blood cell and CD4+T cells concentration. Neubauer hemocytometer is used. There are 48 UV fluorescent images with 100x magnification.

6.1.4 Counting cells inside channels under microscope

In order to obtain capture efficiency and capture specificity cells inside the channel should be counted after capturing. Differential counting under microscope is only possible after staining of cells. It has to be proven that the object seemed under microscope is a cell and it is also a CD4+T cell. Due to these reasons cells should

be stained, DAPI is used to stain the nucleus so cells with nucleus can be counted which are white blood cells in general and Alexa Fluor 488 conjugated anti-CD4 antibody is used to see if the captured cell is a CD4+T cell.

6.1.4.1 Staining of CD4+T cells

First step of staining is fixing the cells so the organic structure of captured cells become concrete. Counting under microscope can take many hours so cells should be intact. Cells were fixed with paraformaldehyde (PFA) solution. PFA solution is 4% (v/v) paraformaldehyde (PFA) solution in PBS. PFA solution is pipetted to the channels and incubated for 10 minutes. Then channels are washed 3 times by PBS in order to remove PFA.

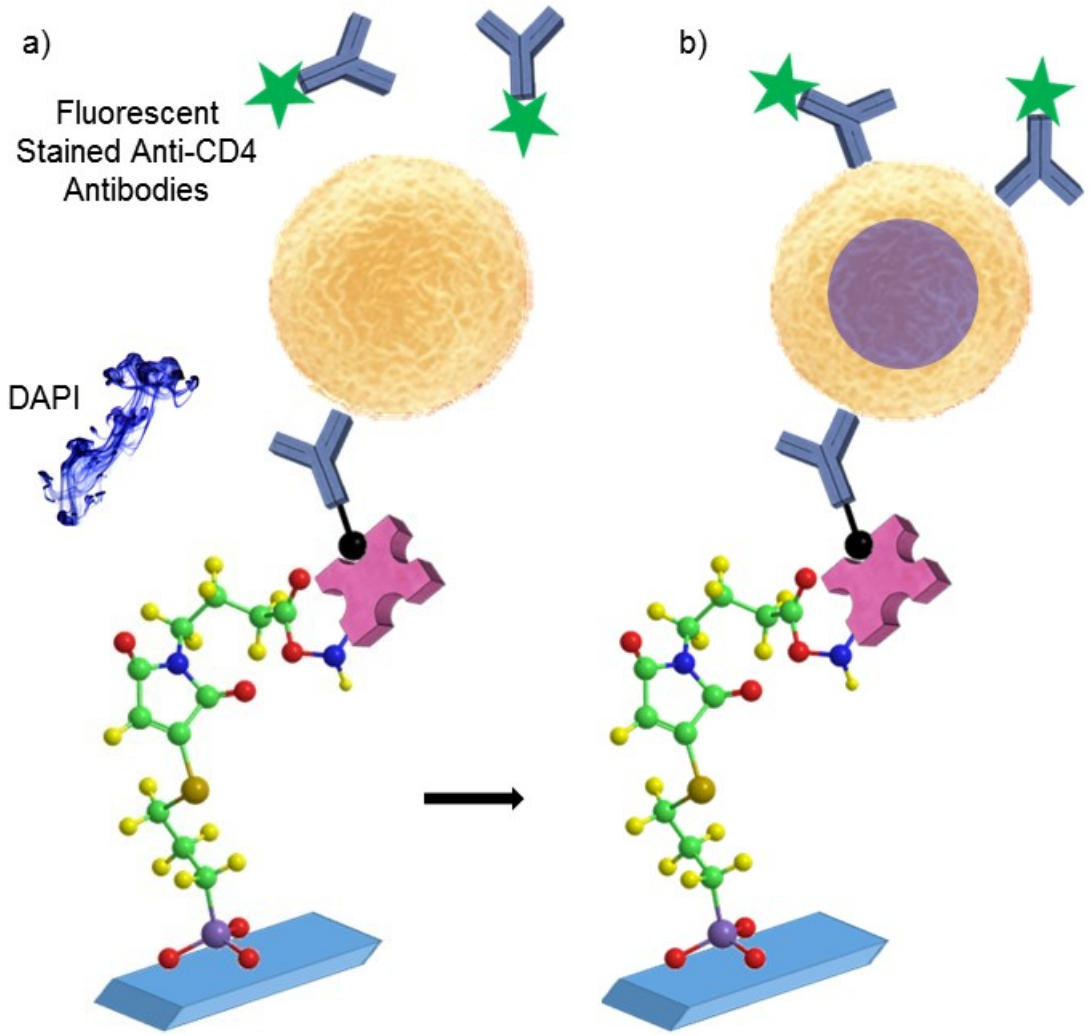

Figure 6.15 Staining of captured and fixed cells on glass slide. a) DAPI and AF-488 conjugated anti-CD4 antibody stains are pipetted to the channels b) after staining.

After fixing cells should be stained. DAPI and AF-488 conjugated anti-CD4 antibody solutions are pipetted to the channel together and incubated for 90 minutes. DAPI solution is 0.2% (v/v) DAPI stock solution in DI water. AF-488 conjugated anti-CD4 antibody solution is 1% (v/v) AF-488 conjugated anti-CD4 antibody stock solution in PBS. Stock solutions are explained in section 6.1.3. Then channels are washed 3 times by PBS in order to remove stains. After staining microfluidics chips are ready for counting under microscope.

DAPI is stained the nucleus of cell and AF-488 conjugated anti-CD4 antibody is bind to the cell wall. Staining procedure is depicted in Figure 6.15 a) and stained cell is depicted in Figure 6.15 b) where DAPI stained the nucleus of cell and AF-488 conjugated anti-CD4 antibody is bind to the cell wall.

Same staining procedure is applied to the control samples, in order to see if there are any captured cells.

6.1.4.2 Manual counting of cells

Cells are counted under fluorescence microscope in bright field and fluorescence mode. Carl Zeiss Fluorescence microscope is used (Jena, Germany). Since cells are stained with DAPI and AF-488, UV and GFP filters are used respectively. UV filter is with 359 nm excitation, 491 nm emission which is blue. GFP filter is with 488 nm excitation, 525 nm emission which is green. DAPI stains nucleus so blue indicates that it is a WBC. AF-488 attaches on CD4+T cells walls so green indicates that it is a CD4+T cell. Cells are counted for whole channel for two fluorescence light, number of blue cells and number blue and green cells are manually counted.

6.1.4.3 Performance Evaluation of CD4+T Cells Counting

Performance evaluation of CD4+T cells count using proposed method depends on capturing right cells and number of those cells. Statistical performance measurement definitions are used which is binary classification test.

In Table 6.1 a binary classification test for CD4+T cell counting is shown. The parameter in this table are, Green: Total number of green and blue stained cells in a channel from fluorescent images of captured cells. Blue: Total number of blue stained cells in a channel from fluorescent images of captured cells. CD4: Actual

number of CD4+T cells in a channel. WBC: Actual number of white blood cells in a channel. Green and Blue is obtained from manual counting of green and blue colors from fluorescent images explained in section 6.1.4.2. WBC and CD4 are actual values and they are obtained from the method explained in section 6.1.3. A: The number of actual CD4+T cells counted in the channel. B: Counted as a CD4+T cells but actually they are not. A+B: Total number of cells captured as CD4+T cells, and counted as blue. C: Actual CD4+T cells that are not captured. D: Actual white blood cell except CD4+T cells that are not captured.

Know parameters obtained from manual counting of channel and hemocytometer and they are placed on the table. Unknowns are simply calculated from those known values. After that statistical performance indicators are obtained. Those indicators are capture accuracy, specificity, sensitivity and precision.

Table 6.1 Binary classification test for CD4+T cell counting performance.

	Actual CD4 count	**Actual other cells count**	**Total**
Test CD4 count	A Green	B Blue – Green	Blue
Test other cells count	C CD4 – Green	D WBC – CD4 – Blue + Green	WBC – Blue
Total	CD4	WBC – CD4	WBC

Capture accuracy is the truthiness of capture and count and given in Equation (6.1).

$$Capture\ Accuracy\ (\%) = \frac{A + D}{A + B + C + D} x100 \tag{6.1}$$

Capture specificity (true negative rate) measures the proportion of other cells (WBC except CD4+T cells) that are counted as other cells, and is given in Equation (6.2).

$$Capture\ Specificity\ (\%) = \frac{D}{B + D} x100 \tag{6.2}$$

Capture sensitivity (true positive rate, probability of detection) measures the proportion of correctly captured and counted CD4+T cells, and is given in Equation (6.3).

$$Capture\ Sensitivity\ (\%) = \frac{A}{A+C} x100 \tag{6.3}$$

Capture precision (positive predictive value) measures the proportion of captured and counted actual CD4+T to all captured cells, and is given in Equation (6.4).

$$Capture\ Precision\ (\%) = \frac{A}{A+B} x100 \tag{6.4}$$

Performance of counting is evaluated using above statistical measures.

6.1.5 Counting cells inside channels using lensless wide-field microscopy system

The lensless wide-field microscopy system uses shadow imaging idea. Simply the sample is placed on top of the image sensor, a light source is placed far from top and the shadow of the cells are on the sensor. The quality of the image is not as good as light microscopy images but the imaging aperture is as wide as the area of the sensor. In this section the construction of the system, cell counting algorithm and automatic counting of cells are described.

6.1.5.1 <u>Lensless wide-field microscopy system development</u>

The lensless wide-field microscope has 4 main parts. Light source, light way, image sensor and sensor stand. Three light sources are tested. One is a blue light emitting diode (LED) with a peak light intensity at 455nm and the other is a high brightness white LED and the last one is warm white LED.

Blue LED (M455L3) and warm white LED (MWWHL3) are purchased from Thor Labs. (Newton, New Jersey, USA). And white LED (276-0024) is purchased form RadioShack (Cambridge, MA, USA). Thor Labs.'s LED with its heat sink is shown in Figure 6.16.

Figure 6.16 LED light source for lensless wide-field microscope. The LED has its heat sink.

Image sensor is a 10 Mega Pixel (MP) Complementary metal oxide semiconductor (CMOS) camera. This camera (UI-1492LE-M) is purchased from IDS Imaging Development Systems (Obersulm, Germany). Sensor imaging area is 6.4 mm × 4.6 mm. There are 3840 × 2748 pixels with a pixel size 1.67 µm ×1.67 µm. The camera is in Figure 6.17.

The stand for imaging sensor is produced by laser cutting of black PMMA sheets. The location where the printed circuit board (PCB) of camera is mounted, is engraved on PMMA and the location where the sensor is encounter is cut. The CAD design is in Figure 6.18, and actual stand with mounted camera is in Figure 6.22.

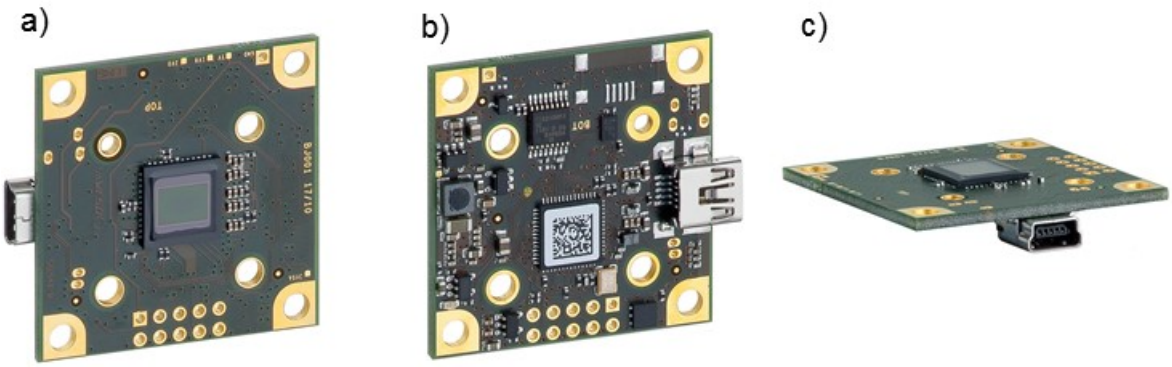

Figure 6.17 10 MP monochrome CMOS camera used as an image sensor for lensless wide-field microscope, a) view of sensor side, b) back side, and c) sensor stand horizontal.

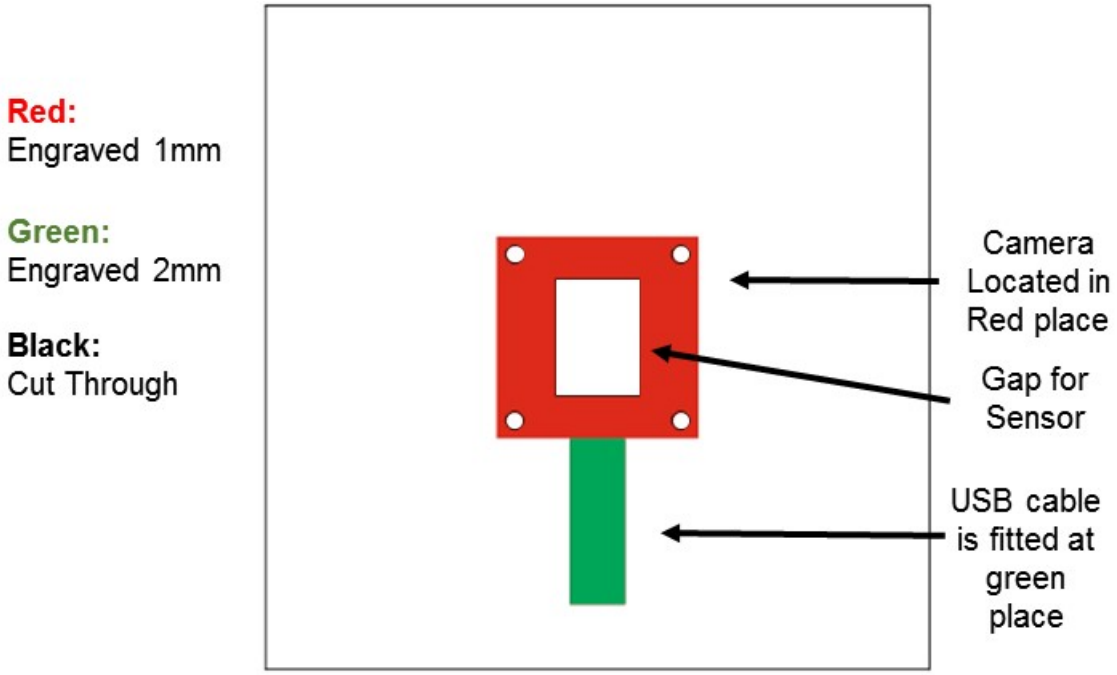

Figure 6.18 CAD design for image sensor stand. Colored parts are engraved on 3mm PMMA. Black lines are cut trough.

The light way or optic way, is designed for guarantying a distance (20cm) between the led and the sensor and a closed box for sample. There are 4 parts, first 3 parts are lens tube (SM2L30 - SM2 Lens Tube, 3"), tube to LED adaptor (SM1A2 - Adapter with External SM1), and tube to box adaptor (SM2T2 - SM2 (2.035"-40)), which are purchased from Thor Labs. (Newton, New Jersey, USA). They are shown in Figure 6.19. The last part is a 10 cm x 10 cm, one side open box. CAD design of the box is in Figure 6.20, and the final box is laser cut from PMMA and shown in Figure 6.23.

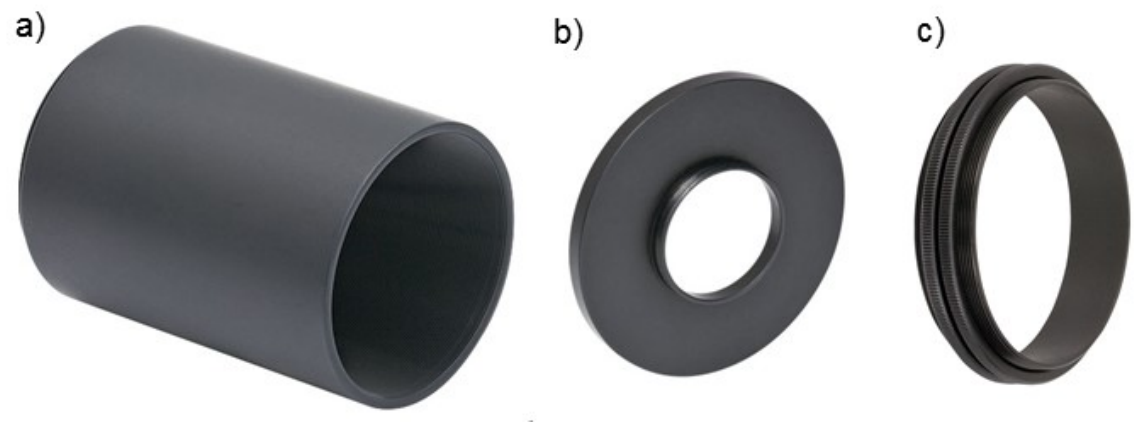

Figure 6.19 Parts of light way a) lens tube b) tube to LED adaptor, c) tube to box adaptor.

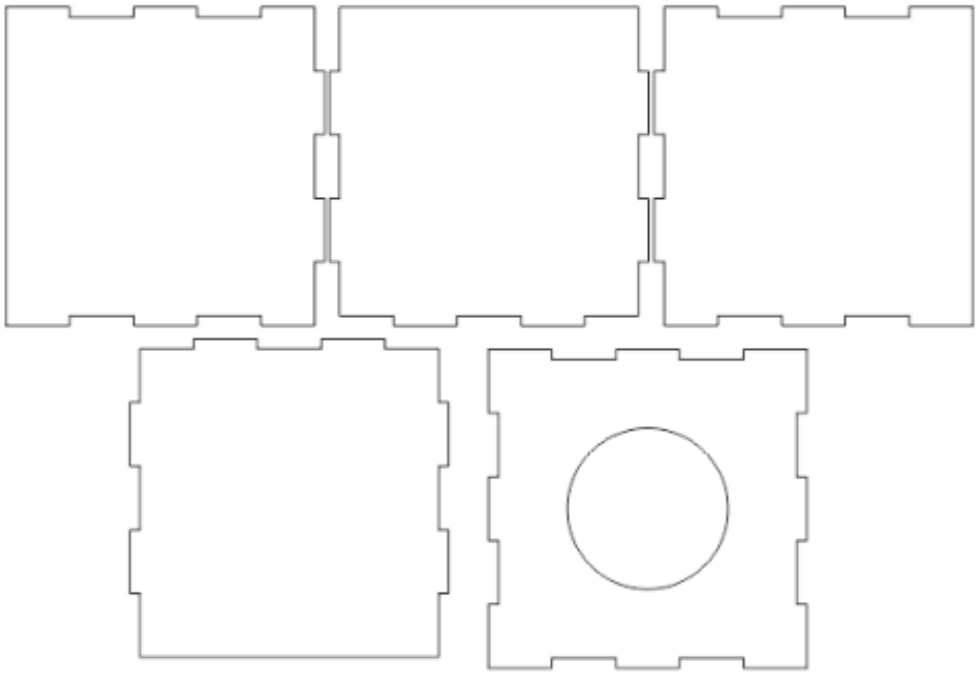

Figure 6.20 CAD design of box part of light way. One side is open for sensor stand and the cross side has an open circle for lens tube connection where the light will shine.

The image sensor stand is designed also as a sample holder. The box with light source can be removed from sensor and sample can be placed and the box with light source can be remounted in order to make dark room for sample. The light intensity can be changed using an LED driver circuit. After sample is placed, light intensity is arranged then CMOS sensor takes images. The laser cutter is shown in Figure 6.21.

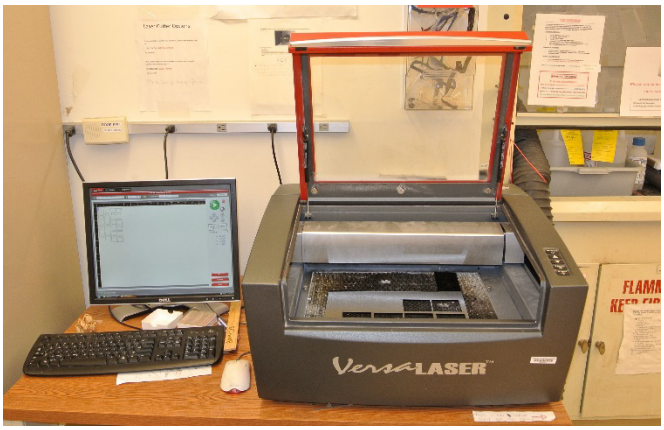

Figure 6.21 Laser cutter used in that thesis work. VLS2.3, Universal Laser Systems Inc.

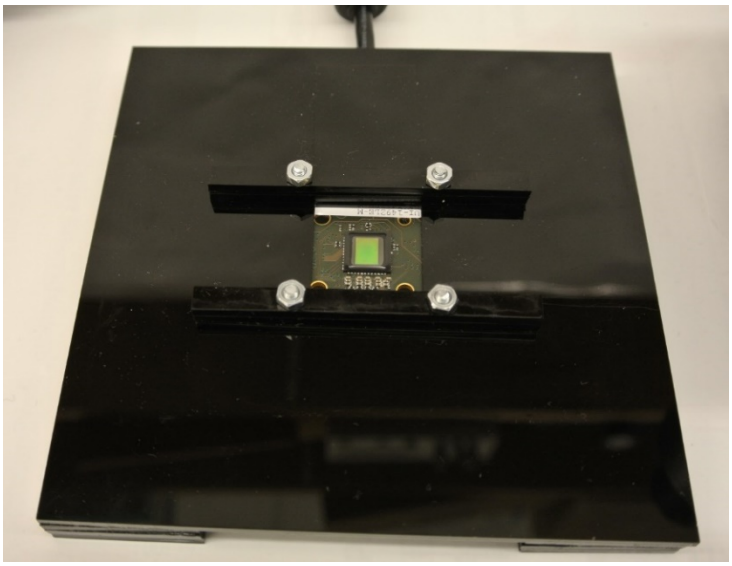

Figure 6.22 Image sensor stand with mounted image sensor.

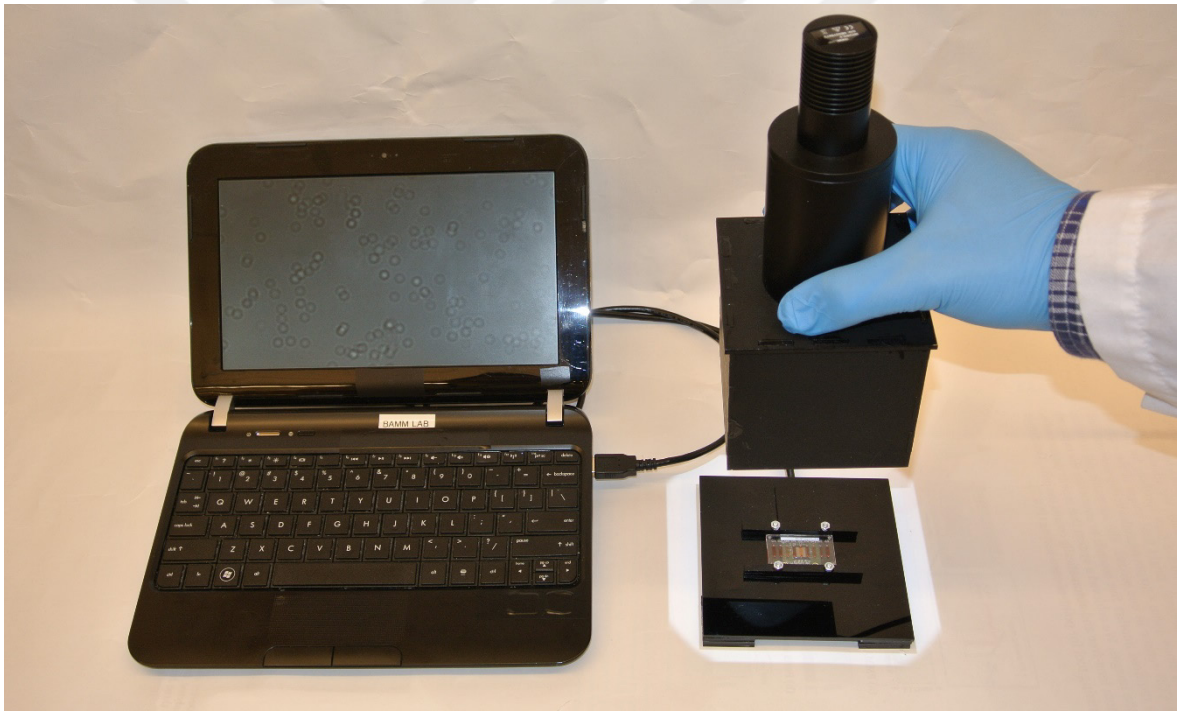

Figure 6.23 lensless wide-field microscopy system.

Whole system can be battery operated full POC device as shown in Figure 6.23. Microfluidics chip channels can be placed on top of sensor as shown in Figure 6.24. The sample in that figure is whole blood. In order to take image of whole channel sample should be scanned 5 times, and total imaging is in less than 1 minutes. The principle of counting CD4+T cells using lensless wide-field microscopy system is depicted in Figure 6.25.

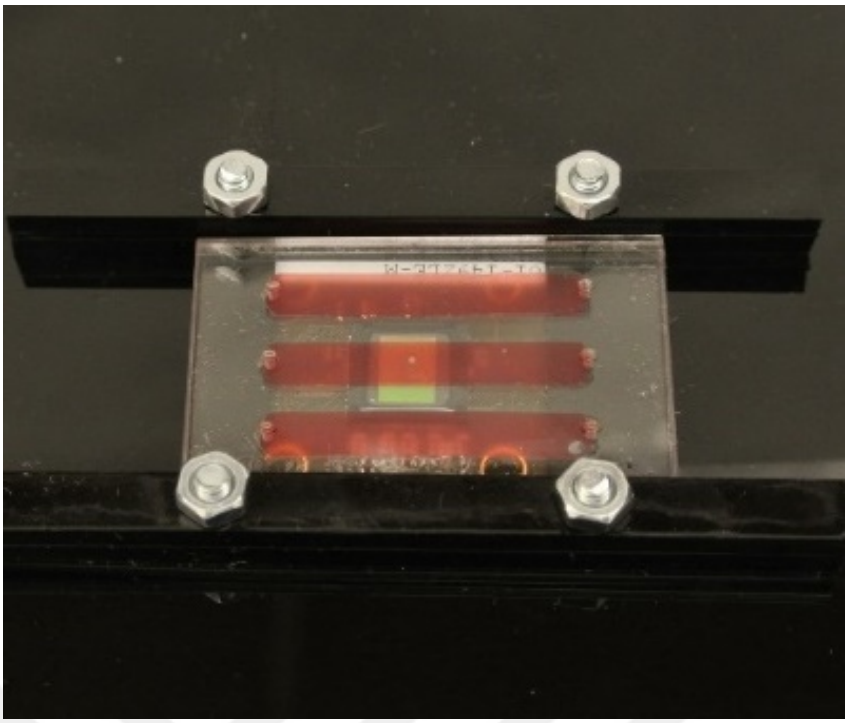

Figure 6.24 Sample in a microfluidic channel on top of image sensor. Whole blood is in the channel in order to show the coverage of sensor area and channel.

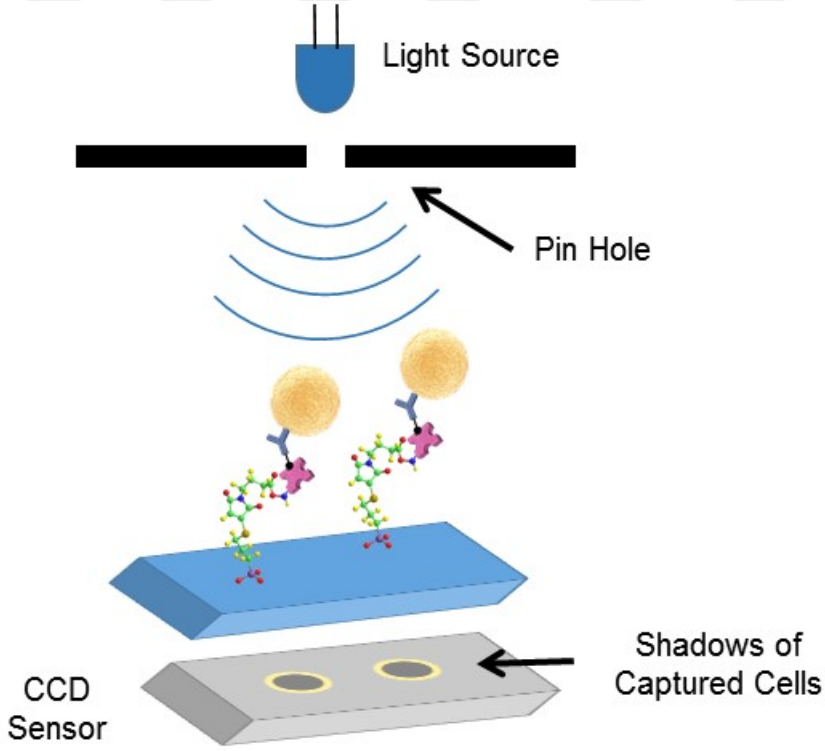

Figure 6.25 lensless wide-field shadow imaging principle for counting of captured CD4+T cells.

6.1.6 Cell counting program

Images are obtained using the developed lensless wide-field microscopy system and automatically counted using a developed program. In this section the details of the image and the algorithm are explained in two programs.

6.1.6.1 Sample image taken by the system

Shadow images of captured cells in the channels are obtained using the lensless wide-field microscopy system. A sample image of a part of the channel is shown in Figure 6.26.

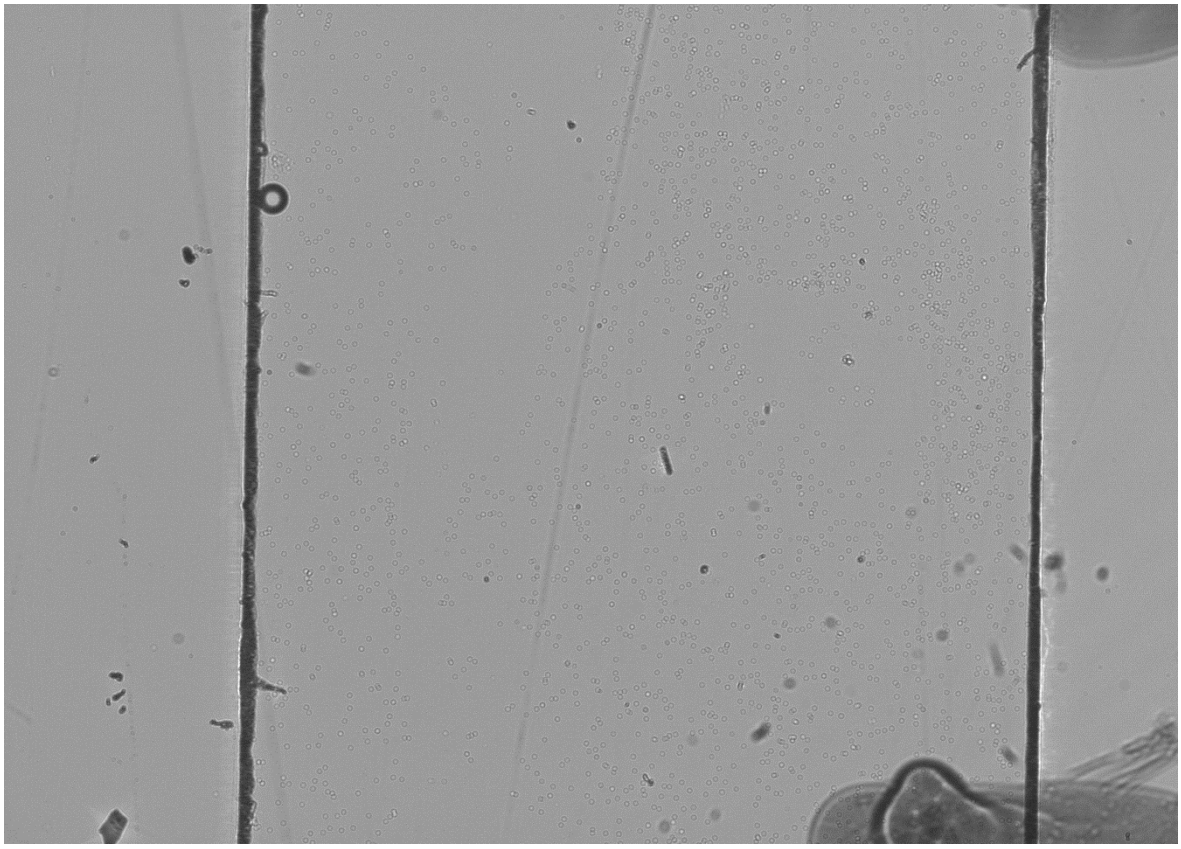

Figure 6.26 Sample image taken by the lensless wide-field microscopy system. The image is a part of a channel in the microfluidic chip. In this channel CD4+T cells are captured. In order to image whole channel 5 of this 6.4 mm × 4.6 mm images are required. This image is 3840 × 2748 pixels (10MP) with a pixel size 1.67 μm ×1.67 μm. Two straight lines are the edges of the channel. On the top and bottom of the right side there are the shadow of pen markings.

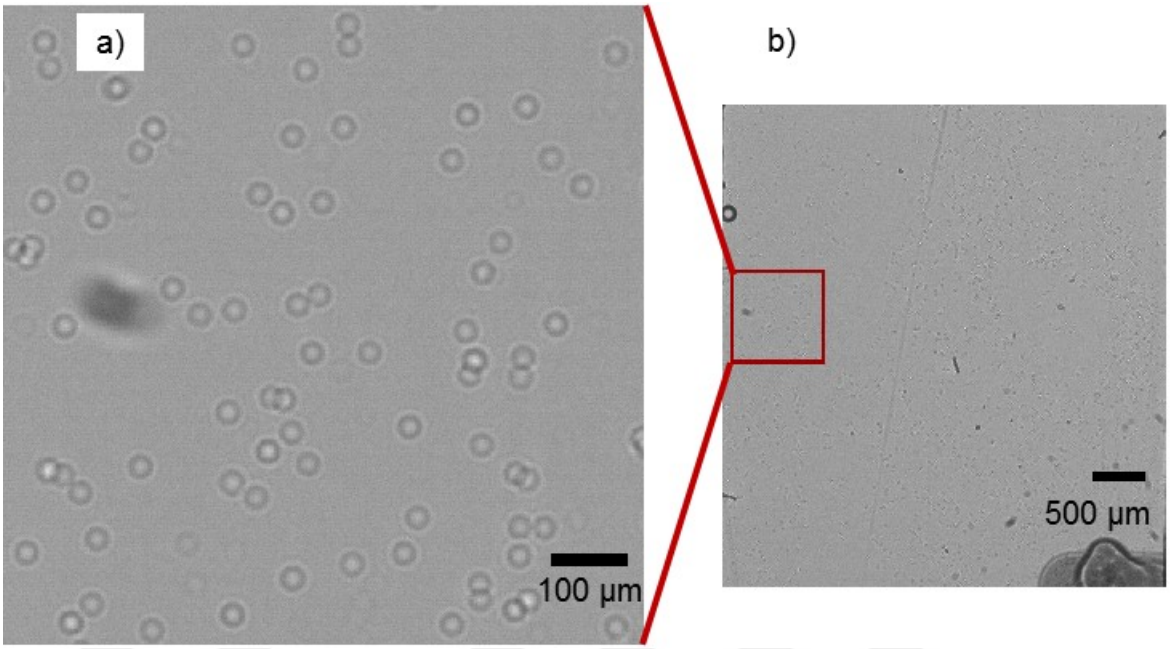

Figure 6.27 Sample image of captured CD4+T cells taken by the lensless wide-field microscopy system. Wide field image of the part of a channel includes inside and some outside part of the channel shown Figure 6.26. The outside part of channel in that image is cropped and only inside of part the channel is shown in b). A small portion from that image is zoomed and shown in figure a), where shadow images of cells are visible. The image in a) is the 1 to 40 portion of the wide-field image in Figure 6.26.

In Figure 6.27, a sample image of captured CD4+T cells taken by the system is shown. The image taken by system is wide-field image. Using a standard microscope with 100x magnification the field of view is a circle with around 1.6 mm diameter. The field of view is around 2 mm^2. For a microscope with a standard digital camera this field is even lower around 1 mm^2. The total field of view of the developed system is around 30 mm^2.

Although image is wide field since it is the shadow of the cells on the pixels of image sensor the raw image resolution is low. The histogram of image is squeezed in a narrow band as shown in Figure 6.28. Image of a single is cell is shown in Figure 6.29 a) and its histogram is shown in Figure 6.29 b). The histogram of the image of the cell is also squeezed in a narrow band. The images are taken for the same light intensity and exposure period but since the images are shadow images their contrasts are low so histogram is squeezed.

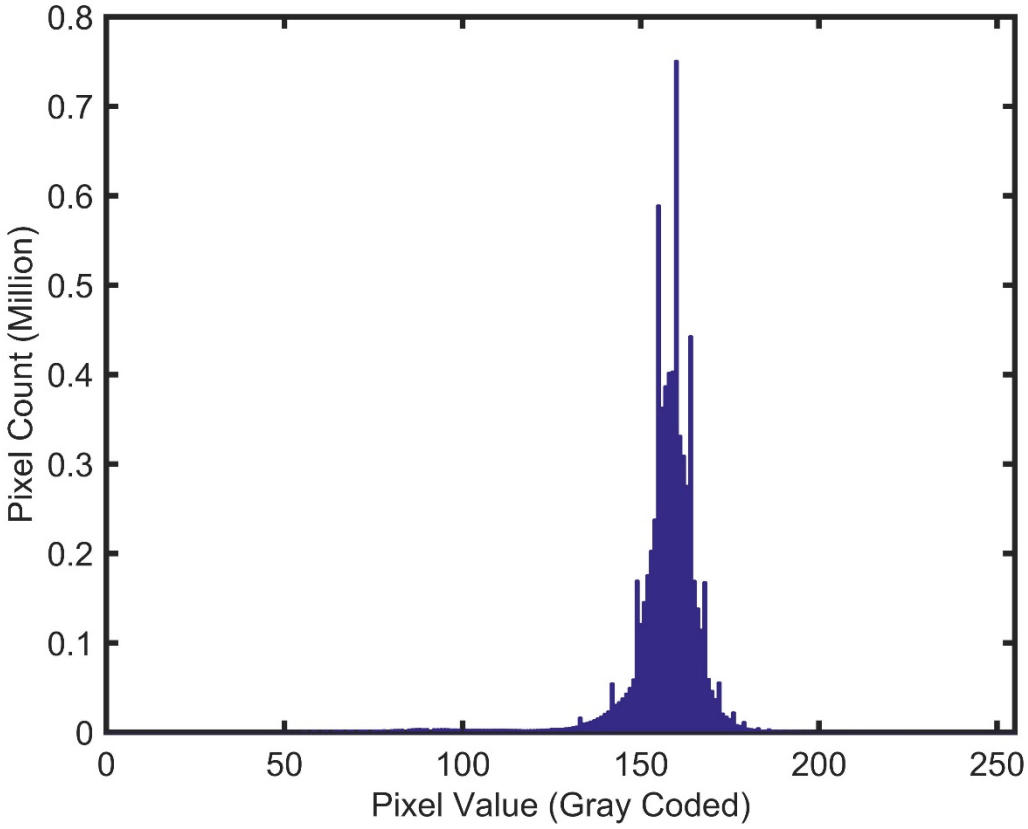

Figure 6.28 Histogram of above image in Figure 6.27 b).

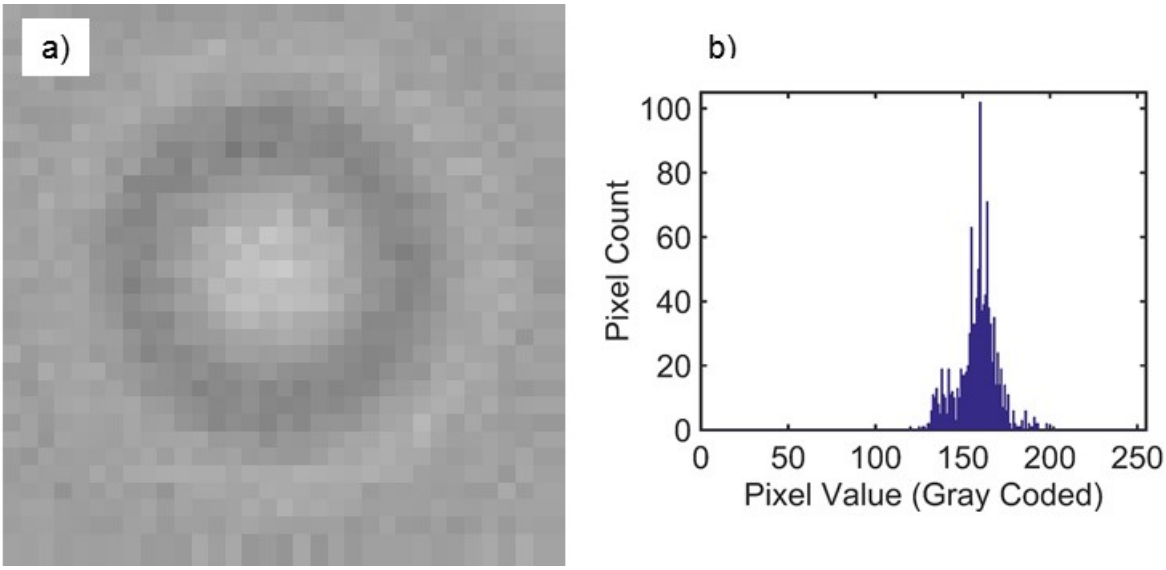

Figure 6.29 a) Sample image for a single cell, b) histogram of that image.

6.1.6.2 First program: Obtaining averaged model cell image

The cell counting algorithm is based on evet detection in 2D signal processing. Event detection is applied using the correlation of sample image of a cell and whole image of cells. In order to count the cells two program code are written. First program is for defining the sample model image of a cell using the already known cell images. Second program is the counting of cells using the similarities between sample model image of a cell and cells is the whole image.

Shadow images of cells have a specific form. Pixel values of them are in specific range and they have a doughnut like shape. In order to better define the shape 30 cells are selected randomly and averaged to find a cell shadow model.

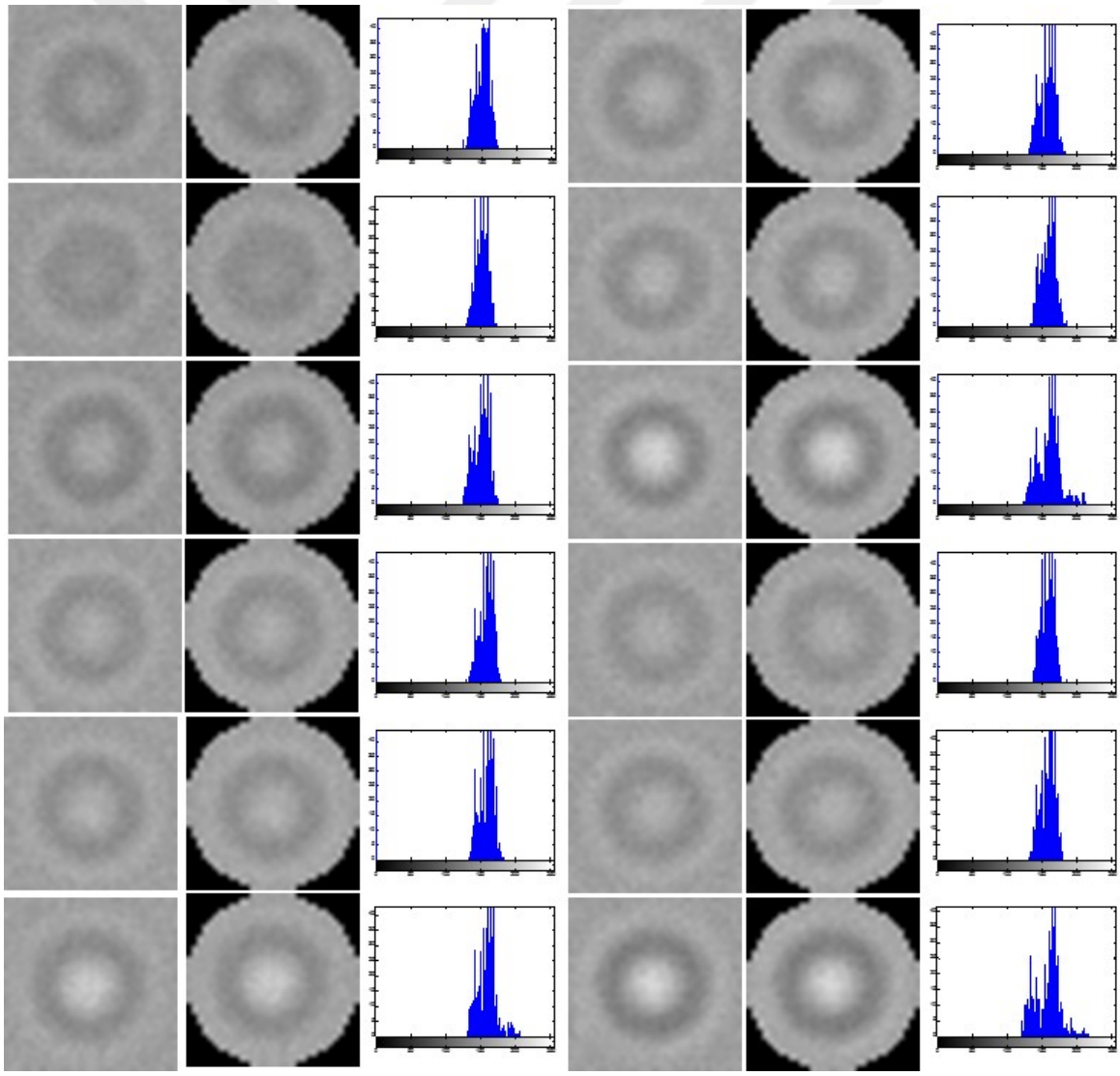

Figure 6.30 Sample cell images for averaging to give a shadow model for a cell.

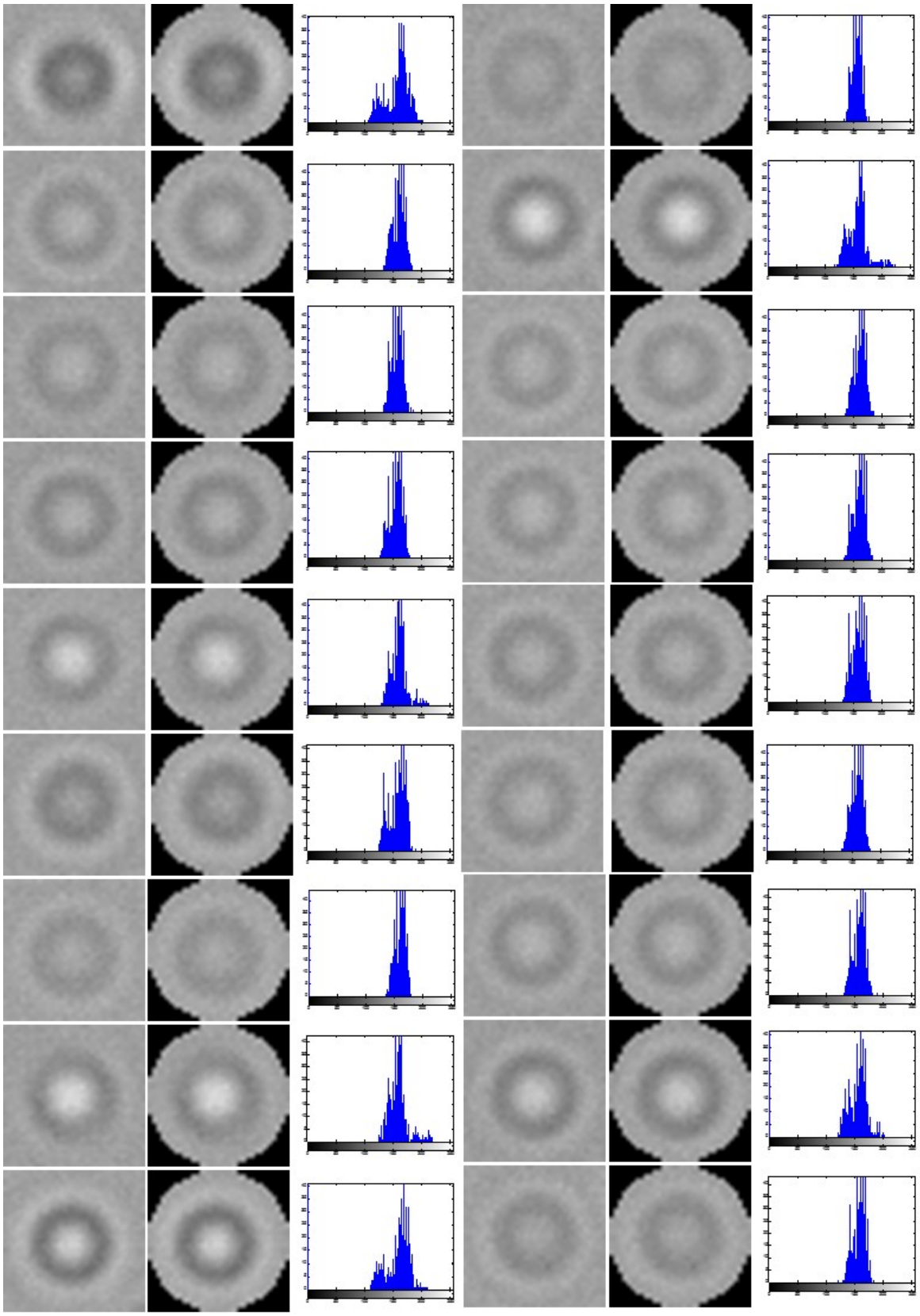

Figure 6.31 Continued of Figure 6.30. From left to right, first image is the square 33x33 pixel image of a cell, second one is the round shape extracted form of the cell image, and third is the histogram of round shape. Total 30 images.

While averaging the histogram of images is also stretched using an adaptive linear histogram stretching algorithm that is also developed. After adaptive linear histogram stretching applied to all single cell images their sum is averaged to give an averaged model cell image.

6.1.6.3 Adaptive linear histogram stretching

The 30 sample cell images given in Figure 6.30 and Figure 6.31 are used to obtain the average model image for a cell. The contrasts of images are low because the histogram of them is squeezed in a very narrow band. Due to that reason their histograms should be stretched in order to increase the details.

For histogram stretching the statistical properties of images are first evaluated. The minimum and maximum pixel values in each cell image round portion are evaluated and expected value of histogram pixel values to pixel counts are evaluated. Mean and standard deviation of those values for 30 images are shown in Figure 6.32. From this graph it is obvious that the histogram values are quite similar and they are squeezed in a narrow band.

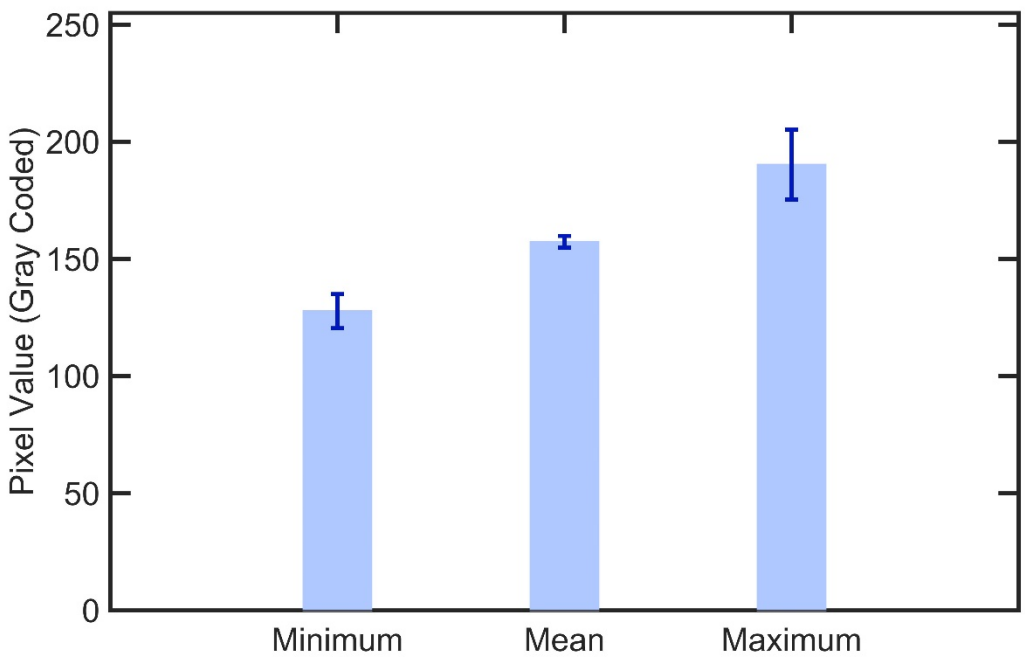

Figure 6.32 Pixel value statistics of single cell images given in Figure 6.30 and Figure 6.31. Minimum is the average of minimum pixel values of images. Maximum

is the average of maximum pixel values of images. Mean is mean of the expected value of histogram pixel values to total pixel count in an image. Error bars are standard deviations of minimum, mean and maximum values.

The adaptive histogram stretching starts with changing the mean value (expected value) of pixels to the median value of gray code which can be named as centering the contrast. In this way the contrast differences in the images are eliminated and contrast of all images becomes similar. This arrangement makes the stretching adaptive. The contrast centering algorithm is shown in Figure 6.33.

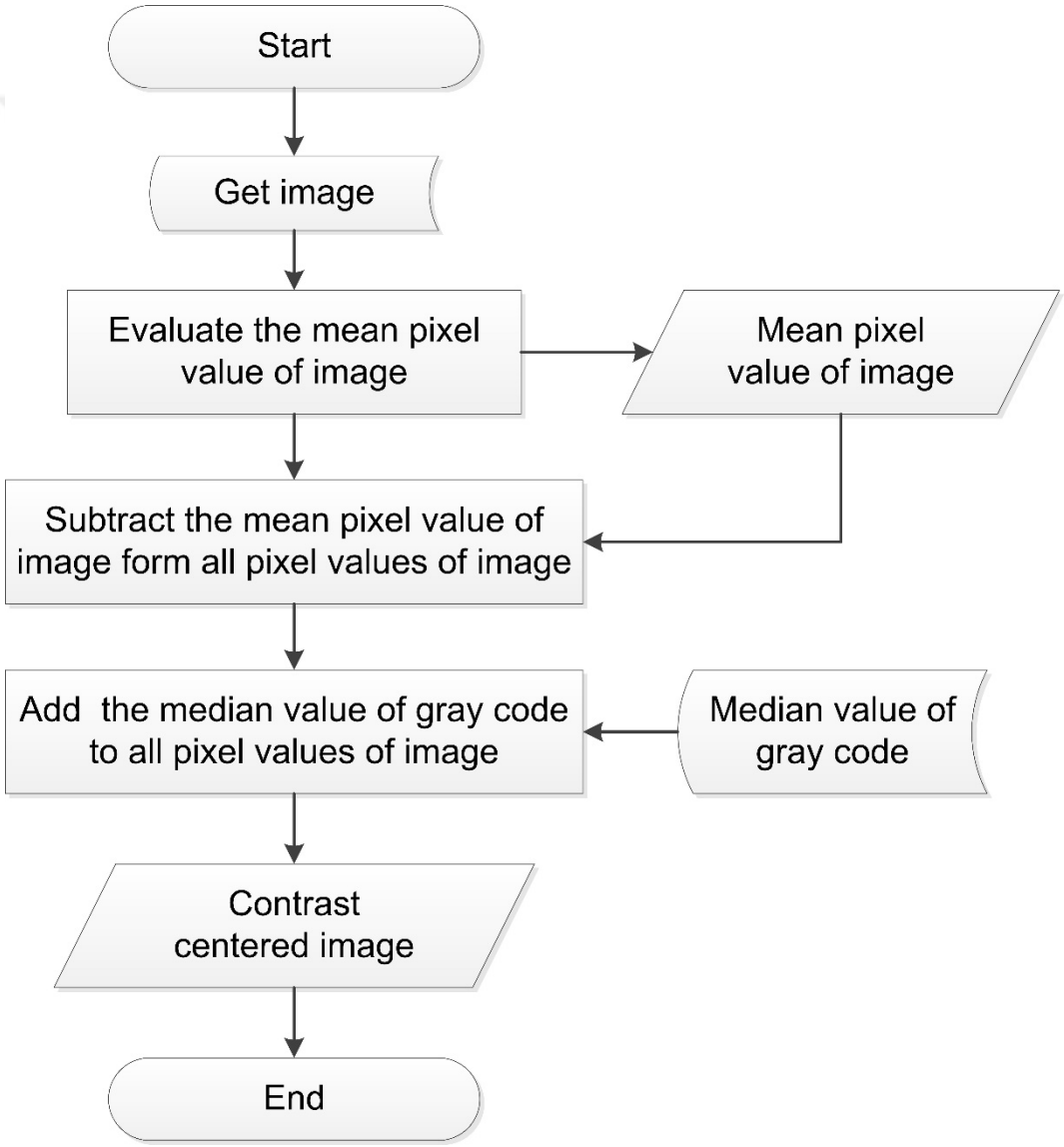

Figure 6.33 Contrast centering algorithm.

After contrast centering linear histogram stretching is applied as explained in section 4.3.1. The stretching ranges are predefined using the statistics of single cell images. After contrast centering the pixel values are mostly between 100 and 150 in gray code so those values are defined as the range. Which becomes also adaptive. The algorithm used for histogram stretching is given in Figure 6.34.

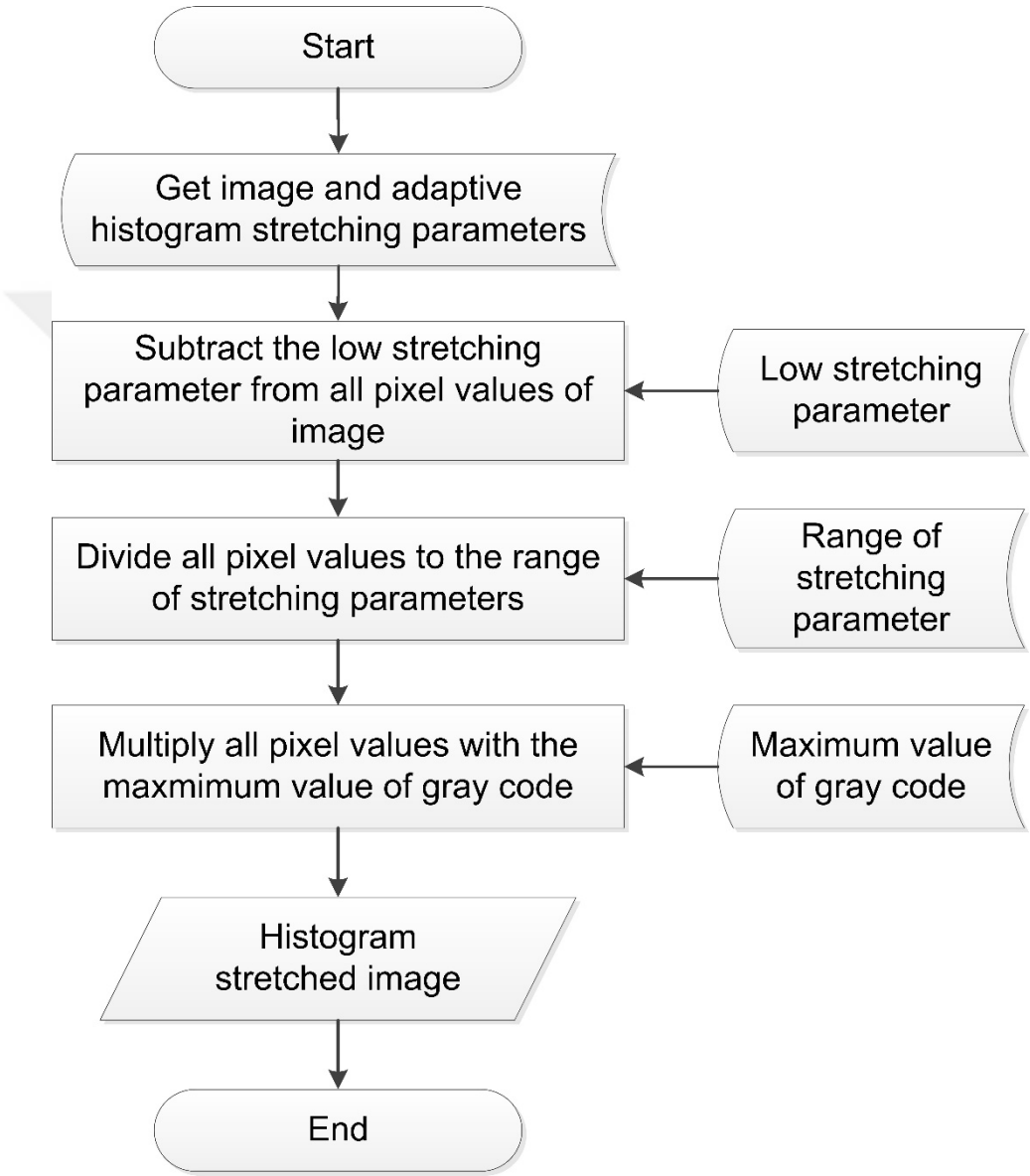

Figure 6.34 Histogram (contrast) stretching algorithm.

The adaptive linear histogram stretching is applied by the two algorithms given Figure 6.33 in and Figure 6.34. After histogram stretching single cell images are similar in terms of contrast values and their contrasts are improved which is shown in Figure 6.35.

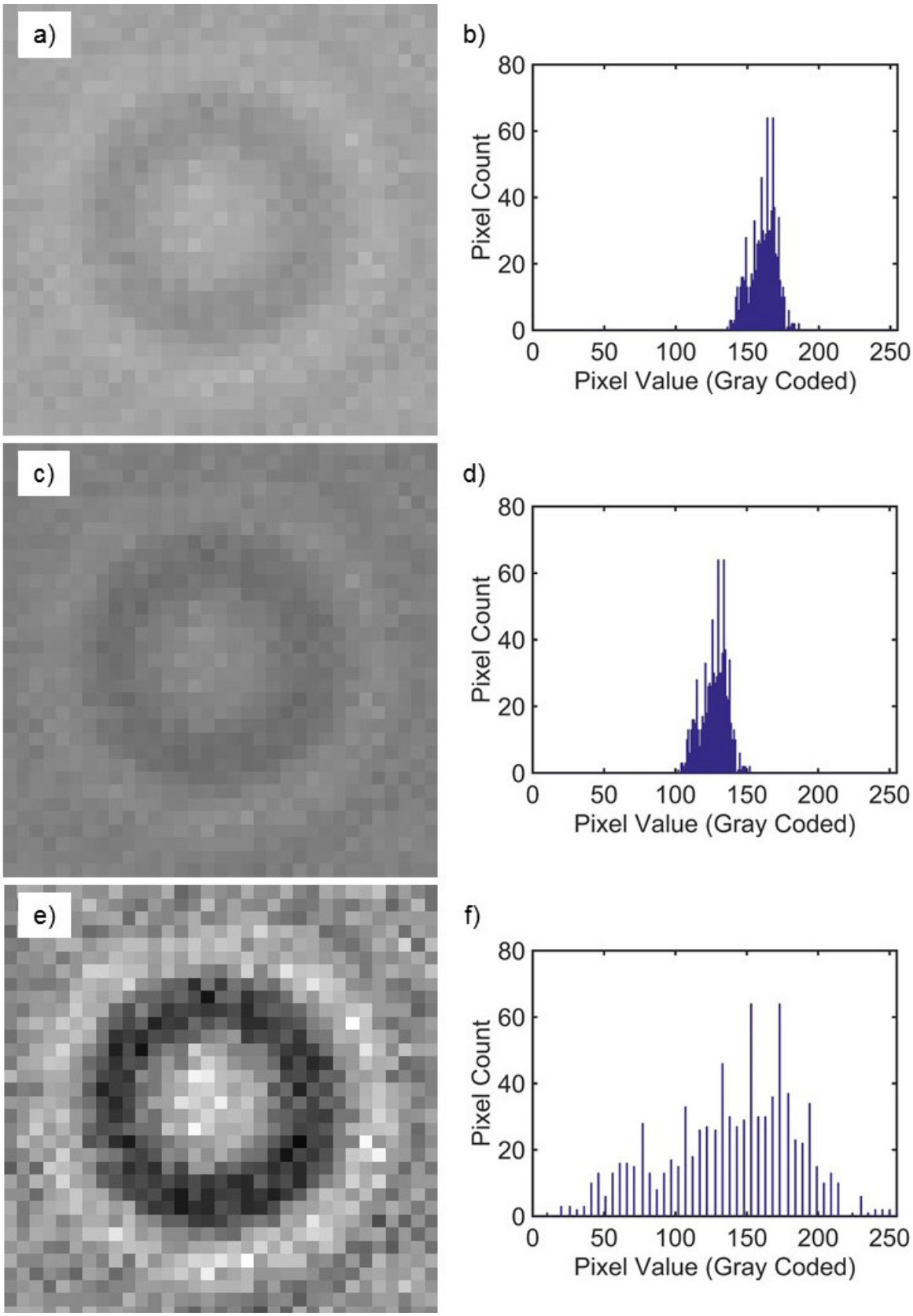

Figure 6.35 Adaptive histogram stretching of a single cell. a) A sample image of a single cell, b) histogram of that image, c) contrast centered image, d) histogram of contrast centered image, e) histogram stretched image, f) histogram of final image.

6.1.6.4 Averaged model cell image

After adaptive linear histogram stretching all the contrast enhanced single cell images are summed and averaged in order to get the averaged model cell image.

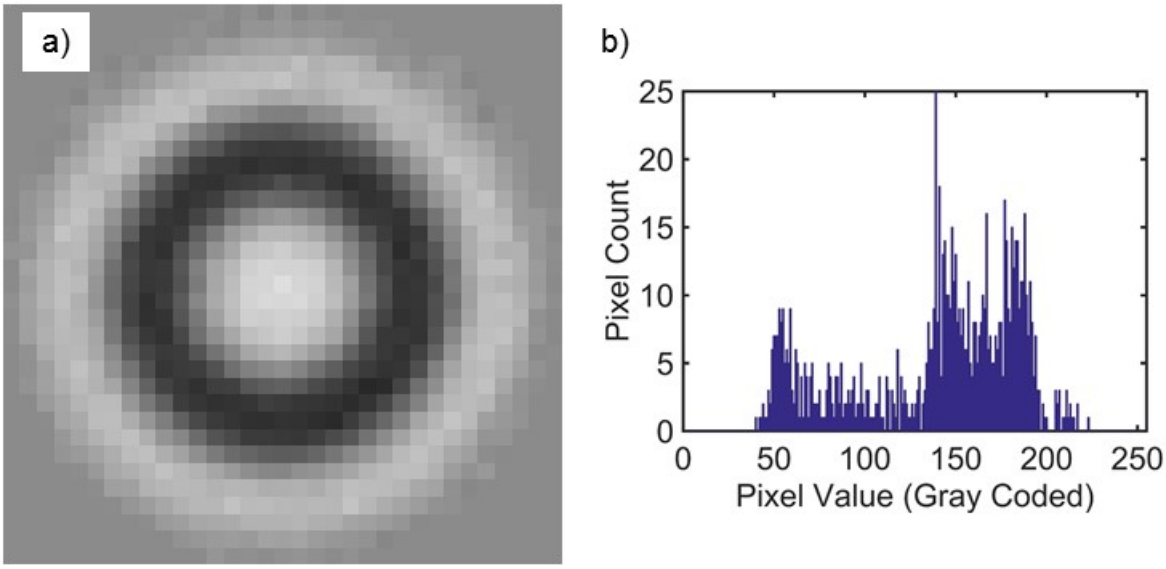

Figure 6.36 a) Averaged model cell image, b) histogram of that image.

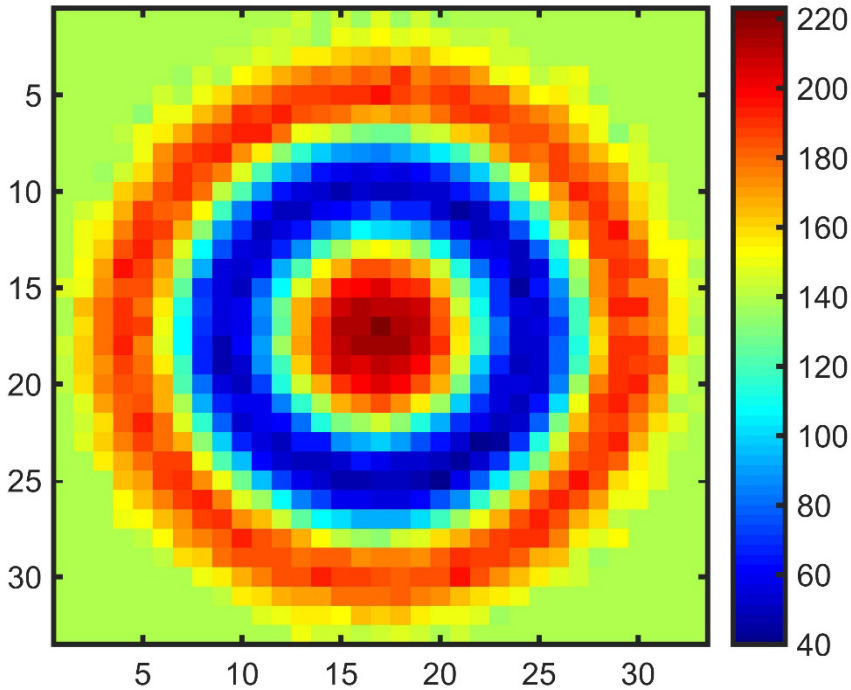

Figure 6.37 2D colored representation of averaged model cell image. The axes are row and column index of pixels and color bar defines the gray color codes.

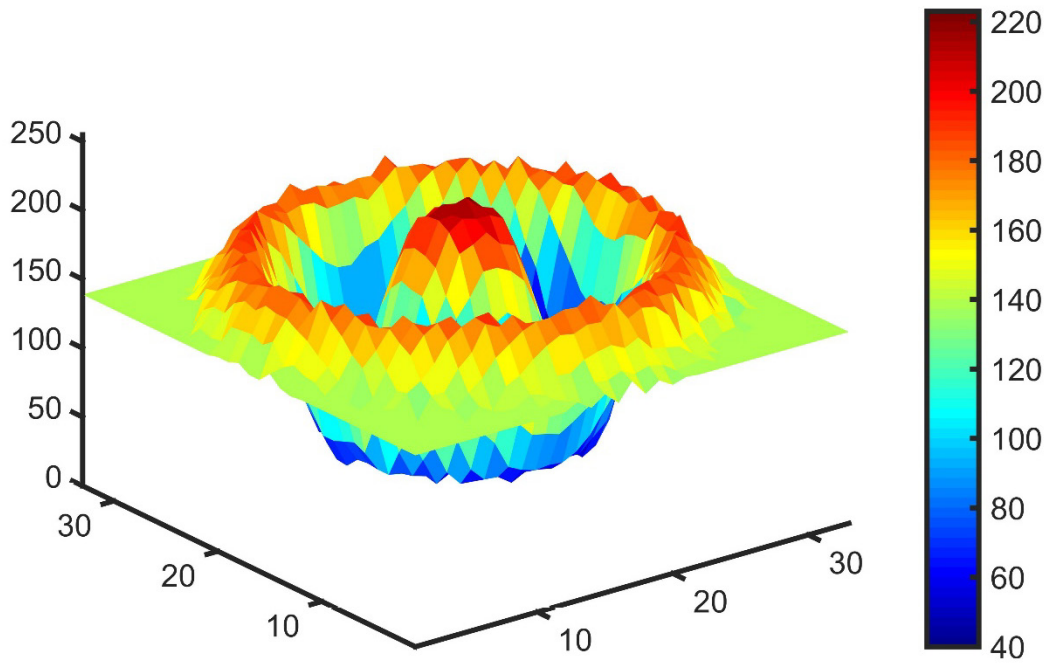

Figure 6.38 3D colored representation of averaged model cell image. The x and y axis's are row and column index of pixels and z and color bar defines the gray color codes.

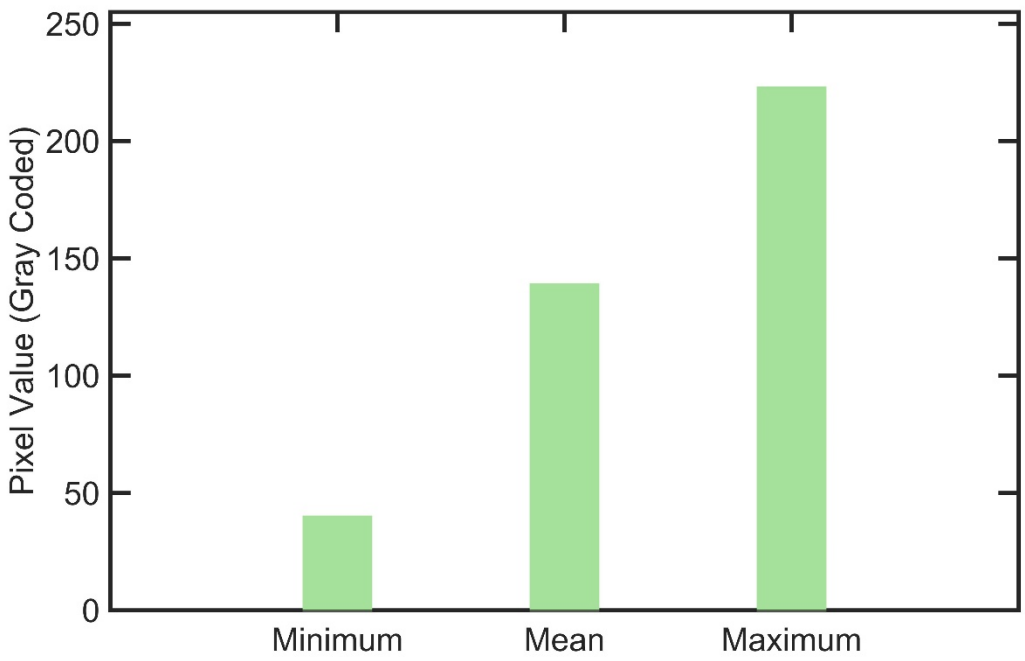

Figure 6.39 Pixel value statistics of the averaged model cell.

This averaged model cell image is used as a mask in second program to detect cells. Averaged model cell image and its histogram is given in Figure 6.36. 2D and 3D colored representation of averaged model cell image is given in Figure 6.37 and Figure 6.38.

The minimum and maximum pixel value and expected value of histogram of model image are shown in Figure 6.39. The contrast of the averaged model cell image is enhanced too. This image is smooth since it is the sum of averages of other similar cells.

6.1.6.5 Second program: Cell detection using correlation

The cell detection is based on event detection using cross correlation. The principle of cross correlation is explained in section 4.3.2. It is based on finding similar objects in an image, in this case object is averaged model cell image, and the image which has objects in it is the image with cells. In order to explain the algorithm sample image in Figure 6.40 is used.

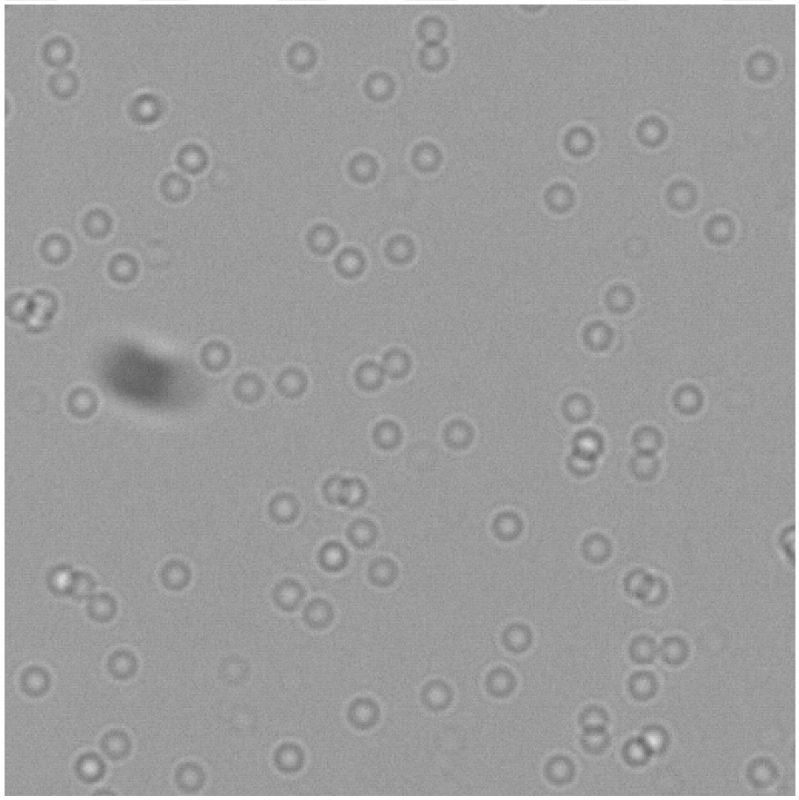

Figure 6.40 Sample image of cells to be counted.

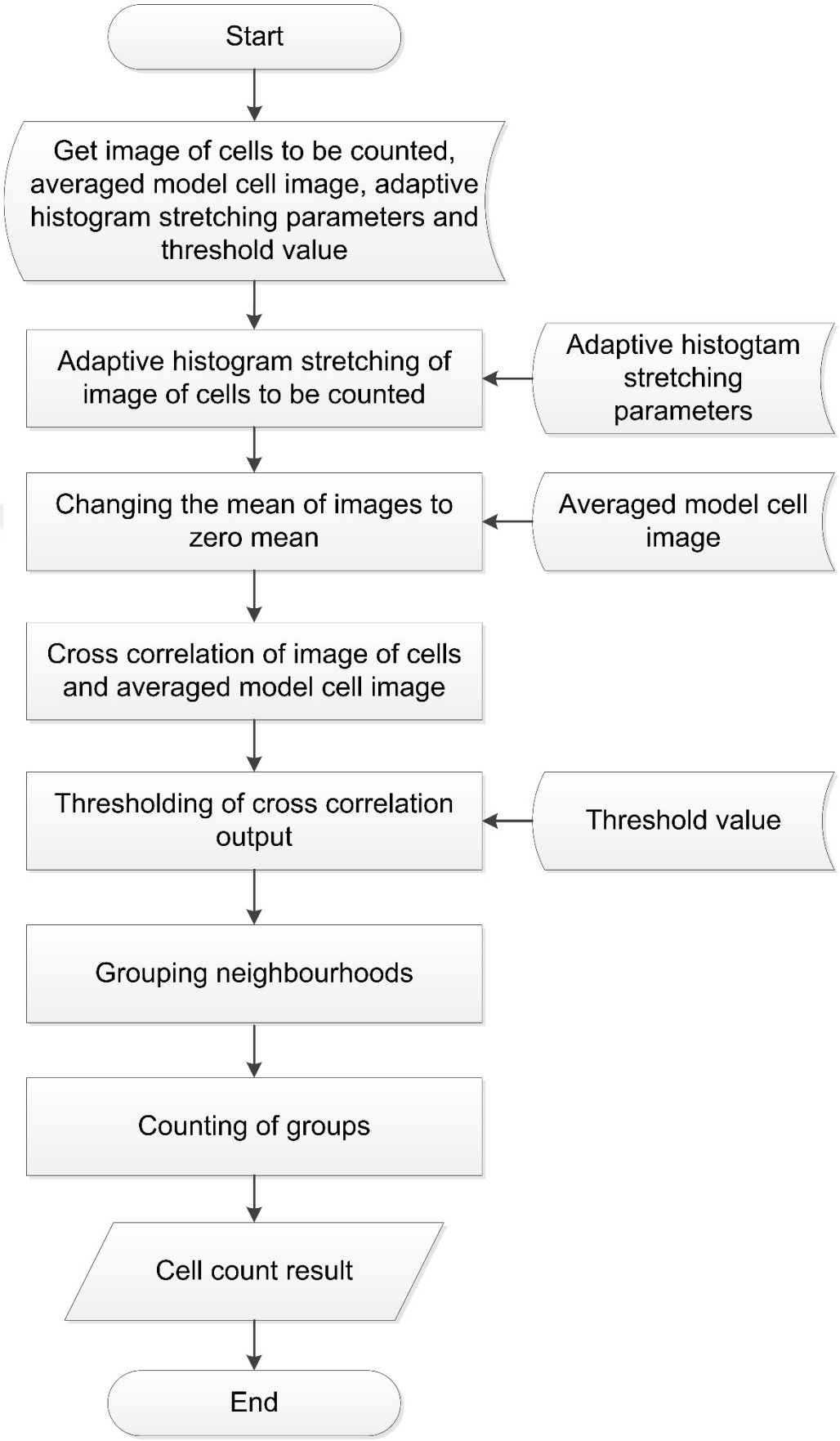

Figure 6.41 Sample image of cells to be counted.

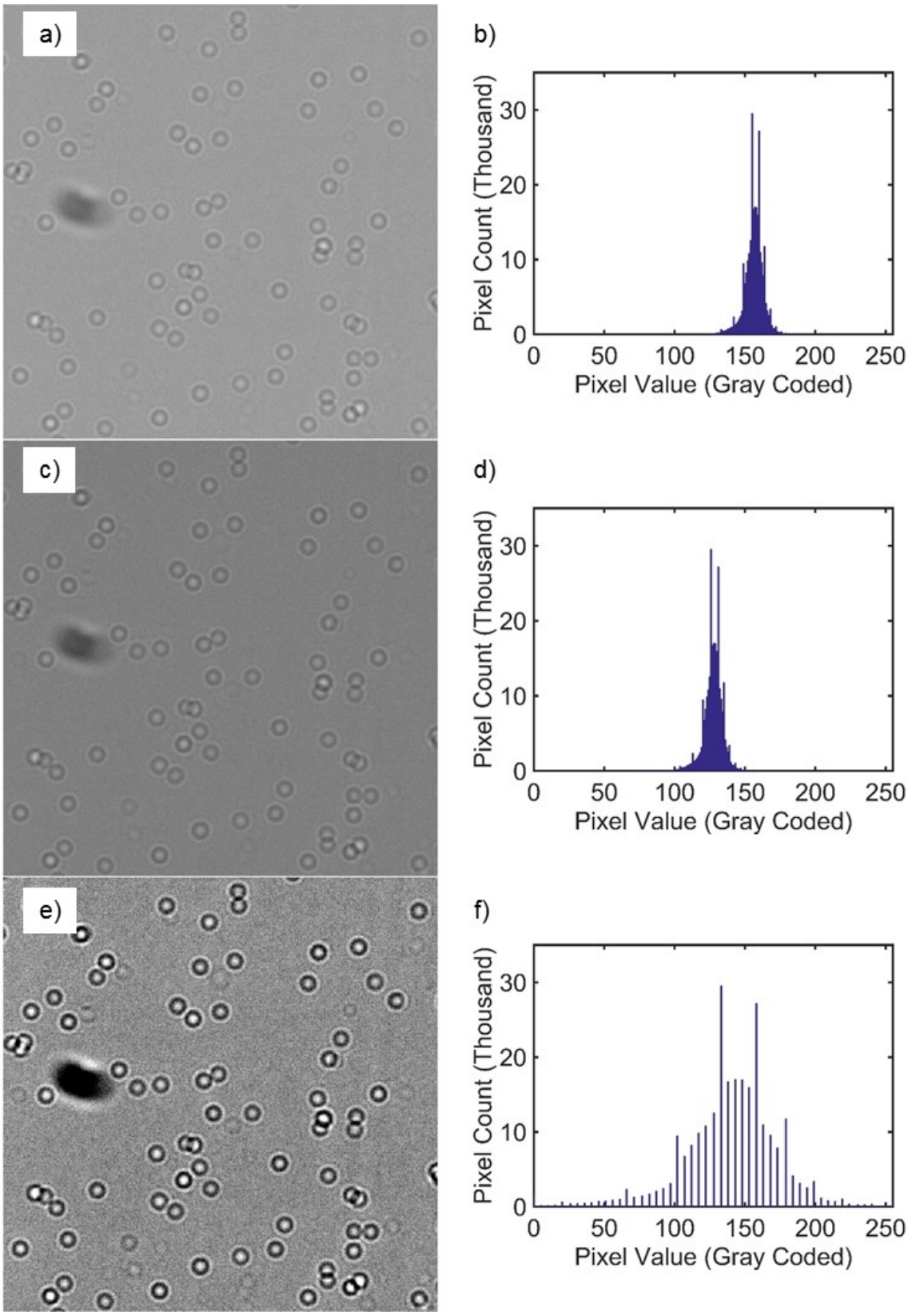

Figure 6.42 Adaptive histogram stretching for image to be counted. a) A sample image, b) histogram of that image, c) contrast centered image, d) histogram of contrast centered image, e) histogram stretched image, f) histogram of final image.

The algorithm for second program is given in Figure 6.41 it starts with adaptive histogram stretching of image with cells. The adaptive histogram stretching steps and output plots are given in Figure 6.42.

Then cross correlation of that image with averaged model cell image is applied. The 3D and 2D plots for output of cross correlation are given in Figure 6.43 and Figure 6.44 respectively.

After that the maximum values of cross correlation output which corresponds to the match of cells are obtained using thresholding, the output image of thresholding is a binary image in which white pixels indicates cells as shown in Figure 6.45.

Than while pixels that are in the neighborhood of each other are grouped together and groups are numbered. A color code is given to each numbered group plotted in Figure 6.46. Finally grouped object indicates cells and their total number is the total cell count. The principle of thresholding and grouping neighborhood pixels are explained in section 4.3.3 and 4.3.4 respectively.

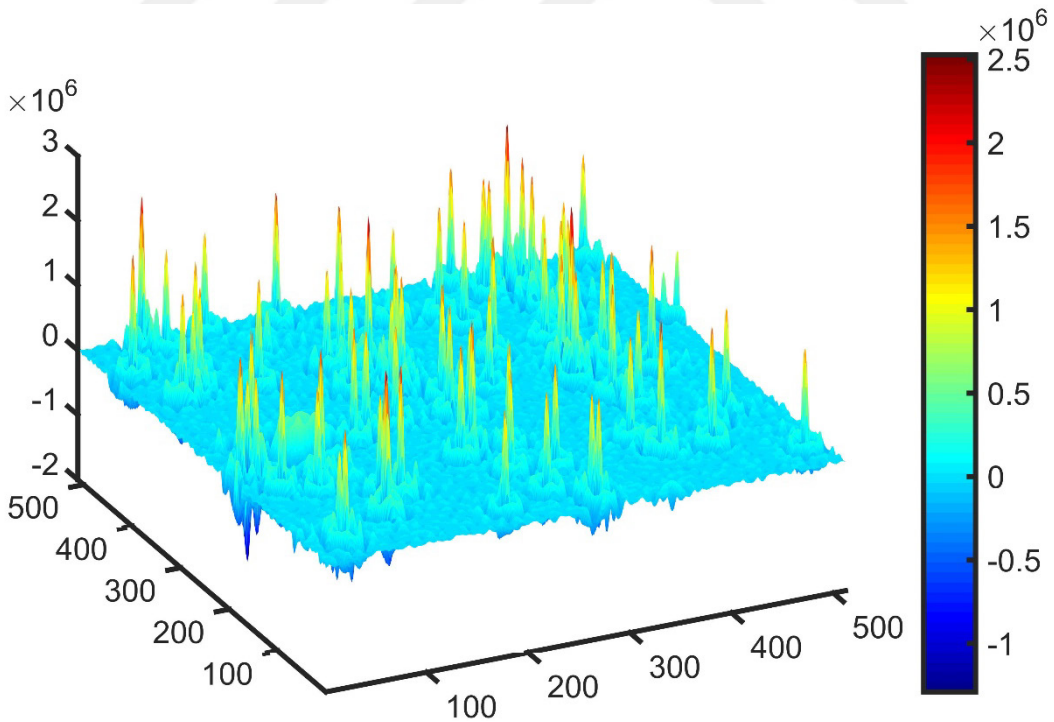

Figure 6.43 3D representation of cross correlation result of sample image and averaged model cell. x and y axis are the pixel index values for sample image and z and color bar indicates the cross correlation output value, arbitrary unit.

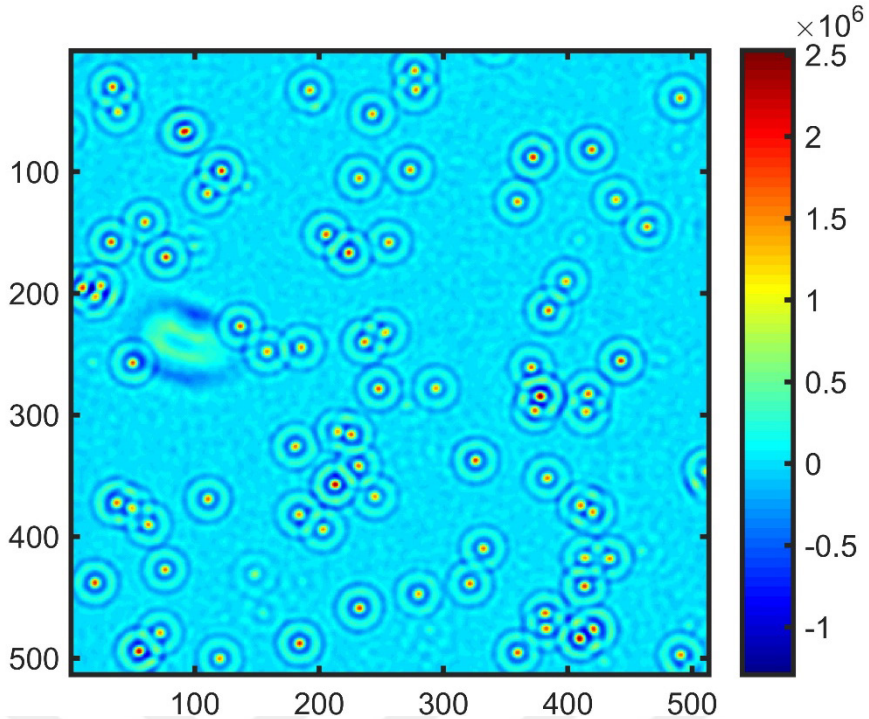

Figure 6.44 2D representation of cross correlation result of sample image and averaged model cell. x and y axis are the pixel index values for sample image and z and color bar indicates the cross correlation output value, arbitrary unit.

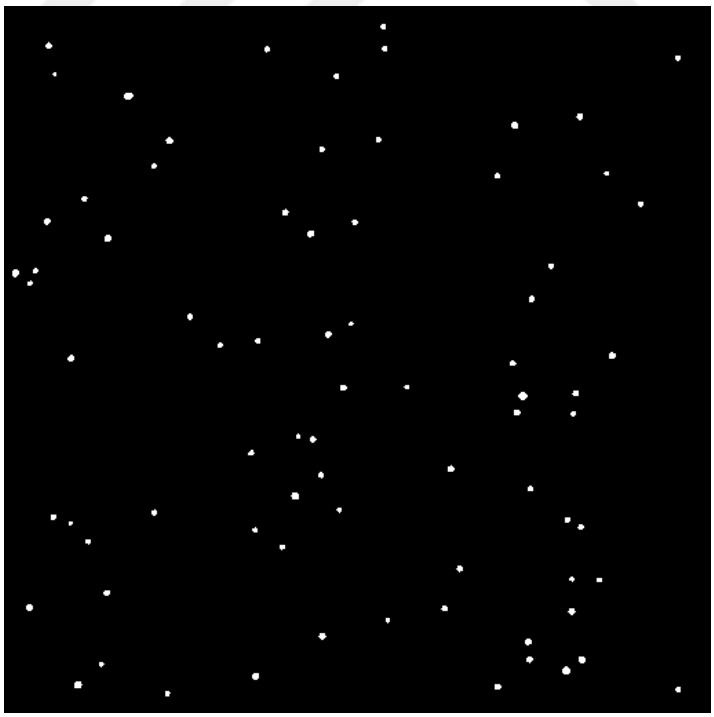

Figure 6.45 Thresholding output of cross correlation white objects indicate the cells. The image is a binary image.

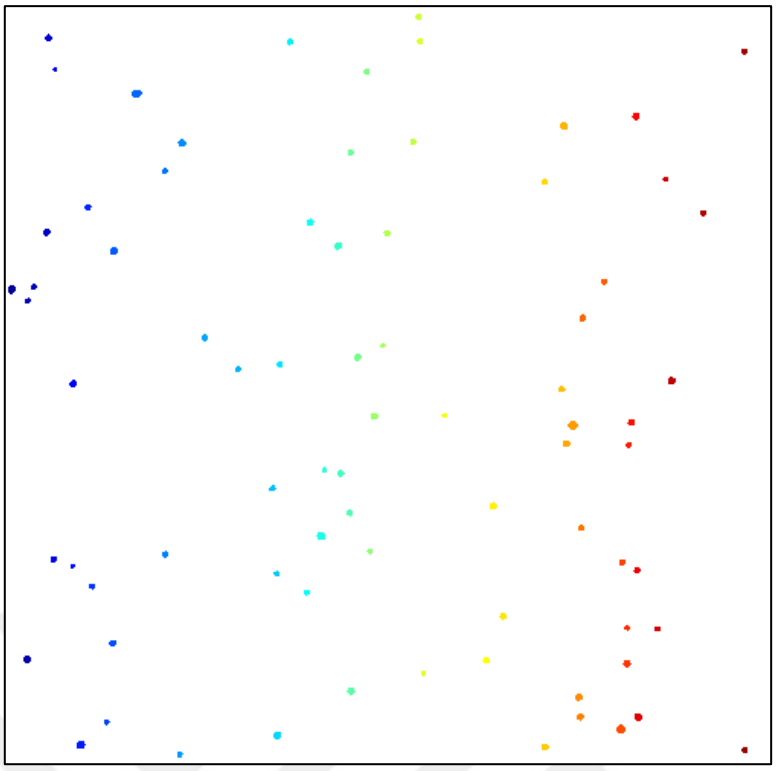

Figure 6.46 The pixels in white objects are grouped together and numbered. The colors codes are given to differentiate each group of pixels. Each group of pixels are corresponds to a cell.

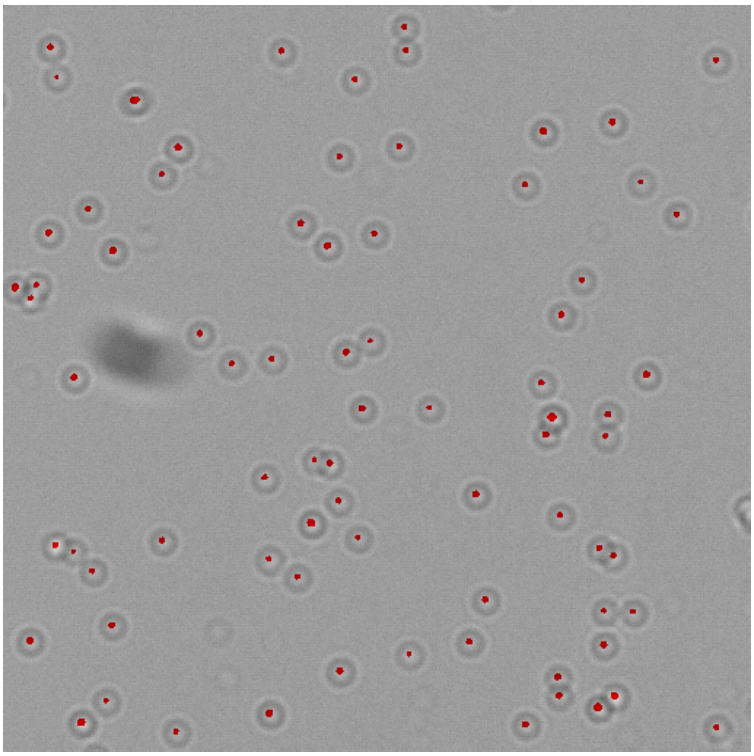

Figure 6.47 Counted cells and sample image to be counted are overlapped.

6.1.7 Automatic counting of cells

The captured CD4+T cells in channels can be counted using lensless wide-field microscopy system and cell counting program. Cell capture channels are placed onto the image sensor as in Figure 6.24. Channel dimensions are 4 mm x 26 mm, and sensor aperture is 6.4 mm x 4.6 mm so in order to cover the channel at least 4 images should be taken however in order not to lose information for experiments at least 5 images are taken for each channel.

The LED light intensity and exposure time of gathering image from sensor is fixed and those parameters are used for all experiments. Due to that reason the contrast and intensity of images are similar to each other. Although they are similar a contrast centering is applied to all images while cell counting. After gathering of images they are counted using an algorithm developed on MATLAB®, which is explained in section 6.1.6. The parameters using for cell counting program are statistically and experimentally defined and since the image gathering parameters are fixed the parameters for cell counting can also fixed.

6.2 Experiments and Results

Until this point design and implementation of chip fabrication, surface functionalization, lensless wide-field microscope and cell counting program are explained. In this section performance of those are evaluated and related experiments are described.

6.2.1 Testing the microfluidic chip

The design and implementation of microfluidic chip is explained in section 6.1.1. Easiest and efficient way of fluid injection to channels is manual pipetting. Channel and hole dimensions are optimized according to manual pipetting of fluids. Since laser cutter burns the PMMA in order to pattern the actual dimensions are different than those in CAD design. So the hole dimensions are experimentally determined according to the used pipet tip.

One of the experiments for evaluation design performance is the washing experiment. In washing experiment different food dyes and blood are injected to the channels and washed with PBS to see the remaining color inside channel. Also this

washing experiment determines the required amount of fluid for washing and how many times channels should be washed in order to get a clean channel.

For washing test 2 experiment is designed, channels are filled with yellow and green dye and blood. 50 µL and 100 µL of PBS are manually pipetted 3 times to the channels in order to wash them. After each washing a photographic image is taken and the clearness of chip is empirically observed. It has been assumed that for 50 µL PBS 3 times wash is enough to get clear channel and for 100 µL PBS 2 times is enough. The washing steps are given in Figure 6.48 and Figure 6.49.

Channels are fully functional and manual pipetting is a convenient method for filling and washing the channels.

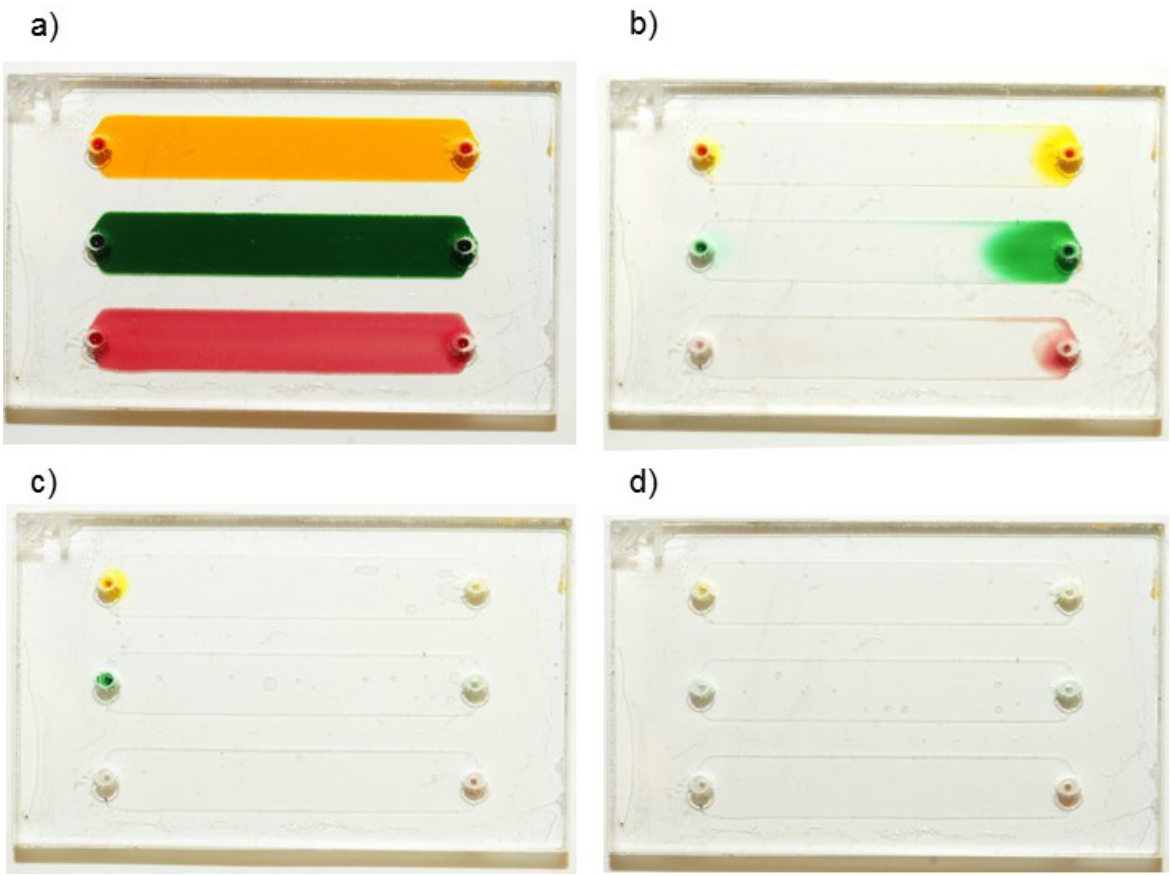

Figure 6.48 Washing test of channels, a) the microfluidic chip channels filled with yellow and green food dye and blood from top to bottom. b), c) and d) are first, second and third washing steps respectively. For each washing step 50 µL of PBS is used.

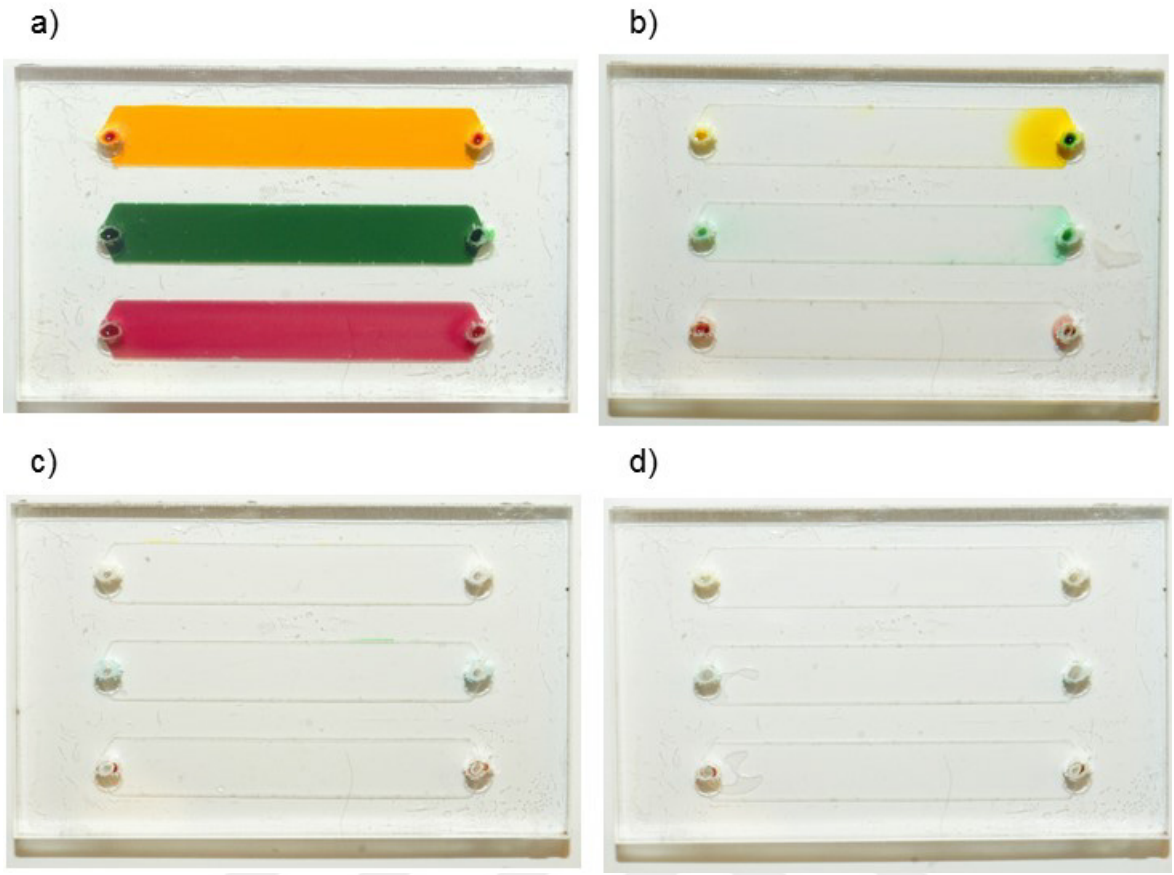

Figure 6.49 Washing test of channels, a) the microfluidic chip channels filled with yellow and green food dye and blood from top to bottom. b), c) and d) are first, second and third washing steps respectively. For each washing step 100 µL of PBS is used.

6.2.2 Optimizing surface functionalization

The idea of surface functionalization is influenced and modified from [66, 164]. The main difference is 3MPS silanization explained in section 6.1.2.1. Where in the above studies the silanization applied after completion of chip. 3MPS solution is dissolved in ethanol and channel walls are made from a double sided adhesive, while 3MPS silanization ethanol degraded the DSA from channel walls. Degradation lowers the capture efficiency because channel surface is contaminated.

In order to eliminate that effect surface functionalization is changed and silanization is applied to glass slide alone and after silanization glass slide is attached to DSA+PMMA in order to make an intact microfluidic chip.

6.2.3 Cell capturing performance

After the incubation of whole blood in the channels, CD4+T cells are captured on the functionalized glass surface and then cells are stained. Whole blood incubation is shown in Figure 6.11.

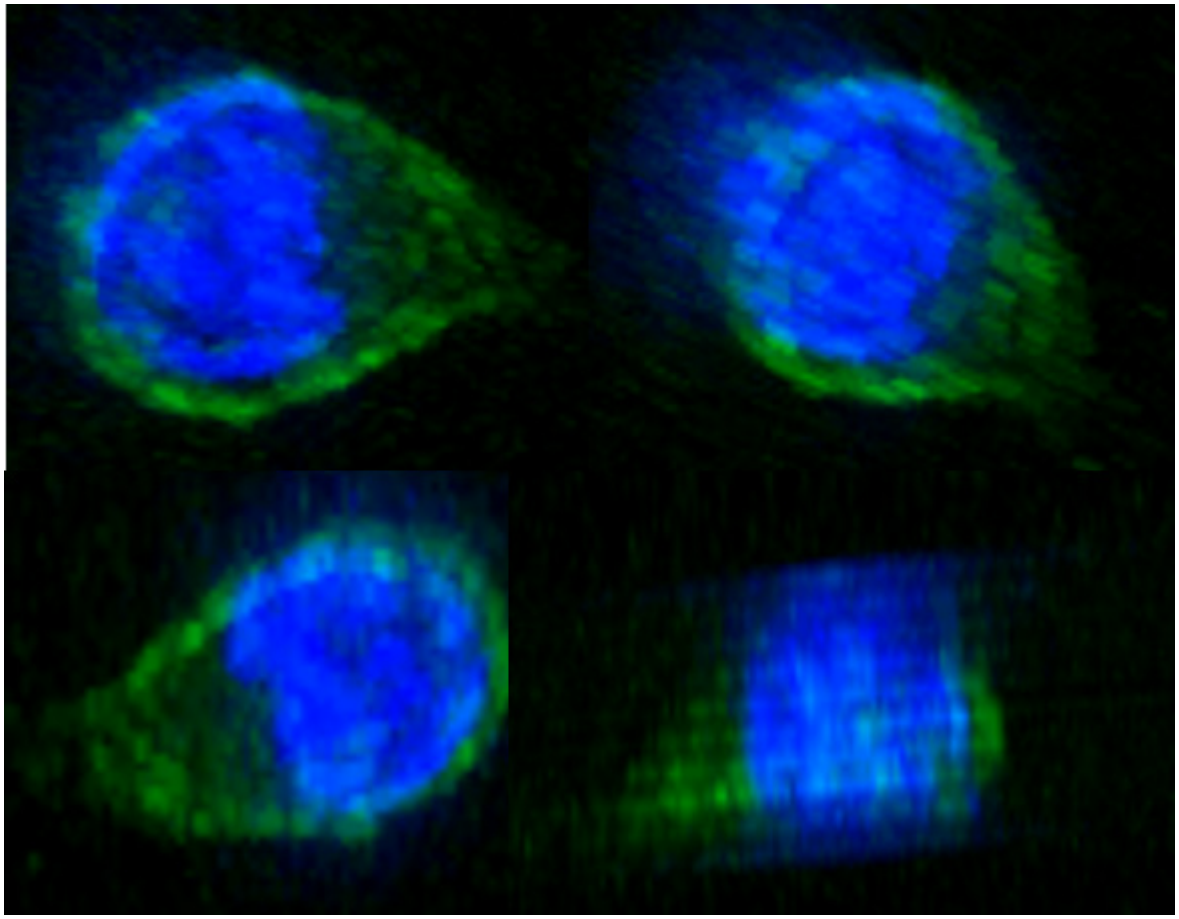

Figure 6.50 A captured CD4+T cell in a channel, image taken by a high quality 3D fluorescence microscope. Blue indicates the nucleus and green stains outside wall of the cell. The images are for different angles, one side of the cell is flat because this side is attached to the functionalized surface of the glass slide. (1000x magnification, UV and GFP fluorescent light for different zoom levels, overlapped to give 3D image)

DAPI stains the nucleus of cells and AF488 stains CD4 antigens around the wall of the cells. DAPI excites blue and AF488 excites green. One of the captured CD4+T cell is monitored with a high power digital microscope BZ-X series of KEYENCE

(Itasca, IL, USA), and the output image is shown in Figure 6.50. Also bright field and fluorescence images of a captured CD4+T cell in a channel taken by fluorescence microscope for 1000x magnification are given in Figure 6.51. In Figure 6.52, 100x magnified bright field and fluorescence microscope images are shown, some of the cells are blue stained but they are not green stained so those cells are not CD4+T cells, but they are indeed cells because DAPI (blue) stains nucleus of a cell. Some of the round shape cell like object are available in bright field but they are not stained blue nor green so they are not white blood cells. An UV fluorescence image for the edge of a channel is shown in Figure 6.53. The edge seems very bright and captured cell's nucleus are visible.

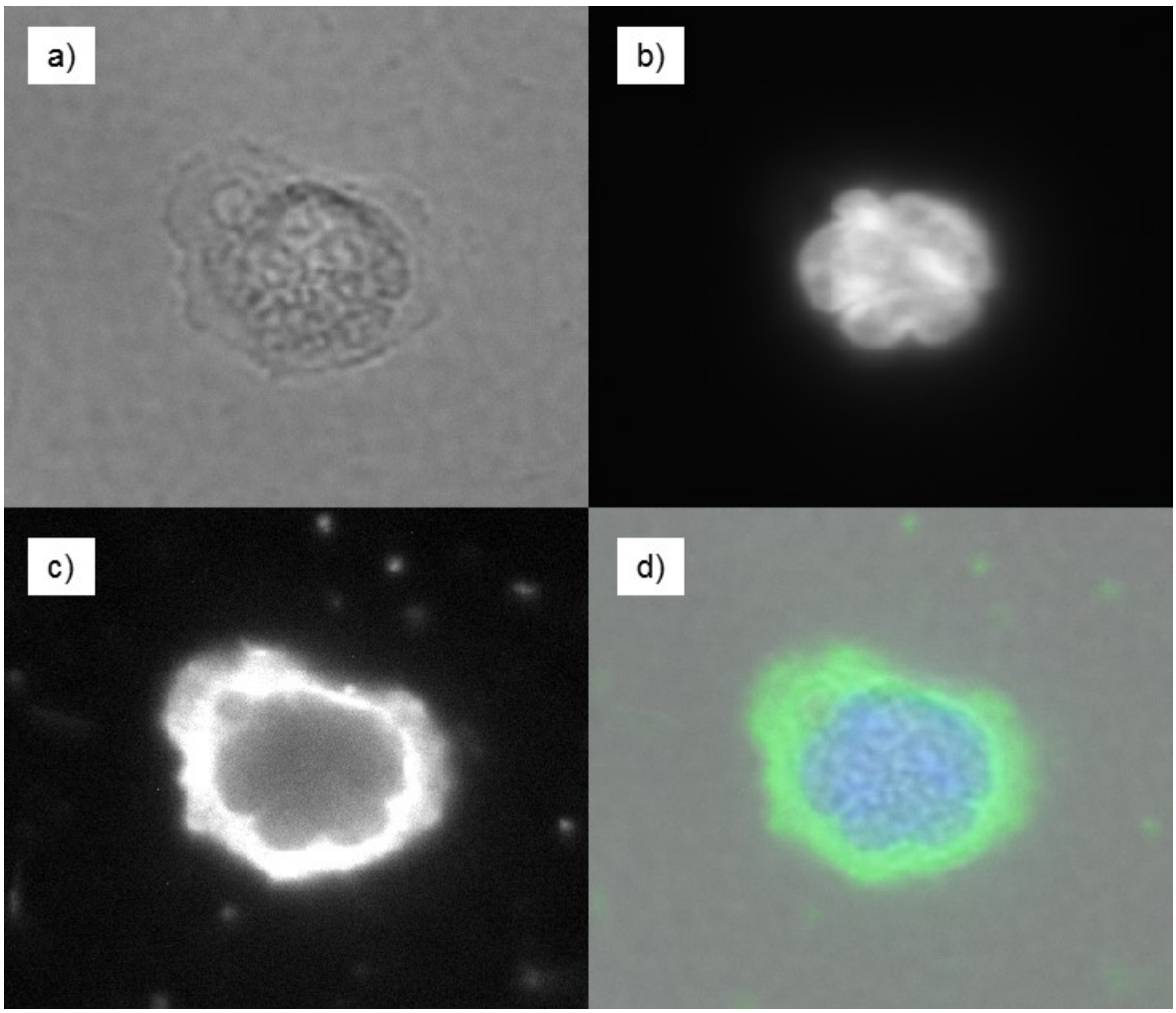

Figure 6.51 A captured CD4+T cell in a channel image taken by fluorescence microscope. Blue indicates the nucleus and green stains outside wall of the cell. a) Bright field image of a cell, b) UV and c) GFP fluorescence image for same cell, d) merge of all 3 images. (1000x magnification)

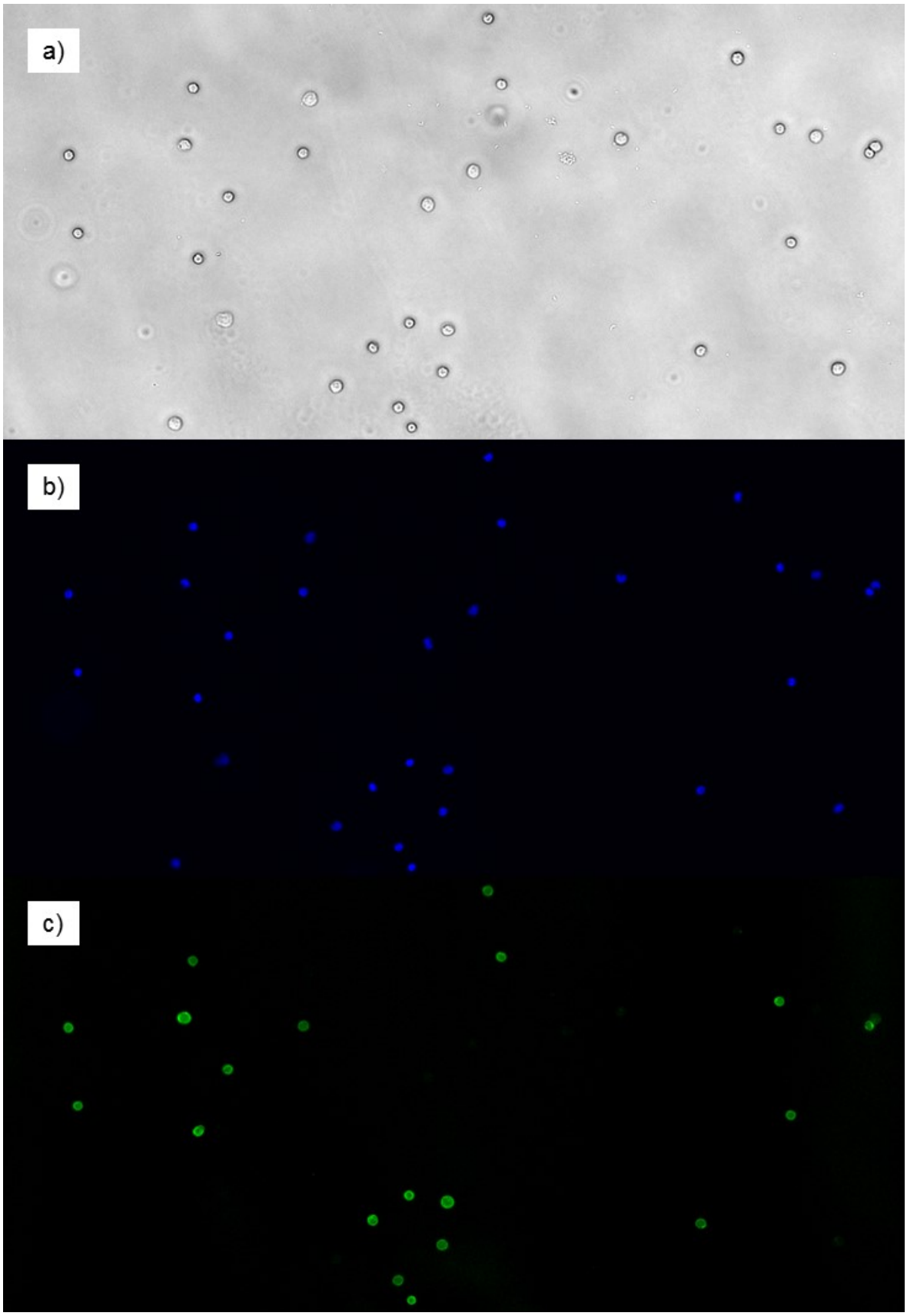

Figure 6.52 CD4+T cells and some WBC in a channel, 100x magnified images. a) Bright field, b) UV filter, c) GFP filter.

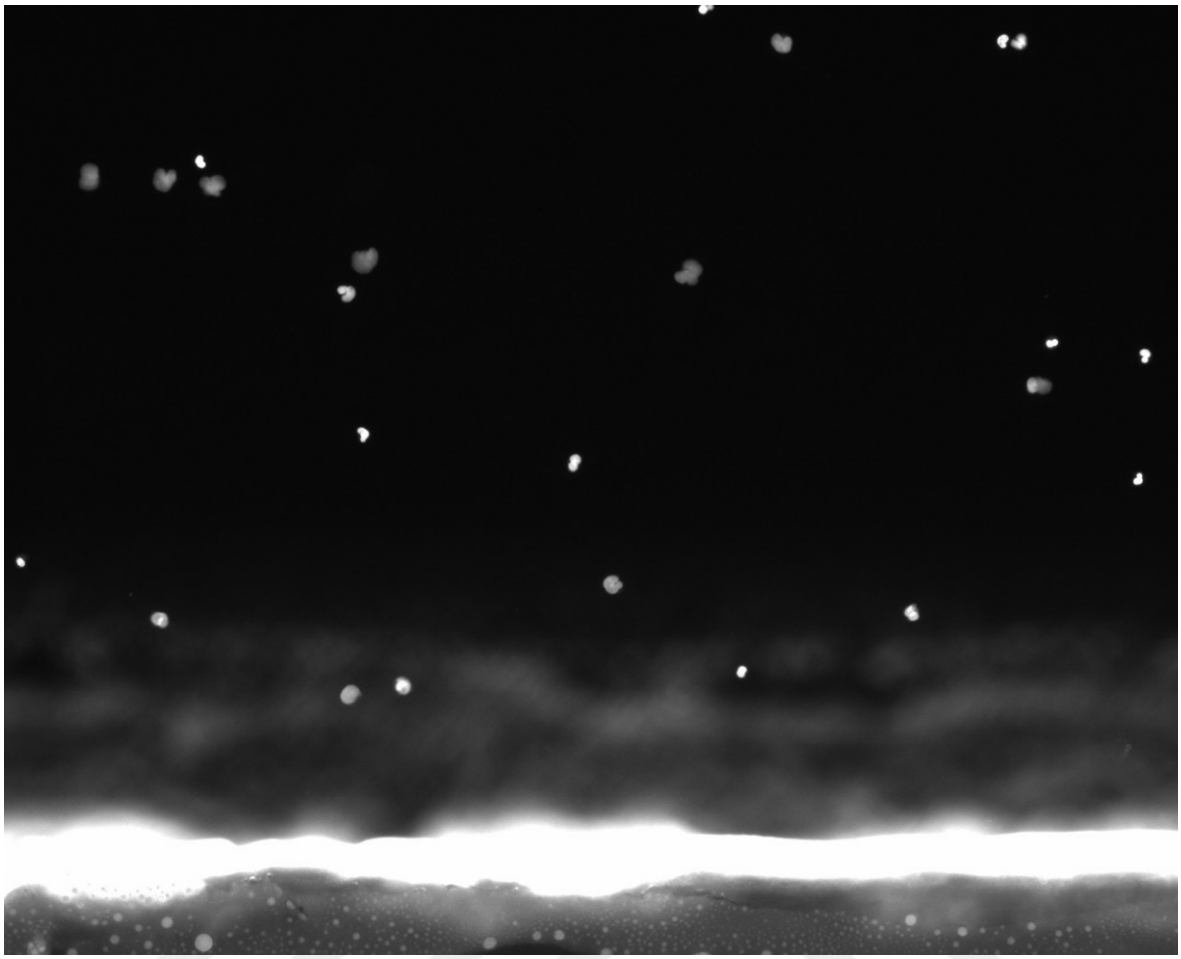

Figure 6.53 A sample image of captured CD4+T cells ate the edge of a channel. Image taken by fluorescence microscope with UV filter. The nucleus of the cell are visible. The edge also very visible, DSA seems to be visible at UV filter.

6.2.4 Cell counting under microscope

In order to evaluate capture performance of CD4+T cell, cells should be count in channels. Since initial concertation of WBC's and prevalence of CD4+T cells in a channel are known, after cell counting of captured cells, performance of capturing CD4+T cells can be obtained.

After staining of cells channels are placed in an inverted fluorescence microscope and bright field and UV and GFP filter images are taken. For one channel and for one filter at 100x magnification 31 x 7 = 217 images are taken. Cell count is applied using those images for both filter. Manual counting of a channel takes at least 4 hours. Sample images are shown in Figure 6.54.

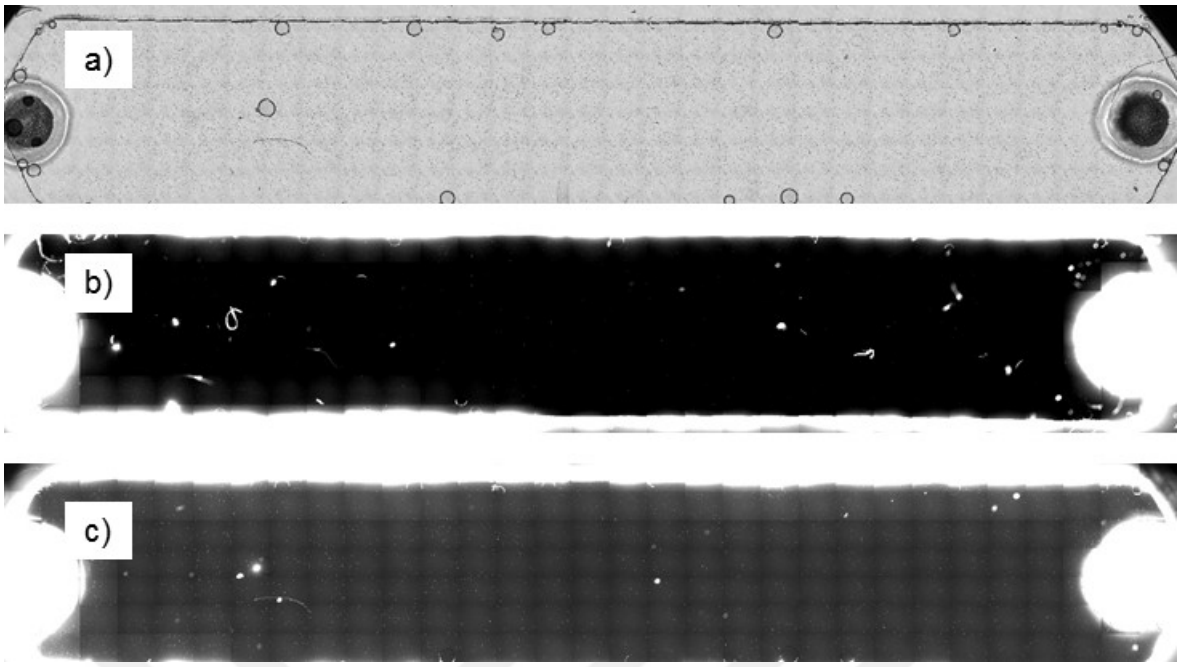

Figure 6.54 Bright field and fluorescence microscope images taken for manual cell counting for a channel. Each group of image is for the same channel and is composed of 31 x 7 = 217 (100x magnified) images. a) Bright field, b) UV filter, c) GFP filter.

Table 6.2 Binary classification test for CD4+T cell counting performance for a sample channel. Green and blue stained cells are counted from microscope images and initial WBC and CD4+T cells pipetted inside the channel are obtained. Other values in the table can be calculated from those values.

	Actual CD4 count	**Actual other cells count**	**Total**
Test CD4 count	A = 11,569 Green	B Blue – Green	A + B = 12,440 Blue
Test other cells count	C CD4 – Green	D WBC – CD4 – Blue + Green	C+D WBC – Blue
Total	A + C = 14,144 CD4	B+D WBC – CD4	A + B + C + D = 101,030 WBC

After counting of cells performance values are evaluated. An example is given in Table 6.2. Blue and Green stained cells are counted in a channel and initial cell

count of WBC's and CD4+T cells are obtained using the method explained in section 6.1.3. These values are used in the binary classification test table and unknowns are calculated using these values. Then performance criterions are evaluated which are given in Table 6.3.

Table 6.3 CD4+T cell counting performance results for the sample channel.

$Capture\ Accuracy\ (\%) = 97\%$
$Capture\ Specificity\ (\%) = 99\%$
$Capture\ Sensitivity\ (\%) = 82\%$
$Capture\ Precision\ (\%) = 93\%$

For three freshly prepared channels capture performances are evaluated, capture accuracy, specificity, sensitivity and precision are 96.1 % ± 1.2 %, 98.8 % ± 0.2 %, 79.9 % ± 7.9% and 91.2 % ± 1.7 % respectively. The bar graphs are given in Figure 6.55.

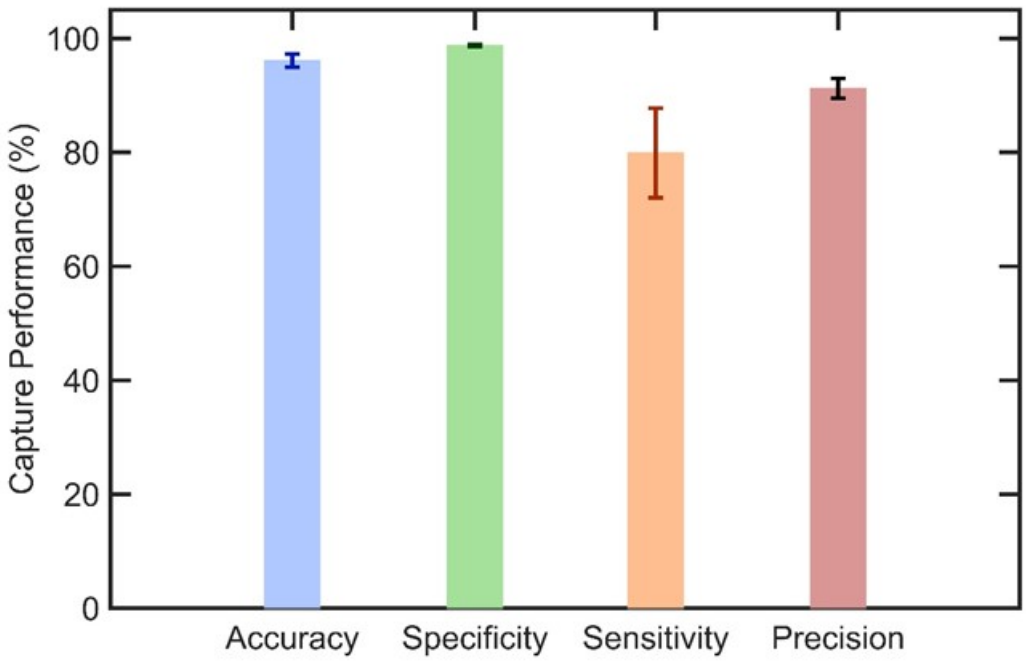

Figure 6.55 CD4+T cell capture performance evaluation results for freshly prepared samples, error bars are standard deviation results.

6.2.5 Cell counting using lensless wide-field microscopy system and cell counting program

In order to count CD4+T cell a selectively cell capturing microfluidic system is developed and the automatic counting can be done using lensless wide-field microscopy system and cell counting algorithm.

Channel images are taken using the developed lensless wide-field microscopy system by simply placing the channel on top of the sensor. Since channel is wider than the CMOS image sensor size the channels should be shifted and images are taken in every shift. Although 4-5 images are enough to cover all channel in this experiment 7 images are taken. Images are connected together by MATLAB®. While gathering images small pen markers are used to as touchstones. The connected images are shown in Figure 6.56, the raw connected images are shown in a), then images are cropped to get only the channel as shown in b) and the active area where manual and automatic counting is applied is highlighted in c). The effective area is the rectangular shaped area without holes which is almost 4 mm x 26 mm.

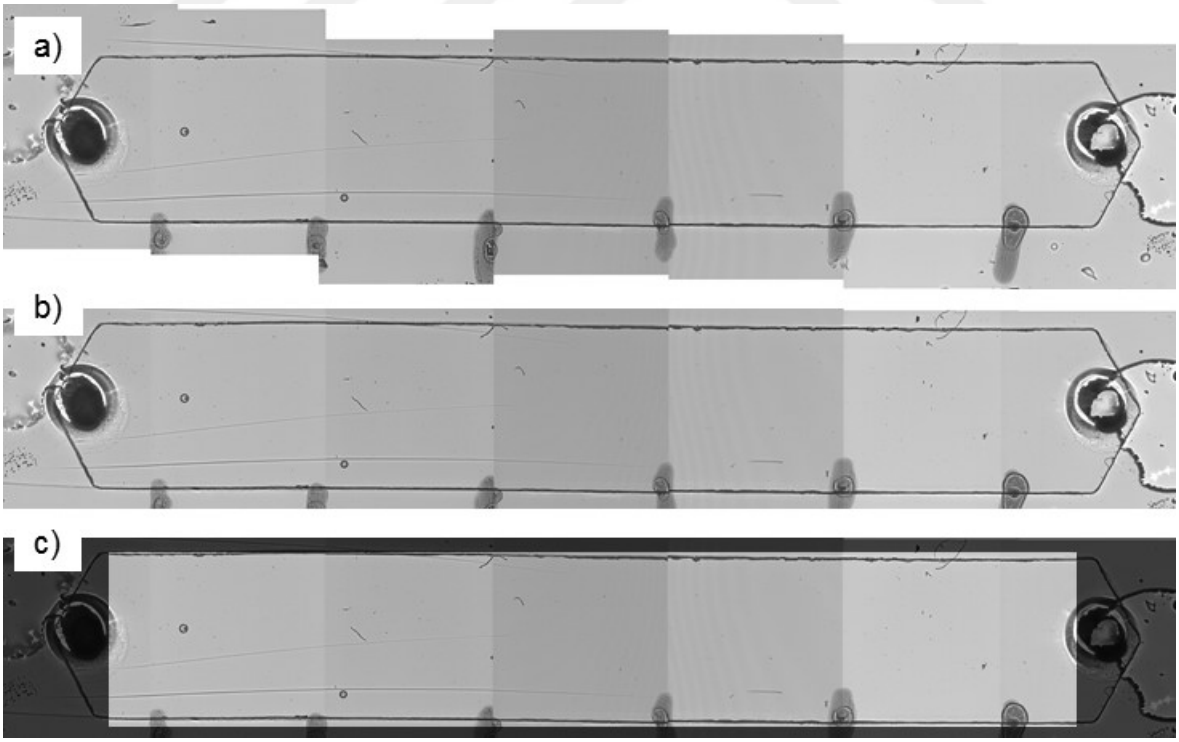

Figure 6.56 Full channel images gathered using lensless wide-field microscopy system. a) Connected images, b) they are cropped to get only the channel, c) the active area where the manual and automatic cell count is applied, is highlighted.

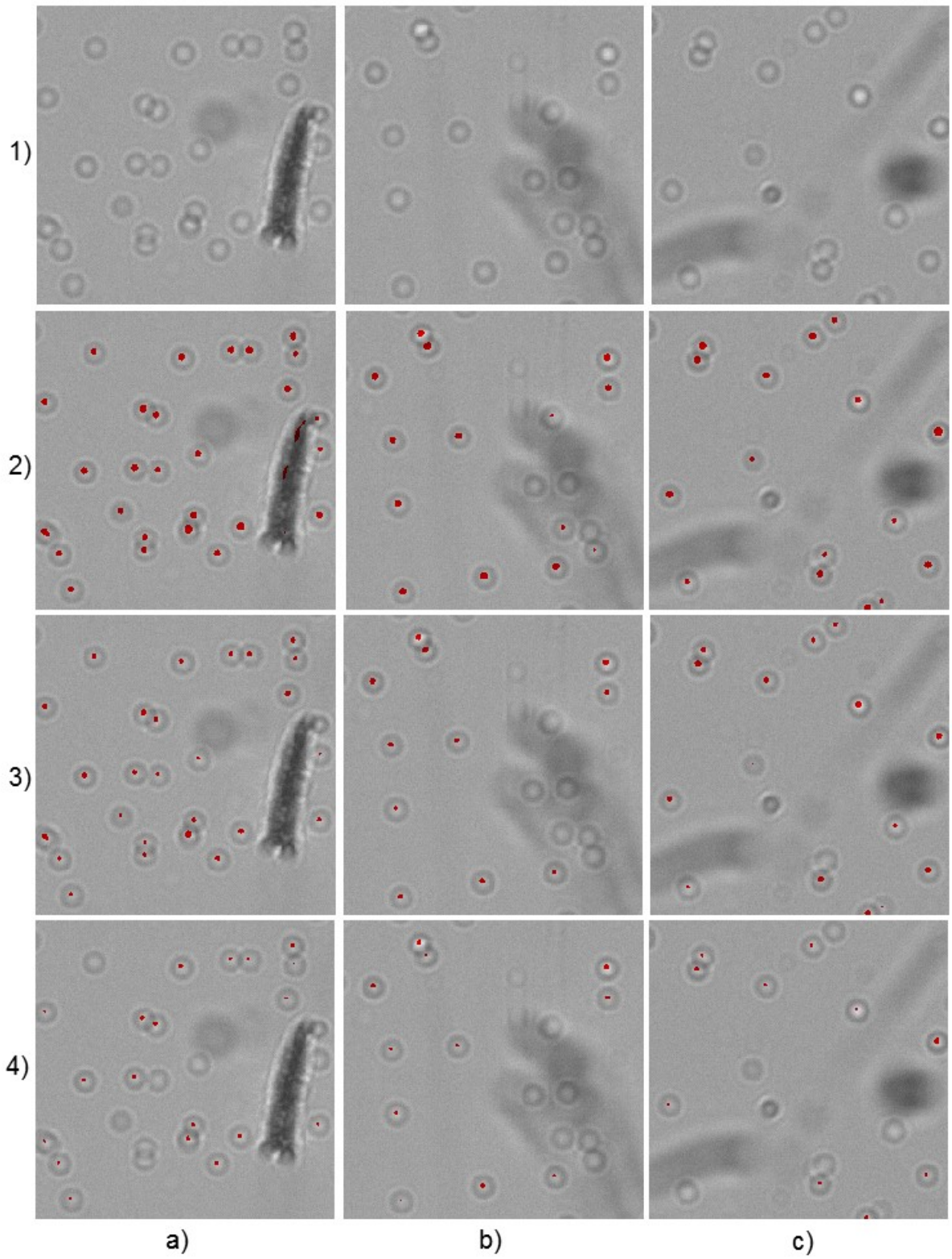

Figure 6.57 Examples of empirically defining threshold process. 3 different location inside a channel is used for detecting cells. 1) Original image, 2), 3), and 4) are showing detected cells (red) for different threshold values of 750 (a.u.), 1000 (a.u.) and 1250 (a.u.), respectively. Cell counts are given in Table 6.4.

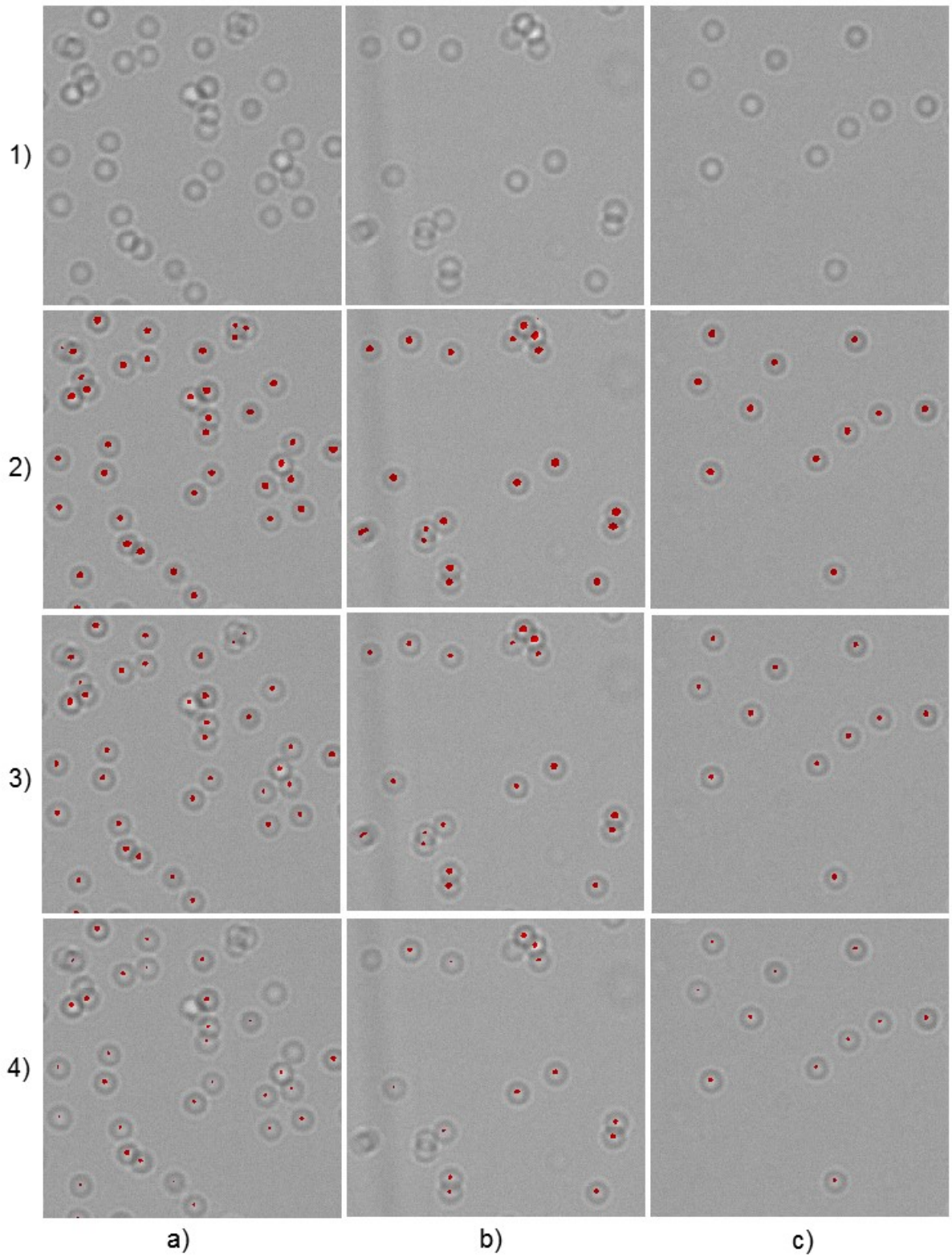

Figure 6.58 Examples of empirically defining threshold process. 3 different location inside a channel is used for detecting cells. 1) Original image, 2), 3), and 4) are showing detected cells (red) for different threshold values of 750 (a.u.), 1000 (a.u.) and 1250 (a.u.), respectively. Cell counts are given in Table 6.4.

A cell counting algorithm for shadow images of cell is developed and explained in details in section 6.1.6. There are 3 parameters to be used in cell counting, the low and high pixel values used for adaptive linear histogram stretching and threshold value for detection of cells. These parameters are empirically and statistically estimated. The images and their histograms are statistically examined in detail and the gray coded data range is estimated. Histogram stretching is based on that estimation and low and high pixel value parameters depend on not to lose cell information.

Threshold is also estimated empirically and statistically. The highest value for correlation cannot exceeds the autocorrelation of averaged model cell for defined histogram stretching parameters. So threshold is compared to the highest value of the autocorrelation of averaged model cell and also empirically defined by checking some of the cell detection performance. An example is shown in Figure 6.57 and Figure 6.58.

Table 6.4 Manual and automatic cell count from lensless wide-field microscope images in Figure 6.57 and Figure 6.58. Different threshold values are tested in terms of detection performance. Actual cell count is performed by user and cells are counted manually.

Cell Count		**Image**	**Figure 6.57**			**Figure 6.58**		
			a)	**b)**	**c)**	**a)**	**b)**	**c)**
Actual Cell Count		**1)**	26	17	16	39	20	11
Threshold Value (a.u.)	**750**	**2)**	30	14	16	39	20	11
	1000	**3)**	26	11	16	37	19	11
	1250	**4)**	20	11	11	32	14	11

In order to determine threshold value empirically different set of images with different debris, artifact and cells on top of each other are chosen as in Figure 6.57 and Figure 6.58. Cells in those images are counted manually, and then for different threshold values the detection performance are evaluated and best threshold in between the statistical range is chosen.

From Table 6.4 actual cell count values and automatic cell count values for different thresholds are compared. The threshold value range is arranged according to the possible highest value which can be determined from autocorrelation of averaged model cell image. Then three alternatives can be tested. For almost all images high threshold is too big and there are many misses. For the first image at lowest threshold value there are many false positives, the debris is also counted but for middle threshold value all the cells are counted. For the second image the contrast of a particular location is quite different from the rest and cells in that location cells are not countable, and lowest threshold seem better. For third image the first two threshold values seem better. For the fourth image the lowest threshold has detected all cells, the second one misses some of the cells which are very close to each other. For the fifth image lowest threshold has again false positives. In the last image, cells are quite visible and separated from each other and there are no debris. Therefore, all cells are counted successfully for all threshold values.

To sum up even if there are some misses the middle threshold value seems better because there are no or very few false negatives it can be used as a threshold value.

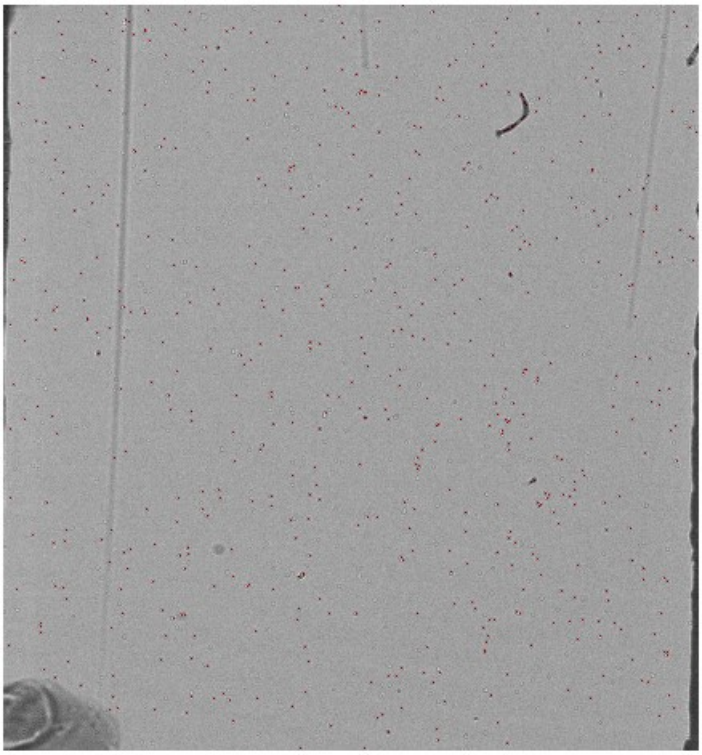

Figure 6.59 One out of five part of a channel is counted using proposed algorithm. 920 cells (red) are counted when threshold was 1000 (a.u.).

For a part of a channel with 4.25 mm x 4.5 mm area shown in Figure 6.59, cell counting algorithm is applied. Total cell count is 920 and counting takes just second.

For a particular cell counting after adaptive histogram stretching parameters and threshold value are defined and cells can be automatically counted. Captured CD4+T cells in channels are used for counting, DAPI fluorescent images are counted as actual cell values and then algorithm is applied and results are given in Table 6.5.

Table 6.5 Automatic cell count using the developed algorithm from lensless wide-field microscope images of captured CD4+T cells in developed microfluidic chips channel. Actual cell count is the manual count of blue stained cells under fluorescence microscope.

Channel	Actual Cell Count	Automatic Cell Count	Difference (%)
1	12326	12646	2.59
2	5366	5467	1.88

6.3 Conclusion

CD4+T cell count has a wide range of applications, e.g. in chemotherapy, transplant patient and AIDS therapy monitoring. [48, 167] Especially for AIDS therapy CD4+T cell counts are used for monitoring the need and performance of ART. Currently especially in low resource settlings half of HIV infected people cannot access ART and one of four person who are getting ART therapy starts therapy late. [89] This can be a result of early death and spread of infection. A practical, easy accessible POC CD4+T cell count can be a solution for those problems.

In this part of the thesis a POC CD4+T cell count biosensor is advised and tested. First a microfluidic chip is fabricated. The fabrication is practical and does not need any lithographic techniques. The fluid flow of chips are tested and microscope images showed that channels are intact. Second the surface functionalization for capturing CD4+T cells is implemented. The specifically capture of cells are reported. Third cell count under fluorescence microscope is performed and statistically analyzed. It is shown that capture accuracy specificity, sensitivity and precision are

96.1 % ± 1.2 %, 98.8 % ± 0.2 %, 79.9 % ± 7.9% and 91.2 % ± 1.7 % respectively. Fourth a lensless wide-field microscope is designed and implemented. Successful shadow images of captured cells are obtained. Finally a novel cell counting algorithm is developed and tested.

Biosensor and POC cell counting system showed good performance and can a battery operated. So it can be used as a practical POC CD4+T cell counting for AIDS and ART monitoring.

7 ENGINEERING A METHOD FOR INCREASING SHELF LIFE AT ROOM TEMPERATURE OF A MICROFLUIDIC POC BIOSENSOR

Microfluidic-based devices for CD4+T cell counts and viral load measurements can be used in point-of-care (POC). [48, 53, 67, 168-171] However, in order to prevent the capture antibody denaturation and functional loss, these devices should be stored at temperatures as low as 4–8 ºC. [172, 173] To transport and store the biomaterials in cold chain is costly. Therefore, the assay cost is also increased. Also low resource settlings may not have this cold storage facility. In order to solve this problem, multi-layer immuno-functionalized microfluidic devices could be protected for settlings without cold storage facility.

The need for multilayer immuno-functionalized surface biopreservation and its differences from protein biopreservation are explained in detail in section 1.5.

In this part of thesis a method to preserve the multilayer immuno-functionalized surface in microfluidic channels for selectively capturing CD4+T, is designed. This method uses trehalose as a sugar solution for biopreservation at refrigeration-free conditions. The biopreservation mechanism theories of trehalose is explained in section 1.5.

In order to develop and test the preservation method, first, 30 CD4+T cell capturing chips are produced and surface functionalization is applied as explained in section 6.1.1 and 6.1.2, respectively. Second, stabilization using trehalose is applied. Third, chips are dried according to developed method and packaged. Finally capture performance of chips are tested over time. In this way longer term storage for CD4+T cell capturing system can be possible at room temperature.

7.1 Materials and Methods

In this section the designed and used materials and methods are explained.

7.1.1 Functionalized groups stabilization method

In order to stabilize protein structures in functionalized surface, trehalose is used as a preservative. Trehalose has the ability to preserve protein structures. After the anti-CD4 antibody was incubated, the surface functionalizing is finished and device

is ready for preservation. So 2.5% (w/v) trehalose dissolved in DI water is prepared. Than trehalose solution is pipetted to the channels and incubated for 30 min. In order to left trehalose on the surface the water should be remove by drying. The method for trehalose treatment is depicted in Figure 7.1. Trehalose is obtained from Sigma-Aldrich Corporation (Saint Louis, MI, USA), (D-(+)-Trehalose dihydrate, T9531).

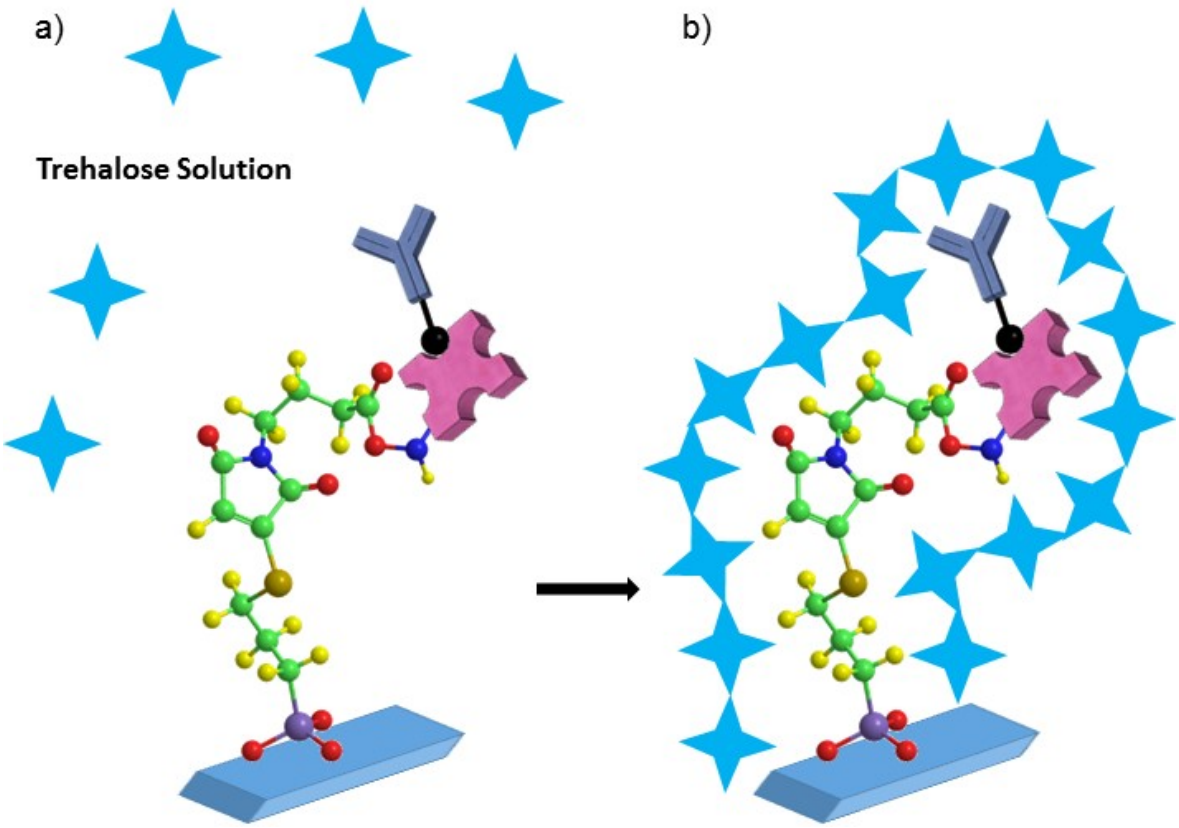

Figure 7.1 Functional groups stabilization, a) trehalose injection to channels b) after drying of DI water trehalose crystallization.

7.1.2 Microfluidic chip drying methods

In order to left the trehalose inside the channel to crystalize water inside the channel should be dried. Main methods for drying can be heating and vacuuming (desiccation). Those methods can be used together. Chips should be dried fast without applying too much heat. So all those methods are tested in order to get the fastest method.

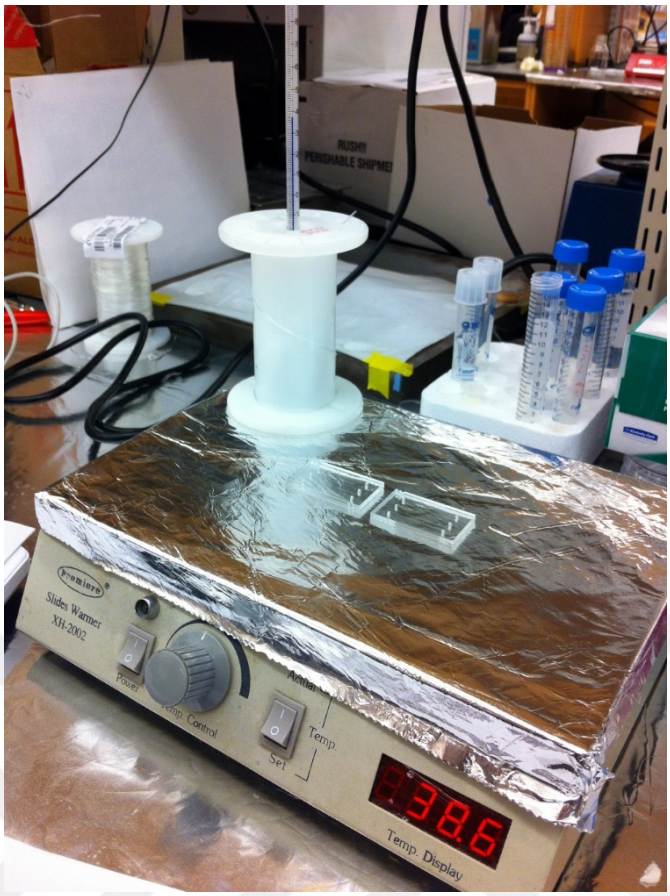

Figure 7.2 Microfluidic chip drying by heating experiment set up. Slide warmer is used as a heather. Thermometer is placed in order to measure exact temperature on the surface.

Evaporation of water inside the channel is first tested by heating using a hot plate (Premier Slide Warmer, XH-2002, LabScientific, Highlands, NJ, USA). Chips are placed on top of the slide warmer and the temperature is set to 37ºC. This temperature is chosen because this temperature is assumed not to be harmful for protein structures. But even the temperature is set to 37ºC the surface of the hot plate becomes cooler because of air circulation. So using a thermometer surface of hot plate is measured and temperature is increased to get 37ºC at the surface. The experiment set up is shown in Figure 7.2.

To evaluate the drying of the chip, images of the chip are taken according to time. From those images wet and dry areas are computed digitally by turning them to black and white. ImageJ computer program (National Institute of Health) is used for that. First contrast is increased and thresholding is applied to get binary image. Histogram of the images are obtained to get white and black pixel count. Black pixel

count divided by total area gives the dry area ratio. Sample images for the method is given in Figure 7.3.

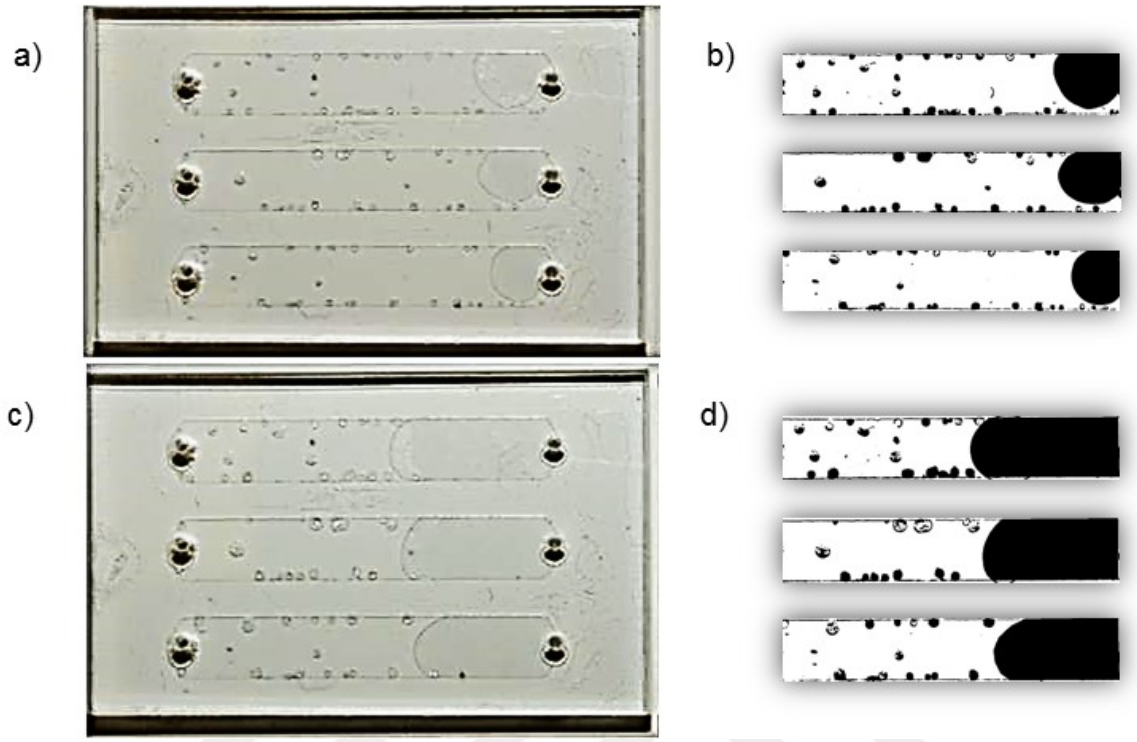

Figure 7.3 Drying chips images for the method of heating at 37ºC. a) Chip image at second hour of heating b) the areas showing the dry and wet parts of channels. c) Chip image at fourth hour of heating d) the areas showing the dry and wet parts of channels. Black is dry, white is wet.

For the method of drying by vacuuming a desiccator or a vacuum oven can be used. The pressure of vacuuming is around 600 mmHg. Chips simply placed in desiccator of oven at room temperature and vacuuming is applied. Figure 7.4 shows a desiccator with chips inside. The sample drying chip and dried areas for fourth hour of experiment are shown in Figure 7.6 c) and d).

For the method of drying by heating and vacuuming together the vacuum oven (Isotemp Vacuum Oven Model 280A, Fisher Scientific, Dubuque, IA, USA) shown in Figure 7.5 is used. The pressure of vacuum is set to 600 mmHg and heat is set to 37ºC. The sample drying chip and dried areas for second hour of experiment are shown in Figure 7.6 a) and b).

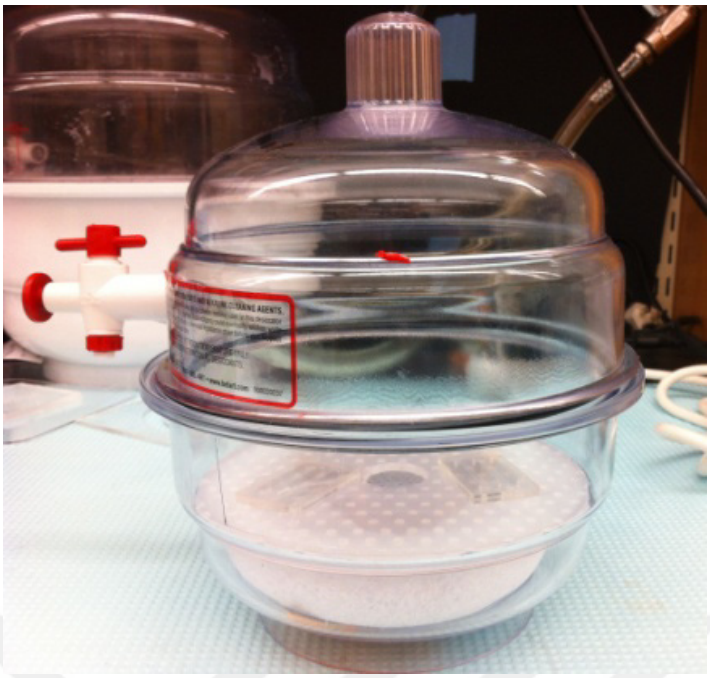

Figure 7.4 The desiccator for drying of chips using vacuum.

Figure 7.5 The vacuum oven for drying of chips, vacuum pressure is set to 600 mmHg and temperature is set to 37ºC.

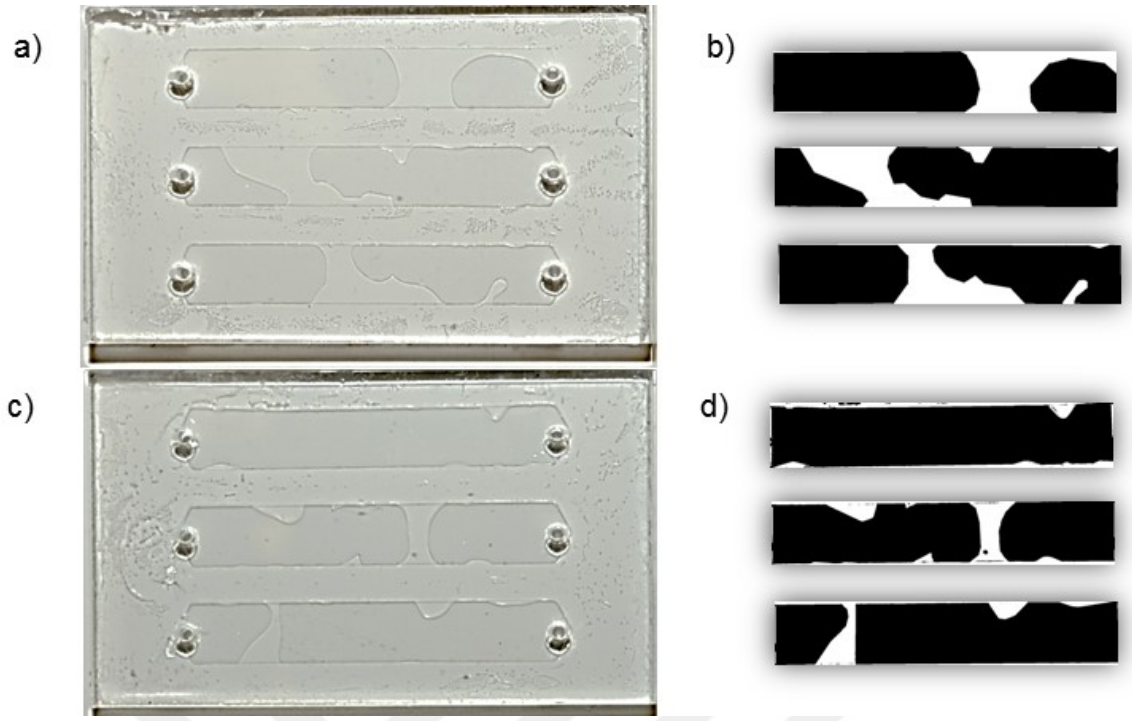

Figure 7.6 Drying chips images for the method of heating at 37ºC and vacuuming with a pressure of -600 mmHg together and just vacuuming. a) Chip image at second hour of heating and vacuuming together b) the areas showing the dry and wet parts of channels. c) Chip image at fourth hour of just vacuuming d) the areas showing the dry and wet parts of channels. Black is dry, white is wet.

In order to preserve chips for longer the channels should be completely dried so removing some of the fluid inside channel mechanically is proposed. So centrifuging the chips is used. A benchtop centrifuge (Fisher Scientific Mini Centrifuge, 05090-100, Dubuque, IA, USA) is used at 6600 rpm for 5 seconds. It has been observed that almost 90% of the fluid has been removed from the chips.

As a fourth method heating and vacuuming is applied after centrifuging in order to get the fastest drying. In the benchtop centrifuge while the chip is settled is shown in Figure 7.7. The chip is settled to the inside chamber where normally small laboratory tubes are stand.

Removing water from the channel without pumping air inside seem better to not to apply so much pressure to the functionalized surface.

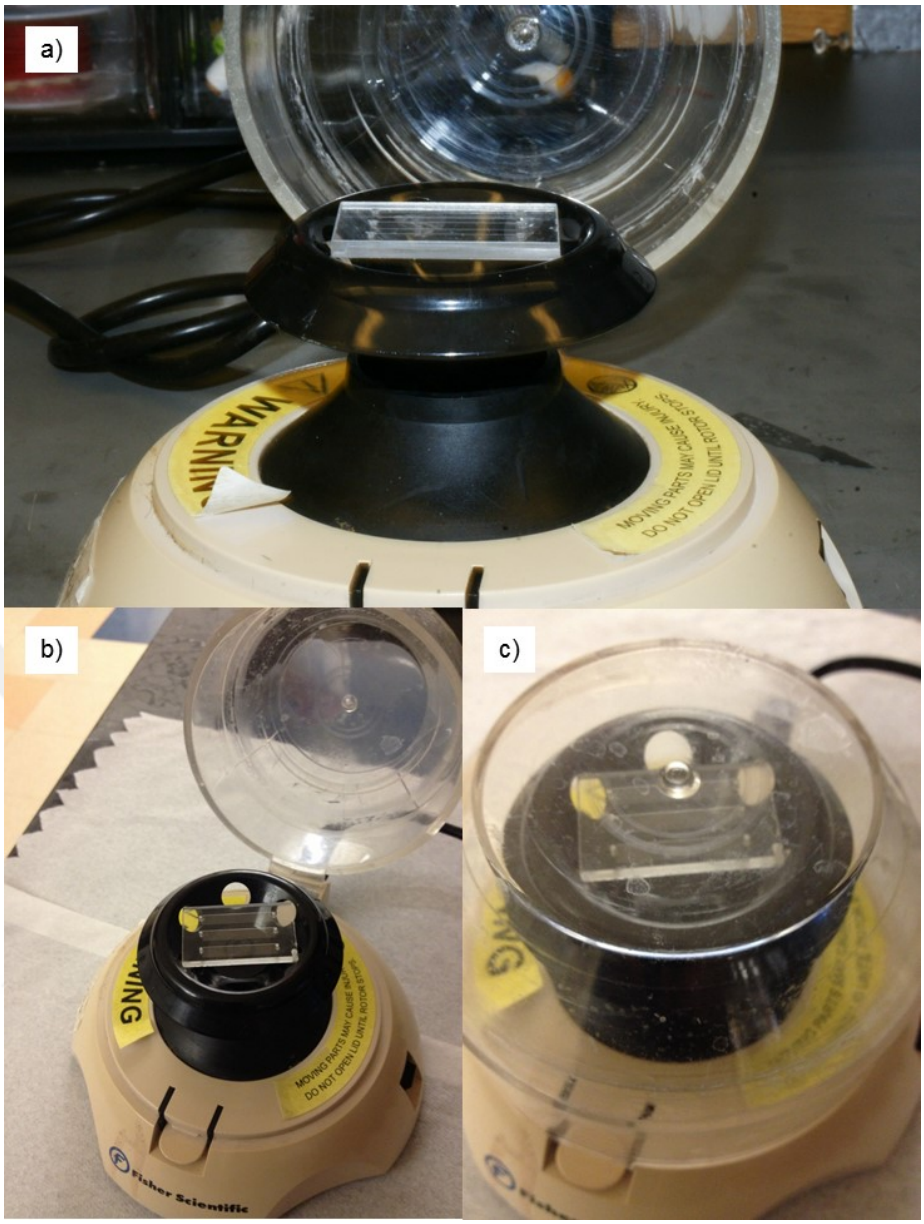

Figure 7.7 Benchtop centrifuge used for removing excessive fluid inside the channels. a) Side view and b) top view of chip inside the centrifuge and c) chamber is closed for centrifuging.

7.1.3 Microfluidic chip preservation method

After the channels in chip are completely dried chips are ready for storing. Chips should store clean and should be kept away from humidity. Vacuum sealing is a sufficient way of storing the chips. A vacuum sealer (FoodSaver® Vacuum Sealer H-340 Uline, Pleasant Prairie, WI, USA) for storing food is used. Vacuum sealer sucks air inside the bag and closes it by burning the bag. Vacuum sealer is shown in Figure 7.8.

Figure 7.8 Vacuum sealer, vacuuming and sealing a bag with a chip and a bag of drying agent.

The chips are packed with humidity absorber silica gels. Silica gel Rubin drying bags (72811, Sigma-Aldrich Corporation, Saint Louis, MI, USA) are used. One of those bags contains 5 gram drying agent. 30 gram of drying agent can absorb 3 gram of water for 20% humidity and 6 gram for 40% humidity at room temperature. A bag with 5 gram of drying agent and a chip are vacuum sealed together to be stored. The sealed bag is shown in Figure 7.9.

Figure 7.9 A functionalized chip, vacuum sealed with a bag of drying agent, ready for storing.

7.2 Experiments and Results

In order to test the shelf life of CD4+T cell counting system a preservation method is applied. And test results are explained in this section.

7.2.1 Performance of microfluidic chip drying methods

In order to use the best drying method all methods are compared in terms of dried channel area according to time. Four methods are developed, heating, vacuuming, heating while vacuuming and centrifuging than heating while vacuuming as explained in section 7.1.2. Dried areas on chip is evaluated on images of channels by using a computer program ImageJ. Dried and wet areas have different contrasts and using that idea images are turned to binary images and black represents dried area and white represents wet area. The methods are also explained in section 7.1.2. Dried area versus time graphs for different methods are given in Figure 7.10, Figure 7.11, Figure 7.12 and Figure 7.13.

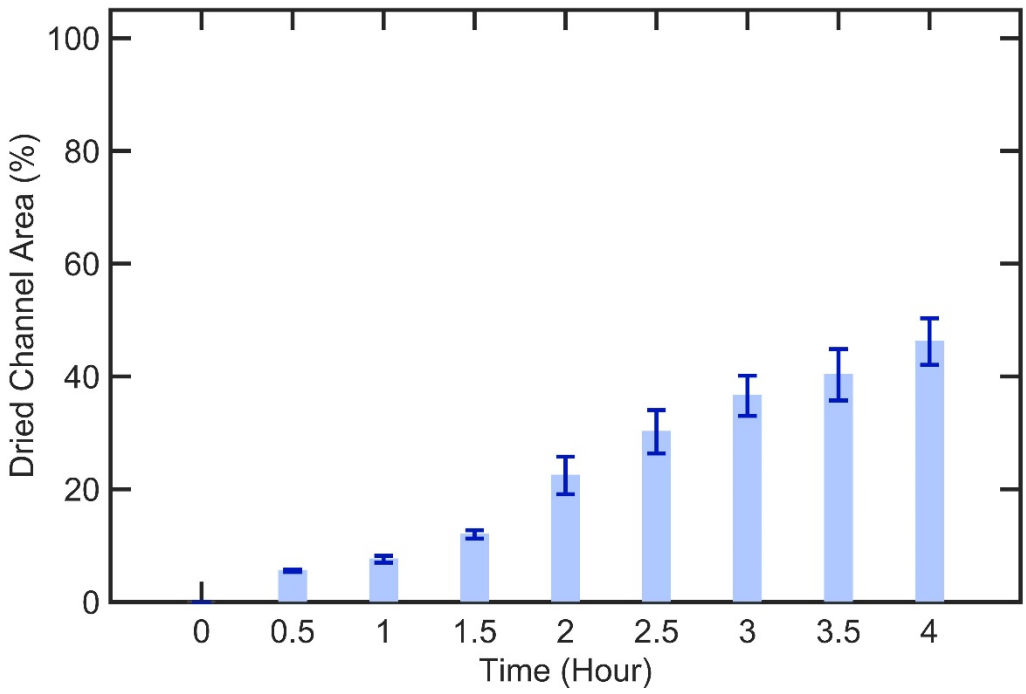

Figure 7.10 Drying the channels by heating. Dried channel area according to time, error bars are standard deviation results (n=3).

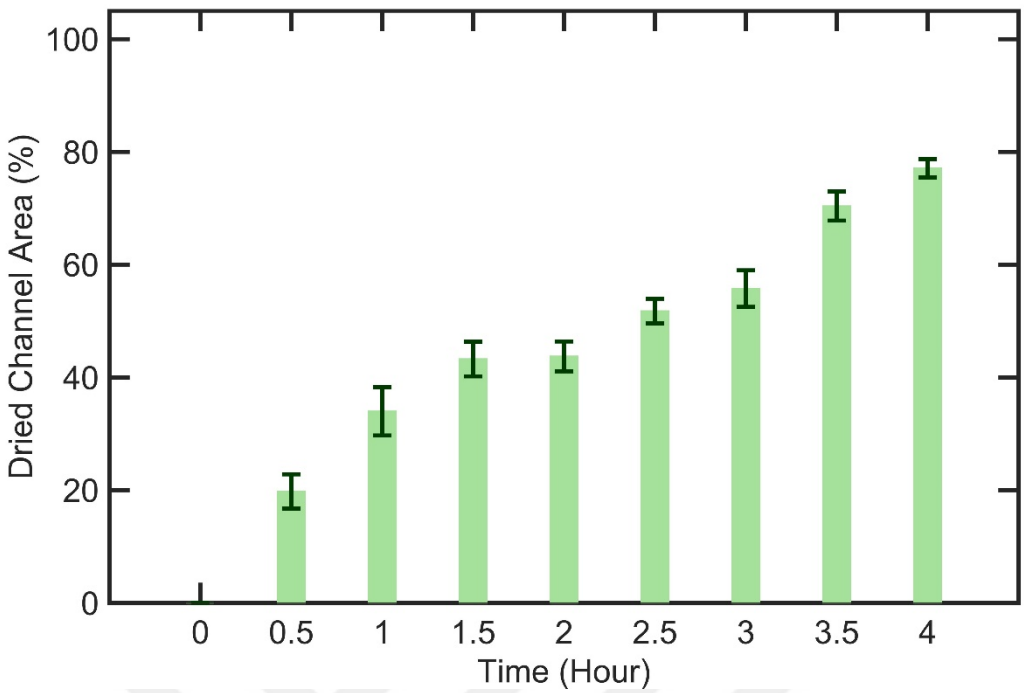

Figure 7.11 Drying the channels by vacuuming. Dried channel area according to time, error bars are standard deviation results (n=3).

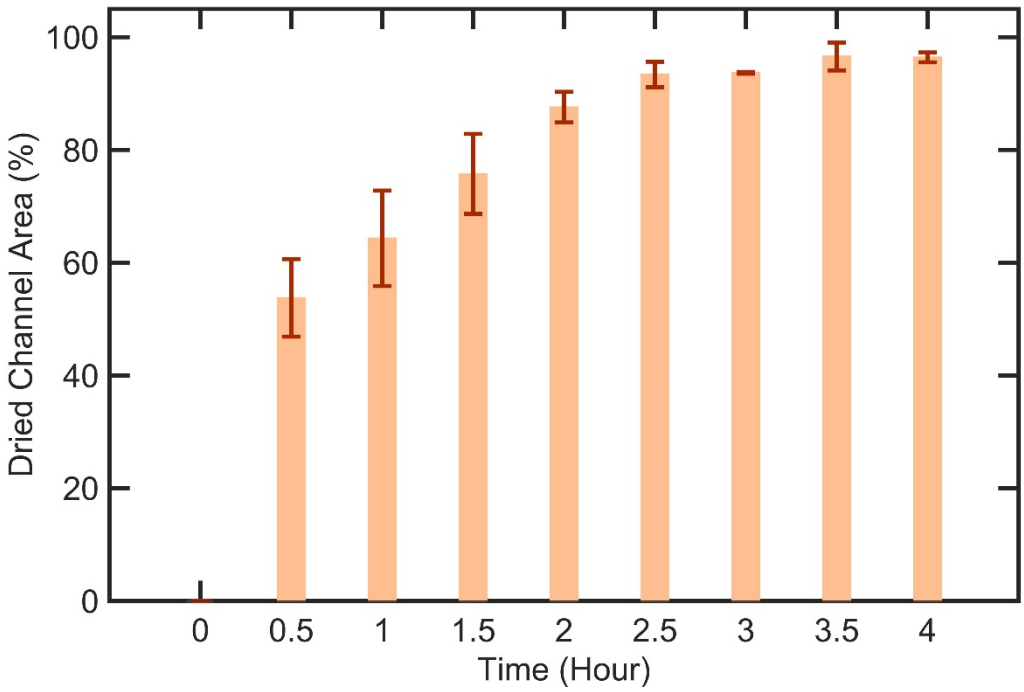

Figure 7.12 Drying the channels by heating and vacuuming together. Dried channel area according to time, error bars are standard deviation results (n=3).

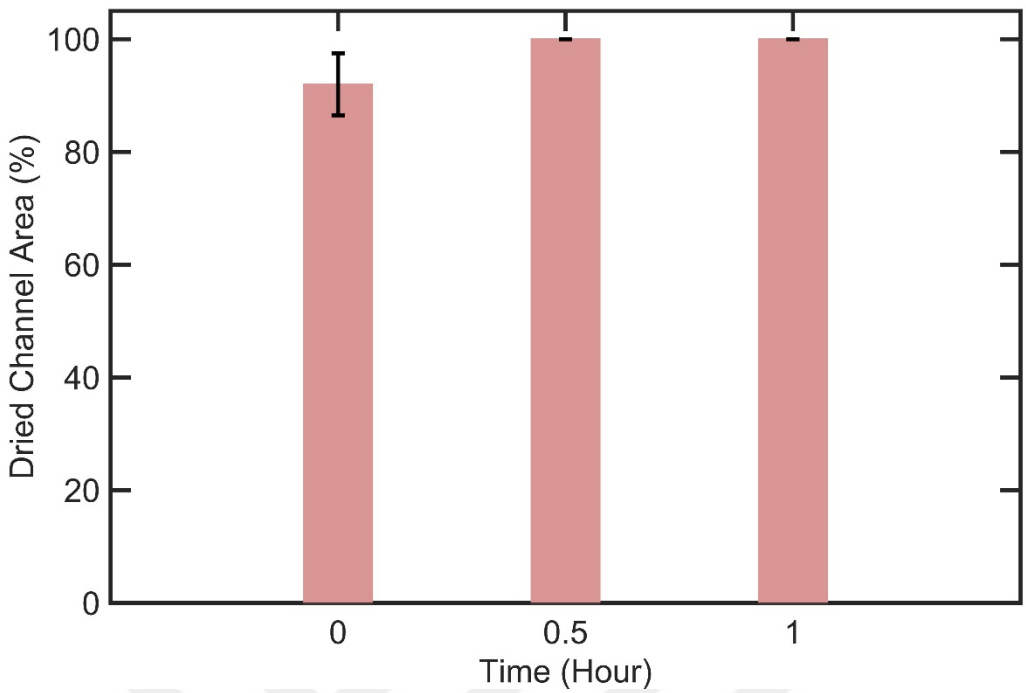

Figure 7.13 Drying the centrifuged channels by heating and vacuuming together. The excessive amount of fluid is already removed from the channel by centrifuging. Dried channel area according to time, error bars are standard deviation results (n=3).

From the graphs comparing first 3 methods. Just heating and vacuuming, channels cannot be dried even after 4 hours. By using those together channels are almost dried after 4 hours. So between first 3 methods heating and vacuuming together has the best performance for drying channels. In order to get a complete and fast drying 4th method is best solution. Since it is used centrifuging followed by heating and vacuuming together. The channels are dried after 30 min. For drying of channels 4th method is chosen.

7.2.2 Cell capturing performance of stabilized microfluidic chips

For testing the shelf life performance of CD4+T cells detection microfluidic chips, their capture statistics are evaluated for 6 months. More than 30 microfluidic chip samples with 3 channels are functionalized, trehalose treated, dried and packaged. Chips are stored at room temperature at Cambridge, MA, USA. Chip are packed in a dark bag in order to block light.

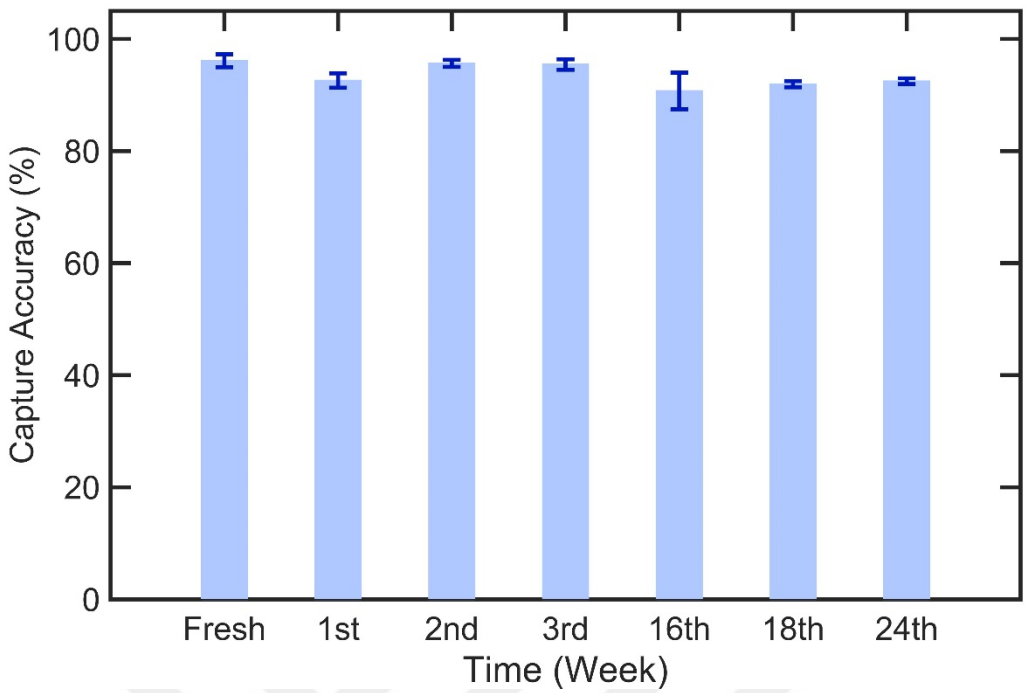

Figure 7.14 CD4+T cell capture shelf life performance evaluation results of accuracy for stabilized samples over time. Error bars are standard deviation results.

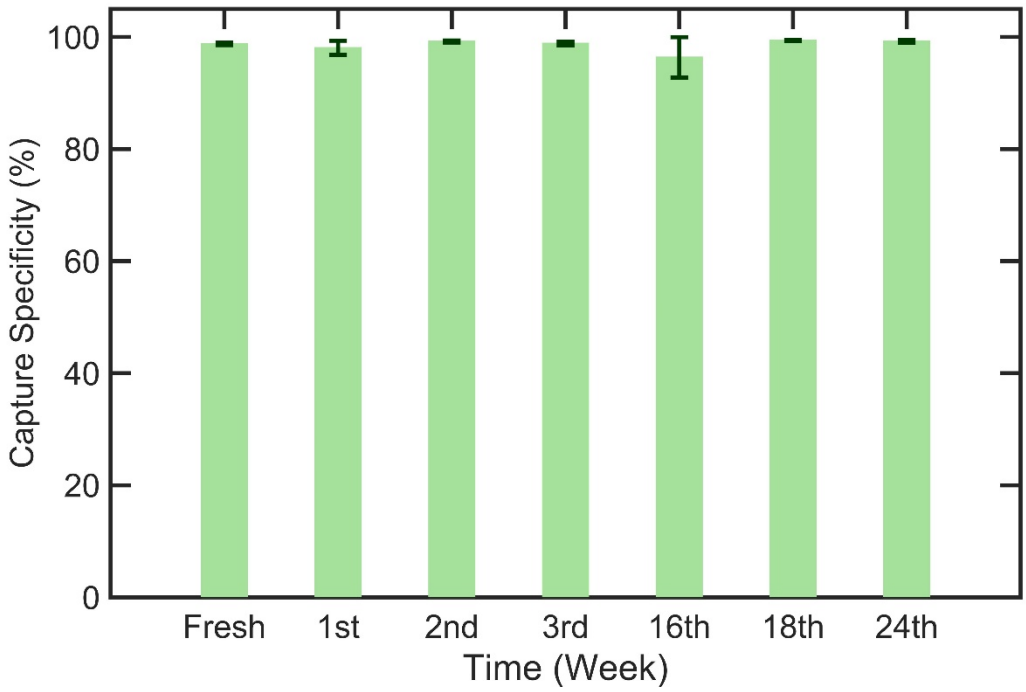

Figure 7.15 CD4+T cell capture shelf life performance evaluation results of specificity for stabilized samples over time. Error bars are standard deviation results.

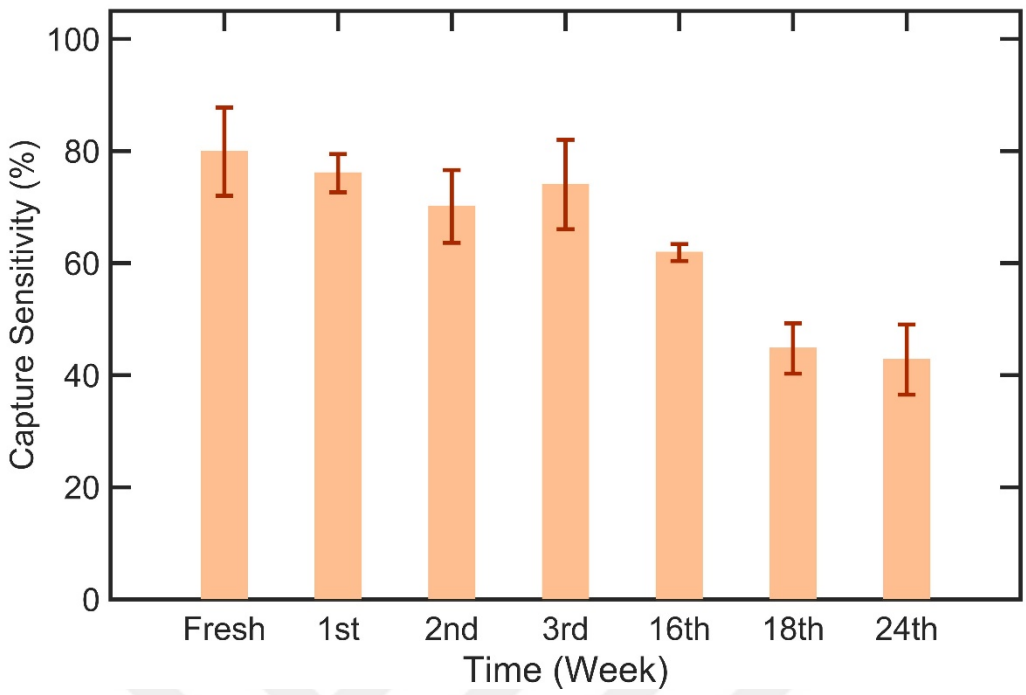

Figure 7.16 CD4+T cell capture shelf life performance evaluation results of sensitivity for stabilized samples over time. Error bars are standard deviation results.

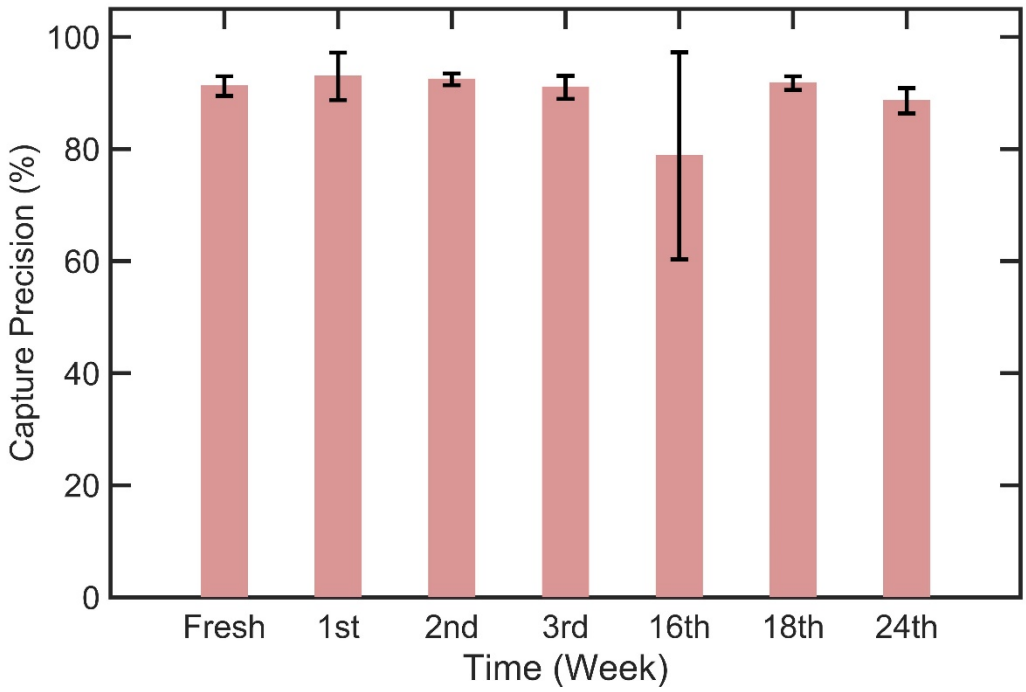

Figure 7.17 CD4+T cell capture shelf life performance evaluation results of precision for stabilized samples over time. Error bars are standard deviation results.

In every test almost three channels are used. Every time point channels are washed from trehalose 3 times with 50µL PBS, CD4+T cells are captured as explained in section 6.1.2.2, stained as explained in section 6.1.4.1, captured cells are manually counted as explained in section 6.1.4.2. Performance statistic of accuracy, specificity, sensitivity and precision values are obtained as explained in section 6.1.4.3. Performance evaluation results are given in Figure 7.14, Figure 7.15, Figure 7.16 and Figure 7.17. From those graphs accuracy and specificity almost does not change according to time for six months. Precision on the other hand is similar only for 16th week there is an unusual effect on a channel which gives low results. Sensitivity is above 70% for almost 1 month than it goes down, for six months it is above 42%.

7.3 Conclusion

In this part of thesis a biopreservation method for preserving multi-layer immuno-functionalized surface inside channel of a microfluidic chip is developed and tested. CD4+T cell capturing multi-layer immuno-functionalized surface chemistry is applied for 30 microfluidic chips with 3 channels each as explained in section 6.1.2.

A biopreservation method using a sugar solution (trehalose) is developed and applied to chips. The biopreservation mechanism theories of trehalose is explained in section 1.5. Trehalose was used to stabilize the multi-layer surface chemistry of proteins and antibodies with functional materials such as 3MPS and GMBS inside the channel of a microfluidic chip.

In order to dry the channels 3 methods (heating, vacuuming and heating and vacuuming together) are explained and used. The best performance is evaluated according to fasted drying. It has been obtained that even for heating and vacuuming together after 4 hours still chips are not completely dried. Due to that reason a method in order to remove excessive fluid inside a channel is developed. Chips are centrifuged before heating and vacuuming. After centrifuging almost 90% of fluid is removed and complete drying takes half an hour.

After drying, each chip is packaged in a vacuumed and sealed plastic bag together with drying agents, in order to keep humidity away. Some of these devices loose vacuum over time. 6 devices out of 30 lost their vacuum after one month. The overall

yield was 80%. These devices were not used in the experiments because of a potential functional loss because of under non-vacuum conditions humidity in the air may affect the surface chemistry over time. This 80% yield can be increased by using quality mylar metalized laminate bags [66] which do not lose vacuum and do not let humidity and vapor inside bags.

Finally CD4+T cell capturing performance of chips are tested over time according to the methods explained in section 6.1.3 and 6.1.4. Results are obtained for fresh and 1, 2, 3, 16, 18 and 24 weeks samples. From those results capture accuracy and specificity are almost above 92% and does not change much according to time for six months. Precision is similar but only for 16th week sample for one channel it gives low results. Those results indicated that captured cells are mostly CD4+T cells. Sensitivity is above 70% for almost 1 month than it goes down, at six months it is above 42%, which indicates than number of captured cells are going down.

8 CONCLUSION and DISCUSSION

The new trend of diagnosis is POC diagnosis because it is rapid, easy-to-use, and deliverable and does not need well equipped infrastructure. However designing a sensitive, rapid and inexpensive diagnostic tool should be well planned. Also the transportation and storage of those biosensor should practical and cost effective. In this thesis 3 main study are realized in order to address and propose solution for POC HIV/AIDS diagnosis and monitoring of therapy and practical and cost effective biopreservation of biosensor.

HIV infection is widespread and a major problem worldwide. Late diagnosis of HIV infection can cause spread of infection and late start to treatment. HIV screening is still not a POCT before seroconversion state which around 25 days after the beginning of infection. There is a high possibility to spread the infection at acute state especially for a pregnant women to transmit the infection to infant. 40% percent of people are unaware of their HIV infection globally. For resource limited settlings HIV screening is a big problem. [48]

Flexible polyester film as a material for biosensor has many advantages, it is light, flexible, thin, inexpensive, easy to fabricate, easy to dispose and mass producible. Electrical impedance spectroscopy is a powerful detecting method, it is rapid, sensitive and can be designed portable.

Due to all of the above reasons in the first part of this thesis a flexible polymer based microfluidic biosensor using electrical impedance detection for POC HIV-1 virus load diagnosis is designed and tested.

The system can selectively capture and detect 10^6-10^8 copies/mL of HIV-1, the material costs is less than US$ 0.2. The diagnosis can give results less than 1 hour. The system is also tested in clinical samples (plasma and whole blood).

In this system the sample preparation, suspending magnetic beads in clinical sample, washing and lysis steps are still off-chip. This part of the system can be improved further. Since the system designed using affinity chromatography based method it can be applied to other pathogens.

ART is the therapy for HIV infection. Only half of the infected individual globally can access ART and in developing countries 1 of 4 HIV infected people who has access to ART, start ART late, due to the lack of well-equipped health facilities and specialists. The consequences of that problem are infection can spread more and early deaths can be increased. [94] ART is started and monitored by checking CD4+T cell counts and there also an urgent need for a POC CD4+T cell counting system. There are some efficient approaches offered for POC CD4+T cell capture in microfluidic using affinity chromatography and cell counting using lensless wide-field microscopy. [66, 164, 165] In the second part of this thesis a POC CD4+T cell counting system is developed by improving ideas proposed in [66, 164, 165] with an addition of developing a novel automatic cell detection and counting program.

A microfluidic chip with 3 channels for capturing the CD4+T cells is developed by non-lithographic, practical and cost effective techniques. Multilayer immuno-functionalization is applied on the surface of the channels. A practical lensless wide-field microscope is developed. A novel cell detection and counting algorithm is developed which is using the idea of cross correlation of an averaged model cell image with cells in an image to be counted. Differential cell counting is applied using florescence microscopy and lensless wide field microscopy system. It had been obtained that capture accuracy specificity, sensitivity and precision are 96.1 % ± 1.2 %, 98.8 % ± 0.2 %, 79.9 % ± 7.9% and 91.2 % ± 1.7 % respectively. And the developed algorithm counts the cells in channels with 2.59% and 1.88% difference from actual cell counts.

CD4+T cell counting can be achieved by using this POC biosensor even with a drop of unprocessed whole blood. The cells can be selectively counted without using fluorescent labels by using microfluidic device integrated lensless CMOS imaging system. Wide-field images of cells are obtained using this microscope which can be increased the accuracy of counting.

In future, in order to count cells automatically, CMOS imaging sensor can be replaced by a cell phone CMOS camera. The system can be used for diagnosis and monitoring therapy of sepsis, tuberculosis, malaria, and cancer.

Most of the diagnostic biosensors for POC uses affinity chromatography to capture the cell, pathogen or biomolecule. One of the problem is to keep those sensors functional till used, so transportation and storing of those should be adequate for resource limited settling. Usually cold chain transportation and storage is used for those sensor but it is not feasible due to the lack of infrastructure and assay cost. POC diagnostic biosensors should be preserved practical and economical.

In the final part of this thesis study, a novel biopreservation method is developed and tested for POC CD4+T cell counting system. The immuno-functionalized chips can be preserved longer at refrigeration-free conditions by using the proposed stabilization, drying and packaging methods.

Using this preservation method microfluidic devices can be stabilized with high capture accuracy, specificity and precision for six months. Future studies can be applied for testing this microfluidic device at different conditions such as different and changing temperature and humidity.

REFERENCES

[1] P. Yager, G. J. Domingo, and J. Gerdes, "Point-of-care diagnostics for global health," *Annu Rev Biomed Eng,* vol. 10, pp. 107-44, 2008.

[2] (2015, 21/05). *Alere TM*. Available: http://www.alere.com/us/en/product-details/inratio-pt-inr-monitoring-systems.html

[3] (2015, 21/05). *Alere TM*. Available: http://www.alere.com/ww/en/product-details/clearview-malaria-combo.html

[4] (2015, 21/05). *Alere TM Company UK*. Available: http://www.alere.co.uk/sexual-health/alere-determinetm-hiv-12-agab-combo-148/product-listing.htm

[5] (2015, 21/05). *Roche*. Available: http://www.roche.com/pages/downloads/photosel/071002/html/detail_6.html

[6] (2015, 21/05). *Astute Medical®*. Available: http://www.astutemedical.com/US/Products

[7] (2015, 21/05). *Becton, Dickinson and Company. © 2015*. Available: http://www.bd.com/ds/veritorsystem/poctesting.asp#

[8] "Point-of-care Testing Checklist," College of American Pathologists2007.

[9] C. A. Holland and F. L. Kiechle, "Point-of-care molecular diagnostic systems-past, present and future," *Curr Opin Microbiol,* vol. 8, pp. 504-9, Oct 2005.

[10] C. Price and J. Hicks, *Point of care testing*. Washington: AACC Press, 1999.

[11] G. J. Kost, N. K. Tran, and R. F. Louie, "Point-of-Care Testing: Principles, Practice, and Critical-Emergency-Disaster Medicine," in *Encyclopedia of Analytical Chemistry*, R. A. Meyers, Ed., ed: John Wiley and Sons, Inc., 2008.

[12] C. D. Chin, V. Linder, and S. K. Sia, "Lab-on-a-chip devices for global health: past studies and future opportunities," *Lab Chip,* vol. 7, pp. 41-57, Jan 2007.

[13] P. Yager, T. Edwards, E. Fu, K. Helton, K. Nelson, M. R. Tam*, et al.*, "Microfluidic diagnostic technologies for global public health," *Nature,* vol. 442, pp. 412-8, Jul 27 2006.

[14] B. H. Weigl, R. L. Bardell, and C. R. Cabrera, "Lab-on-a-chip for drug development," *Advanced Drug Delivery Reviews,* vol. 55, pp. 349-377, 2003.

[15] P. A. Singer, A. D. Taylor, A. S. Daar, R. E. Upshur, J. A. Singh, and J. V. Lavery, "Grand challenges in global health: the ethical, social and cultural program," *PLoS Med,* vol. 4, p. e265, Sep 2007.

[16] L. Gervais, N. de Rooij, and E. Delamarche, "Microfluidic chips for point-of-care immunodiagnostics," *Adv Mater,* vol. 23, pp. H151-76, Jun 24 2011.

[17] Y. P. J. Bourquin, "Shaping surface waves for diagnostics," Doctor of Philosophy, School of Engineering College of Science and Engineering University of Glasgow, 2012.

[18] V. Gubala, L. F. Harris, A. J. Ricco, M. X. Tan, and D. E. Williams, "Point of care diagnostics: status and future," *Anal Chem,* vol. 84, pp. 487-515, Jan 17 2012.

[19] P. J. Santrach, "Current & Future Applications of Point of Care Testing," ed. Rochester, MN: Mayo Clinic & Centers for Disease Control and Prevention (CDC) Clinical Laboratory Improvement Advisory Committee (CLIAC)

[20] R. F. Louie, Z. Tang, D. G. Shelby, and G. J. Kost, "Point-of-Care Testing: Millennium Technology for Critical Care," *Laboratory Medicine,* vol. 31, pp. 402-408, 2000.

[21] C. P. Price, "Point of care testing," *BMJ,* vol. 322, pp. 1285-1288, 2001.

[22] M. R. Fiallos, U. A. Hanhan, and J. P. Orlowski, "Point-of-care testing," *Pediatric Clinics,* vol. 48, pp. 589-600, 2001/06/01 2001.

[23] newschannel10.com, "Point Of Care Diagnostics or Testing (POCT) Market is Expected to Hit $28,346.8 Million By 2022: Credence Research," ed, 2016.

[24] (2016, 03.05.2016). *Point-Of-Care Diagnostics / Testing Market, Size And Forecast To 2022*. Available: http://www.credenceresearch.com/report/point-of-care-diagnostics-or-testing-market

[25] H. Kettler, K. White, and S. Hawkes, "Mapping the landscape of diagnostics for sexually transmitted infections.," World Health Organization on behalf of the Special Programme for Research and Training in Tropical Diseases, Geneva2004.

[26] M. Pai, M. Ghiasi, and N. P. Pai, "Point-of-care diagnostic testing in global health: what is the point?," *Microbe,* vol. 10, pp. 103-107, 2015.

[27] H. Shafiee, S. Wang, F. Inci, M. Toy, T. J. Henrich, D. R. Kuritzkes*, et al.*, "Emerging technologies for point-of-care management of HIV infection," *Annu Rev Med,* vol. 66, pp. 387-405, 2015.

[28] A. Touhami, "Biosensors and nanobiosensors: design and applications," in *Nanomedicine*, A. Seifalian, A. de Mel, and D. M. Kalaskar, Eds., ed London, UK: One Central Press (OCP), 2014, pp. 374-403.

[29] J.-Y. Yoon, *Introduction to Biosensors: From Electric Circuits to Immunosensors*: Springer, 2016.

[30] Y. H. Lee and R. Mutharasan, "Biosensors," in *Sensor Technology Handbook*. vol. 1, J. S. Wilson, Ed., ed Oxford, UK: Elsevier Inc., 2005, pp. 161-180.

[31] G. Luka, A. Ahmadi, H. Najjaran, E. Alocilja, M. DeRosa, K. Wolthers*, et al.*, "Microfluidics Integrated Biosensors: A Leading Technology towards Lab-on-a-Chip and Sensing Applications," *Sensors (Basel),* vol. 15, pp. 30011-31, Dec 01 2015.

[32] D. J. Beebe, G. A. Mensing, and G. M. Walker, "Physics and applications of microfluidics in biology," *Annu Rev Biomed Eng,* vol. 4, pp. 261-86, 2002.

[33] S. K. Mitra and S. Chakraborty, *Microfluidics and Nanofluidics Handbook: Fabrication, Implementation, and Applications*. New York, USA: CRC Press, 2016.

[34] G. Karniadakis, A. Beskok, and N. Aluru, *Microflows and Nanoflows Fundamentals and Simulation* vol. 29: Springer, 2005.

[35] G. Galilei, "Dialogues Concerning Two New Sciences [Original work publihed at 1638]," ed. New York: The Macmillan Company, 1914/1638.

[36] R. M. van Dam, "Solvent-Resistant Elastomeric Microfluidic Devices and Applications," Doctor of Philosophy, California Institute of Technology, Pasadena, California, 2005.

[37] A. M. Streets and Y. Huang, "Chip in a lab: Microfluidics for next generation life science research," *Biomicrofluidics,* vol. 7, p. 11302, Jan 2013.

[38] P. Tabeling, *Introduction to Microfluidics*. Oxford: Oxford University Press, 2005.

[39] Y. H. Ghallab and W. Badawy, *Lab-on-a-Chip Techniques, Circuits, and Biomedical Applications*. Norwwod, MA: Artech House, 2010.

[40] M. Brivio, W. Verboom, and D. N. Reinhoudt, "Miniaturized continuous flow reaction vessels: influence on chemical reactions," *Lab Chip,* vol. 6, pp. 329-44, Mar 2006.

[41] C. D. Chin, V. Linder, and S. K. Sia, "Commercialization of microfluidic point-of-care diagnostic devices," *Lab Chip,* vol. 12, pp. 2118-34, Jun 21 2012.

[42] S. Sharma, J. Zapatero-Rodriguez, P. Estrela, and R. O'Kennedy, "Point-of-Care Diagnostics in Low Resource Settings: Present Status and Future Role of Microfluidics," *Biosensors (Basel),* vol. 5, pp. 577-601, Aug 13 2015.

[43] M. A. Burns, "An Integrated Nanoliter DNA Analysis Device," *Science,* vol. 282, pp. 484-487, 1998.

[44] A. W. Martinez, S. T. Phillips, Z. Nie, C. M. Cheng, E. Carrilho, B. J. Wiley*, et al.*, "Programmable diagnostic devices made from paper and tape," *Lab Chip,* vol. 10, pp. 2499-504, Oct 07 2010.

[45] E. J. Maxwell, A. D. Mazzeo, and G. M. Whitesides, "Paper-based electroanalytical devices for accessible diagnostic testing," *MRS Bulletin,* vol. 38, pp. 309-314, 2013.

[46] (2016). *Whitesides Research Group: Research > Paper as a Material*. Available: http://gmwgroup.harvard.edu/research/index.php?page=31

[47] A. W. Martinez, S. T. Phillips, G. M. Whitesides, and E. Carrilho, "Diagnostics for the developing world: microfluidic paper-based analytical devices," *Anal Chem,* vol. 82, pp. 3-10, Jan 01 2010.

[48] H. Shafiee, W. Asghar, F. Inci, M. Yuksekkaya, M. Jahangir, M. H. Zhang*, et al.*, "Paper and flexible substrates as materials for biosensing platforms to detect multiple biotargets," *Sci Rep,* vol. 5, p. 8719, Mar 06 2015.

[49] H. Shafiee, M. K. Kanakasabapathy, F. Juillard, M. Keser, M. Sadasivam, M. Yuksekkaya*, et al.*, "Printed Flexible Plastic Microchip for Viral Load Measurement through Quantitative Detection of Viruses in Plasma and Saliva," *Sci Rep,* vol. 5, p. 9919, Jun 05 2015.

[50] A. W. Martinez, S. T. Phillips, M. J. Butte, and G. M. Whitesides, "Patterned paper as a platform for inexpensive, low-volume, portable bioassays," *Angew Chem Int Ed Engl,* vol. 46, pp. 1318-20, 2007.

[51] S. Magdeldin, *Affinity Chromatography*. Rijeka, Croatia: InTech, 2012.

[52] M. Zourob, "Recognition Receptors in Biosensors," ed. New York: Springer, 2010.

[53] S. Wang, M. Esfahani, U. A. Gurkan, F. Inci, D. R. Kuritzkes, and U. Demirci, "Efficient on-chip isolation of HIV subtypes," *Lab Chip,* vol. 12, pp. 1508-15, Apr 21 2012.

[54] H. J. Yoon, T. H. Kim, Z. Zhang, E. Azizi, T. M. Pham, C. Paoletti*, et al.*, "Sensitive capture of circulating tumour cells by functionalized graphene oxide nanosheets," *Nat Nanotechnol,* vol. 8, pp. 735-41, Oct 2013.

[55] K. Gekko and S. N. Timasheff, "Mechanism of protein stabilization by glycerol: preferential hydration in glycerol-water mixtures," *Biochemistry,* vol. 20, pp. 4667-4676, May 1, 2002 1981.

[56] J. C. Lee and S. N. Timasheff, "The stabilization of proteins by sucrose," *J Biol Chem,* vol. 256, pp. 7193-201, Jul 25 1981.

[57] J. F. Carpenter, S. J. Prestrelski, and T. Arakawa, "Separation of freezing- and drying-induced denaturation of lyophilized proteins using stress-specific stabilization. I. Enzyme activity and calorimetric studies," *Arch Biochem Biophys,* vol. 303, pp. 456-64, Jun 1993.

[58] G. Xie and S. N. Timasheff, "Mechanism of the stabilization of ribonuclease A by sorbitol: preferential hydration is greater for the denatured then for the native protein," *Protein Sci,* vol. 6, pp. 211-21, Jan 1997.

[59] T. Arakawa and S. N. Timasheff, "Preferential interactions of proteins with salts in concentrated solutions," *Biochemistry,* vol. 21, pp. 6545-6552, May 1, 2002 2002.

[60] M. Mueller, M. Q. Loh, R. Tscheliessnig, D. H. Tee, E. Tan, M. Bardor*, et al.*, "Liquid formulations for stabilizing IgMs during physical stress and long-term storage," *Pharm Res,* vol. 30, pp. 735-50, Mar 2013.

[61] A. Y. Kolosova, W. B. Shim, Z. Y. Yang, S. A. Eremin, and D. H. Chung, "Direct competitive ELISA based on a monoclonal antibody for detection of aflatoxin B1. Stabilization of ELISA kit components and application to grain samples," *Anal Bioanal Chem,* vol. 384, pp. 286-94, Jan 2006.

[62] G. Wu, J. Srivastava, and M. H. Zaman, "Stability measurements of antibodies stored on paper," *Anal Biochem,* vol. 449, pp. 147-54, Mar 15 2014.

[63] S. Wang, F. Inci, T. L. Chaunzwa, A. Ramanujam, A. Vasudevan, S. Subramanian*, et al.*, "Portable microfluidic chip for detection of Escherichia coli in produce and blood," *Int J Nanomedicine,* vol. 7, pp. 2591-600, 2012.

[64] *Global report: UNAIDS report on the global AIDS epidemic 2013.*: Joint United Nations Programme on HIV/AIDS, 2013.

[65] U. A. Gurkan, S. Moon, H. Geckil, F. Xu, S. Wang, T. J. Lu*, et al.*, "Miniaturized lensless imaging systems for cell and microorganism visualization in point-of-care testing," *Biotechnol J,* vol. 6, pp. 138-49, Feb 2011.

[66] S. Moon, U. A. Gurkan, J. Blander, W. W. Fawzi, S. Aboud, F. Mugusi*, et al.*, "Enumeration of CD4+ T-cells using a portable microchip count platform in Tanzanian HIV-infected patients," *PLoS One,* vol. 6, p. e21409, 2011.

[67] S. Wang, F. Xu, and U. Demirci, "Advances in developing HIV-1 viral load assays for resource-limited settings," *Biotechnol Adv,* vol. 28, pp. 770-81, Nov-Dec 2010.

[68] B. Hock, M. Rahman, S. Rauchalles, A. Dankwardt, M. Seifert, S. Haindl*, et al.*, "Stabilisation of immunoassays and receptor assays," *Journal of Molecular Catalysis B: Enzymatic,* vol. 7, pp. 115-124, 1999.

[69] A. Dankwardt, J. Müller, and B. Hock, "Stabilization of enzyme immunoassays for atrazine," *Analytica Chimica Acta,* vol. 362, pp. 35-45, 1998.

[70] D. Y. Stevens, C. R. Petri, J. L. Osborn, P. Spicar-Mihalic, K. G. McKenzie, and P. Yager, "Enabling a microfluidic immunoassay for the developing world by integration of on-card dry reagent storage," *Lab Chip,* vol. 8, pp. 2038-45, Dec 2008.

[71] C. D. Chin, T. Laksanasopin, Y. K. Cheung, D. Steinmiller, V. Linder, H. Parsa*, et al.*, "Microfluidics-based diagnostics of infectious diseases in the developing world," *Nature Medicine,* vol. 17, pp. 1015-1019, 2011-07-31 2011.

[72] J. Carpinelli, R. Kramer, and E. Agosin, "Metabolic engineering of Corynebacterium glutamicum for trehalose overproduction: role of the TreYZ trehalose biosynthetic pathway," *Appl Environ Microbiol,* vol. 72, pp. 1949-55, Mar 2006.

[73] B. Kempf and E. Bremer, "Uptake and synthesis of compatible solutes as microbial stress responses to high-osmolality environments," *Archives of Microbiology,* vol. 170, pp. 319-330, 1998.

[74] L. M. Crowe, "Lessons from nature: the role of sugars in anhydrobiosis," *Comparative Biochemistry and Physiology Part A: Molecular & Integrative Physiology,* vol. 131, pp. 505-513, 2002.

[75] D. Corradini, E. G. Strekalova, H. E. Stanley, and P. Gallo, "Microscopic mechanism of protein cryopreservation in an aqueous solution with trehalose," *Sci Rep,* vol. 3, p. 1218, 2013.

[76] S. Ramachandran, E. Fu, B. Lutz, and P. Yager, "Long-term dry storage of an enzyme-based reagent system for ELISA in point-of-care devices," *Analyst,* vol. 139, pp. 1456-62, Mar 21 2014.

[77] N. Guo, I. Puhlev, D. R. Brown, J. Mansbridge, and F. Levine, "Trehalose expression confers desiccation tolerance on human cells," *Nat Biotechnol,* vol. 18, pp. 168-71, Feb 2000.

[78] J. H. Crowe, S. B. Leslie, and L. M. Crowe, "Is vitrification sufficient to preserve liposomes during freeze-drying?," *Cryobiology,* vol. 31, pp. 355-66, Aug 1994.

[79] W. Q. Sun and A. C. Leopold, "Cytoplasmic Vitrification and Survival of Anhydrobiotic Organisms," *Comparative Biochemistry and Physiology Part A: Physiology,* vol. 117, pp. 327-333, 1997.

[80] Y. S. Kim, L. S. Jones, A. Dong, B. S. Kendrick, B. S. Chang, M. C. Manning*, et al.*, "Effects of sucrose on conformational equilibria and fluctuations within the native-state ensemble of proteins," *Protein Sci,* vol. 12, pp. 1252-61, Jun 2003.

[81] Y. Han, B. S. Jin, S. B. Lee, Y. Sohn, J. W. Joung, and J. H. Lee, "Effects of sugar additives on protein stability of recombinant human serum albumin during lyophilization and storage," *Arch Pharm Res,* vol. 30, pp. 1124-31, Sep 2007.

[82] T. Chen, A. Fowler, and M. Toner, "Literature review: supplemented phase diagram of the trehalose-water binary mixture," *Cryobiology,* vol. 40, pp. 277-82, May 2000.

[83] N. K. Jain and I. Roy, "Effect of trehalose on protein structure," *Protein Sci,* vol. 18, pp. 24-36, Jan 2009.

[84] S. J. Prestrelski, N. Tedeschi, T. Arakawa, and J. F. Carpentert, "Dehydration-induced conformational transitions in proteins and their inhibition by stabilizers," *Biophysical Journal,* vol. 65, pp. 661–671, 1993.

[85] J. F. Carpenter and J. H. Crowe, "An infrared spectroscopic study of the interactions of carbohydrates with dried proteins," *Biochemistry,* vol. 28, pp. 3916-3922, 2002.

[86] S. J. Prestrelski, T. Arakawa, and J. F. Carpenter, "Separation of freezing- and drying-induced denaturation of lyophilized proteins using stress-specific stabilization. II. Structural studies using infrared spectroscopy," *Arch Biochem Biophys,* vol. 303, pp. 465-73, Jun 1993.

[87] W. Asghar, M. Yuksekkaya, H. Shafiee, M. Zhang, M. O. Ozen, F. Inci*, et al.*, "Engineering long shelf life multi-layer biologically active surfaces on microfluidic devices for point of care applications," *Sci Rep,* vol. 6, p. 21163, Feb 17 2016.

[88] E. V. Koonin, T. G. Senkevich, and V. V. Dolja, "The ancient Virus World and evolution of cells," *Biol Direct,* vol. 1, p. 29, Sep 19 2006.

[89] (2016). *WHO | HIV/AIDS*. Available: http://www.who.int/mediacentre/factsheets/fs360/en/

[90] K. S. Stolley and J. E. Glass, *HIV/AIDS*. Santa Barbara, USA: Greenwood, 2009.

[91] C. Goldsmith, P. Feorino, E. L. Palmer, and W. R. McManus. (2017). *Center for Disease Control and Prevention (CDC) - Public Health Image Library (PHIL) ID#:10000*. Available: https://phil.cdc.gov/phil/details.asp?pid=10000

[92] G. Doitsh, N. L. K. Galloway, X. Geng, Z. Yang, K. M. Monroe, O. Zepeda*, et al.*, "Cell death by pyroptosis drives CD4 T-cell depletion in HIV-1 infection," *Nature,* vol. 505, pp. 509-514, 2013-12-19 2013.

[93] (2017). *Global HIV and AIDS statistics*. Available: https://www.avert.org/global-hiv-and-aids-statistics

[94] Fact sheet - Latest statistics on the status of the AIDS epidemic | UNAIDS [Online]. Available: http://www.unaids.org/en/resources/fact-sheet

[95] "2015 World Population Data Sheet," Population Reference Bureau, Washington DC, USA 0085-8315, 2015.

[96] "Prevention Gap Report," Joint United Nations Programme on HIV/AIDS, Geneva, Switzerland2016.

[97] "Centers for Disease Control and Prevention. HIV surveillance—United States, 1981–2008.," *MMWR Morb Mortal Weekly Report,* vol. 60, pp. 689-693, 2011.

[98] (2017). *Basic Statistics | HIV Basics | HIV/AIDS | CDC*. Available: https://www.cdc.gov/hiv/basics/statistics.html

[99] D. H. Davis, R. Smith, A. Brown, B. Rice, Z. Yin, and V. Delpech, "Early diagnosis and treatment of HIV infection: magnitude of benefit on short-term mortality is greatest in older adults," *Age Ageing,* vol. 42, pp. 520-6, Jul 2013.

[100] (2007). *File:HIV Prevalence - Adult by Country.png - Wikimedia Commons*. Available: https://commons.wikimedia.org/wiki/File:HIV_Prevalence_-_Adult_by_Country.png

[101] Y. G. Kuznetsov, J. G. Victoria, W. E. Robinson, and A. McPherson, "Atomic Force Microscopy Investigation of Human Immunodeficiency Virus (HIV) and HIV-Infected Lymphocytes," *Journal of Virology,* vol. 77, pp. 11896-11909, 2003.

[102] R. Pantophlet and D. R. Burton, "GP120: target for neutralizing HIV-1 antibodies," *Annu Rev Immunol,* vol. 24, pp. 739-69, 2006.

[103] (2014). *Diagram of the HIV virion, Splettstoesser, Thomas, www.scistyle.com*. Available: https://commons.wikimedia.org/wiki/File:HI-virion-structure_en.svg

[104] Y. Wu and A. Yoder, "Chemokine coreceptor signaling in HIV-1 infection and pathogenesis," *PLoS Pathog,* vol. 5, p. e1000520, Dec 2009.

[105] D. Weissman, R. L. Rabin, J. Arthos, A. Rubbert, M. Dybul, R. Swofford*, et al.*, "Macrophage-tropic HIV and SIV envelope proteins induce a signal through the CCR5 chemokine receptor," *Nature,* vol. 389, pp. 981-985, 1997-10-30 1997.

[106] A. Yoder, D. Yu, L. Dong, S. R. Iyer, X. Xu, J. Kelly*, et al.*, "HIV envelope-CXCR4 signaling activates cofilin to overcome cortical actin restriction in resting CD4 T cells," *Cell,* vol. 134, pp. 782-92, Sep 05 2008.

[107] C. Berndt, B. Möpps, S. Angermüller, P. Gierschik, and P. H. Krammer, "CXCR4 and CD4 mediate a rapid CD95-independent cell death in CD4+ T cells," 1998-10-13 1998.

[108] (2017). *Disease Control and Prevention (CDC) - Public Health Image Library (PHIL) ID#:18162*. Available: https://phil.cdc.gov/phil/details.asp

[109] J. K. Cornett and T. J. Kirn, "Laboratory diagnosis of HIV in adults: a review of current methods," *Clin Infect Dis,* vol. 57, pp. 712-8, Sep 2013.

[110] B. M. Branson, S. M. Owen, L. G. Wesolowski, B. Bennett, B. G. Werner, K. E. Wroblewski*, et al.*, *Laboratory testing for the diagnosis of HIV infection : updated recommendations*: Centers for Disease Control and Prevention and Association of Public Health Laboratories, 2014.

[111] (2011). *HIV viral load in relation to CD4+ lymphocyte count*. Available: https://commons.wikimedia.org/wiki/File:Hiv-timecourse_copy.svg

[112] "Global update on HIV treatment 2013: results, impact and opportunities," ed. Kuala Lumpur, Malaysia: WHO Press, World Health Organization, 2013.

[113] V. F. Lvovich, *Impedance Spectroscopy: Applications to Electrochemical and Dielectric Phenomena*, 2012.

[114] A. Lasia, *Electrochemical Impedance Spectroscopy and its Applications - Springer*. New York, USA: Springer, 2014.

[115] S. Grimnes and O. G. Martinsen, *Bioimpedance and Bioelectricity Basics*: Academic Press, 2005.

[116] S. Krause, "Impedance Methods," in *Encyclopedia of Electrochemistry*, ed: Wiley-VCH Verlag GmbH & Co. KGaA, 2007.

[117] F. Lisdat and D. Schäfer, "The use of electrochemical impedance spectroscopy for biosensing," *Analytical and Bioanalytical Chemistry,* pp. 1555–1567, 2008.

[118] X. Luo and J. J. Davis, "Electrical biosensors and the label free detection of protein disease biomarkers," *Chem Soc Rev,* vol. 42, pp. 5944-62, Jul 07 2013.

[119] (2017). *Basics of EIS: Electrochemical Research-Impedance*. Available: https://www.gamry.com/application-notes/EIS/basics-of-electrochemical-impedance-spectroscopy/

[120] M. E. Orazem and B. Tribollet, *Electrochemical Impedance Spectroscopy*. Hoboken, NJ, USA.: John Wiley & Sons, Inc., 2008.

[121] J. Hong, D. S. Yoon, S. K. Kim, T. S. Kim, S. Kim, E. Y. Pak*, et al.*, "AC frequency characteristics of coplanar impedance sensors as design parameters," *Lab Chip,* vol. 5, pp. 270-9, Mar 2005.

[122] P. Córdoba-Torres, T. J. Mesquita, and R. P. Nogueira, "Relationship between the Origin of Constant-Phase Element Behavior in Electrochemical Impedance Spectroscopy and Electrode Surface Structure," *The Journal of Physical Chemistry C,* vol. 119, pp. 4139-4147, February 18, 2015 2015.

[123] V. F. Lvovich, C. C. Liu, and M. F. Smiechowski, "Optimization and fabrication of planar interdigitated impedance sensors for highly resistive non-aqueous industrial fluids," *Sensors and Actuators B: Chemical,* vol. 119, pp. 490-496, 2006.

[124] (2013). *File:EDLC-Potentialdistribution.png - Wikipedia*. Available: https://en.wikipedia.org/wiki/File:EDLC-Potentialdistribution.png

[125] K.-C. Ho, V.-C. Su, D.-Y. Huang, M.-L. Lee, N.-K. Chou, and C.-H. Kuan, "Investigation of low frequency electrolytic solution behavior with an accurate electrical impedance method," *Chemical Physics Letters,* vol. 667, pp. 120-123, 2017.

[126] S. Brosel-Oliu, N. Uria, N. Abramova, and A. Bratov, "Impedimetric Sensors for Bacteria Detection," in *Biosensors - Micro and Nanoscale Applications*, T. Rinken, Ed., ed: Intech, 2015, pp. 257-288.

[127] K. Eckhard and W. Schuhmann, "Alternating current techniques in scanning electrochemical microscopy (AC-SECM)," *Analyst,* vol. 133, pp. 1486-97, Nov 2008.

[128] B. Y. Chang and S. M. Park, "Electrochemical impedance spectroscopy," *Annu Rev Anal Chem (Palo Alto Calif),* vol. 3, pp. 207-29, 2010.

[129] M. Pacios, I. Martín-Fernández, R. Villa, P. Godignon, M. Del Valle, J. Bartrolí*, et al.*, "Carbon Nanotubes as Suitable Electrochemical Platforms for Metalloprotein Sensors and Genosensors," in *Carbon Nanotubes - Growth and Applications*, M. Naraghi, Ed., ed: InTech, 2011.

[130] E. P. Randviir and C. E. Banks, "Electrochemical impedance spectroscopy: an overview of bioanalytical applications," *Analytical Methods,* vol. 5, p. 1098, 2013.

[131] A. Ahmed, J. V. Rushworth, N. A. Hirst, and P. A. Millner, "Biosensors for whole-cell bacterial detection," *Clin Microbiol Rev,* vol. 27, pp. 631-46, Jul 2014.

[132] S. M. R. Niyaa and M. Hoorfar, "On a possible physical origin of the constant phase element," *Electrochimica Acta,* vol. 188, pp. 98–102, 10 January 2016 2016.

[133] T. Barrès, B. Tribollet, O. Stephan, H. Montigaud, M. Boinet, and Y. Cohin, "Characterization of the porosity of silicon nitride thin layers by Electrochemical Impedance Spectroscopy," *Electrochimica Acta,* vol. 227, pp. 1-6, 2017.

[134] A. V. Mamishev, K. Sundara-Rajan, Y. Fumin, D. Yanqing, and M. Zahn, "Interdigital sensors and transducers," *Proceedings of the IEEE,* vol. 92, pp. 808-845, 2004.

[135] J. Z. Chen, A. A. Darhuber, S. M. Troian, and S. Wagner, "Capacitive sensing of droplets for microfluidic devices based on thermocapillary actuation," *Lab Chip,* vol. 4, pp. 473-80, Oct 2004.

[136] C. Elbuken, T. Glawdel, D. Chan, and C. L. Ren, "Detection of microdroplet size and speed using capacitive sensors," *Sensors and Actuators A: Physical,* vol. 171, pp. 55-62, 2011.

[137] E. B. Bahadir and M. K. Sezginturk, "A review on impedimetric biosensors," *Artif Cells Nanomed Biotechnol,* vol. 44, pp. 248-62, 2016.

[138] D. Grieshaber1, R. MacKenzie, J. Voros, and E. Reimhult, "Electrochemical Biosensors - Sensor Principles and Architectures," *Sensors,* vol. 8, pp. 1400-1458, 2008.

[139] N. J. Ronkainen, H. B. Halsall, and W. R. Heineman, "Electrochemical biosensors," *Chemical Society Reviews,* 2010/02/01 2010.

[140] J.-G. Guana, Y.-Q. Miaoa, and Q.-J. Zhanga, "Impedimetric biosensors," *Journal of Bioscience and Bioengineering,* vol. 97, pp. 219–226, 2004 2004.

[141] M. Varshney and Y. Li, "Interdigitated array microelectrodes based impedance biosensors for detection of bacterial cells," *Biosens Bioelectron,* vol. 24, pp. 2951-60, Jun 15 2009.

[142] A. Abdelghani, "Electrochemical Biosensors for Virus Detection," in *Biosensors for Health, Environment and Biosecurity*, P. A. Serra, Ed., ed: InTech, 2011, pp. 321-330.

[143] L. Krejcova, D. Hynek, V. Adam, J. Hubalek, and R. Kizek, "Electrochemical Sensors and Biosensors for Influenza Detection," *International Journal of Electrochemical Science,* vol. 7, pp. 10779 - 10801, 2012.

[144] X. Cheng, Y. S. Liu, D. Irimia, U. Demirci, L. Yang, L. Zamir*, et al.*, "Cell detection and counting through cell lysate impedance spectroscopy in microfluidic devices," *Lab Chip,* vol. 7, pp. 746-55, Jun 2007.

[145] H. Shafiee, M. Jahangir, F. Inci, S. Wang, R. B. Willenbrecht, F. F. Giguel*, et al.*, "Acute on-chip HIV detection through label-free electrical sensing of viral nano-lysate," *Small,* vol. 9, pp. 2553-63, 2478, Aug 12 2013.

[146] M. Toner, R. Bashir, X. Cheng, U. Demirci, D. Irimia, W. Rodriguez*, et al.*, "Methods for counting cells," USA Patent EP2156376 A1, 2010.

[147] U. Demirci and H. Shafiee, "System and method for detecting pathogens," USA Patent, 2014.

[148] (2017). *Introduction to Fluorescence Microscopy*. Available: https://www.microscopyu.com/techniques/fluorescence/introduction-to-fluorescence-microscopy

[149] P. P. Mondal and A. Diaspro, *Fundamentals of Fluorescence Microscopy Exploring Life with Light*. Netherlands: Springer, 2014.

[150] B. Valeur and M. N. Berberan-Santos, *Molecular Fluorescence: Principles and Applications*. Weinham, Germany: Wiley-VCH, 2012.

[151] *Optical Fluorescence Microscopy From the Spectral to the Nano Dimension*. Heidelberg: Springer, 2011.

[152] H. Mühlpfordt and K. Blachnicki. (2017). *Fluorescence Filters*. Available: https://commons.wikimedia.org/wiki/File:FluorescenceFilters_2008-09-28.svg

[153] D. Brennan, J. Justice, B. Corbett, T. McCarthy, and P. Galvin, "Emerging optofluidic technologies for point-of-care genetic analysis systems: a review," *Anal Bioanal Chem,* vol. 395, pp. 621-36, Oct 2009.

[154] A. C. Sobieranski, F. Inci, H. C. Tekin, M. Yuksekkaya, E. Comunello, D. Cobra, *et al.*, "Portable lensless wide-field microscopy imaging platform based on digital inline holography and multi-frame pixel super-resolution," *Light: Science & Applications,* vol. 4, p. e346, 2015.

[155] A. Ozcan and U. Demirci, "Ultra wide-field lens-free monitoring of cells on-chip," *Lab Chip,* vol. 8, pp. 98-106, Jan 2008.

[156] W. Burger and M. J. Burge, *Digital Image Processing An Algorithmic Introduction Using Java*. London, UK: Springer, 2016.

[157] R. C. Gonzalez and R. E. Woods, *Digital Image Processing*. New Jersey, USA: Pearson, 2008.

[158] R. M. Haralick and L. G. Shapiro, *Computer and Robot Vision, Volume 1*: Addison-Wesley, 1992.

[159] A. K. Yetisen, M. S. Akram, and C. R. Lowe, "Paper-based microfluidic point-of-care diagnostic devices," *Lab Chip,* vol. 13, pp. 2210-51, Jun 21 2013.

[160] *Thermo Scientific Avidin-Biotin Technical Handbook*. USA: Thermo Fisher Scientific Inc., 2009.

[161] B. N. Taylor and C. E. Kuyatt, "Guidelines for Evaluating and Expressing the Uncertainty of NIST Measurement Results," Physics Laboratory National Institute of Standards and Technology1994.

[162] (2017). *Dielectric Constant of Polymers*. Available: http://omnexus.specialchem.com/polymer-properties/properties/dielectric-constant

[163] H. A. Pohl, "Giant polarization in high polymers," *Journal of Electronic Materials,* vol. 15, pp. 201-203, 1985.

[164] X. Cheng, D. Irimia, M. Dixon, K. Sekine, U. Demirci, L. Zamir, *et al.*, "A microfluidic device for practical label-free CD4(+) T cell counting of HIV-infected subjects," *Lab Chip,* vol. 7, pp. 170-8, Feb 2007.

[165] M. A. Alyassin, S. Moon, H. O. Keles, F. Manzur, R. L. Lin, E. Haeggstrom, *et al.*, "Rapid automated cell quantification on HIV microfluidic devices," *Lab Chip,* vol. 9, pp. 3364-9, Dec 07 2009.

[166] U. Demirci , A. Khademhosseini, R. Langer, and J. Blander, *Microfluidic Technologies for Human Health*. Hackensack, NJ, USA: World Scientific, 2013.

[167] S. Lee, S. Y. Oh, S. H. Kim, J. H. Lee, M. C. Kim, K. H. Kim, *et al.*, "Prognostic significance of neutrophil lymphocyte ratio and platelet lymphocyte ratio in advanced gastric cancer patients treated with FOLFOX chemotherapy," *BMC Cancer,* vol. 13, p. 350, Jul 22 2013.

[168] S. Tasoglu, U. A. Gurkan, S. Wang, and U. Demirci, "Manipulating biological agents and cells in micro-scale volumes for applications in medicine," *Chem Soc Rev,* vol. 42, pp. 5788-808, Jul 07 2013.

[169] O. Tokel, F. Inci, and U. Demirci, "Advances in Plasmonic Technologies for Point of Care Applications," *Chemical Reviews,* vol. 114, pp. 5728-5752, April 18, 2014 2014.

[170] W. Asghar, R. El Assal, H. Shafiee, S. Pitteri, R. Paulmurugan, and U. Demirci, "Engineering cancer microenvironments for in vitro 3-D tumor models," *Mater Today,* vol. 18, pp. 539-553, Dec 2015.

[171] A. Ilyas, W. Asghar, S. Ahmed, Y. Lotan, J.-T. Hsieh, Y.-t. Kim*, et al.*, "Electrophysiological analysis of biopsy samples using elasticity as an inherent cell marker for cancer detection," *Analytical Methods,* vol. 6, p. 7166, 2014.

[172] J. Giri, W. J. Li, R. S. Tuan, and M. T. Cicerone, "Stabilization of proteins by nanoencapsulation in sugar-glass for tissue engineering and drug delivery applications," *Adv Mater,* vol. 23, pp. 4861-7, Nov 09 2011.

[173] F. Löscher, T. Ruckstuhl, and S. Seeger, "Ultrathin Cellulose-Based Layers for Detection of Single Antigen Molecules," *Advanced Materials,* vol. 10, pp. 1005-1009, 1998 1998.

APPENDIX

A. Impedance Value Derivation for Randles Electrical Equivalent Circuit Model 194

B. Capacitance Value Derivation for Electrical Equivalent Circuit Model with a Resistor Parallel to a Capacitor..... 198

A. Impedance Value Derivation for Randles Electrical Equivalent Circuit Model

The derivation of impedance value according to frequency of Randles electrical equivalent circuit model in Figure 3.5 is given below:

Z_W Warburg impedance,

$$Z_W = \frac{\sigma_D\,(1-j)}{\sqrt{w}}$$

$X_{C_{DL}}$ is the electrical reactance of double layer capacitance,

$$X_{C_{DL}} = \frac{1}{jwC_{DL}} \tag{A.1}$$

Z is the Impedance of Randles electrical equivalent circuit model, R_{sol} is bulk resistance of the solution and R_{CT} is the charge transfer resistance.

$$Z_{RM} = R_{sol} + (R_{CT} + Z_W)||X_{C_{DL}} \tag{A.2}$$

$$Z_{RM} = R_{sol} + (R_{CT} + Z_W)||\frac{1}{jwC_{DL}}$$

Z_E is the impedance of the Randles electrical equivalent circuit model without the bulk resistance solution.

$$(R_{CT} + Z_W)||\frac{1}{jwC_{DL}} => \qquad \frac{1}{Z_E} = \frac{1}{R_{CT} + Z_W} + \frac{1}{\frac{1}{jwC_{DL}}}$$

$$\frac{1}{Z_E} = \frac{1}{R_{CT} + Z_W} + jwC_{DL} = \frac{1 + jwC_{DL}(R_{CT} + Z_W)}{R_{CT} + Z_W}$$

$$\frac{1}{Z_E} = \frac{1 + jwR_{CT}C_{DL} + jwZ_WC_{DL}}{R_{CT} + Z_W}$$

$$Z_E = \frac{R_{CT} + Z_W}{1 + jwR_{CT}C_{DL} + jwZ_W C_{DL}}$$

$$Z_E = \frac{R_{CT} + \frac{\sigma_D\ (1-j)}{\sqrt{w}}}{1 + jwR_{CT}C_{DL} + jwC_{DL}\frac{\sigma_D\ (1-j)}{\sqrt{w}}}$$

$$Z_E = \frac{R_{CT} + \sqrt{w^{-1}}\sigma_D\ (1-j)}{1 + jwR_{CT}C_{DL} + j\sqrt{w}\sigma_D C_{DL}\ (1-j)}$$

$$Z_E = \frac{R_{CT} + \sqrt{w^{-1}}\sigma_D - j\sqrt{w^{-1}}\sigma_D}{1 + jwR_{CT}C_{DL} + j\sqrt{w}\sigma_D C_{DL} + \sqrt{w}\sigma_D C_{DL}}$$

In order to change the impedance value to complex form the denominator is multiplied with conjugate of it:

$$Z_E = \frac{\left(R_{CT} + \sqrt{w^{-1}}\sigma_D - j\sqrt{w^{-1}}\sigma_D\right)\left(1 - jwR_{CT}C_{DL} - j\sqrt{w}\sigma_D C_{DL} + \sqrt{w}\sigma_D C_{DL}\right)}{\left(1 + \sqrt{w}\sigma_D C_{DL}\right)^2 + \left(wR_{CT}C_{DL} + \sqrt{w}\sigma_D C_{DL}\right)^2}$$

$$Z_E = \frac{N}{D}$$

$$N = \left(R_{CT} + \sqrt{w^{-1}}\sigma_D - j\sqrt{w^{-1}}\sigma_D\right)\left(1 - jwR_{CT}C_{DL} - j\sqrt{w}\sigma_D C_{DL} + \sqrt{w}\sigma_D C_{DL}\right)$$

$$N = R_{CT} + \sqrt{w^{-1}}\sigma_D - j\sqrt{w^{-1}}\sigma_D$$

$$-R_{CT}jwR_{CT}C_{DL} - \sqrt{w^{-1}}\sigma_D jwR_{CT}C_{DL} + j\sqrt{w^{-1}}\sigma_D jwR_{CT}C_{DL}$$

$$-R_{CT}j\sqrt{w}\sigma_D C_{DL} - \sqrt{w^{-1}}\sigma_D j\sqrt{w}\sigma_D C_{DL} + j\sqrt{w^{-1}}\sigma_D j\sqrt{w}\sigma_D C_{DL}$$

$$+R_{CT}\sqrt{w}\sigma_D C_{DL} + \sqrt{w^{-1}}\sigma_D\sqrt{w}\sigma_D C_{DL} - j\sqrt{w^{-1}}\sigma_D\sqrt{w}\sigma_D C_{DL}$$

$$N = R_{CT} + \sqrt{w^{-1}}\sigma_D - j\sqrt{w^{-1}}\sigma_D$$

$$+\sqrt{w}\sigma_D\, R_{CT}C_{DL} + \sigma_D{}^2 C_{DL} - j\sigma_D{}^2 C_{DL}$$

$$-jwR_{CT}{}^2 C_{DL} - j\sqrt{w}\sigma_D R_{CT}C_{DL} - \sqrt{w}\sigma_D R_{CT}C_{DL}$$

$$-j\sqrt{w}\sigma_D R_{CT}C_{DL} - j\sigma_D{}^2 C_{DL} - \sigma_D{}^2 C_{DL}$$

$$N = R_{CT} + \sqrt{w^{-1}}\sigma_D - j\sqrt{w^{-1}}\sigma_D - 2j\sigma_D{}^2 C_{DL} - jwR_{CT}{}^2 C_{DL} - 2j\sqrt{w}\sigma_D R_{CT}C_{DL}$$

$$N = R_{CT} + \sqrt{w^{-1}}\sigma_D - j\left(\sqrt{w^{-1}}\sigma_D + 2\sigma_D{}^2 C_{DL} + wR_{CT}{}^2 C_{DL} + 2\sqrt{w}\sigma_D R_{CT}C_{DL}\right)$$

$$D = \left(1 + \sqrt{w}\sigma_D C_{DL}\right)^2 + \left(wC_{DL}R_{CT} + \sqrt{w}\sigma_D C_{DL}\right)^2$$

$$Z_E = \frac{R_{CT} + \sqrt{w^{-1}}\sigma_D - j\left(\sqrt{w^{-1}}\sigma_D + 2\sigma_D{}^2 C_{DL} + wR_{CT}{}^2 C_{DL} + 2\sqrt{w}\sigma_D R_{CT}C_{DL}\right)}{\left(1 + \sqrt{w}\sigma_D C_{DL}\right)^2 + \left(wR_{CT}C_{DL} + \sqrt{w}\sigma_D C_{DL}\right)^2}$$

$$Z_E = \frac{R_{CT} + \sqrt{w^{-1}}\sigma_D}{\left(1 + \sqrt{w}\sigma_D C_{DL}\right)^2 + \left(wR_{CT}C_{DL} + \sqrt{w}\sigma_D C_{DL}\right)^2} - j\frac{\sqrt{w^{-1}}\sigma_D + 2\sigma_D{}^2 C_{DL} + wR_{CT}{}^2 C_{DL} + 2\sqrt{w}\sigma_D R_{CT}C_{DL}}{\left(1 + \sqrt{w}\sigma_D C_{DL}\right)^2 + \left(wR_{CT}C_{DL} + \sqrt{w}\sigma_D C_{DL}\right)^2}$$

Final result for impedance for Randles electrical equivalent circuit model is given Equation (A.3).

$$Z_{RM} = R_{sol} + \frac{R_{CT} + \sqrt{w^{-1}}\sigma_D}{\left(1+\sqrt{w}\sigma_D C_{DL}\right)^2 + \left(wR_{CT}C_{DL} + \sqrt{w}\sigma_D C_{DL}\right)^2} - j\frac{\sqrt{w^{-1}}\sigma_D + 2{\sigma_D}^2 C_{DL} + w{R_{CT}}^2 C_{DL} + 2\sqrt{w}\sigma_D R_{CT} C_{DL}}{\left(1+\sqrt{w}\sigma_D C_{DL}\right)^2 + \left(wR_{CT}C_{DL} + \sqrt{w}\sigma_D C_{DL}\right)^2} \quad \text{(A.3)}$$

B. Capacitance Value Derivation for Electrical Equivalent Circuit Model with a Resistor Parallel to a Capacitor

The impedance magnitude spectra and phase spectra are measured for FFChip with air filled channel. Then capacitance value is derived assuming the channel model is composed of a resistor parallel to a capacitor.

The reactance (X_C) for the capacitor is;

$$X_C = \frac{1}{jwC} \tag{B.4}$$

where w is the angular frequency, C is capacitance and j is √-1.

The complex impedance for FFChip with air filled channel electrical equivalent model is:

$$Z = R||X_C$$

$$\frac{1}{Z} = \frac{1}{R} + \frac{1}{X_C} = \frac{1}{R} + \frac{1}{\frac{1}{jwC}} = \frac{1}{R} + jwC = \frac{1 + jwRC}{R}$$

$$Z = \frac{R}{1 + jwRC} \tag{B.5}$$

where R is the resistance, Z is the impedance.

The complex impedance value can be written as a sum of real and imaginary components;

$$Z = Z_{real} + jZ_{im} \tag{B.6}$$

where Z_{real} is the real impedance value, Z_{im} is the imaginary impedance value.

Than the capacitance value can be derived as;

$$Z_{real} + jZ_{im} = \frac{R}{1 + jwRC}$$

$$(Z_{real} + jZ_{im})(1 + jwRC) = R$$

$$Z_{real} + jZ_{im} + jwRCZ_{real} - wRCZ_{im} = R$$

The real and imaginary components can be written as two equations as;

$$Z_{real} - wRCZ_{im} = R \tag{B.7}$$

$$jZ_{im} = -jwRCZ_{real} \tag{B.8}$$

Using Equation (B.7) and (B.8) Resistor value can be derived as;

$$\frac{-Z_{im}}{wZ_{real}} = RC$$

$$Z_{real} - w\frac{-Z_{im}}{wZ_{real}}Z_{im} = R$$

$$R = \frac{{Z_{real}}^2 + {Z_{im}}^2}{Z_{real}} \tag{B.9}$$

$$R = \frac{Z^2}{Z_{real}} \tag{B.10}$$

And finally using Equation (B.8) and (B.9) capacitance is;

$$Z_{im} = -w\left(\frac{{Z_{real}}^2 + {Z_{im}}^2}{Z_{real}}\right)CZ_{real}$$

$$C = -\frac{Z_{im}}{w\left({Z_{real}}^2 + {Z_{im}}^2\right)} \tag{B.11}$$

$$C = -\frac{Z_{im}}{wZ^2} \tag{B.12}$$